

# Theoretical and Numerical Investigation of the Physics of Microstructured Optical Fibres

*A thesis submitted for the degree of  
Doctor of Philosophy*

*by*

**Boris T. KUHLMEY**

**Department of Theoretical Physics  
School of Physics  
The University of Sydney  
Australia**

and through the cotutelle scheme

**Université de Droit, d'Économie et des Sciences d'Aix-Marseille  
(Aix Marseille III)  
France**

submitted May 2003, revised final edition printed in  
**June 2004**

*Title page of the French version:*

UNIVERSITÉ DE DROIT, D'ÉCONOMIE ET DES SCIENCES D'AIX-MARSEILLE  
(AIX MARSEILLE III)

N° attribué par la bibliothèque  
03AIX30024

**Theoretical and Numerical Investigation of the Physics of  
Microstructured Optical Fibres**

*Étude Théorique et Numérique de la Physique des Fibres Optiques Microstructurées*

**THÈSE**

pour obtenir le grade de

DOCTEUR DE L'UNIVERSITÉ DE DROIT, D'ÉCONOMIE ET DES SCIENCES  
D'AIX-MARSEILLE

*et, dans le cadre d'une cotutelle, de PhD de la School of Physics, University of Sydney*

**École Doctorale de Physique et des Sciences de la Matière**

*Discipline:* Optique et Photonique

présentée et soutenue publiquement par

**Boris KUHLMÉY**

le 4 juillet 2003

*Les Directeurs de thèse:* Daniel MAYSTRE et Ross McPHEDRAN

JURY:

Dr. J.-L. OUDAR	Directeur de Recherche, LPN / CNRS	Rapporteur
Pr. J. C. KNIGHT	Professeur, School of Physics, University of Bath	Rapporteur
Dr. Ph. LALANNE	Directeur de Recherche, Institut d'Optique / CNRS	Rapporteur
Pr. B. EGGLETON	Professeur, School of Physics, University of Sydney	Rapporteur
Dr. G. RENVERSEZ	Maître de Conférence, Université Aix Marseille III	Tuteur de thèse
Pr. R. C. McPHEDRAN	Professeur, School of Physics, University of Sydney	Directeur de thèse
Dr. D. MAYSTRE	Directeur de Recherche, Insitut Fresnel / CNRS	Directeur de thèse

Année: 2003

# Abstract

## Theoretical and Numerical Investigation of the Physics of Microstructured Optical Fibres

We describe the theory and implementation of a multipole method for calculating the modes of microstructured optical fibers (MOFs). We develop tools for exploiting results obtained through the multipole method, including a discrete Bloch transform. Using the multipole method, we study in detail the physical nature of solid core MOF modes, and establish a distinction between localized defect modes and extended modes. Defect modes, including the fundamental mode, can undergo a localization transition we identify with the mode's cutoff. We study numerically and theoretically the cutoff of the fundamental and the second mode extensively, and establish a cutoff diagram enabling us to predict with accuracy MOF properties, even for exotic MOF geometries. We study MOF dispersion and loss properties and develop unconventional MOF designs with low losses and ultra-flattened near-zero dispersion on a wide wavelength range. Using the cutoff-diagram we explain properties of these MOF designs.

## Étude Théorique et Numérique de la Physique des Fibres Optiques Microstructurées

Nous détaillons la théorie et l'implémentation d'une méthode multipolaire pour le calcul de modes de fibres optiques microstructurées (FOM). Nous développons des outils pour l'exploitation de résultats obtenus par la méthode multipolaire, dont une transformée de Bloch discrète. À l'aide de la méthode multipolaire, nous étudions en détail la nature physique de modes de FOMs à cœur plein. Nous distinguons entre modes de défaut localisés et modes étendus. Les modes de défaut, y compris le mode fondamental, peuvent subir une transition de localisation que nous identifions à la coupure du mode. Nous étudions numériquement et théoriquement la coupure du mode fondamental et du second mode, puis établissons un diagramme de régime opératoire nous permettant de prédire avec précision les propriétés de FOMs même aux géométries complexes. Nous étudions la dispersion et les pertes des FOMs et proposons un nouveau type de FOM à faible pertes et à courbe de dispersion ultra plate, proche de zéro sur une vaste plage de longueur d'ondes. En s'appuyant sur le diagramme de régime opératoire, nous expliquons les propriétés de ce nouveau type de FOMs.

# Acknowledgments

I have enough friends who have gone through, or are still doing, a PhD, and heard enough anonymous horror stories about PhDs to realize how lucky I have been throughout my own PhD. It appears that for many students, a PhD is a long and obscure time at the blurry frontier of student and working life, more often than not punctuated by times of doubts, vicious cycles of depressive unproductivity, meta-physical questioning on the significance of science in an immoral world ruled by the intricately interdependent super-powers of money, media, tradition and politics, and disillusion with academia and science itself. Not that I haven't gone through some of these tribulations myself, but they were kept to a strict minimum – in fact a welcome diversion from work necessary to avoid the ivory tower syndrome – thanks to the extraordinarily motivating environment I had the pleasure to work in, the constant and friendly attention of my supervisors, and many other factors I will attempt to recall and enumerate below.

While trying to remember and analyse the factors which contributed to the relative smoothness of my PhD, the contrast between the quite theoretical physics I dealt with during my postgraduate studies and the intricate complexity of the world we actually live in became strikingly obvious: whereas for the mostly linear phenomena I studied every effect has a straightforwardly and uniquely identifiable cause, in nature in general and for human interaction and personal development in particular, causality takes unfathomable detours and ramifications. The overly famous allegory of the butterfly in Brazil causing (or more accurately contributing to cause) a hurricane over the Caribbean came to my mind, and it seemed an impossible task to track back all the little butterflies at the tip of the branches of the fractal causal structure leading not to a hurricane but rather to the predominantly quite – yet exciting – stream of my PhD. Nevertheless, using the same imagery it appears that butterfly effects mostly influence *weather*, whereas *climate* is predominantly determined by larger, more identifiable effects, such as steady, planet-scaled oceanic and atmospheric streams. Identifying the people and events that played the role of the latter seemed much more feasible. (I will, however, certainly not resist the temptation of throwing in a few butterflies as they come to my mind.)

At the source of all lie of course my parents, without whom I wouldn't exist in the first place, and that essential gift of life shall not be unacknowledged. Although being born is a necessary condition for the completion of a PhD, it is certainly not sufficient: my parents wouldn't deserve their position at the top of the present acknowledgments had they contented themselves with dropping yet another being on this planet. Instead, they raised my brother and myself with care and attention, the right balance between parental authority and personal freedom, in a climate of tolerance and justice, giving us access to high quality education, helping us out whenever needed without rendering us dependent, in short they achieved the balance most parents endeavour but few achieve. Although I don't believe they intended for

me to become a scientist, they certainly didn't try to discourage me once I had caught the passion of science (to the point of indulging my whim of wanting a Helium-Neon laser for my thirteenth birthday). My brother also played an important role in my personal development – among many other things by being a perfect example I admired and tried to follow. In terms of academic achievement he set very high standards, and without the untold challenge of attempting to do as well as he did (whether this challenge came out of jealousy, sibling rivalry or something else I am not sure), I would certainly have been more slack about my studies.

Next in the list come the teachers and lecturers I had the privilege and pleasure of being taught by, especially, but not solely, my science teachers in high-school. More specifically, I'd like to thank my biology teachers (M. and Mme Margerie and especially Mlle Castel), who initiated me into the *méthode scientifique* more than any other teachers or lecturers later on; they believed I would continue my studies in biology – it is probably most ungrateful to their more than praiseworthy efforts that I didn't. M. Monnet, my maths teacher during the final year at high-school is without any doubt the one who gave me the first glimpse of the beauty of mathematics; M. Goldsztejn and M. Mantin in first and second year University deepened my appreciation of that beauty. Among my physics lecturers Dr. Barbet-Massin is certainly the one who left the most lasting and awe-inspiring impression, and is probably the one who made the difference, making me chose physics rather than biology or computer sciences for my further studies.

Now regarding the PhD itself, first I'd like to thank the referees for accepting the tedious task of reading the entire thesis and coming all the way to Marseille for the defence. I thank them also for their insightful comments and questions, my only regret is that some of them couldn't stay for the post-defence barbecue which I hoped to be a modest compensation for their work.

My deepest gratitude goes of course to my three supervisors – Dr. Gilles Renversez, Dr. Daniel Maystre and Prof. Ross McPhedran. The three of them have contributed towards the achievement of my thesis in different, complementary, essential ways. Gilles, a hard and hence demanding worker, has been a constant support throughout the PhD, of course as far as research is concerned, but also for practical and administrative matters. He didn't shy away from doing all derivations himself to check my results or from staying at the lab until undue hours when I needed his help, but at the same time he managed to leave me a total freedom in my research. He is an exceptionally reliable person whom I am proud to be able to call a friend. I should add that I was his first PhD student, which I have heard has made him a little nervous at the beginning, but he has proved that he is an excellent supervisor, and his future PhD students – and I hope he will have plenty of them – should deem themselves extremely lucky.

I knew Ross from a research project done under his supervision two years prior to the beginning of my PhD; it is during that research project that I discovered that theoretical and numerical physics are at least as beautiful, interesting, rewarding and fascinating as experimental physics. That research project having been an extremely positive experience, I contacted Ross a year and a half later regarding a possible PhD. He put forward the possibility of a *cotutelle* PhD between Marseille and Sydney, and soon we agreed on the topic of the PhD, which I was very enthusiastic about. I am most grateful to Ross for offering me that opportunity to work on a current topic of research at the edge of theory and applications, in an international environment and under shared supervision through the cotutelle scheme. Over the years, Ross has become much more than just an excellent, as motivating as demanding,

supervisor; I consider him a friend and mentor, his wisdom will remain an inspiration, his wit and anecdotes a delight. I'm looking forward to collaborate with him for many more years.

I had a more distant relationship with Daniel Maystre, since it was Gilles' assigned task and vocation to supervise me on a day to day basis in Marseille. Dr. Maystre gave Gilles and myself the initial impulse for the work, and kept on giving us much appreciated guidance throughout the PhD. I like to compare him to an oracle whom we went to seek answers from when we ran out of inspiration; his wisdom and breadth of knowledge certainly support the likening, but thankfully his answers didn't come in riddles – at least most of the time.

I consider Prof. Martijn de Sterke to have been my second supervisor in Sydney, although officially he wasn't. Martijn's dynamism, frankness and pragmatism are exemplary and appreciated by everyone I know who had the privilege to work with him, including myself. Without his comments and advice my work would probably have been much more of a random walk and hence much less productive.

It was also a great pleasure to work with Prof. Lindsay Botten, also known as the wizard of matrices, who – as wizards do – has an inclination for manipulating the most cryptic runes with the most powerful meaning, but – unlike wizards – doesn't shy away from explaining them in terms understandable to common mortals.

One of the things I appreciated most in the Department of Theoretical Physics at the University of Sydney was the fact that it was multidisciplinary, covering most aspects of modern theoretical physics. This made my collaboration with Prof. Peter Robinson possible, who brought his knowledge on phase transitions and critical systems without which our study on modal cutoffs would probably have been much less fruitful. Other people at the University of Sydney I'd like to thank for interesting discussions include the whole Department of Theoretical Physics (especially Dr. Ara Asatryan, for insightful comments on localization theory, Dr. Nicolae Nicorovici, for bug reports and comments, and of course Tom White for many things, but I'll come back to that), and colleagues from the Optical Fibre Technology Centre (especially Dr. Maryanne Large and Dr. Leon Poladian).

I also had the pleasure of frequent e-mail contact with A. Prof. Niels Asger Mortensen, who was working with Crystal Fibre at that time. He raised many very interesting questions, and our e-mail conversations were scientifically very fertile.

The highlight of my stay in Marseille were certainly the mostly political (but sometimes also scientific) debates occurring during the daily lunch and coffee breaks, bringing together almost all my colleagues from the CLARTE and TEM teams at the Institut Fresnel. Among them Dr. Frédéric Zolla and Dr. Anne Sentenac were probably the loudest and most entertaining. Besides politics, I also had many interesting scientific discussion with Frédéric Zolla, although he often assumed my knowledge of spectral theory was much broader than it actually was or should be, Prof. Gérard Tayeb, Prof. André Nicolet and Dr. Stefan Enoch. Also in Marseille, I'd like to thank Gabriel Soriano and Niña Gralak for many things but especially for food and accommodation, Charles Antoine Guérin, Boris Gralak and Nicolas Guérin. A big thank you to Mireille Frizzi and Françoise Maillet for helping out with all the administrative matters. Finally for Marseille, I'm very much indebted to Anthony Dubois, Joelle and Frédéric Forestier (as well as, again, to Tom White) for helping out (*le mot est bien faible...*) with the post-defence barbecue. Without them it just wouldn't have happened at all. Merci infiniment !!!!

Mentioning Frédéric Forestier, who is the system administrator of the CLARTE and TEM teams at the Insitut Fresnel, I'd like to acknowledge his work, along with the work of the sysadmins in Sydney, Sebastian Juraszek, Tony Monger and George Shan. We (*we* including everyone who uses a computer) wouldn't get much work done without the sysadmins' help

and constant efforts at maintaining the hardware and software infrastructure.

None of the work in the present PhD would have been possible without the support of the French educational system. By *support* I don't only mean the financial support, from which I have benefited since my third year of studies, but also the qualitative support, from the simple fact that a high quality education does exist in France, to the fact that education and studies (*still...*) are basically free of charge. I hope that the current changes in the French education system will not negatively affect this relative guarantee of equal opportunities.

More specifically, I'd like to congratulate whoever has initiated the *cotutelle* scheme for PhDs. It is a great invention, and I can only encourage all starting PhD students to consider doing their PhD in cotutelle. Working in two different laboratories, in two different countries, and with two different supervisors is highly beneficial in many ways. It enables one to be confronted with different approaches of science, different point of views, different work atmospheres. I mentioned at the beginning of the present acknowledgments that I know quite a few cases of PhD students giving up in the midst of their thesis. I am convinced that most of these students wouldn't have given up had they been given the chance of seeing science from another perspective in another lab, another country.

In that context I'd also like to thank the *Ministère de l'Éducation Nationale, de l'Enseignement Supérieur et de la Recherche*, the French Embassy in Australia, and the University of Sydney for financial support specific to the cotutelle. At the French Embassy in Australia, I'd like to express my gratitude to Alain Moulet, the *Attaché pour la Science et la Technologie*, who is universally recognized for having done a magnificent job in terms of initiating, coordinating and promoting the cotutelle arrangements and associated funding.

Tom White, whom I have already mentioned several times above, deserves a separate paragraph in the present acknowledgments. He has indeed helped me out in many ways throughout the past three years. As a colleague, he has helped me significantly in the early stages of implementing the multipole method. As a friend, he arranged for accommodation when I first arrived in Sydney, organized bushwalks in the Barrington Tops and in Tasmania and invited me to stay at his family's place in Tasmania. As a housemate, not only has he endured my most excessive cooking crises, he has actively participated in them, taking up the most ungrateful peeling, slicing, seeding or cleaning tasks I could imagine, and was even able to show enthusiasm when asked to carve half-millimetre apple slices or spiral segments in grapefruits. He is the best food-carver I know, and more generally the best cooking assistant I ever had the pleasure to work with. His patience has no limits, and his friendliness and helpfulness are incommensurable.

I'm also grateful to my other flatmates over the years of my PhD, Stéphane Ravier in Marseille, Fiona Reardon, Mert Akin and later Kathryn Topp and Ross McKerracher in Sydney, among so many other things especially for supporting my culinary experiments and washing up the literally thousands of things I can dirty within hours while cooking. My flatmates in Sydney shall also be thanked for pushing me to take up sport, and more generally for making me want to come back to Sydney.

My flatmates weren't the only ones who suffered from my cooking, and all the others who at some point or other have innocently declared themselves willing to help me in my cooking, accepting such tedious and unrewarding tasks as peeling and seeding grapes, carving roses in potatoes or filling 150 profiteroles shall not be forgotten.

Nor should be forgotten all those who have initiated me into the art of cooking: my mother and grandmothers, Noémie Favier, Jean-Marc Hénique, who all directly taught me, but also

Jean Brouilly, for making me discover *haute cuisine* good enough to bring tears to my eyes and for lifting my psychological barrier to cheese, Michel and Pierre Troisgros, Alain Ducasse and Franck Cerutti for making me understand the full meaning of the word perfection, and Tetsuya Wakuda for proving that Australia's chefs can be at least as good as the best French chefs.

And last but most importantly, I'd like to thank all my friends for being what they are. Tommy Wommy, Zoe, Stephen, Karen, Félicien, Antoine, Delph, Babeth, Pluc, Ben, Seb, Greg, Carron, Rachel, Cathrine, Kathryn, Tom, Thomas, Severine, Gilles, Isa, Emilie, Jérem, Marco, Solène, Marion, Marie, Steph, Mert, Fi, Coops, Drew, Rémi, Claude, Florent, Stan, Cécile, Vincent, Nathalie, Maraboule, Isaboule, Noémie, Sam, Didier... you all are the answer to the question of the meaning of life.

# Preface

The work presented in this thesis was carried out at the Institut Fresnel, Université d'Aix-Marseille III, France and at the School of Physics, University of Sydney, Australia. Most of the work was done in close collaboration with researchers from these institutions, and has been published in several journals under the name of all participating researchers (see Appendix I). It is hence necessary to detail which part of the work presented in this thesis is due to the author. Chapters 1 and 2 are merely an introduction and don't present any new results. Chapter 3 presents the theory of the multipole method used for the study of microstructured optical fibres. Both the Institut Fresnel and the School of Physics, University of Sydney, have used multipole methods for studies of gratings and photonic crystals well before the work presented in this thesis started. The extension of this method to the study of microstructured optical fibres presented in Chapter 3 was done independently and simultaneously in slightly different ways at the School of Physics, University of Sydney by T. White, R. C. McPhedran, C. M. de Sterke and L. C. Botten, and at the Institut Fresnel by D. Maystre, G. Renversez and the author of this thesis. After a few months, R. C. McPhedran, L. C. Botten and the author sorted out the slight differences between both formalisms and agreed on the unified formalism presented in Ref. [1] and in Chapter 3. Chapter 4 presents the implementation of the multipole method, collecting experience gained by T. White and the author when implementing the method. In particular, T. White provided Figures 4.7 and 4.8 in Chapter 4. Chapters 5-7 result mainly from the author's work at the School of Physics, University of Sydney. However, through very frequent discussions, the work has benefited from the knowledge and guidance of many people from the School of Physics, especially Ross McPhedran, Martijn de Sterke, Thomas White and Peter Robinson. The idea of using a Fourier transform to analyse modes came from M. de Sterke, and the idea of the Bloch transform emerged during a discussion between R. McPhedran and the author. P. Robinson brought his knowledge of phase transitions and extrapolations from finite to infinite systems essential to the studies of scaling laws in Chapter 7. Chapter 8 results mainly from the work of G. Renversez, who directed and run all dispersion simulations. The author's contribution to the work on dispersion merely consisted in providing the software and suggesting a few interpretations. The derivation of the Wijngaard identity in Appendix B is the work of D. Maystre. The correct choice of the square root described in Appendix A results from many discussions between the Australian and the French team, but the correct square root cutoff for  $n_i$  was established by G. Renversez who generalized earlier work by M. Nevière. Finally, regarding the culinary part of the present thesis, the recipes for two side dishes are directly taken from Ref. [2], while all other recipes are the fruit of the author's culinary experiments undertaken during his PhD.

Author's signature:

# Contents

<b>Preface</b>	<b>9</b>
<b>Amuse-gueule: Sashimi de Thon, Gingembre Frais et Nougatine de Sésame</b>	<b>14</b>
<b>1 Introduction</b>	<b>15</b>
<b>Mise en bouche: Laksa de Cigale des Mers et Shiitake</b>	<b>20</b>
<b>2 Optical Fibres, Photonic Crystals and Leaky Modes</b>	<b>21</b>
2.1 Conventional Optical Fibres . . . . .	21
2.1.1 Guidance Mechanism . . . . .	21
2.1.2 Fibre Modes . . . . .	22
2.1.3 Properties . . . . .	23
2.2 Photonic Crystals . . . . .	27
2.2.1 One Dimension: Bragg Mirrors . . . . .	27
2.2.2 Photonic Crystals in Two and Three Dimensions . . . . .	28
2.3 Guiding Light with Photonic Crystals . . . . .	29
2.3.1 Bragg Fibres . . . . .	29
2.3.2 Photonic Crystal Fibres, Microstructured Optical Fibres and Holey Fibres	30
2.4 Leaky Modes . . . . .	33
2.4.1 Confinement Losses . . . . .	33
2.4.2 Modes of a Leaky Structure . . . . .	34
2.4.3 Heuristic Approach to Physical Properties of Leaky Modes . . . . .	34
2.4.4 Mathematical Considerations . . . . .	37
2.4.5 Spectral Considerations . . . . .	38
<b>Hors d'œuvre: Escalope de Crocodile d'Estuaire en Croûte d'Herbes</b>	<b>39</b>
<b>3 The Multipole Method: Fundamentals</b>	<b>40</b>
3.1 Introduction . . . . .	40
3.2 Multipole Formulation . . . . .	41
3.2.1 Geometry . . . . .	41
3.2.2 Choice of Propagating Fields . . . . .	42
3.2.3 Multipole Method: Simplified Approach . . . . .	42
3.2.4 Rigorous Formulation of the Field Identities . . . . .	46
3.2.5 Boundary Conditions and Field Coupling . . . . .	49
3.2.6 Derivation of the Rayleigh Identity . . . . .	49

<i>CONTENTS</i>	11
-----------------	----

<b>Note on the Field Distribution Figures</b>	<b>51</b>
---	-----------

<b>Entrée : Daurade et Écrevisses, Tomate «Cariocas»</b>	<b>53</b>
--	-----------

<b>4 The Multipole Method: Implementation</b>	<b>55</b>
---	-----------

4.1	Introduction . . . . .	55
4.2	Geometry . . . . .	55
4.3	Mode Location . . . . .	56
4.3.1	Solving the Rayleigh Identity . . . . .	56
4.3.2	Implementation . . . . .	57
4.4	Computing Dispersion Characteristics . . . . .	58
4.5	Symmetries . . . . .	59
4.5.1	Symmetry Properties of Modes . . . . .	59
4.5.2	Using the Symmetries . . . . .	60
4.5.3	Implementation . . . . .	61
4.6	Software and Computational Demands . . . . .	61
4.7	Validation and Self Consistency . . . . .	62
4.7.1	Convergence and Wijngaard Test . . . . .	62
4.7.2	Comparison with Other Methods . . . . .	65
4.7.3	Theory and Experiment . . . . .	65

<b>Trou: Granité du Vigneron</b>	<b>69</b>
----------------------------------	-----------

<b>5 Tools</b>	<b>70</b>
----------------	-----------

5.1	Lowering the Loss Limit . . . . .	70
5.2	Bloch Transform . . . . .	72
5.2.1	Definition . . . . .	72
5.2.2	Basic Properties . . . . .	74
5.2.3	Implementation . . . . .	75
5.2.4	Examples . . . . .	76
5.2.5	Advanced Properties . . . . .	77
5.2.6	Bloch Transform for Other Methods . . . . .	82

<b>Plat de Rôt : Filet de Kangourou Sauce Poivrade «Oz»</b>	<b>84</b>
---	-----------

<b>6 Modes in MOFs</b>	<b>86</b>
------------------------	-----------

6.1	Introduction . . . . .	86
6.2	Identifying Modes . . . . .	86
6.2.1	Differences to Conventional Fibres . . . . .	86
6.2.2	Similar Modes of Similar Structures . . . . .	87
6.2.3	Using the Bloch Transform . . . . .	89
6.3	Continuous Growth of Rings . . . . .	89
6.3.1	Mode Trajectories and Identification . . . . .	90
6.3.2	Evolution of Mode Properties . . . . .	91
6.3.3	Extended and Localized Modes . . . . .	94

<b>Fromage: Chèvre frais, Raisin Chasselas, Tuile au Thé Vert</b>	<b>100</b>
---	------------

<b>7</b>	<b>Modal Cutoff</b>	<b>101</b>
7.1	Introduction . . . . .	101
7.2	Modal Cutoff of the Second Mode . . . . .	102
7.2.1	Towards the Endlessly Single-Mode Fibre . . . . .	102
7.2.2	Characterization of the Transition – Definition of Cutoff . . . . .	104
7.2.3	Scaling Properties . . . . .	106
7.2.4	Second Mode “Phase Diagram” . . . . .	112
7.3	Modal Cutoff of the Fundamental Mode . . . . .	115
7.3.1	Observation of the Cutoff . . . . .	115
7.3.2	Scaling Properties . . . . .	116
7.4	Asymptotic Analysis of Cutoffs . . . . .	121
7.4.1	Asymptotic Model for Long Wavelengths: CF1 Model . . . . .	122
7.4.2	Asymptotic Model for Short Wavelengths: CF2 Model . . . . .	126
7.5	Interpretation of the Cutoff . . . . .	133
7.5.1	Fundamental Mode . . . . .	133
7.5.2	Second Mode . . . . .	137
7.5.3	Study of the Cutoff-Point and Disclaimer . . . . .	138
7.6	MOF Phase Diagrams . . . . .	139
7.6.1	Fundamental Mode Phase Diagram . . . . .	139
7.6.2	Using the Phase Diagram . . . . .	142
7.6.3	Towards Other Phase Diagrams and Charts of Operation . . . . .	147
7.6.4	Impact on Results of the Previous Chapters . . . . .	147
	<b>Dessert : Stratifié de Chocolat, de Pralin et d’Orange</b>	<b>149</b>
<b>8</b>	<b>Dispersion Properties</b>	<b>151</b>
8.1	Introduction . . . . .	151
8.2	Chromatic Dispersion and Losses of Microstructured Optical Fibers . . . . .	152
8.2.1	Introduction and Background . . . . .	152
8.2.2	Validation . . . . .	153
8.2.3	Results . . . . .	154
8.2.4	Conclusion and Discussion . . . . .	158
8.3	“Chromatic Dispersion and Losses of MOFs”: Comments . . . . .	158
8.4	Dispersion management with microstructured optical fibers: Ultra-flattened chromatic dispersion with low losses . . . . .	161
8.5	“Dispersion management with MOFs...”: Comments . . . . .	167
8.5.1	Conventional MOF Designs . . . . .	167
8.5.2	New MOF Designs . . . . .	167
8.6	Theory and Experiment . . . . .	169
	<b>Conclusion</b>	<b>171</b>
<b>A</b>	<b>Choice of the Square Roots</b>	<b>172</b>
<b>B</b>	<b>Derivation of the Wijngaard expansion</b>	<b>175</b>

<b>C</b>	<b>Change of basis</b>	<b>177</b>
C.1	Cylinder to Cylinder Conversion . . . . .	177
C.2	Jacket to Cylinder Conversion . . . . .	177
C.3	Cylinder to Jacket Conversion . . . . .	178
<b>D</b>	<b>Scattering Matrices in Conical Incidence</b>	<b>179</b>
<b>E</b>	<b>Algorithm</b>	<b>182</b>
<b>F</b>	<b>Symmetrization of modes</b>	<b>184</b>
<b>G</b>	<b>Bloch Transform and Fourier Transform</b>	<b>187</b>
<b>H</b>	<b>Modes and Mode Classes</b>	<b>189</b>
<b>I</b>	<b>Publications</b>	<b>191</b>
<b>J</b>	<b>Notations</b>	<b>194</b>

*This thesis includes a CD-ROM containing a colour version of the manuscript and a document detailing some of the numerical experiments undertaken to validate our code (in French).*

Amuse-gueule :

## Sashimi de Thon, Gingembre Frais, Nougatine de Sésame

*Tuna Sashimi, Ginger, Sesame Nougatine*

**Pour 6 personnes :**

*200 g de thon qualité sashimi  
50 g de graines de sésame  
150 g de sucre  
2 cuillerée à soupe de miel  
huile de sésame  
gingembre frais*

**D**ÉTAILLER le thon en six cylindres de 2 cm de diamètre et de 3 cm de hauteur à l'aide d'un emporte pièce. Conserver au réfrigérateur. Raper une petite quantité de gingembre.

**P**RÉPARER la nougatine au sésame : chauffer le miel dans une casserole en inox à fond épais, le répartir afin qu'il recouvre bien le fond de la casserole. Ajouter le sucre. Cuire jusqu'à obtention d'un caramel doré. Arrêter la cuisson et ajouter les graines de sésame ainsi qu'une cuillerée à café d'huile de sésame. Couler un peu de caramel sur une feuille de papier sulfurisée huilée à l'huile de sésame, recouvrir d'une autre feuille de papier sulfurisée huilée et étaler rapidement au rouleau à pâtisserie. La graine de sésame limitera l'épaisseur de la plaque de caramel. Laisser reposer cinq à dix secondes. Détailler des disques de nougatine au sésame dans cette plaque à l'aide de l'emporte pièce utilisé lors de la découpe du thon. Recommencer l'opération jusqu'à avoir six disques de nougatine. Les disques peuvent être conservés dans un boîte métallique, au sec.

**M**ONTER les sashimis : Sur chaque cylindre de thon déposer une pointe de couteau de gingembre frais, recouvrir d'un disque de nougatine, servir sans attendre.

# Chapter 1

## Introduction

With the invention of lasers and the development of optical fibres able to carry light over hundreds of kilometres came the advent of a new era of worldwide high speed telecommunications, with consequences reaching from benefits in everyday life to the reshaping of the world economy. The first visible effects were cheaper transcontinental phone connections, and the latest certainly the “Internet revolution”. Although one can bemoan the fact that the technologically unprecedented possibilities for people and populations to communicate don’t yet seem to have brought better understanding and tolerance between cultures, the optimist will say that this is only a matter of time. Indeed it is easy to forget (especially for younger generations) that optical fibres “transparent” enough to make long haul data transfer possible were invented only about 30 years ago or that the first transatlantic optical fibre was laid less than 20 years ago.

For a decade, the speed (or bandwidth) at which a single optical fibre could carry data seemed pretty much unlimited. Every now and then the bandwidth of telecommunication networks became too small, but it appeared that the limitation was not so much due to the intrinsic limits of the fibre, but much more to the limited speed of the signal sources and receivers, so that increasing the bandwidth was for a long time a matter of improving sources and receivers. Intrinsic limits to the bandwidth of optical fibres had been predicted as early as the 1970s, but seemed as theoretical and out of reach as the speed of light for aeroplanes. Research on increasing the bandwidth of optical networks in those times was more a question of how to get the best out of fibres through injecting more information, *e.g.* through multiplexing, than a question of improving optical fibres. Of course the new data injection principles found required new types of fibres, but these were merely more or less adapted versions of the original step index fibre.<sup>1</sup> Given the incredible possibilities offered by existing fibres, there was little eagerness to try to find something radically new, as there was little reason to believe that anything better could ever exist.

It is only in recent years, with the exponentially increasing demand for bandwidth (essentially due to the popularization of the Internet and multimedia contents) along with the progress made in high speed electronics and optoelectronics, that the intrinsic limits of optical fibres were reached. New, higher density data injection is now possible, but because of non-linear effects, polarization mode dispersion and other effects we will detail in the next Chapter, good old optical fibres can’t keep pace anymore.

---

<sup>1</sup>What we claim here is that the fibres were based on the same principle of guidance as step index fibres, which doesn’t in any way detract from the work and ingenuity needed for the task of designing such fibres.

Fortunately, at about the same time, the principles of photonic crystals were discovered, leading to the suggestion of radically new mechanisms of light guidance. In the early 1990s the idea of optical fibres using photonic crystal claddings emerged, and after a few years the first photonic crystal fibre was demonstrated. The very first experimental work on these fibres already showed that they could have unprecedented properties and overcome many limitations intrinsic to step index fibres. With photonic crystal fibres, almost everything seemed feasible, from *guiding light in vacuum*, hence overcoming all limitations inherent to interactions between light and matter, to achieving dispersion properties unthinkable with step index fibres, from enhancing non-linear effects through extreme confinement of light to minimizing the same non-linear effects through very large core single mode fibres. The discovery of these possibilities brought prospects of totally new fields of application for fibre optics, such as optical fibres for high power applications, optical fibres for non-conventional wavelength ranges (*e.g.* far infrared, ultra violet), revolutionary optical fibre sensors, particle guidance through hollow core optical fibres, extremely versatile dispersion management, compact high precision metrology, and low-threshold non-linear optics.

Unsurprisingly, the field of photonic crystal fibres became extremely popular, and soon numerous research groups around the world started drawing all kinds of photonic crystal fibres, with hollow or solid cores, with regular or irregular structures, using silica or polymers. Inevitably the pioneers of the field all gave those fibres different names – photonic crystal fibres (PCF), microstructured optical fibres (MOF), crystal fibres (CF), holey fibres (HF) – each having different connotations; we will discuss the meaning of each of these in the next Chapter. In the present thesis we will concentrate on one type of photonic crystal fibres, called solid core microstructured optical fibres (solid core MOFs). At the beginning of our work, the first of these fibres had appeared only three years earlier, so that their study was still in its infancy. Some of their most promising properties had already been discovered either experimentally or through early models of their guidance mechanism, but numerous unknowns remained:

- The first models of the guidance in these fibres assumed the photonic crystal cladding to extend from the fibre core to infinity. The effect of the finite width of the photonic crystal cladding in real fibres could not be accounted for. There was no estimate whatsoever of tunneling losses due to the finite width of the cladding, and to a great extent it remained unknown whether these fibres could have low losses compatible with applications. More generally, the influence of the diameter of the photonic crystal cladding on mode properties was completely unexplored.
- One of the first properties of solid core MOFs discovered is that they can be single-mode over an infinite range of wavelengths. But since losses are inevitable in these fibres, all modes are actually leaky. Given that there are in fact an infinity of leaky modes, the definition of a “single mode fibre” was to be clarified. A clear distinction between the few guided or confined modes, and the remaining cladding modes was yet to be drawn.
- Early fibres were more or less designed through trial and error or using early models with limited predictive capabilities, and only a few values of hole size and hole to hole spacing had been tried. The full range of these parameters had still to be explored with regard to losses, dispersion, confinement and number of modes. Further, the domain of validity of the early models was to be clarified.

From the above list it becomes clear that some unknowns weren’t so much unexplored because

of the youth of the field but more because of the lack of an accurate and versatile tool to model MOFs with finite cross section.<sup>2</sup>

In the framework of the present thesis we have developed a rigorous formulation for MOFs with finite claddings. The formulation enables the precise and efficient computation of modes, their losses and chromatic dispersion. Using this tool, we have explored in detail properties of solid core MOFs. In particular, from a systematic analysis of MOF modes, we have established a clear criterion for the distinction between cladding and confined modes, clarifying the question of the definition of the number of modes.

We have studied the confinement and losses of modes with varying MOF geometry (hole diameter and spacing, width of the cladding), and have discovered that mode properties don't necessarily converge with increasing cladding diameter, even for apparently confined modes.

The study has brought us to define modal cutoff in MOFs, taking the form of a mode transition from confined to unconfined states. We have studied extensively the second mode cutoff, and established the first precise cutoff diagram marking the limits between single and multi-mode guidance in MOFs.

We have shown that unlike step index fibres and contrary to popular belief, solid core MOFs have a fundamental mode cutoff. We have studied the latter numerically and analytically, using an asymptotic analysis of the mode before and beyond cutoff. This has brought insights into the physics of the cutoff and has led us to partition the parameter space of MOFs into three regions corresponding to different operation regimes. Qualitative and quantitative properties of the fundamental mode differ significantly from one region to another, and it is only in one of these regions that mode properties differing significantly from those of step index fibres can be achieved. We have drawn the contours of this region in parameter space, and have found all published results concerning MOFs with unconventional properties to be within this region.

We have found the map of the different operation regimes to be of great generality and of fundamental interest in designing innovative MOFs. It further gives an answer to the question of validity of the well known "effective index" model and of models using the supercell approximation.

Finally, we have studied the fundamental mode chromatic dispersion systematically along with losses and had to face the truth that most promising dispersion properties are found close to the fundamental mode cutoff and hence are associated with large losses. Using the map of operation regions, we developed unconventional MOF designs overcoming this difficulty, and designed new types of solid core MOFs associating highly desirable dispersion properties with very low losses.

The remainder of the present thesis is arranged as follows:

Chapter 2 is a general technical introduction to microstructured optical fibres. We review the principles and main properties of conventional step index fibres as well as characteristics desirable for applications, with an emphasis on telecommunication applications. We give a short overview of photonic crystals and how they can be used to achieve novel types of waveguides. We introduce the different types of photonic crystal fibres and what can be expected from them. Finally, we discuss the concept of leaky modes.

Chapter 3 presents the multipole method we use to model MOFs. We briefly evoke other methods available for the simulation of MOFs, their main advantages and limitations. We then use an heuristic approach to understand the physics behind the multipole method before tackling the slightly tedious task of deriving the formulation mathematically.

---

<sup>2</sup>Note that the lack of accurate model is certainly a consequence of the youth of the field.

In Chapter 4 we examine the numerical implementation of the multipole method. We discuss the algorithm used to solve the equation given by the multipole method, the choice of parameters to guarantee accurate results and the use of symmetry properties. We briefly present the software resulting from these considerations before checking simulation results through self-consistency tests and through comparisons with experimental data and with results obtained through other numerical methods.

Chapter 5 introduces two numerical tools we have developed to exploit the results given by the multipole method. The first tool, derived from Poynting's theorem, lowers the limit of the smallest losses the multipole method can compute. The second tool, which we have called *Bloch transform*, is similar to the Fourier transform but is tailored to project MOF modes on a basis of Bloch waves rather than plane waves. We define the Bloch transform in the context of the multipole method, noting that it could be used with other models, and derive a few of its properties. The most useful property of the Bloch transform is that it can be used to follow modes with accuracy and enables us to draw conclusions regarding the physical nature of modes.

Chapter 6 is a survey of modes encountered in solid core MOFs. We show that the Bloch transform is a powerful means of identifying modes. We analyse the behaviour of various modes with varying MOF size. This leads us to distinguish between two fundamentally different types of modes: extended modes, resulting from resonances of Bloch waves, and defect modes, which are confined in the core. A secondary result with some practical consequences is that increasing the cladding width does not necessarily give lower losses if the outer holes are not of the same size as the inner holes.

Chapter 7 is a detailed study of modal cutoff in solid core MOFs. We study the evolution of the second mode with varying fibre parameters and discover that the mode can be in two qualitatively very different states, one confined in the core, the other extending over the whole cladding. We analyse in detail these two states as well as the transition leading from one to the other. The locus in parameter space of the transition appears to be largely independent of the number of rings of holes surrounding the core, whereas the transition becomes increasingly sharp with increasing number of rings. This enables us to define a precise transition point which we identify with the second mode cutoff. We establish the “phase-diagram” of the second mode, showing the locus of the cutoff as a function of fibre parameters. We determine the precise limit of the endlessly-single mode regime. A similar study for the fundamental mode shows that there is a fundamental mode cutoff, with properties differing slightly from those of the second mode cutoff. We use two asymptotic models to get insights into the physics of MOF mode cutoff, giving us a better understanding of mode properties on each side of the cutoff but also near cutoff. The results from the asymptotic analysis lead us to define a *cutoff point* and a *cutoff region* for the fundamental mode. It appears that three operation regimes with very different mode properties can be distinguished. Only two of these are of practical interest, one with strong mode confinement and another with broader field distributions. The former is of interest for single mode guidance with strong confinement, whereas the latter, the cutoff region, is where highly adjustable chromatic dispersion can be achieved. We provide a map of the parameter space summarizing the operating regimes of MOFs, and show for a few examples how this map can be used for deterministic MOF design. Finally, we discuss the validity of other MOF modeling tools in each region of operation.

Chapter 8 deals with dispersion properties of solid core MOFs. The chapter consists of two of our recent papers we have included ‘as is’ and commented on in the light of the operating regime diagram from the preceding chapter. The first paper is a general analysis

of the dependence of chromatic dispersion *and* losses on fibre parameters, including fibre size, concluding with the observation that most previously-suggested, near-zero dispersion-shifted MOF designs would not be usable in practice because of prohibitive losses. The second paper suggests innovative MOF designs achieving both low losses and desirable dispersion properties.

Mise en bouche :

## Laksa de Cigale des Mers et Shiitake

*Morton Bay Bug and Shiitake Laksa*

**Pour 6 personnes :**

*4 cigales de mer cuites*  
*4 champignons*  
*«shiitake» (ou lentin*  
*comestible)*  
*1 citron vert*  
*6 feuilles de citron vert*  
*1 piment rouge frais de*  
*taille moyenne*  
*30 cl de crème de noix*  
*de coco*  
*un tiers de botte de*  
*coriandre fraîche*  
*4 cl de cognac*  
*50 g de beurre clarifié*  
*1 cuillerée à café*  
*d'huile de sésame*  
*16 grains de coriandre*  
*poivre noir et poivre de*  
*setchuan*  
*sel*  
*Et, éventuellement :*  
*Sauce soja*  
*Gingembre frais*

**D**ÉCORTIQUER les queues des cigales de mer, les couper en dés de 5 mm de côté. Réserver. Concasser les carcasses des cigales de mer, les faire revenir à feu vif avec le beurre dans une sauteuse. Quand les carcasses sont bien colorées, déglacer avec le cognac. Laisser réduire à sec puis ajouter 50 cl d'eau. Laisser frémir une demi heure. Passer le contenu de la sauteuse au chinois, en pressant bien afin de recueillir le maximum de jus. Faire réduire le jus jusqu'à n'en avoir plus que 10 cl.

**E**NLEVER les graines et les parties blanches du piment. Le hacher très finement au couteau. Parer et nettoyer les shiitakes, les déliter en cubes de 5 mm de côté. Réserver 4 belles feuilles de coriandre, ciseler grossièrement le reste des feuilles. Prélever le zeste du citron vert à l'aide d'un zesteur, hacher le zeste finement. Presser le citron vert et réserver le jus. Concasser les poivres.

**P**ORTER la crème de coco à frémissement avec les feuilles de citronnier, les grains de coriandre, et la moitié du jus de citron vert. Laisser infuser une dizaine de minutes. Passer au chinois. Ajouter le zeste du citron, le jus de cigales de mer, les champignons shiitake délités en cubes de 5 mm de côté, le piment, l'huile de sésame et les poivres. Laisser infuser 5 minutes supplémentaires, à très petit frémissements. Ajuster l'assaisonnement, éventuellement ajouter une pointe de gingembre frais et quelques gouttes de sauce soja. Ajouter les cubes de queues de cigale de mer et la coriandre feuille ciselée, laisser reposer une petite minute. Servir en petites tasses individuelles, décoré d'une feuille de coriandre, d'une goutte d'huile de sésame et éventuellement de zestes de citron vert.

## Chapter 2

# Optical Fibres, Photonic Crystals and Leaky Modes

This Chapter is a technical introduction to microstructured optical fibres. Our aim is to introduce the fundamental concepts and notions we will encounter throughout the thesis. First, we review the principles and main properties of conventional optical fibres (CF). We then give a short overview of photonic crystals (PC) and light guidance in PC defects. This leads us to introduce the principles of guidance in photonic crystal fibres and more generally in microstructured optical fibres (MOFs) or holey fibres. The finite width of the confining structure of MOFs implies all guided modes are in fact leaky; in a final section we discuss what leaky modes represent physically as well as mathematically.

## 2.1 Conventional Optical Fibres

### 2.1.1 Guidance Mechanism

Conventional optical fibres [3, 4] rely on total internal reflection to guide light. The simplest optical fibre – the step index fibre – consists of a dielectric core with refractive index  $n_{\text{CO}}$  surrounded by another dielectric (called *cladding*) with refractive index  $n_{\text{CL}}$ . Using a ray-approach and the Snell-Descartes law, it is easy to see that if  $n_{\text{CO}} > n_{\text{CL}}$ , light propagating in the core reaching the core/cladding interface is totally reflected back into the core as soon as the angle between the direction of propagation and the core/cladding interface is small enough.

More rigorously, we consider the infinitely long step index fibre with circular cross section (radius  $\rho$ ) depicted in Fig. 2.1. We consider light with free-space wavelength  $\lambda$  and wavenumber  $k_0$  propagating along the axis of the fibre ( $z$ -axis). The studied system is invariant under any translation in the  $z$ -direction, which implies that all fields must have a dependence of  $\exp(i\beta z)$  along  $z$ .  $\beta$  is called the *propagation constant*.  $\beta$  is the common  $z$ -component of the wave vectors in the core and in the cladding. Since the norm of the wave vectors in the core and in the cladding are  $n_{\text{CO}}k_0$  and  $n_{\text{CL}}k_0$  respectively,  $\beta$  must be less or equal to  $n_{\text{CO}}k_0$  to propagate in the core and less or equal to  $n_{\text{CL}}k_0$  to propagate in the cladding. If  $n_{\text{CL}} < \beta/k_0 < n_{\text{CO}}$ , light can propagate in the core, but not in the cladding: the light is trapped in the core. We will sometimes also use the perpendicular wavenumber  $k_{\perp}$ , defined by

$$k_{\perp}^2 + \beta^2 = n^2 k_0^2, \quad (2.1)$$

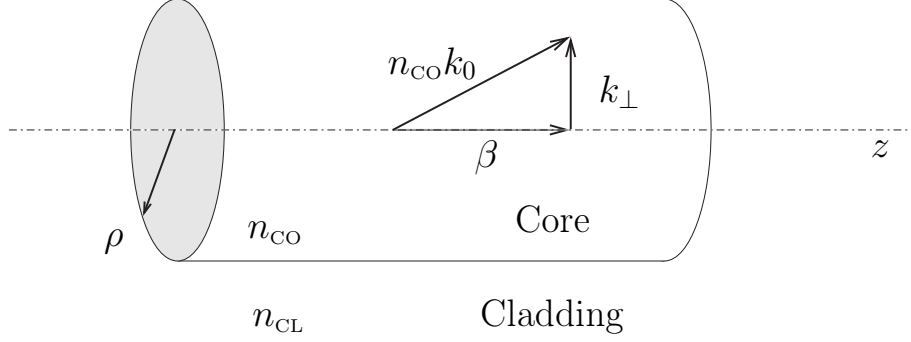


Figure 2.1: Conventional step index fibre.

where  $n$  is the local refractive index, and the numerical aperture ( $NA$ )

$$NA = \sqrt{n_{CO}^2 - n_{CL}^2}. \quad (2.2)$$

Note that the numerical aperture is equal to the sine of the fibre acceptance angle. The acceptance angle is defined by the maximum angle from the  $z$ -axis a ray entering the fibre can have and still be guided by the fibre. In other words light entering a fibre with an angle from the  $z$ -axis greater than the acceptance angle will be refracted into the cladding and eventually lost. Hence, the larger the numerical aperture, the easier it is to inject light into a fibre.

### 2.1.2 Fibre Modes

Considerations on total internal reflection or equivalently on possible propagation constants in the core and the cladding give a necessary but not sufficient condition on  $\beta$  for light to be guided. Indeed, we have seen that the only variation the fields can have along  $z$  is given by the phase factor  $\exp(i\beta z)$ . Between two arbitrary values  $z_1$  and  $z_2$  of  $z$ , the fields propagate and undergo reflection at the core/cladding interface, but the transverse field distribution at  $z = z_1$  and  $z = z_2$  must only differ by the phase factor  $\exp[i\beta(z_2 - z_1)]$ . This defines a resonance condition, and only a discrete, finite set of transverse field distributions and associated  $\beta$  values fulfill this condition. Mathematically speaking, the values  $\beta$  and their associated transverse field distributions are eigenvalues and associated eigenfunctions of the propagation equation. The value of  $\beta$  together with its field distribution constitute a *mode* of the fibre. There are a finite number of modes with  $n_{CL}k_0 < \beta < n_{CO}k_0$ , these are called guided modes.

Note that the propagation equation also has solutions with  $0 < \beta < n_{CL}k_0$ , *i.e.* outside the range where total internal reflection occurs. These modes can propagate in the cladding, and are called radiation modes. For these modes, the set of  $\beta$  is infinite and continuous.

Each mode has a specific field distribution, with its specific symmetry properties. From symmetry considerations it can be shown that for circularly symmetric fibres, modes can be either non degenerate or twofold degenerate. In the latter case two field distributions with complementary symmetries are associated with the same propagation constant.

Considerations on the orthogonality of modes show that in an ideal fibre different modes don't interact. However, unavoidable defects in experimental fibres can cause mode coupling.

### 2.1.3 Properties

#### Number of Modes

The number of guided modes depends on the fibre parameter

$$V = k_0 \rho (n_{\text{CO}}^2 - n_{\text{CL}}^2)^{1/2}. \quad (2.3)$$

The smaller this parameter, the fewer guided modes a fibre can carry. If at a given wavelength  $V < 2.405$ , there is a single degenerate pair of modes guided by the fibre. Since there is only one possible value of  $\beta$ , the fibre is said to be *single-mode*. The pair of guided modes, associated with the same value of  $\beta$ , is referred to as the fundamental mode. Note that for a fibre to be single-mode, it needs to be designed with a combination of small core size to wavelength ratio and small difference in refractive indices between core and cladding. Conversely, a given fibre always is multi-mode for sufficiently small wavelengths. Further it is worth noting that however small the parameter  $V$  is, there is always a guided fundamental mode of the fibre.

#### Losses

In the ideal step index fibre attenuation of a guided mode while propagating is solely due to material absorption. The intrinsic material absorption of pure silica for wavelengths between approximately  $0.8 \mu\text{m}$  and  $1.8 \mu\text{m}$  is very small, and in theory light in that wavelength range could be carried hundreds of kilometers without noticeable loss. Nevertheless, until the early 1970s material absorption in fibres was considerable, due to contamination by water or metallic ions of the silica used to draw fibres. Since the work of Keck *et al.* [5] great improvements have been achieved in avoiding contamination and nowadays fibres can be drawn in which attenuation of modes is no longer limited by absorption, but by Rayleigh scattering from nanoscopic fluctuations of the refractive indices [6]. This kind of fibre can have loss coefficients as low as  $0.18\text{dB/km}$  at  $\lambda = 1.55 \mu\text{m}$ , allowing the transmission of information over hundreds of kilometers without amplification.

Of course, for intercontinental telecommunication networks, the distances which have to be covered are still an order of magnitude larger than what is feasible with the best fibres. To compensate for losses, signal amplifiers and regenerators (repeaters) are introduced at intervals. Servicing these remains the main cost of long haul telecommunication links, and the fewer repeaters needed, the cheaper telecommunication becomes.

Outside the low absorption wavelength range mentioned above, silica fibres are quite lossy. This is of no concern for telecommunications, where the loss minimum has determined the used wavelength, but other applications where guided optics would prove very useful, suffer from these limitations. Optical fibres operating with acceptable losses at the carbon dioxide laser wavelength ( $10.6 \mu\text{m}$ ) would for example revolutionize industrial and surgical laser applications. Note that for high power applications, the limiting factor is not as much the power lost between the source and the target, but the temperature elevation in the fibre if losses are due to absorption.

#### Dispersion

In telecommunication networks, information is transmitted as binary data, taking the form of light pulses in optical fibres. In the field of optical waveguides, dispersion is a generic

term referring to all phenomena causing these pulses to spread while propagating. There are essentially four causes of dispersion:

- **Inter-modal dispersion:** In a multi-mode fibre different modes are associated with different values of  $\beta$  and hence different propagation velocities. This results, for a signal exciting more than one mode, in pulse spreading or echoing, depending on the propagation length. The obvious solution to avoid inter-modal dispersion is to use single-mode fibres.
- **Material dispersion:** All materials are intrinsically dispersive, *i.e.* the refractive index is wavelength dependent. Spectrally, a pulse of light is associated with a superposition of a whole range of frequencies, centered on the frequency of the modulated light source. Due to material dispersion, each spectral component of the pulse will propagate at different speeds, resulting in pulse spreading and deformation.
- **Waveguide dispersion:** Even without material dispersion, the solutions of the propagation equation are wavelength dependent: the propagation constant of a given mode is wavelength dependent. This leads to pulse spreading and deformation for the same reasons as above.
- **Polarization mode dispersion** [7] is in fact the same phenomenon as inter-modal dispersion, but the relevant modes are here originally degenerate. We have seen that a single-mode fibre in fact carries two degenerate modes. Because of anisotropic perturbations (stress, bends, torsion...) the degeneracy between these modes is *de facto* lifted, and inter-modal dispersion occurs. Until recently, the effects of polarization mode dispersion were negligible, but with the bit-rates and propagation lengths aimed at today, and since other sources of dispersion can be compensated for, polarization mode dispersion becomes a significant problem.

Chromatic dispersion, or the dependence of the  $\beta$  of a given mode on wavelength, is the dispersion resulting from the combined effects of material and waveguide dispersion, and is the main contribution to dispersion in single-mode fibres. Chromatic dispersion is said to be normal if shorter wavelengths propagate faster than longer wavelengths. In the opposite case it is said to be anomalous.

In optical telecommunications, to maximize bandwidth it is essential that light pulses keep their initial width. Indeed, if light pulses spread, they eventually overlap and light pulses can't be distinguished by the receiver. There are several ways of constraining the pulses to keep their initial width. The first and most obvious is to design dispersionless fibres, through compensating material dispersion with waveguide dispersion. This is generally possible at only one wavelength, so that all information must be carried within a very narrow range of wavelengths. Shifting the zero-dispersion wavelength in silica fibres while keeping single-mode behaviour is generally achieved through sharp triangular index profiles of the core, with additional layers of different refractive indices between the core and the cladding. However, through such designs it is only possible to shift the zero-dispersion wavelength of 1.3  $\mu\text{m}$  towards longer wavelengths.

A second way of keeping a constant pulse width during propagation is to use solitons, high power pulses for which the nonlinearity (more precisely the self phase modulation) of the fibre exactly compensates the dispersion. For solitons to exist, the fibre must have a relatively small anomalous dispersion. A third method of keeping the pulse width constant is to keep

a small, well known normal dispersion in the fibres, and to add dispersion compensating devices at each repeater. The latter can take the form of optical fibres with strong anomalous dispersion, which exactly compensate for the normal dispersion resulting from fibres between the repeaters. The reason for preferring the latter solution to optical fibres with strict zero dispersion is twofold. First, through careful design it is possible to obtain an effective zero-dispersion wavelength range (*i.e.* the range where the combined effects of dispersion and dispersion compensation result in a negligible overall dispersion) much wider than the effective zero-dispersion wavelength range of zero-dispersion fibres. The wider available wavelength range enables wavelength multiplexing of information, *i.e.* encoding the signal with pulses carried by different wavelengths (*channels*) on a single fibre, which multiplies the bandwidth. Second, pulses carried in zero-dispersion optical fibres are subject to non-linear interactions, even if their power density is not large. Indeed since dispersion is negligible at the carrier wavelength, neighboring wavelengths will have a very long coupling length, multiplying the effect of non-linear interaction. When using multiple wavelengths channels, these undergo non-linear interactions (especially four-wave mixing) leading to channel cross-talk and information loss. State of the art long haul telecommunication networks use fibres having small but non-zero, normal dispersion around  $\lambda = 1.55 \mu\text{m}$ ,<sup>1</sup> and dispersion compensators at each repeater. The operating wavelength  $\lambda = 1.55 \mu\text{m}$  was chosen for two reasons: it is the wavelength at which losses in silica are smallest, and it corresponds to the wavelength range at which Erbium doped fibre light amplifiers are most effective. These light amplifiers [8] were invented relatively recently; they now replace electronic repeaters, enabling an all optical signal processing from source to receiver.

Regarding polarization mode dispersion, there are mainly two ways of avoiding it. The first is to use polarization maintaining fibres, the second is to use single-mode single-polarization fibres. Polarization maintaining fibres are optical fibres in which a birefringence has been introduced, generally through applying stress to the fibre during the drawing process or through using elliptical cores. The degeneracy between the two fundamental modes is then lifted, and since both modes have different polarization properties, they can be separated with polarizers by the receiver, eliminating polarization mode dispersion. In practice the whole process is not as straightforward as it sounds, and polarization maintaining fibres have numerous drawbacks. In order to keep a good coupling efficiency between two fibres or between fibres and devices, care must be taken to keep a precise alignment of the polarization axes, which is tricky given the apparent circular symmetry of the fibres. Further, even with the birefringence, with long propagation distances crosstalk between the two fundamental modes appears because of residual imperfections, so that polarization mode dispersion is not completely eliminated. Single-mode single polarization fibres are fibres which carry a single polarization. They are produced in much the same way as polarization maintaining fibres, but they need a larger birefringence. Their main drawback is that the same physical effect of eliminating one of the two polarizations of the fundamental mode gives rise to leakage for the other polarization, so that low loss single polarization fibres are not achievable with conventional optical fibres.

In the frame of telecommunications, current work to further improve dispersion management – and hence bandwidth – concerns achieving fibres with a flat near-zero dispersion, improvement of dispersion compensating devices and management of polarization mode dispersion.

---

<sup>1</sup>These fibres are called Non-Zero Dispersion Shifted Fibres, or NZ-DSF.

For other fields of application other dispersion properties are sought. Anomalous and zero-dispersion at wavelengths below  $\lambda = 1.3 \mu\text{m}$  in single-mode fibres can be useful for super-continuum generation [9–12], ultrashort pulse compression, soliton generation and propagation.

### Bend Loss

As soon as a fibre is bent, losses occur. In simple terms [3] the origins of bend loss can be understood as follows. In an unbent fibre, the planes of equal phase are perpendicular to the fibre axis. When the fibre is bent, these planes are no longer parallel. The phase velocity has consequently to increase with increasing distance from the center of curvature, and eventually reaches the local velocity of light. Fields in the cladding beyond the point where the phase velocity is larger than the local velocity of light are no longer evanescent, they become radiative and power is lost. From this simple approach we can understand that the further the mode leaks into the cladding, the larger bend losses are. Modes with a significant amount of their fields in the cladding will be more subject to bend loss than modes well confined in the core. Since the mode area increases with wavelength, conventional optical fibres must keep a reasonably small wavelength to core size ratio to keep bend losses acceptable. On the other hand, the wavelength to core size ratio has to remain large enough when the fibre is required to be single-mode. Note that a better confinement in the core and hence smaller bend losses can be achieved through adding regions of depressed refractive index between the cladding and the core (*W-fibres*). Although it is important to keep bend losses in mind when designing a fibre, it is relatively easy to minimize them through proper design, so that they rarely are of concern for applications.

### Non-linearity

Non-linear optical effects always appear when the power density of light is large enough, regardless of the material. Since in optical fibres light is well confined in a narrow core, non-linear effects can appear even in straight silica at relatively modest injection powers. These effects are generally a nuisance in long haul telecommunication networks, but can also become useful for some applications.

As far as the negative aspects are concerned, there are three major non-linear effects in optical fibres rising from the Kerr effect (four wave mixing, self phase modulation and cross-phase modulation), and two due to scattering (stimulated Brillouin and Raman scattering). We have already mentioned that four wave mixing leads to channel crosstalk in wavelength multiplexed systems. Self phase modulation and cross phase modulation result in chirping of the pulse frequency (the frequency at the beginning of the pulse differs from the frequency at the end of the pulse), which, combined with dispersion, gives rise to signal deformation and spreading, but also to a broadening of the spectrum and hence crosstalk. Four wave mixing can be reduced through dispersion in the fibre, whereas the penalty due to phase modulation effects tends to be less important if the dispersion is as small as possible.<sup>2</sup> Both stimulated scattering effects result in pulse power being scattered into frequency-shifted waves. In the case

---

<sup>2</sup>Note that with large chromatic dispersion, interaction between channels is diminished and hence crosstalk modulation is reduced as well; there is no easy general rule regarding the ideal dispersion properties to minimize cross phase modulation: Predicting and compensating cross phase modulation is far from easy and is a topic of current research.

of stimulated Brillouin scattering, the scattered wave propagates in the opposite direction to the incoming signal, and above a certain power threshold more power is scattered back than propagated forward. The stimulated Brillouin scattering threshold sets the upper limit of power which can be propagated efficiently through an optical fibre. In the case of stimulated Raman scattering, the scattered, frequency-shifted wave propagates in the same direction as the incoming signal. In wavelength multiplexed systems, the Raman scattered signal of one channel can hence overlap with another channel. Note that both scattering phenomena generally increase with fibre doping. All these effects are of course power dependent, and smaller power densities at same injection powers can only be of benefit.

Most of the previous effects can also be exploited to create devices. When controlled, four wave mixing and cross phase modulation can be used for all-optical switching, frequency conversion, pulse reshaping and other forms of optical signal processing. Self phase modulation is essential for soliton propagation. Stimulated Raman scattering can be used for signal amplification. Note that for applications, other non-linear effects are available. Very efficient light amplification can for example be achieved through doping. Efficient second (and higher) harmonic generation and other parametric processes may be obtained by breaking the inversion symmetry of silica, *e.g.* through poling. The main restriction of applications using nonlinearities of conventional step index optical fibres is that the material interacting with light must be able to be drawn into a usable fibre. In practice this severely limits candidate materials, and most non-linear fibre applications either use the nonlinearities inherent to silica or nonlinear material that can be introduced into silica through doping.

## 2.2 Photonic Crystals

The idea of photonic crystals originated in 1987 from work in the field of strong localization of light [13] and of inhibition of spontaneous emission [14]. It was subsequently shown that in periodic arrangements of –ideally lossless – dielectrics, the propagation of light can be totally inhibited at certain wavelengths, regardless of propagation direction and polarization. This inhibition doesn't result from absorption but rather from the periodicity of the arrangement, and is quite fundamental: in the frequency range where no propagation is possible (the *photonic band-gap*), the density of possible states for the light vanishes, so that even spontaneous emission becomes impossible. Such periodic arrangements of dielectrics have been called *photonic crystals*, or photonic band gap materials.<sup>3</sup>

### 2.2.1 One Dimension: Bragg Mirrors

The simplest device using the principles of photonic crystals is the one-dimensional photonic crystal, well known under the name of the Bragg mirror or the multilayer reflector. It consists of a periodic stack of two alternating dielectric layers. Light propagating in a direction normal to the layers undergoes successive reflection and transmission at each interface between layers. With an appropriate choice of layer thickness and refractive indices, waves reflected from each interface are in phase, whereas waves transmitted are out of phase. In that case, the transmitted wave components cancel each other out, and only the interference of the reflected components is constructive: the light is totally reflected. This works for a range of wavelengths. Bragg mirrors have been in use for decades, it is only recently that they were regarded as being

---

<sup>3</sup>Note that photonic crystals can also result from periodic arrangements of conductors.

a special case of photonic crystals. The classical way of analysing them, focused on Bragg mirrors with a finite number of layers, uses reflection and transmission matrices at each layer, and it is then quite straightforward to prove through recurrence relationships that reflection can be perfect with an infinite number of layers. There is nevertheless another approach to deal with a stack with an infinite number of layers, coming from solid state physics. If the stack is infinite, it has a discrete translational symmetry. The Bloch Theorem then applies, and solutions to the propagation equation in the stack are Bloch waves. Hence two wave vectors differing by a vector of the reciprocal lattice associated with the periodic stacking are physically the same: the dispersion diagram “folds back” along the limits of the Brillouin zone. At the edge of the Brillouin zone, two solutions exist having same wave vector but different frequencies, and in between those two frequencies no solutions exist at all. The gap of frequencies for which no solutions exist is called a photonic band gap. Note that, until recently, reflection on Bragg mirrors was thought to be possible only within a relatively narrow range of angles of incidence. Recent work by Fink *et al.* has demonstrated the feasibility of omnidirectional reflection with Bragg mirrors [15].

### 2.2.2 Photonic Crystals in Two and Three Dimensions

Photonic crystals with two or three-dimensional periodicity can be seen as a generalization of Bragg mirrors. The simple approach with reflection and transmission matrices cannot be applied analytically here, and this is probably why their properties were discovered relatively recently, although, for example, important work on stacked grids for filtering in the far infrared was carried out by R. Ulrich in the 1960s [16, 17]. The Bloch approach can be used similarly, and shows that band gaps can open up. The point of using periodicities along two or three-dimensions is to open an omnidirectional band gap: for the Bragg mirror, band gaps usually only exist for a narrow range of angles of incidence, and propagation parallel to the Bragg layers can never be inhibited. With photonic crystals using a two-dimensional periodic arrangement of parallel rods, band gaps can exist for all directions of propagation in the the plane of periodicity, and for photonic crystals with three-dimensional periodicity, propagation of light in all directions can be prohibited. When a band gap exists regardless of direction of propagation and polarization, one speaks of a total photonic band gap.

Photonic crystals with two-dimensional periodic arrangements are usually either made of parallel dielectric (or metallic) rods in air, or through drilling holes in a dielectric material. In the frame of integrated optics, holes of a fraction of a micrometer etched in slab waveguides are very promising for integrated photonic circuits, and have been succesfully demonstrated experimentally. Photonic crystals with three dimensional periodicity are a bit more tricky to achieve.<sup>4</sup> Yablonovitz suggested drilling holes at three different angles into dielectric material. The so called wood-pile structure has attracted much attention [18–23], and recent progress with artificial inversed opals is promising [24, 25].

Note that the term photonic crystal was originally introduced to refer to materials having a photonic bandgap. It seems that it is now more and more often used to refer to any kind of perodic arrangement of dielectrics or metals, with or without photonic band gaps. The latter generalization of the term makes sense considering that in solid state physics, a crystal is defined by the periodicity of its lattice, band gaps appearing as a consequence. Usual practice

---

<sup>4</sup>Nature, as so often, has demonstrated its supremacy in achieveing three dimensional photonic crystals billons of years before man. They can be found in opals. Note that one, two and three dimensional photonic crystals are also found elsewhere in nature: they give bright colours to beetles, butterflies, sea-mice and birds.

is then to call *photonic band gap material* photonic crystals having a photonic band gap. In the remaining chapters of the thesis we will avoid any confusion and speak of microstructures, since sometimes the dielectric structures won't even be periodic.

## 2.3 Guiding Light with Photonic Crystals

For frequencies within a total photonic bandgap, no propagation is allowed in an infinite photonic crystal. If a defect is introduced in the infinite lattice, localized defect states for frequencies within the band gap can emerge, similar to bound states associated with defects in semiconductors. For three dimensional photonic crystal lattices, this can be a single point defect: in that case light emitted within the defect will remain confined in the vicinity of the defect. It could also be a linear defect, in which case light remains in the defect but can propagate along it. Another way of looking at defect states is to consider the photonic crystal to be a perfect mirror in a certain frequency range. If one drills a hole across the photonic crystal, light injected in the hole will be reflected at the borders of the hole and propagate within it, very similarly to what happens in optical fibres. Given that photonic crystals have a high reflection coefficient even with a relatively small number of periods, the width of the photonic crystal around the defect can be reduced to a few layers: we can hence imagine optical fibres consisting of a micrometric core surrounded by a photonic crystal cladding only a few times wider than the core. The resulting optical fibre is called a *photonic crystal fibre* and has an important difference from conventional optical fibres: in the latter, the core, in which light is guided, has to be of higher refractive index than the cladding. Using photonic bandgap material for the cladding, reflection is guaranteed regardless of the refractive index of the material inside the defect. A defect in a photonic crystal can hence confine and guide light in low refractive index media, such as air, gas or vacuum. This opens up possibilities never dreamt of before. An optical fibre guiding light in vacuum would have absorption losses and non-linear effects reduced by orders of magnitude<sup>5</sup> compared with solid core fibres, paving the way for optical fibres for high power applications; material dispersion would become negligible, giving rise to completely new forms of dispersion management; guiding highly confined light in gas or liquids would enable new forms of non-linear fibres as well as a whole new family of fibre sensors; even guidance of atoms, molecules or cells through hollow core optical fibres would become possible [26].

If one seeks to guide light along a linear defect, it is not necessary to use a three dimensional periodicity or a total photonic band gap. Indeed, considering Fig. 2.1 but with the cladding now being a perfect mirror,  $k_{\perp}$  will be set by the size of the defect, and  $\beta$  will follow from Eq. (2.1). If for the range of wave vectors given by these considerations no propagation is possible in the photonic crystal, a guided mode will exist. This can be achieved with two dimensional and even one dimensional (concentric) periodicities.

### 2.3.1 Bragg Fibres

The idea behind Bragg fibres is to use Bragg mirrors as a cladding of an optical fibre. Accordingly, a Bragg fibre is made out of a concentric arrangement of dielectrics, wound around a core which might be hollow or not. W-fibres could be seen as an extreme case of a simple

---

<sup>5</sup>Material absorption, non-linear effects and material dispersion wouldn't completely vanish because of the evanescent part of the fields remaining in the photonic crystal.

Bragg fibre. Theoretical studies have shown only recently that hollow core Bragg fibres could be feasible, given the possibility of attaining large refractive index contrasts (*e.g.* 3 to 1.1 or 2.4 to 1.6, see Ref. [27]) between successive layers. The first working experimental hollow core Bragg fibre has nonetheless been demonstrated recently, and had in some wavelength ranges losses orders of magnitude smaller than any conventional optical fibre [28]. Furthermore, Bragg fibres can be single-mode, single-polarization even with full circular symmetry and without birefringence [29, 30].

### 2.3.2 Photonic Crystal Fibres, Microstructured Optical Fibres and Holey Fibres

Strictly speaking, Bragg fibres are a particular type of photonic crystal fibres. The term photonic crystal fibre is however mostly used to refer to fibres with a cladding consisting of a two dimensional periodic array of inclusions. The most immediate advantage compared with Bragg fibres is that lower refractive index contrasts are needed to achieve photonic bandgaps: a lattice of air (or vacuum) holes in silica or polymer is sufficient.

Fibres with a lattice of microscopic holes running along the fibre axis can be manufactured by drawing a preform with macroscopic holes. The holey preform can readily be obtained either by stacking capillaries together, or through drilling (mainly for polymers) or extruding the preform. In the drawing process, the overall shape of the preform is generally maintained, but the diameter of the cross-section is scaled down from centimetric to micrometric dimensions. Note that this process can be used to produce fibres with regular arrays of holes as well as fibres with non-periodic arrangements of holes, either with a solid or a hollow core (see Fig. 2.2). The general terms *holey fibre* and *microstructured optical fibre* (MOF) refer to any kind of fibres with a set of inclusions running along the fibre axis, whereas the term photonic crystal fibre is generally only used to refer to MOFs in which guidance results from a photonic band gap effect. Note that some authors also use the term *crystal fibre* referring to MOFs in which the inclusions form a subset of a periodic array, but for which guidance may or may not result from photonic band gap effects.

#### Hollow Core MOFs

Light guidance in hollow core MOFs can only be achieved using the photonic band gap effect. Hollow core MOFs are hence necessarily photonic crystal fibres. They offer the whole range of benefits of hollow core fibres we have evoked above. Light guidance being possible solely within a photonic band gap, the wavelength range in which these fibres guide light is very narrow, only a few tens of nanometres for guidance in the infrared or the visible spectrum. Further the accuracy of the periodicity of the lattice required to obtain a clear band gap effect makes the manufacture of these fibres challenging. Experimental hollow core MOFs have nonetheless been demonstrated using a cladding consisting of a hexagonal array of large air holes in silica [31], as have been first applications [26].

#### Solid Core MOFs

For solid core MOFs it is often argued that guidance is due to *modified total internal reflection*: in a solid core MOF, the “average” refractive index of the cladding is lower than the core refractive index, leading to an equivalent geometry similar to those of conventional step index fibres. Following this argument, there is no need to evoke photonic band gaps, and any

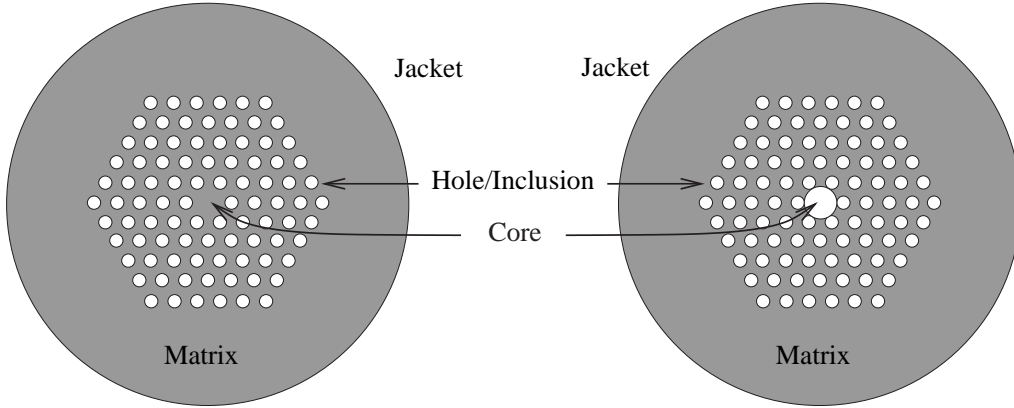


Figure 2.2: Schematic representation of the cross-section of a typical solid core MOF (left) and hollow core MOF (right) with holes on a hexagonal lattice and a single central core. We will often refer to the microstructured part as the cladding. The jacket represents the physical boundaries of the MOF, and can be a physical jacket *e.g.* for mechanical protection or simply air. Note that the hexagonal lattice is also referred to as triangular lattice.

arrangement of holes – periodic or random – around a silica core results in a wave-guiding structure. It is easy to see the limits of such an interpretation of guidance, raising the question of what “average” means in this context: in the extreme case of a random hole distribution with holes concentrating around a few spots, leaving wide straight pathways for light to escape, it would be very surprising to find any kind of guidance. In fact, the “average” refractive index referred to when explaining guidance with modified total internal reflection is not a geometric average, nor for example a value coming from homogenization theories. It is actually not an average at all, but is a value extracted from the band structure of the surrounding arrangement of holes. It corresponds to an “effective index” associated with the largest possible value of the propagation constant  $\beta$  for a given frequency in the microstructure: at a given frequency, light with a component  $\beta$  of the wave vector along the axis of the holes larger than a specific value  $\beta_{\text{MAX}}$  cannot propagate in the microstructured part of the fibre. This is analogous to total internal reflection in the case of step index fibres, where light with  $\beta > n_{\text{CL}}k_0$  cannot propagate in the cladding. The average, or effective, index of the cladding of a MOF is then given by  $\beta_{\text{MAX}}/k_0$ . But since  $\beta_{\text{MAX}}$  is a band property, it is slightly contrived to distinguish the band gap between  $\beta_{\text{MAX}}$  and  $\beta = \infty$  from any other band gap limited by finite values of  $\beta$ . Modified total internal reflection can therefore also be seen as a specific case of band gap guidance. The only true difference with band gap guidance using other band gaps is that the band gap between  $\beta_{\text{MAX}}$  and  $\beta = \infty$  always exists, regardless of frequency or the exact structure of the cladding, so that guidance relying on this band gap is much easier to achieve. Further this clarifies the idea that the effective index is in fact a property of the infinite periodic lattice surrounding the core, and thus the concept of modified total internal reflection must be used with circumspection when the holes around the core are not arranged periodically. Note that we will discuss the model of modified total internal reflection and its validity in detail in Chapter 7. The argument that modified total internal reflection guidance is not fundamentally different from band gap guidance is further discussed in Ref. [32].

Guidance due to modified total internal reflection in solid core MOFs is much easier to achieve than band gap guidance, and indeed the first MOF in which guidance was demons-

trated had a solid core [33, 34]. All the new possibilities offered by photonic crystal fibres hitherto mentioned were based on the fact that guidance could be achieved in a hollow core, and guidance using photonic crystals in solid cores might seem uninteresting at a first sight. Nevertheless, the study of the first experimental solid core MOFs showed that these possess unique properties of their own, unachievable by conventional optical fibres. The most striking among these is certainly their ability to be single mode over an infinite range of wavelengths. In other words, for some solid core MOFs, however small the wavelength is compared with the core size, only a single-mode is guided. This is fundamentally different from conventional fibres where, at small wavelength to core ratios, multi-modedness is unavoidable. The importance of this property is not as much linked to the possibility of having single-mode guidance over a large range of wavelengths in a same fibre – most of the time the wavelength range at which a fibre will be used is quite narrow – but rather remains in the converse property: for a given range of wavelengths a solid core MOF with arbitrarily large core can be single-mode. Possibilities offered by the resulting large core single-mode fibres are unprecedented: in the field of telecommunications for example, where single-mode guidance is essential, if the core is larger light can be injected with higher power without the power density reaching levels at which non-linear effects become prohibitive, so that the distance between repeaters can be greatly increased.

On the opposite side of the core size scale, it appears that because of the large index contrast modes are very well confined in the core, even when the wavelength to core size ratio is not small. This again differs from conventional fibres, where the fraction of the field in the cladding at large wavelength to core size ratios is far from being negligible because of the very small difference of refractive indices between the core and the cladding. Good confinement in small cores enables higher power densities and hence accentuated non-linear properties.

The large available parameter space of solid core MOFs (position, size, shape of the holes, refractive index of the inclusions if they are not holes) makes the waveguide dispersion, which can have strong effects due to the high index contrast, highly configurable. Almost any dispersion curve seems accessible to MOFs with the correct design. The combination of endlessly single-mode guidance and adjustable dispersion has led to solid-core, single-mode MOFs with anomalous dispersion, to single-mode fibres with a zero-dispersion wavelength shifted down to the visible, as well as to single-mode fibres with ultra-flat normal or anomalous dispersion over a large wavelength range [35–39]. With the additional possibility of good mode confinement, the configurable dispersion also gave rise to promising non-linear applications, either impossible to achieve with conventional fibres or having much lower power thresholds than in conventional fibres. These include temporal soliton formation and propagation [12, 40–43], super-continuum generation [10–12, 40, 41, 43] and new types of stable spatial solitons [44].

Finally, given the ease with which a defect is introduced in the MOF lattice at the stage of the preform, MOFs with multiple cores or MOFs with large form-birefringence are straightforward to produce. Most MOFs consist of an array of holes in which one hole has been left out, playing the role of the core. With the symmetries of the lattice of holes generally used (mostly six- or four-fold symmetries), this results in the fundamental mode being doubly degenerate, as in conventional optical fibres [45]. If the core is now extended to two adjacent missing holes, or if the symmetry around the core is reduced to two-fold symmetry (*e.g.* through changing the size of two diametrically opposed holes [46], or with elliptical holes [47]), the degeneracy is lifted and the fibre becomes birefringent: the MOF becomes polarization maintaining. The resulting birefringence can be orders of magnitude larger than stress-induced birefringence in conventional polarization maintaining fibres, so that coupling between the two modes is great.

tly reduced. Single-mode single-polarization fibres can be achieved in the same way. We have already mentioned how important this could be in removing polarization mode dispersion.

The main advantage of MOFs with multiple cores compared to conventional multiple core fibres is the ease with which they can be produced. If the cores are separated by a large number of lattice periods, the cores become independent, with negligible cross-talk, enabling for example a spatial multiplexing of signals.<sup>6</sup> If on the contrary the cores are separated by a few layers only, modes guided in different cores are coupled. This can be useful *e.g.* for sensors, and a bend sensor relying on multiple core MOFs has already been demonstrated [48]. Further, through filling one or more holes with polymers, liquids, or gas, or through writing gratings into the MOF core, fibres with *in situ* adjustable properties as well as a great range of sensors and other devices can be achieved [49].

To sum up, although solid core MOFs don't seem as radically different from conventional fibres as hollow core MOFs at first sight, the range of new prospects they offer and the numerous fields in which they could outdo conventional fibres is at least as exciting as hollow core guidance. Further, since guidance in solid core MOFs relies on modified total internal reflection<sup>7</sup> and not on the use of a very narrow band gap, solid core MOFs are also much easier to realize than hollow core MOFs. Solid core and hollow core MOFs are both extremely promising new types of fibres, with completely different properties and possible applications; given their differences there is not much point comparing them directly. In the remainder of this thesis we will concentrate on solid core MOFs.

## 2.4 Leaky Modes

### 2.4.1 Confinement Losses

In the solid core MOFs we will study, light guidance is due to modified total internal reflection between the core and a microstructured cladding consisting of inclusions in a matrix. The core and matrix material are generally the same, and hence have same refractive index. In practice, the cladding has a finite width, as it consists of several layers of inclusions. Beyond the microstructured part of the fibre, the matrix extends without any inclusions until the jacket. If we consider the jacket to be far from the cladding and core, and hence neglect its influence, guidance in the core is solely due to a finite number of layers of holes in bulk silica extending to infinity. *A priori*, the cladding doesn't "insulate" the core from the surrounding matrix material since the holes are disjoint and the matrix is connected between the core and the exterior. Physically we can imagine the light to leak from the core to the exterior matrix material through the bridges between holes, and expect losses. In the frame of the modified total internal reflection approach to guidance, in which the microstructured part of the fibre is replaced by homogeneous material with an effective refractive index lower than the core, the core is completely surrounded by the cladding. The exterior matrix material and the core are then no longer directly connected. Nevertheless the width of the "effective cladding" is finite, and hence tunneling losses are unavoidable. Regardless of the approach one uses to explain guidance in MOFs, as long as guidance is due to a finite number of layers of holes, leakage from the core to the outer matrix material is unavoidable. We will call the losses due to the finite extent of the cladding *confinement losses*, or *geometric losses*.

---

<sup>6</sup>Note that the theoretical and practical feasibility of such multiplexing remains to be proved.

<sup>7</sup>...*i.e.* on a wide band gap existing for all materials.

### 2.4.2 Modes of a Leaky Structure

Confinement losses being unavoidable, modes of a MOF decay while propagating. They are no longer called guided modes, but *leaky modes*. The equations satisfied by the fields being linear, losses are proportional to the field intensity. Simple mathematics show that in that case the decay of the fields must be exponential along the direction of propagation. This is reflected by the propagation constant  $\beta$  taking an imaginary part. Indeed, we have seen that modes are characterized by a transverse field distribution invariant with  $z$ , which is modulated by a phase factor taking the form  $\exp(i\beta z)$ . For leaky modes,  $\beta$  is complex, and the phase factor becomes  $\exp(i\Re(\beta)z)\exp(-\Im(\beta)z)$  ( $\Re$  and  $\Im$  denoting the real and imaginary parts respectively). For the mode to decay in the direction of propagation (which is the case with leakage), the real and imaginary parts of  $\beta$  must be of the same sign.

This simple and elegant way of accounting for the decay of modes through a complex propagation constant is nevertheless only the tip of the iceberg of dealing with leaky modes. Indeed, using a complex propagation constant raises more difficulties than it provides simplifications. First,  $\beta$  being complex, the value of  $k_\perp$  (Eq. (2.1)) becomes complex as well. This has two consequences: it complicates the choice of the square root in Eq. (2.1), and the fields of the modes become divergent at large distances from the core. This in turn renders the modal field distributions non square-integrable, so that dealing with them becomes mathematically very delicate. As a consequence, leaky modes are not orthogonal in the usual sense and their completeness is not self-evident [3]. The very notion of modes becomes unclear, since the lack of orthogonality implies that two modes could interact: if for example the fundamental mode and the second mode have an intrinsic crosstalk, their distinction would become totally arbitrary. Finally we have seen that confined guided modes in the case of conventional step index fibres are found for values of beta satisfying  $n_{\text{CL}}k_0 < \beta < n_{\text{CO}}k_0$ , and that for  $0 < \beta < n_{\text{CL}}k_0$  there is a continuum of radiating modes. Since there is no natural ordering in the complex plane, we can no longer use such considerations to locate leaky modes. Further, the continuum of radiating modes still exists and the range of  $\beta$  associated with radiating modes is not *a priori* disjoint from the range of  $\beta$  of leaky modes. This seriously complicates the task of finding leaky modes, since a leaky mode can be “lost” in the middle of a continuum of radiating solutions to the wave equations. Some of the difficulties pointed out here have not been overcome yet, and are the topic of current research. Since we use leaky modes throughout this thesis, we will nevertheless explain in more detail what leaky modes represent physically and mathematically, how some of the difficulties linked to their use can be circumvented, and more generally how we can justify our approach.

### 2.4.3 Heuristic Approach to Physical Properties of Leaky Modes

To fully understand the slightly disconcerting properties of leaky modes, we have to keep in mind that modes are defined for a fibre that is *infinitely long*. The exponential decay of the mode with increasing  $z$  being equivalent to an exponential growth with decreasing  $z$ , the modal fields diverge when  $z$  approaches  $-\infty$ . We show here how this implies that the fields have to diverge radially in the cross section of the fibre.

For the sake of simplicity, we consider a step index fibre consisting of a core with refractive index  $n_{\text{CO}}$  and a cladding of finite size with refractive index  $n_{\text{CL}}$  surrounded by the same material as the core: beyond the cladding, the refractive index keeps a constant value  $n_{\text{CO}}$  everywhere (Fig. 2.3). In such a fibre, all modes are leaky because of tunneling losses [50, 51].

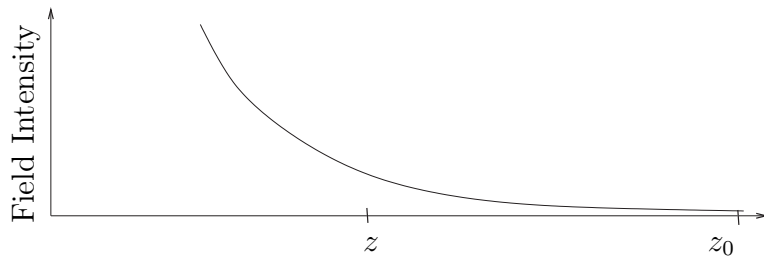


Figure 2.3: Leaky modes and radial divergence, a heuristic approach. See text for details.

We consider the fundamental (leaky) mode of that structure, propagating in the direction of increasing  $z$ . In the core, its power density distribution is similar to that of the fundamental mode of a lossless step index fibre. It is centrosymmetric with maximum value at the centre of the core. In the cladding the fields are evanescent, the power density decays exponentially with increasing distance from the core, until the exterior boundary of the cladding is reached. The propagation constant and the norm of the wave-vector being the same in the core and in the matrix surrounding the cladding, the amount of power which has reached the exterior cladding boundary can radiate away, and it does so at an angle of

$$\alpha = \cos^{-1} \left( \frac{\Re(\beta)}{n_{\text{CO}} k_0} \right). \quad (2.4)$$

In terms of rays, a radiated ray originating from the cladding at  $z$  will arrive at a reference position  $z_0 > z$  at a radial distance

$$r(z) = \rho_{\text{CL}} + (z_0 - z) \tan \alpha \quad (2.5)$$

from the core centre. The whole power emitted from the cladding boundary in an infinitesimally long cylinder of length  $dz$  at  $z$  is found in the cross-section located at  $z_0$  on an annulus with radius  $r(z)$  and width  $dr = dz \tan \alpha$ . The power density in that annulus is hence the total power radiated from  $dz$  at  $z$  divided by the area of the annulus  $2\pi r dr$ . The total power radiated from the infinitesimal cylinder being proportional to the total power density at  $z$  and hence to  $\exp(-2\Im(\beta)z)dz$ ,<sup>8</sup> outside the cladding the power density  $S(r)$  is proportional to

$$S(r) \propto \frac{1}{r \tan \alpha} \exp \left[ -2\Im(\beta) \left( z_0 - \frac{r - \rho_{\text{CL}}}{\tan \alpha} \right) \right]. \quad (2.6)$$

The power density at the center of the core  $r = 0$  at  $z_0$  being proportional to  $\exp(-2\Im(\beta)z_0)$ , the normalized power density outside the cladding at  $z_0$  is given by

$$\frac{S(r)}{S(0)} \propto \frac{1}{r \tan \alpha} \exp \left[ 2\Im(\beta) \left( \frac{r - \rho_{\text{CL}}}{\tan \alpha} \right) \right]. \quad (2.7)$$

$\Im(\beta)$  being positive, we see that the power diverges exponentially with increasing radial distance.

Counter-intuitive though it may seem, the radial exponential growth of field distributions is a fundamental property of leaky modes. Of course such a field distribution is physically impossible. Real fibres nevertheless are always of finite length, and hence a reasoning similar to the one above will have to be limited by the value  $z_s$  of  $z$  at which the fibre starts. Doing so, we would find an exponential growth in the cross-section of the fibre, but the exponential growth would stop at  $r(z_s)$ , and for larger values of  $r$  the field would be strictly zero. Further the total power flowing through a cross-section at any given  $z$  would be equal to the power flowing through the cross-section at  $z_s$ . The exponential growth in the cross-section is not in contradiction with energy conservation: it is a direct consequence of it. This remains true in the case of infinitely long fibres, but the power flow through any cross-section is then infinite.

---

<sup>8</sup>The factor 2 in the exponential comes from the power being a square function of fields.

#### 2.4.4 Mathematical Considerations

In the example we have considered above, we were led by intuition to the conclusion that the losses due to tunnelling were small, and that their influence on the mode should thus remain small. Implicitly, we adapted the truly guided modes of a fibre with infinite cladding to their lossy nature through letting  $\beta$  take a small imaginary part. Mathematically, this would amount to letting the lossless boundary conditions become slightly lossy without reformulating the whole problem. However, lossy boundary conditions, usually referred to as *open boundary conditions* are mathematically not straightforward to deal with.

Until recently, the only rigorous way of treating open boundary conditions was to avoid them: instead of considering the system consisting solely of the core and the cladding, with lossy boundary conditions at the outer cladding boundary, we would consider the system consisting of the core, the cladding, and the rest of the universe, so that energy conservation is satisfied. The drawback of this approach is that the only modes which are solutions to the problem lie in a continuum of real  $\beta$  values. The leaky modes, which allow us to analyse the physics of fibres with finite and infinite claddings along parallel lines, are not a natural solution to the physical problem englobing the fibre and its exterior.

In contrast, the solutions to the true open boundary problem are the leaky modes. However, with open boundary conditions the system doesn't satisfy energy conservation. The mathematical operators used are then no longer hermitian, and the mathematics of non-hermitian operators is no picnic. First, eigenfunctions of non-hermitian operators don't form a complete orthogonal basis, but a set of non-orthogonal functions which may or may not be complete. Decomposing a field on this set is hence not straightforward, and the usual tools involving modal decomposition (*i.e.* almost all techniques in the theory of guided optics) cannot be used. Second, deriving rigorously the solutions to the physical problem raises difficulties. The work presented in this thesis is no exception in this regard, and the derivation we give of the multipole method is in fact mathematically not rigorous: for some key points of the derivation, we implicitly assume the fields to be square integrable, yet leaky modes aren't. More specifically, in the derivation of the Wijnngaard identity, Appendix B, we use the Green's function

$$G_e = -\frac{i}{4}H_0^{(1)}(k_{\perp}^M r). \quad (2.8)$$

The value of  $k_{\perp}^M$  is not determined at that point of the derivation, but for leaky modes  $k_{\perp}^M$  will be complex with a positive imaginary part, so that the Green's function will not be square integrable. The convolution used in the remainder of the derivation then becomes dubious. The derivation of the multipole method is rigorous for guided modes, but we cannot justify its extension to leaky modes with rigorous mathematics. However, the agreement between results obtained from the multipole method and results from other numerical methods or experiments (*cf.* Sec. 4.7.3), even when involving leaky modes, somewhat legitimates the confidence we have in the method.

Open boundary problems are a topic of current research. Recent work initiated by P. T. Leung and K. M. Pang [52–59] suggests the set of leaky modes of a class of open boundary problems, similar to the one considered here, forms a complete orthonormal basis if the space of functions and its inner product are adequately defined. In the frame of their work, the solution to the open boundary problem doesn't include a continuum of eigenvalues, but solely the discrete, complete set of leaky modes. It is not yet clear if guidance in MOFs is strictly speaking a specific case of the class of problems studied by Leung *et al.*, but it might well be

that the way to a rigorous derivation of multipole methods for leaky modes has already been paved.

### 2.4.5 Spectral Considerations

There is a discrete infinity of leaky modes [3, 56]. For a step index fibre with infinite cladding, propagation constants satisfying  $n_{\text{CL}} < \beta/k_0 < n_{\text{CO}}$  give strictly guided modes. The propagation constant of leaky modes being complex, we can not use this argument any more. Nevertheless, we can assume that the “most confined” leaky modes of a fibre with finite cladding are similar to the guided modes of the fibre with same parameters but with an infinite cladding, the main difference being that the propagation constant takes a small imaginary part. These modes would satisfy  $n_{\text{CL}} < \Re(\beta)/k_0 < n_{\text{CO}}$ . For a solid core MOF, we could replace  $n_{\text{CL}}$  by the effective index of the cladding, as long as one can define such an effective index. Otherwise, another lower bound can be used, namely the refractive index of the inclusions  $n_i$ . Indeed, if  $\Re(\beta)/k_0 < n_i$ , light is “likely to propagate” in the inclusions; there would be no barrier between the core and the exterior, and hence losses should be extremely high. On the contrary, for hollow core MOFs, light has to propagate in the hollow core and hence we must have  $\Re(\beta)/k_0 < 1$ . Note that when the imaginary part of  $\beta$  becomes very large, say one order of magnitude less than  $\Re(\beta)$ , considerations on ordering become dangerous, and very leaky modes exist having values of  $\Re(\beta)$  well outside the mentioned boundaries. On the other hand, a mode for which  $\Im(\beta) \sim \Re(\beta)$  attenuates within a few wavelengths, and is hence physically meaningless. Finally, it is worth noting that having  $n_{\text{CL}} < \Re(\beta)/k_0 < n_{\text{CO}}$  does not imply that the imaginary part of  $\beta$  is small.

The fundamental mode of a step index fibre with infinite cladding is the mode with largest  $\beta$ . Consequently, it is also the mode with fastest decaying evanescent tail in the cladding. For a fibre with a cladding of finite width, we can thus expect the losses of the fundamental mode to be smallest, so that its propagation constant would have both, the smallest  $\Im(\beta)$  and the largest  $\Re(\beta)$ . When the similarity between solid core MOFs and step index fibres with finite cladding holds, we can expect the same behaviour of the fundamental mode for MOFs. To locate the fundamental mode of a MOF it is therefore a good idea to start to look for values of  $\beta$  with small imaginary part, and with real part in the vicinity of  $k_0 n_{\text{CO}}$ .

Hors d'œuvre :

## Escalope de Crocodile d'Estuaire en Croûte d'Herbes, Petite Salade d'Herbes Fraîches

*Herb Crusted Estuarine Crocodile, Herb Salad*

### Pour 6 personnes :

Pour le Crocodile :

*300 g de queue de Crocodile  
d'Estuaire  
50 g de chapelure fine  
120 g de beurre demi-sel  
15 feuilles d'estragon  
un quart de botte de  
marjolaine  
un quart de botte d'origan  
5 branches de thym citronné  
un tiers de botte de cerfeuil  
5 feuilles de sauge  
poivre noir  
fleur de sel*

Pour la salade :

*60 g de jeunes pousses de  
roquette  
une demi botte de cerfeuil  
un quart de botte de  
marjolaine  
un quart de botte d'origan  
24 feuilles d'estragon  
12 feuilles de basilic opale  
5 g de ciboulette  
2 branches de thym citronné  
12 fleurs d'estragon  
huile d'olive pour  
assaisonnement  
le jus d'un citron  
fleur de sel*

### La salade

**L**AVER et essorer la roquette. Préparer les herbes : ôter toutes les tiges, ne garder que les feuilles. Bien mêler les herbes et la salade, effeuiller les branches de thym citronné par dessus.

### Le crocodile

**P**RÉPARER la panure d'herbe : travailler le beurre en pommade, hacher finement au couteau les herbes débarrassées de leurs tiges. Incorporer au beurre les herbes et la chapelure. Abaisser en une couche de 2 mm d'épaisseur, entre deux feuilles de papier cuisson, au rouleau à pâtisserie. Laisser prendre au froid.

**D**ÉTAILLER le crocodile en tranches de 4 mm d'épaisseur à l'aide d'un couteau bien affûté. Disposer les tranches de crocodile sur un plaque à pâtisserie recouverte de papier cuisson. Saler à la fleur de sel, donner un tour de moulin à poivre. Superposer sur chaque morceau de crocodile une tranche de panure de même taille. Laisser colorer au grill quelques minutes.

**S**ERVIR une à deux escalopes de crocodile par assiette, accompagnées de salade d'herbe arrosée d'un filet d'huile d'olive et de jus de citron et saupoudrée de fleur de sel.

## Chapter 3

# The Multipole Method: Fundamentals

*This Chapter and the related appendices are based on ref. [1]*

### 3.1 Introduction

To develop the potential of MOFs, accurate modeling tools are necessary. A range of methods has been developed, some of which use approximate scalar [60] or vector [61–63] treatments. A common strategy is to apply in the transverse plane periodic boundary conditions, enforced for example using plane wave expansions [64, 65]. However, such supercell treatments effectively replace the necessarily finite MOF structure with an infinite one, and thus cannot address the issue of the loss associated with propagation in a transversely-finite confining structure.

One method that somewhat accommodates for the shape of the expected modal field expands it in terms of Hermite-Gaussian functions [66, 67]. However, these have an intrinsic width, which ideally matches the width of the solution. Hence the method requires some *a priori* knowledge of the solution, which may not be available.

Beam propagation methods use a numerical algorithm to simulate the propagation of a coherent beam along a fibre [68, 69], from which the modes and their properties must be extracted *a posteriori*. Both scalar and vector versions are available, and fibres of any geometry can be dealt with. One can calculate modal losses by observing the attenuation upon propagation, but the propagation distance required increases as the loss decreases. Further, when the wavelength to pitch ratio is not small, leaky modes are source of numerical instabilities and inaccuracies, restricting the wavelength range over which beam propagation methods can be used [47].

Finite element methods are another very versatile tool for the study of MOFs. They can in principle deal with any MOF geometry of finite cross-section, including MOFs with anisotropic or non-linear dielectrics. Recent work shows that confinement losses can be estimated [70, 71]. However, the price of the high versatility of the method is that it is generally computationally expensive.

Recently, L. Poladian *et al.* suggested a new method, the adjustable boundary condition Fourier decomposition method or ABC-FDM, using polar-coordinate harmonic Fourier decompositions of fields inside the MOF, and a Fourier-Bessel expansion outside the MOF [72]. This method, initially published in the frame of the scalar wave equation, correctly models the outward radiating leakage field, has no *a priori* limitations on the geometries it can deal with, and has recently been extended to the vector wave equation [73]. An improved version

of the method appeared even more recently which makes the method computationally very competitive and hence extremely promising [74].

Here we extend multipole formulations for multicore conventional fibres [75] to treat MOFs. A key aspect of the method described here is that it makes use of the circularity of the inclusions. It is therefore of high accuracy, converging sufficiently rapidly to be able to treat precisely systems containing quite large numbers of inclusions. The formulation respects accurately the symmetry properties of modes in MOFs having regularly arranged inclusions [45, 76], and indeed has been adapted to take into account those symmetry properties to increase computational efficiency. Furthermore, it yields both the real and imaginary parts of the mode propagation constant, the latter giving the confinement loss associated with the finite extent of the MOF's set of confining inclusions. It can deal with the two types of MOF of current interest: those with a solid core, surrounded with air holes, and those with an air core (a cylindrical hole of somewhat larger radius), again surrounded by air holes, which tend to be more numerous than in the solid core case. Finally, the multipole method has the frequency  $\omega$  as an input parameter, with the propagation constant  $\beta$  following from the calculation. It is thus well-suited for calculations involving material dispersion. We stress that though we only consider circular inclusions, the multipole method is not necessarily limited to these. Its extension to non-circular inclusions would follow along lines suggested by Felbacq *et al.* [77]. We note that Yamashita *et al.* use a similar method for conventional multicore fibres [78]. However, they use a point matching technique at the inclusion boundaries, whereas we enforce boundary conditions by projection onto an orthonormal basis. Further, multipole expansions have already been used in the field of MOF studies to compute the far-field pattern emitted from a dipole located in the core of a MOF [79].

## 3.2 Multipole Formulation

Our formulation is similar to that of Lo *et al.* [75], who considered the modes of high-index cylindrical inclusions in a low-index background. Therefore, these structures have properly bound modes, irrespective of the geometry. In contrast, here the inclusions have a low index, and these therefore do not support bound modes. Rather, the modes arise from the geometry of the inclusions and, for a finite cladding, they are not bound, but leaky. This difference has important consequences for the method, and we therefore describe it in some detail here. We concentrate on solid core MOFs, with the modifications for air core MOFs discussed in passing.

### 3.2.1 Geometry

The geometry we treat is given in Fig. 3.1, which represents a transverse  $xy$  cut of the fibre, which is infinitely extended along the  $z$  axis. It shows a silica matrix of (real) refractive index  $n_M$ , perforated with a finite number  $N_i$  of inclusions indexed by  $j$  and of diameter  $d_j$ , whose centers are specified by the vectors  $\mathbf{c}_j$ . The refractive index of inclusion  $j$  is  $n_j$ .

Outside this *hole region*, the MOF is enclosed in a jacket (radius  $r > R_0$ ), whose index  $n_0$  may be complex. One possibility is to take a jacket with refractive index of 1, simulating a MOF in air or vacuum. This enables us to investigate modes confined between the microstructured part of the fibre and the air region, as well as effects due to the finite nature of the silica region surrounding fibres. More generally, our method can deal with any type of cladding surrounding the structure.

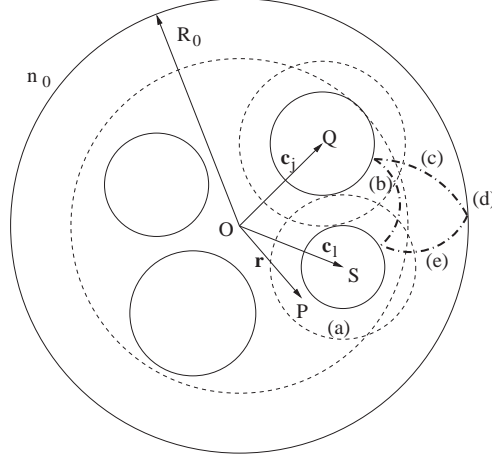


Figure 3.1: Geometry of the MOFs considered, together with the contributions to the fields just outside a generic hole  $i$ . Regions of convergence of multipole expansions are indicated by dashed lines. Note that  $\overrightarrow{QP}$  is  $\mathbf{r}_j$  in Eq. (3.23), while  $\overrightarrow{SP}$  is  $\mathbf{r}_l$  and  $\overrightarrow{OP}$  is  $\mathbf{r}$ . Solid lines indicate physical boundaries, dashed lines indicate regions of convergence.

### 3.2.2 Choice of Propagating Fields

We characterize in the complex representation the electric and magnetic fields  $\mathcal{E}$  and  $\mathcal{H}$  in the MOF by specifying the components  $\mathcal{E}_z$  and  $\mathcal{H}_z$  along the fibre axis, with transverse fields following from Maxwell's equations [3]. In fact, it is convenient to work with scaled magnetic fields:  $\mathcal{K} = Z\mathcal{H}$ , where  $Z = (\mu_0/\epsilon_0)^{1/2}$  denotes the impedance of free space. Each mode is characterized by its propagation constant  $\beta$ , and the transverse dependence of the fields

$$\mathcal{E}(r, \theta, z, t) = \mathbf{E}(r, \theta) e^{i(\beta z - \omega t)}, \quad (3.1)$$

$$\mathcal{K}(r, \theta, z, t) = \mathbf{K}(r, \theta) e^{i(\beta z - \omega t)}, \quad (3.2)$$

with  $\omega$  denoting the angular frequency, related to the free space wavenumber by  $\omega = kc$ . Note that  $\beta$  is complex for leaky modes, the imaginary part of  $\beta$  accounting for attenuation along the  $z$  axis. Here we will use the modes' *effective index*, which is related to  $\beta$  by  $n_{\text{eff}} = \beta/k$ .

Each of the fields ( $V = E_z$  or  $V = K_z$ ) satisfies the Helmholtz equation

$$(\nabla^2 + (k_{\perp}^M)^2)V = 0 \quad (3.3)$$

in the matrix, where  $k_{\perp}^M = \sqrt{k^2 n_M^2 - \beta^2}$ , and

$$(\nabla^2 + (k_{\perp}^i)^2)V = 0 \quad (3.4)$$

in inclusion  $i$ , where  $k_{\perp}^i = \sqrt{k^2 n_i^2 - \beta^2}$ . Care is required when computing complex square roots. We will discuss this matter in Appendix A.

### 3.2.3 Multipole Method: Simplified Approach

The multipole method simply results from considering the balance of incoming and outgoing fields. Its aim is to solve the problem of scattering from a system consisting of multiple

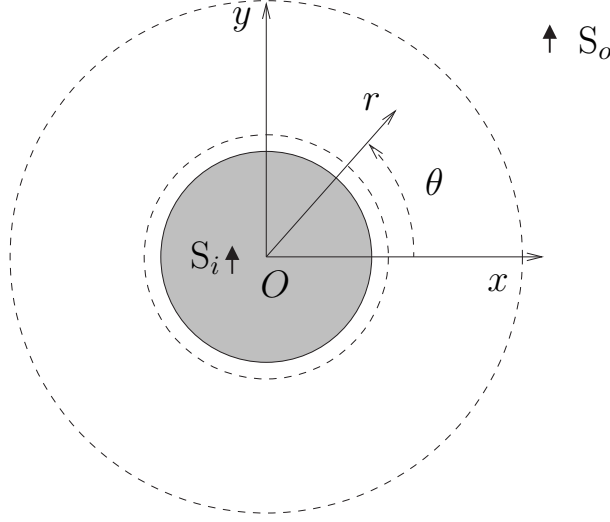


Figure 3.2: Single inclusion in the matrix, with center at the origin.  $S_i$  and  $S_o$  represent sources. The dashed circles represent the borders of an homogenous annulus around the inclusion.

inclusions. In this section we go through each step of the multipole method in a very simplified manner, with simplified notations, to extract the physics behind the multipole method without being blinded by too many new notations or too much mathematics.

### Fourier-Bessel Series

We consider a single inclusion in the matrix (see Fig. 3.2), with center at the origin of the coordinate system  $O$ . In cylindrical coordinates a field  $V(r, \theta)$  is  $2\pi$  periodic along the angular coordinate ( $V(r, \theta + 2\pi) = V(r, \theta)$ ). In any homogeneous annulus around the inclusion (delimited by dashed circles in Fig. 3.2), for fixed  $r$ ,  $V(r, \theta)$  is a regular and  $2\pi$ -periodic function of  $\theta$ , so that we can expand  $V(r, \theta)$  in a Fourier series:

$$V(r, \theta) = \sum_{n \in \mathbb{Z}} f_n(r) \exp(in\theta). \quad (3.5)$$

Note that because  $V(r, \theta)$  is regular in the annulus, the Fourier coefficients  $f_n(r)$  are regular functions of  $r$ . Using the Fourier expansion in the Helmholtz equation (Eq. (3.3)), we obtain

$$\sum_{n \in \mathbb{Z}} \nabla^2 (f_n(r) \exp(in\theta)) + (k_{\perp}^M)^2 f_n(r) \exp(in\theta) = 0 \quad (3.6)$$

$$\Leftrightarrow \sum_{n \in \mathbb{Z}} \left[ \frac{\partial^2 f_n(r)}{\partial r^2} + \frac{1}{r} \frac{\partial f_n(r)}{\partial r} + \left( (k_{\perp}^M)^2 - \frac{n^2}{r^2} \right) f_n(r) \right] \exp(in\theta) = 0. \quad (3.7)$$

$V(r, \theta)$  being a continuous function in the annulus, we can equate the Fourier coefficients on the right hand side and on the left hand side of Eq. (3.7). This yields the equation valid for all  $n$

$$\frac{\partial^2 f_n(r)}{\partial r^2} + \frac{1}{r} \frac{\partial f_n(r)}{\partial r} + \left( (k_{\perp}^M)^2 - \frac{n^2}{r^2} \right) f_n(r) = 0. \quad (3.8)$$

With a linear change of variable  $u = k_{\perp}^M r$  this equation becomes

$$\frac{\partial^2 f_n(u)}{\partial u^2} + \frac{1}{u} \frac{\partial f_n(u)}{\partial u} + \left(1 - \frac{n^2}{u^2}\right) f_n(u) = 0 . \quad (3.9)$$

Eq. (3.9) is the Bessel differential equation of order  $n$ . The functions  $f_n(u)$  are hence linear combinations of Bessel functions of the first and second kind of order  $n$  ( $J_n(u)$  and  $Y_n(u)$  respectively), or, equivalently, of Bessel and Hankel functions of the first kind of order  $n$ , the latter being defined by  $H_n^{(1)}(u) = J_n(u) + \imath Y_n(u)$ :

$$f_n(u) = A_n J_n(u) + B_n H_n^{(1)}(u) . \quad (3.10)$$

Replacing  $f_n(r)$  in the Fourier expansion Eq. 3.5, we have

$$V(r, \theta) = \sum_{n \in \mathbb{Z}} \left( A_n J_n(k_{\perp}^M r) + B_n H_n^{(1)}(k_{\perp}^M r) \right) \exp(\imath n \theta) . \quad (3.11)$$

The expansion of the field  $V$  in Eq. (3.11) is called a Fourier-Bessel series. Any function which is regular and satisfies the Helmholtz equation in an annulus can be expressed as a Fourier-Bessel series.

### Physical Interpretation of Fourier-Bessel Series

The Fourier-Bessel series can be split in two very different parts: the Bessel functions of the first kind are regular everywhere, whereas the Hankel functions have a singularity at 0 where they diverge. Further, Hankel functions of the first kind satisfy the outgoing wave equation, whereas Bessel functions of the first kind don't.

To understand the meaning of the two parts of the Fourier-Bessel function, we consider the same annulus as above, but without inclusion. The whole space is now homogeneous. If a source is placed inside the inner circle of the annulus ( $S_i$  in Fig. 3.3), the field it radiates has a singularity inside the inner circle of the annulus, and satisfies the outgoing wave condition. In the annulus, it hence cannot be represented by Bessel series, but only by a superposition of Hankel functions. Conversely, a source placed beyond the outer ring of the annulus ( $S_o$  in Fig. 3.2) radiates a field which is regular in the annulus and in the region delimited by the inner circle of the annulus. Its field expansion in the annulus can hence not contain Hankel functions, but only Bessel functions.

Eq. (3.11) can be written as

$$V(r, \theta) = \mathcal{R}(r, \theta) + \mathcal{O}(r, \theta) \quad (3.12)$$

with

$$\mathcal{R}(r, \theta) = \sum_{n \in \mathbb{Z}} A_n J_n(k_{\perp}^M r) \exp(\imath n \theta) \quad (3.13)$$

$$\mathcal{O}(r, \theta) = \sum_{n \in \mathbb{Z}} B_n H_n^{(1)}(k_{\perp}^M r) \exp(\imath n \theta) . \quad (3.14)$$

$\mathcal{R}$  is the regular part of  $V$ . It describes fields radiated from sources situated beyond the outer circle of the annulus.  $\mathcal{O}$  is the singular part of  $V$ . It describes fields radiated from sources situated inside the inner circle of the annulus. Note that if a source is placed inside the annulus, the field it radiates has a singularity in the annulus. A field radiated by a source inside the annulus hence cannot be described by Fourier-Bessel series in that annulus.

### Change of Basis

In the local coordinate system with origin in  $S_o$ , the field radiated by  $S_o$  is an outgoing, singular field. In an annulus surrounding  $S_o$ , the radiated field is described by a series of Hankel functions  $\mathcal{O}_s(r_s, \theta_s)$ , with  $(r_s, \theta_s)$  being local coordinates associated with  $S_o$ . In the coordinate system with center  $O$ , the same field is regular and incident in the annulus surrounding  $O$  and excluding  $S_o$ : the nature of the field depends on the system of coordinates. We can construct a linear operator associating the outgoing field in one coordinate system to the resulting incoming field in another coordinate system. We define the operator  $\mathcal{H}$  by

$$\mathcal{R} = \mathcal{H}\mathcal{O}_s, \quad (3.15)$$

where  $\mathcal{R}$  is the regular field in an annulus around  $O$  (Eq. 3.14). In practice, operator  $\mathcal{H}$  will be represented by a matrix linking the Fourier-Bessel coefficients  $A_n$  of  $\mathcal{R}$  to the Fourier Bessel coefficients  $B_n$  of  $\mathcal{O}_s$ . The coefficients of the matrix are well known, and given by Graf's theorem as we will see in the mathematical derivation of the multipole method.

### Fourier-Bessel Series and one Inclusion: Scattering Operator

We now put the inclusion back in the annulus, and consider fields originating outside the annulus, *e.g.* from  $S_o$ . In the annulus, the field radiated from  $S_o$  is regular and follows from Eq. 3.15. The field reaching the inclusion will be scattered. The scattered field radiates away from the inclusion: there are now sources inside the region delimited by the inner circle of the annulus. The scattered field is hence described in the annulus by an outgoing field  $\mathcal{O}$  while the incoming field is associated with  $\mathcal{R}$ . Since we only consider linear scattering,  $\mathcal{R}$  and  $\mathcal{O}$  are linked by a linear scattering operator,  $\mathcal{S}$ , defined by

$$\mathcal{O} = \mathcal{S}\mathcal{R}. \quad (3.16)$$

Once  $\mathcal{H}$  and  $\mathcal{S}$  are known, we can compute the scattered field using Eq. (3.15) and (3.16). In practice, the scattering operator is represented by a matrix linking the Fourier Bessel coefficients  $A_n$  of  $\mathcal{R}$  and  $B_n$  of  $\mathcal{O}$ . For simple geometries of inclusions (*e.g.* circular inclusions), the coefficients of the matrix can be expressed in exact analytic form. For inclusions with arbitrary geometry, the matrix can be computed numerically.

### Fourier-Bessel Series and Two Inclusions: The Multipole Method

We now consider two inclusions (1 and 2), and a source  $S_o$  exterior to both inclusions.  $\mathcal{R}_1$ , the incoming regular field for inclusion 1 now results from the superposition of the field  $\mathcal{O}_s$  radiated from  $S_o$  and the scattered field  $\mathcal{O}_2$  from inclusion 2. Using the change of basis operators  $\mathcal{H}_{s,1}$  and  $\mathcal{H}_{2,1}$  defined as in Eq. (3.15), we have

$$\mathcal{R}_1 = \mathcal{H}_{2,1}\mathcal{O}_2 + \mathcal{H}_{s,1}\mathcal{O}_s. \quad (3.17)$$

Similarly,  $\mathcal{R}_2$ , the regular incoming field for inclusion 2 is given by

$$\mathcal{R}_2 = \mathcal{H}_{1,2}\mathcal{O}_1 + \mathcal{H}_{s,2}\mathcal{O}_s. \quad (3.18)$$

The two equations above simply explicit that the incoming field on one inclusion results from the superposition of the field radiated by the other inclusion and the source. Using the

scattering operators  $\mathcal{S}_1$  and  $\mathcal{S}_2$  for inclusions 1 and 2 respectively, we have

$$\begin{cases} \mathcal{O}_1 = \mathcal{S}_1(\mathcal{H}_{2,1}\mathcal{O}_2 + \mathcal{H}_{s,1}\mathcal{O}_s) \\ \mathcal{O}_2 = \mathcal{S}_2(\mathcal{H}_{1,2}\mathcal{O}_1 + \mathcal{H}_{s,2}\mathcal{O}_s) \end{cases} \quad (3.19)$$

This linear system of equations links the two unknown scattered fields  $\mathcal{O}_1$  and  $\mathcal{O}_2$  to the known source field  $\mathcal{O}_s$  through change of basis and scattering operators. Once the scattering and change of basis operators are computed, one can hence deduce the fields scattered from the system constituted of both cylinders through solving Eq. (3.19). It is straightforward to generalize the technique used here to more than two cylinders.

In practice, all operators are represented by matrices and the fields  $\mathcal{O}$  and  $\mathcal{R}$  by the vectors consisting of the Fourier-Bessel coefficients of the fields. The matrices are readily computed, so that given the Fourier-Bessel expansion of a source  $\mathcal{O}_s$ , the Fourier-Bessel coefficients describing  $\mathcal{O}_1$  and  $\mathcal{O}_2$  follow from solving the matrix equations equivalent to Eq. (3.19). Once  $\mathcal{O}_1$  and  $\mathcal{O}_2$  are known, the regular part of the field around inclusions 1 and 2 can be deduced *e.g.* from the scattering matrices through Eq. (3.16). The fields are then known in any homogeneous annulus surrounding the inclusions. In fact it appears that the superposition of outgoing fields  $\mathcal{O}_s$ ,  $\mathcal{O}_1$  and  $\mathcal{O}_2$  describes the field accurately *everywhere*.

Using change of basis operators, we have resumed the computation of the field scattered from a complex system consisting of several inclusions to the computation of scattering operators of single inclusions. Guided modes of a structure consisting of several inclusions correspond to non-zero fields around the inclusions in the absence of any exterior sources. To find modes, one hence has to find inclusion-parameters for which Eq. (3.19) has solutions with non-zero  $\mathcal{O}_1$  and  $\mathcal{O}_2$  in the absence of the  $\mathcal{O}_s$  term.

In the next few subsections we describe the multipole method more rigorously, explicitly defining all required fields, operators and vectors, and detailing the domains of validity of expansions. Further, we adapt the method to the case where the matrix containing the inclusions is surrounded by a jacket.

### 3.2.4 Rigorous Formulation of the Field Identities

In the vicinity of the  $l^{th}$  cylindrical inclusion (see Fig. 3.1), we represent the fields in the matrix in local coordinates  $\mathbf{r}_l = (r_l, \theta_l) = \mathbf{r} - \mathbf{c}_l$  and express the fields in Fourier-Bessel series. With  $J_m(z)$  and  $H_m^{(1)}(z)$  being the usual Bessel function of order  $m$  and the Hankel function of the first kind of order  $m$  respectively, we have for the electric field

$$E_z = \sum_{m \in \mathbb{Z}} \left[ A_m^{\text{El}} J_m(k_{\perp}^{\text{M}} r_l) + B_m^{\text{El}} H_m^{(1)}(k_{\perp}^{\text{M}} r_l) \right] e^{im\theta_l} \quad (3.20)$$

and similarly for  $K_z$ , but with coefficients  $A_m^{\text{Kl}}$  and  $B_m^{\text{Kl}}$ . In (3.20) the  $J_m$  terms represent the regular incident part<sup>1</sup>  $\mathcal{R}^{\text{El}}$  of the field  $E_z$  for cylinder  $l$  since it is finite everywhere, including in the inclusion, while the  $H_m^{(1)}$  terms represent the outgoing wave part<sup>2</sup>  $\mathcal{O}^{\text{El}}$  of the field, associated with a source inside the cylinder. We thus have  $E_z = \mathcal{R}^{\text{El}} + \mathcal{O}^{\text{El}}$ .

<sup>1</sup>The Bessel functions  $J_m$  are continuous and finite in a bound domain, the field they describe must therefore have its origin in sources outside that domain.

<sup>2</sup>Hankel functions  $H_m^{(1)}$  satisfy the outgoing wave condition and diverge at 0; their contribution to the field in an annulus surrounding an inclusion is therefore associated with fields originating in sources in or on the inclusion, and radiating away from it.

Local expansion (3.20) is valid only in an annulus extending from the surface of the cylinder to the nearest cylinder or source (region (a) in Fig. 3.1). The same expression may be used around the jacket boundary which we designate by the superscript 0 (region d in Fig. 3.1).

Another description of the fields is originally due to Wijngaard [80]. He reasoned that a field in a region can be written as a superposition of outgoing waves from all source bodies in the region. If the waves originate outside the region, their expansion is in terms of  $J$ -type waves, which are source free. Of course this physical argument can be supplemented by rigorous mathematical arguments [75, 80, 81], as discussed in Appendix B. For MOFs, the Wijngaard expansion takes the form

$$E_z = \sum_{l=1}^{N_i} \sum_{m \in \mathbb{Z}} B_m^{\text{El}} H_m^{(1)}(k_{\perp}^{\text{M}} |\mathbf{r}_l|) e^{im \arg(\mathbf{r} - \mathbf{c}_l)} + \sum_{m \in \mathbb{Z}} A_m^{\text{E0}} J_m(k_{\perp}^{\text{M}} r) e^{im\theta} , \quad (3.21)$$

and is valid everywhere in the matrix. Each term of the  $m$  series is an outgoing wave field with a source at cylinder  $l$ , while the final term, indexed by 0, is the regular field originating at the jacket boundary.

Equating (3.20) and (3.21), thus enforcing consistency, yields, in the vicinity of cylinder  $l$ ,

$$\sum_{m \in \mathbb{Z}} A_m^{\text{El}} J_m(k_{\perp}^{\text{M}} r_l) e^{im\theta_l} = \sum_{\substack{j=1 \\ j \neq l}}^N \sum_{m \in \mathbb{Z}} B_m^{\text{Ej}} H_m^{(1)}(k_{\perp}^{\text{M}} r_j) e^{im\theta_j} + \sum_{m \in \mathbb{Z}} A_m^{\text{E0}} J_m(k_{\perp}^{\text{M}} r) e^{im\theta} , \quad (3.22)$$

since the  $H_m^{(1)}(k_{\perp}^{\text{M}} r_l)$  terms are common to both expansions. Note that the sum on the left hand side of Eq. (3.22) is associated with the regular incident field for inclusion  $l$ , while the double sum on the right hand side is associated with the outgoing field originating from all other inclusions ( $j \neq l$ ), and the last sum represents the field coming from the jacket. Eq. (3.22) hence simply results from detailing the origin of the field incident on inclusion  $l$ .

Evaluating Eq. (3.22) is not straightforward because different terms refer to different origins. We therefore use Graf's addition theorem [82] which lets us transform the origin of the cylindrical waves. A full discussion is given in Appendix C, where we show that it may be viewed as a change of basis transformation. For example the contribution to the local regular field in the vicinity of cylinder  $l$  due to cylinder  $j$  (line b, Fig. 3.1) is

$$\sum_{n \in \mathbb{Z}} A_n^{\text{Elj}} J_n(k_{\perp}^{\text{M}} r_l) e^{in \arg(\mathbf{r}_l)} = \sum_{m \in \mathbb{Z}} B_m^{\text{Ej}} H_m^{(1)}(k_{\perp}^{\text{M}} r_j) e^{im \arg(\mathbf{r}_j)} , \quad (3.23)$$

where

$$A_n^{\text{Elj}} = \sum_{m \in \mathbb{Z}} \mathcal{H}_{nm}^{lj} B_m^{\text{Ej}} , \quad (3.24)$$

$$\mathcal{H}_{nm}^{lj} = H_{n-m}^{(1)}(k_{\perp}^{\text{M}} c_{lj}) e^{-i(n-m) \arg(\mathbf{c}_{lj})} , \quad (3.25)$$

and  $\mathbf{c}_{lj} = \mathbf{c}_j - \mathbf{c}_l$ , as shown in Appendix C.1. The physics behind Eq. (3.23) is quite intuitive, and corresponds to the *Change of Basis* paragraph in Sec. 3.2.3: the right hand term is

associated with an outgoing wave originated from sources inside inclusion  $j$ . In any annulus not intersecting or including inclusion  $j$ , and in particular in an annulus centered on inclusion  $l$ , this field is regular and satisfies the Helmholtz equation. It can hence be expressed in terms of a series of Bessel functions, which is exactly what Eq. (3.23) does.

At this point we introduce the notation  $\mathbf{A}^{\text{El}j} = [A_n^{\text{El}j}]$ , that lets us generate vectors of mathematical objects. A similar notation is used for matrices, i.e.,  $\mathfrak{H}^{lj} = [\mathcal{H}_{nm}^{lj}]$ . In matrix form, then, we represent the basis change (3.24) as

$$\mathbf{A}^{\text{El}j} = \mathfrak{H}^{lj} \mathbf{B}^{\text{E}j}. \quad (3.26)$$

Similarly, the contribution to the regular incident field at cylinder  $l$  due to the jacket (line  $e$ , Fig. 3.1) is

$$\sum_{n \in \mathbb{Z}} A_n^{\text{El}0} J_n(k_{\perp}^{\text{M}} r_l) e^{in \arg(\mathbf{r}_l)} = \sum_{m \in \mathbb{Z}} A_m^{\text{E}0} J_m(k_{\perp}^{\text{M}} r) e^{im\theta}, \quad (3.27)$$

where the change of basis (derived in Appendix C.2) is

$$\mathbf{A}^{\text{El}0} = \mathfrak{J}^{l0} \mathbf{A}^{\text{E}0}, \quad (3.28)$$

with

$$\mathfrak{J}^{l0} = [\mathfrak{J}_{nm}^{l0}] = [(-1)^{(n-m)} J_{n-m}(k_{\perp}^{\text{M}} c_l) e^{i(m-n) \arg(\mathbf{c}_l)}]. \quad (3.29)$$

Accumulating these contributions for all cylinders and the jacket we have, in the annulus (a) around cylinder  $l$  (see Fig. 3.1)

$$\mathbf{A}^{\text{El}} = \sum_{\substack{j=1 \\ j \neq l}}^{N_i} \mathbf{A}^{\text{El}j} + \mathbf{A}^{\text{El}0} = \sum_{\substack{j=1 \\ j \neq l}}^{N_i} \mathfrak{H}^{lj} \mathbf{B}^{\text{E}j} + \mathfrak{J}^{l0} \mathbf{A}^{\text{E}0}, \quad (3.30)$$

a result that holds for both the  $E_z$  and  $K_z$  fields.

In a similar way, the outgoing field in the vicinity of the jacket boundary due to cylinder  $j$  (line  $c$ , Fig. 3.1) is

$$\sum_{n \in \mathbb{Z}} B_n^{\text{E}0j} H_n^{(1)}(k_{\perp}^{\text{M}} r) e^{in\theta} = \sum_{m \in \mathbb{Z}} B_m^{\text{E}j} H_m^{(1)}(k_{\perp}^{\text{M}} r_j) e^{im \arg(\mathbf{r}_j)}, \quad (3.31)$$

with the change of basis represented by

$$\mathbf{B}^{\text{E}0j} = \mathfrak{J}^{0j} \mathbf{B}^{\text{E}j}, \quad (3.32)$$

where

$$\mathfrak{J}^{0j} = [\mathfrak{J}_{nm}^{0j}] = [J_{n-m}(k_{\perp}^{\text{M}} c_j) e^{-in(n-m) \arg(\mathbf{c}_j)}], \quad (3.33)$$

as shown in Appendix C.3.

Adding the contributions for all cylinder sources we reexpress the first term on the right-hand side of Wijngaard expansion (3.21) in a form valid just inside the jacket (region  $d$ )

$$\sum_{l=1}^{N_i} \mathcal{O}^{\text{El}} = \sum_{n \in \mathbb{Z}} B_n^{\text{E}0} H_n^{(1)}(k_{\perp}^{\text{M}} r) e^{in\theta} = \mathcal{O}^{\text{E}0}, \quad (3.34)$$

where

$$\mathbf{B}^{\text{E}0} = \sum_{l=1}^{N_i} \mathbf{B}^{\text{E}0l} = \sum_{l=1}^{N_i} \mathfrak{J}^{0l} \mathbf{B}^{\text{El}}, \quad (3.35)$$

a result that also holds for both  $E_z$  and  $K_z$ .

### 3.2.5 Boundary Conditions and Field Coupling

While the field identities of the previous section apply individually to each field component, cross coupling between them occurs at boundaries. In what follows, it is most convenient to formulate the boundary conditions in terms of cylindrical reflection coefficients as derived in Appendix D. For circular inclusions, for the reflected fields outside each cylinder we have

$$\begin{aligned} B_n^{El} &= R_n^{EEl} A_n^{El} + R_n^{EKl} A_n^{Kl} , \\ B_n^{Kl} &= R_n^{KEl} A_n^{El} + R_n^{KKl} A_n^{Kl} , \end{aligned} \quad (3.36)$$

where the expression for the reflection coefficients are given in Eqs (D.14) in Appendix D. The reflection matrices are derived for each inclusion treated in isolation, and are thus known in closed form for circular inclusions, in which case they are diagonal. For non-circular inclusions, they could be replaced by either analytic expressions for other special cases, or numerical estimates from a differential or integral equation treatment [77, 83]. In these cases they generally also have off-diagonal elements.

Equations (3.36) can be written as

$$\begin{bmatrix} \mathbf{B}^{El} \\ \mathbf{B}^{Kl} \end{bmatrix} = \begin{bmatrix} \mathbf{R}^{EEl} & \mathbf{R}^{EKl} \\ \mathbf{R}^{KEl} & \mathbf{R}^{KKl} \end{bmatrix} \begin{bmatrix} \mathbf{A}^{El} \\ \mathbf{A}^{Kl} \end{bmatrix}, \quad (3.37)$$

or

$$\tilde{\mathbf{B}}^l = \tilde{\mathbf{R}}^l \tilde{\mathbf{A}}^l, \quad (3.38)$$

with  $\mathbf{R}^{EE,l} = \text{diag}(R_n^{EEl})$  and similar definitions for the other reflection matrices. We also need an interior form at the jacket boundary (point  $d$  in Fig. 3.1),

$$\tilde{\mathbf{A}}^0 = \tilde{\mathbf{R}}^0 \tilde{\mathbf{B}}^0 \quad (3.39)$$

where  $\tilde{\mathbf{A}}^0$ ,  $\tilde{\mathbf{B}}^0$  and  $\tilde{\mathbf{R}}^0$  are defined as in (3.37)–(3.38), and the coefficients of  $\tilde{\mathbf{R}}^0$  are given by Eqs (D.10). In this form the outgoing field ( $\tilde{\mathbf{B}}^0$ ) generated by all inclusions (line  $c$ ) is reflected by the jacket to generate the regular field ( $\tilde{\mathbf{A}}^0$ ), which feeds into the incident field for inclusion  $l$  (line  $e$  in Fig. 3.1). It is straightforward to adapt  $\tilde{\mathbf{R}}^0$  to cases where multiple films surround the hole region.

### 3.2.6 Derivation of the Rayleigh Identity

With the structure of the field coupling derived in the Section 3.2.5, we now form field identities applying to the vector components  $\tilde{\mathbf{A}}^l$  and  $\tilde{\mathbf{B}}^l$ . From Eq. (3.30) we have

$$\tilde{\mathbf{A}}^l = \sum_{\substack{j=1 \\ j \neq l}}^{N_i} \tilde{\mathcal{H}}^{lj} \tilde{\mathbf{B}}^j + \tilde{\mathcal{J}}^{l0} \tilde{\mathbf{A}}^0, \quad (3.40)$$

where  $\tilde{\mathcal{H}}^{lj} = \text{diag}(\mathcal{H}^{lj}, \mathcal{H}^{lj})$ , and  $\tilde{\mathcal{J}}^{l0} = \text{diag}(\mathcal{J}^{l0}, \mathcal{J}^{l0})$ . Equation (3.40) is the representation of the regular incident field at cylinder  $l$  in terms of outgoing components  $\tilde{\mathbf{B}}^j$  from all other cylinders and an incident field contribution  $\tilde{\mathbf{A}}^0$  from the jacket.

Combining (3.40) for all cylinders  $l = 1 \dots N_i$  and introducing  $\mathcal{A} = [\tilde{\mathbf{A}}^l]$  and  $\mathcal{B} = [\tilde{\mathbf{B}}^l]$ , we derive

$$\mathcal{A} = \tilde{\mathcal{H}} \mathcal{B} + \tilde{\mathcal{J}}^{\text{B}0} \tilde{\mathbf{A}}^0, \quad (3.41)$$

where  $\tilde{\mathcal{H}} = [\tilde{\mathcal{H}}^{lj}]$  for  $l, j = 1 \dots N_i$  with  $\tilde{\mathcal{H}}^{ll} \equiv \mathbf{0}$  and

$$\tilde{\mathcal{J}}^{B0} = [\tilde{\mathcal{J}}^{l0}] = [(\tilde{\mathcal{J}}^{10})^T, (\tilde{\mathcal{J}}^{20})^T, \dots, (\tilde{\mathcal{J}}^{N_i 0})^T]^T, \quad (3.42)$$

where the  $T$  indicates the transpose. Similarly, the vector outgoing field in the vicinity of the jacket due to all the cylinders is given by

$$\tilde{\mathbf{B}}^0 = \sum_{j=1}^{N_i} \tilde{\mathcal{J}}^{0l} \tilde{\mathbf{B}}^l = \tilde{\mathcal{J}}^{0B} \mathcal{B} \quad (3.43)$$

from Eq.(3.35). Here

$$\tilde{\mathcal{J}}^{0B} = [\tilde{\mathcal{J}}^{0l}] = [\tilde{\mathcal{J}}^{01}, \tilde{\mathcal{J}}^{02}, \dots, \tilde{\mathcal{J}}^{0N_i}] . \quad (3.44)$$

Combining (3.38), (3.39), (3.41) and (3.43) and eliminating  $\tilde{\mathbf{A}}^0$  and  $\tilde{\mathbf{B}}^0$  we form a homogeneous system of equations (which represents the *Rayleigh identity*, and we will also call *field identity*) in the source coefficients

$$[\mathbf{I} - \mathcal{R}(\tilde{\mathcal{H}} + \tilde{\mathcal{J}}^{B0} \tilde{\mathbf{R}}^0 \tilde{\mathcal{J}}^{0B})] \mathcal{B} \equiv \mathcal{M} \mathcal{B} = \mathbf{0}, \quad (3.45)$$

where the right-hand side indicates the absence of external sources, and

$$\mathcal{R} = \text{diag} [\tilde{\mathbf{R}}^1, \tilde{\mathbf{R}}^2, \dots, \tilde{\mathbf{R}}^{N_i}] . \quad (3.46)$$

Non-trivial solutions to the homogeneous system (3.45) correspond to non-zero fields propagating in the  $z$ -direction. The solutions represent a non-zero field existing without any exterior source of energy, in other words propagating (possibly leaky) fibre modes. We will see in the next Chapter how this equation can be solved to obtain the modes of a MOF structure.

# Note on the Field Distribution Figures

In subsequent chapters we will make an extensive use of figures showing the field distribution of modes. In order to fully understand those figures it is worth knowing exactly what they depict and how they were constructed. All field distribution and Bloch transform figures are drawn in a normalized, linear colour scale. The brightest colour represents the maximum value of the distribution within the depicted frame, the darkest represents the smallest value. Fig. 3.3 represents the colour scale used. The aim is not to give quantitative results concerning the values of the fields, but rather qualitative results on the geometry of the modal fields. One thing this kind of representation *can not* be used for is for example to see the relative importance between values taken by the  $E_z$  and  $K_z$  fields in order to get an idea on the rather TE or TM nature of a mode. Further, since the plots don't give any quantitative information, scaled magnetic field distribution plots are rigorously identical to unscaled magnetic field distribution plots. Since the reader is likely to be more familiar with the unscaled magnetic field  $\mathbf{H}$ , from chapter 5 on we will come back to the unscaled magnetic field notation  $\mathbf{H}$ .

Field distribution plots represent the magnitude of the  $z$  components of the fields  $\mathbf{E}$  or  $\mathbf{K}$ , or the real part of the  $z$  component of the Poynting vector  $\mathbf{S}$ . In almost all modes we study, the  $z$  components of  $\mathbf{E}$  and  $\mathbf{K}$  are not the most important in magnitude, the magnitude of the transverse components of these fields is generally larger. The reason we depict the longitudinal rather than the transverse components of the fields is that  $E_z$  and  $K_z$  are the components we use in our multipole expansions.  $E_z$  and  $K_z$  directly reflect the multipole expansions they are constructed from. The real part of  $S_z$  on the contrary is a more “physical” quantity, as it reflects the density of power carried along the axis of the fibre: The  $\Re(S_z)$  plots show how the power carried along the fibre is distributed in the cross section of the fibre.

The field distribution plots are constructed from the Fourier-Bessel expansions of the modes (Eq. (3.20)), the coefficients of these expansions being given by the eigenvectors associated to near-zero eigenvalues of Eq. (3.45). In most of our simulations, the jacket and the matrix have same refractive index, so that the confinement is solely due to the cylindrical inclusions around the core. In that case the boundary conditions at the matrix/jacket interface are associated to an identity transmission matrix and a null reflection matrix. These don't affect the computation of modes, so that to speed up the computations we reduced the order of truncation of the Fourier-Bessel series in the jacket to 1.<sup>3</sup> This nevertheless had a small side-effect on the field distribution plots: in these, the fields in the cladding and jacket are computed using Bessel functions of order -1 to 1, so that the field appears discontinuous at and dipolar beyond the matrix/cladding interface. This is only an artefact in the representation of the fields and should not disconcert the reader.

---

<sup>3</sup>We could also have suppressed those matrices completely, but only at the cost of changing the eigenvalue equation.

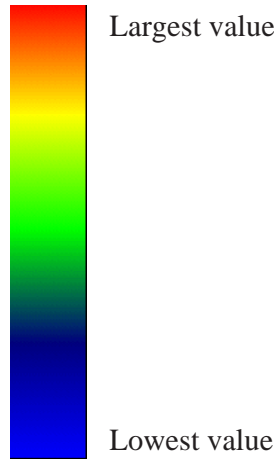


Figure 3.3: Colour scale used for field distribution and Bloch transform plots, unless otherwise mentioned.

Finally, the field distribution figures, as almost all the figures in this thesis, are printed in their black and white version, colour versions being available in the electronic version of the thesis. The black and white figures do not result from a simple graphical colour to black and white conversion, since this would have given a redundant and unreadable colour scale: The colour version of the density plots use a continuous colour scale, whereas the black and white version of the plots use a discrete colour scale, so that the plots are in fact filled contour plots. Note that the colour version of the field density plots is much more readable than the printed black and white version, especially when the number of inclusions becomes large.

Entrée :

## Daurade et Écrevisses

Sauce Écrevisse, Tomate «Cariocas»

*Sea Bream and Yabbis, Yabbi Sauce and Tomato "Cariocas"*

### Pour 6 personnes :

Pour la daurade :

*3 petites daurades  
80 g de beurre clarifié  
fleur de sel  
poivre*

Pour la sauce écrevisse :

*24 écrevisses vivantes  
5 L de court-bouillon  
1 gousse d'ail  
1 cuillerée à soupe d'huile  
d'olive  
50 g de beurre clarifié  
50 g de beurre  
3 cl de cognac fine de  
champagne  
1 cuillerée à café de concentré  
de tomates  
piment d'Espelette en poudre  
sel  
poivre*

Pour les tomates «Cariocas» :

*6 tomates cerise en grappes  
huile d'olive  
sel  
sucre  
poivre*

### Les tomates «Cariocas» [2]

**D**ÉTACHER les tomates des tiges en préservant le pédoncule. Les ébouillanter pendant 5 secondes. Avec la pointe d'un couteau, inciser chaque tomate à mi-hauteur, puis la peler sur sa partie inférieure. Retourner la peau restante vers le haut. Les assaisonner de sel, de poivre du moulin et de sucre. Les réserver 15 minutes à température ambiante, puis les ranger dans une sauteuse en les maintenant bien droites. Les recouvrir d'huile d'olive. Démarrer la cuisson sur le feu jusqu'à ce que l'huile frémissse, puis enfourner à 90°C pendant une heure. Les laisser dans la sauteuse jusqu'au moment de servir.

### La sauce écrevisse

**P**ORTER le court-bouillon à ébullition. Plonger une demi-douzaine d'écrevisses vivantes dans le court bouillon, compter 3 minutes puis retirer à l'aide d'une écumoire. Réitérer avec les autres écrevisses, toujours par demi-douzaines. Laisser refroidir les écrevisses, puis décoriquer les queues de 18 d'entre elles. Réserver les 6 autres pour la décoration.

**P**ILER les coffres d'écrevisses. Faire chauffer le beurre clarifié et l'huile d'olive dans une sauteuse. Y ajouter la gousse d'ail non épluchée et les coffres pilés ; laisser colorer à feu vif en remuant fréquemment. Une fois les coffres bien rouges, déglacer au cognac. Retirer la gousse d'ail et passer le contenu de la sauteuse au moulin à légumes puis au chinois en pressant bien afin d'extraire le maximum de jus. Verser le jus obtenu dans une casserole.

**A**U moment de servir réchauffer à feu doux, incorporer le beurre par petits bouts, lier avec le concentré de tomates et assaisonner de piment d'espelette, de sel et de poivre.

### La daurade

**É**CAILLER et vider les daurades. En lever les filets sans retirer la peau, retirer les arrêtes à l'aide d'une pince à épiler. Tailler les filets en «sifflets». Les essuyer sur du papier absorbant. Faire chauffer le beurre clarifié dans une poêle à feu vif. Déposer les filets de daurade, côté peau. Lorsque le bord des filets blanchit, les retourner puis compter 20 secondes. Retirer les filets, les égouter sur du papier absorbant.

**T**IÉDIR les tomates cariocas, les égouter. Disposer sur chaque assiette chauffée une tomate "Cariocas", une écrevisse, trois queues d'écrevisses décortiquées, un filet de daurade saupoudré de fleur de sel et de poivre et un cordon de sauce écrevisse. Servir.

## Chapter 4

# The Multipole Method: Implementation

*This Chapter is based on ref. [84]*

### 4.1 Introduction

In the previous Chapter, we presented the development of a multipole formulation leading to a matrix equation satisfied by modes of MOFs. Here we discuss how to use this formulation to analyse propagation and field characteristics numerically, the choice of its parameters to guarantee accurate results, and its numerical verification. The last is achieved through internal consistency tests, and through a comparison both with other methods and with experimental results.

The description of numerical strategies here is of necessity detailed, since the location of modes requires the finding of an approximate zero of the determinant of a large complex matrix. Such zeros are often difficult to distinguish from false minima at first sight, and it is necessary to employ various validation criteria on the "modes" corresponding to the various putative zeros to identify physically meaningful solutions. It is of course valuable to have numerical or experimental values for similar systems to guide the mode search, and the curves and tables we provide here and throughout the next chapters should provide a comprehensive aid to future workers.

### 4.2 Geometry

In the examples used to illustrate the implementation of the multipole method as well as in subsequent chapters we will concentrate – unless otherwise mentioned – on MOFs with identical air holes in silica, arranged following a hexagonal packing<sup>1</sup>, as shown in Fig. 4.1. The jacket is taken to have same refractive index as the matrix, so that guidance of modes is solely due to a finite set of air holes in bulk silica. The dispersion properties of silica are taken into account using Sellmeier expansions of the refractive index [4]. The hexagonal array of holes is characterized by its hole to hole spacing or *pitch* ( $\Lambda$ ). The holes all have same diameter  $d$ . At the origin, a hole is missing: we will see that this defect in the hexagonal lattice can

---

<sup>1</sup>The hexagonal packing is also known as the triangular lattice.

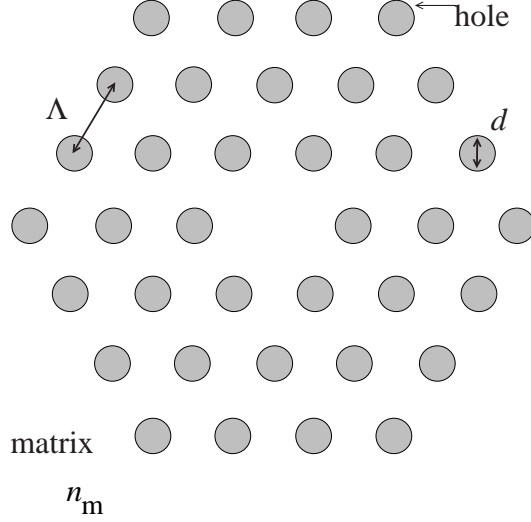


Figure 4.1: Geometry of the MOFs considered in most numerical studies of the forthcoming chapters. The core is surrounded by  $N_r = 3$  layers. Beyond the hole layers, the jacket is made out of the same material as the matrix.

pin modes, and that under certain conditions the modes can be localized around the missing hole, therefore also called the *core* or *core region*. Around the core are concentric, hexagonal layers of holes, and we note  $N_r$  the number of layers, or *rings*. The set of holes around the core is responsible for the confinement of modes: we will refer to it as the *cladding structure* or the *cladding* when no confusion is possible with an actual dielectric cladding layer between the matrix and the jacket. Note that this kind of MOF has  $C_{6v}$  symmetry properties.

## 4.3 Mode Location

### 4.3.1 Solving the Rayleigh Identity

The homogeneous equation (3.45), the main result of the previous Chapter, corresponds to a non-trivial field vector  $\mathbf{B}$  only if the determinant of the matrix  $\mathbf{M}$  is effectively zero. Once the structure and wavelength are given, the matrix  $\mathbf{M}$  depends only on  $\beta$ , or, equivalently, its effective index  $n_{\text{eff}}$ . The search for modes therefore becomes a matter of finding zeros of the complex function  $\det(\mathbf{M})$  of the complex variable  $n_{\text{eff}}$ . To investigate this numerically, field expansions such as (3.20) must be truncated, say to have  $m$  running from  $-M$  to  $M$ . In Fig. 4.2 we show a determinant surface in the neighbourhood of a well defined minimum, corresponding to a mode with a well-characterized propagation constant  $n_{\text{eff}} = 1.43858501 + 4.986 \times 10^{-7}i$ . This example, and those following, refer to a structure as described in Section 3.2.1, with a single ring of six equally spaced holes with  $d = 5 \mu\text{m}$ ,  $\Lambda = 6.75 \mu\text{m}$ ,  $\lambda = 1.45 \mu\text{m}$ ,  $R_0 = 14.25 \mu\text{m}$  and  $n_M = 1.45$ ,  $n_0 = n_M + 10^{-8}i$  and  $M = 5$ . The small imaginary part of  $n_0$  has been introduced for mathematical convenience (to render fields square integrable, *cf.* Section 2.4). Its existence is not essential in the computations presented here and its exact value does not have a significant impact on results<sup>2</sup>, as we will understand in Chapter 7.

<sup>2</sup>A complete study of the impact of the imaginary part of  $n_0$  on the results of the computations shown here can be found in T.P. White's honours thesis [85].

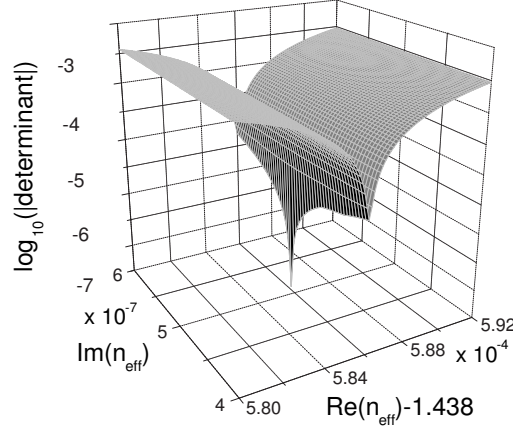


Figure 4.2: Logarithm of the magnitude of the determinant of  $\mathbf{M}$  versus the real and imaginary parts of the complex refractive index, for the MOF given in the text.

We know from a group theoretical study of waveguides by McIsaac [76], that the modes of the fibres we are considering are either nondegenerate or doubly degenerate. Since  $\det(\mathbf{M})$  is the product of the eigenvalues of  $\mathbf{M}$ , we must look for minima in which one or two of the eigenvalues have magnitudes that are substantially smaller than the others. However, a minimum of the determinant may also correspond to an artefact resulting from many eigenvalues being small simultaneously (what we call a *false minimum*). To distinguish these from genuine solutions, we consider the *singular values* [86] of  $\mathbf{M}$ , which, for our case, correspond to the magnitudes of the eigenvalues. False minima can be distinguished by a singular value decomposition at the putative minimum.

The null vectors corresponding to small singular values are approximate solutions to the field identity (3.45). For non-degenerate modes, the null vector is unique to within an arbitrary multiplicative constant. For a two-fold degenerate mode, we let the basis states be prescribed by group theory (see Section 4.5.1), though any linear combination of these is equally justified.

### 4.3.2 Implementation

For this task we need an algorithm aimed at finding all the zeros of the determinant of  $\mathbf{M}$  in a region of the complex  $n_{\text{eff}}$  plane. The algorithm should be economical in function calls as each evaluation of the determinant is computationally very expensive for large structures. As shown in Fig. 4.2, the zeros are very sharp, so that a very accurate first estimate of the zero is necessary for most simple root-finding routines. More specific algorithms for finding zeros of analytic or meromorphic functions [87,88] have good convergence for simple structures (with six cylinders for example) but fail for more complex structures, even with good initial guesses: they need an accuracy in the Cauchy-like integrals which is numerically difficult and expensive to reach as  $\det(\mathbf{M}(n_{\text{eff}}))$  is ill-behaved. Our present approach to root finding seems computationally efficient. We first compute a map of the modulus of the determinant over the region of interest, and then use the local minima of this map as initial points for a mixed zooming and modified Broyden [89] algorithm (an iterative minimization algorithm, guaranteed to converge for parabolic minima). The algorithm used makes it extremely unlikely

to miss a zero of the determinant; further details of this method are given in Appendix E.

The initial scanning region has to be chosen in accordance with the physical problem studied: if the fibre is air cored and air guided modes are sought, we choose  $\Re(n_{\text{eff}}) < 1$ , whereas if the fibre has a solid core we usually choose to search for modes in a region where  $\Re(n_{\text{eff}})$  is between the optical indices of the inclusions and the matrix<sup>3</sup>. In the latter case hundreds of modes may exist for small  $\Re(n_{\text{eff}})$  which are of little interest because of their high losses. We therefore often concentrate on a smaller  $n_{\text{eff}}$  scanning region near the highest index of the structure. A scanning region for  $\Im(n_{\text{eff}})$  giving good results in almost any case is  $10^{-14} < \Im(n_{\text{eff}}) < 10^{-3}$ . For imaginary parts lower than  $10^{-14}$  numerical inaccuracies in the imaginary part make the used algorithm unstable, and it is then required to set  $\Im(n_{\text{eff}}) = 0$  and find the minima of the determinant on the real axis.

## 4.4 Computing Dispersion Characteristics

The above process of finding modes is carried out for a specific wavelength. We could reiterate the search for modes for many different wavelengths to obtain dispersion characteristics, but this process would be quite laborious. We have found two alternative methods to be of value. One computes and identifies the modes for three or four different wavelengths, then uses a spline interpolation to estimate the  $n_{\text{eff}}$  values for other wavelengths and refines the estimate with the mixed zooming and Broyden algorithm. Each newly determined point of the  $n_{\text{eff}}(\lambda)$  curve can be used to enhance the spline estimate. The second (and often more efficient) method is to compute the modes for only one wavelength  $\lambda_0$ , then slightly perturb the wavelength to get  $n_{\text{eff}}(\lambda_0 + \delta\lambda)$  using  $n_{\text{eff}}(\lambda_0)$  as a first guess, and then use a first order estimate of  $n_{\text{eff}}$  at the next wavelength. One can then compute  $n_{\text{eff}}(\lambda + m\delta\lambda)$  using a first order estimate computed from the two preceding values. For both methods, the wavelength step has to be chosen very small: for small steps more points are necessary to compute the dispersion characteristics in a given wavelength range, but for large steps the first order guess becomes inaccurate and the convergence of the zooming and Broyden algorithm unacceptably slow. Having small steps and therefore numerous numerical values on the dispersion curve is also of benefit when evaluating second order derivatives, as is necessary to compute the group velocity dispersion.

Material dispersion can be included easily by changing the optical indices according to the current wavelength at each step using, for example, a Sellmeier approximation [4] for silica.

The method described here can be adapted to study the change of  $n_{\text{eff}}$  of a mode for any continuously varying parameter, for example cylinder radius, cylinder spacing or optical index. One problem that can occur when following the evolution of a mode with a continuously varying parameter is mode crossing. This results in wrong data, but can easily be detected in most cases through a discontinuity of derivatives,<sup>4</sup> and can also easily be eliminated by restarting the algorithm with the correct mode on the other side of the crossing.

The correct choice for  $\delta\lambda$  strongly depends on wavelength and structure, so that no general advice can be given. However, as a rough guide, satisfactory results have generally required 200 or more points on curves.

---

<sup>3</sup>cf. Section 2.4.

<sup>4</sup>...and a radical change of the Bloch transform, see Chapter 5.

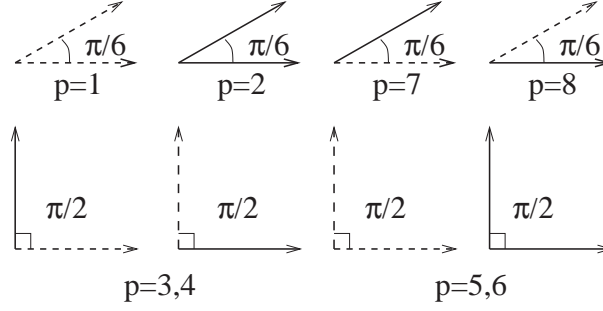


Figure 4.3: Minimum sectors for waveguides with  $C_{6v}$  symmetry. Mode classes  $p = 1, 2, 7$  and  $8$  are non-degenerate, while  $p = 3, 4$  and  $p = 5, 6$  are two-fold degenerate. Solid lines indicate Dirichlet boundary conditions for the electric field, dashed lines indicate Neumann boundary conditions.

## 4.5 Symmetries

### 4.5.1 Symmetry Properties of Modes

McIsaac [76] classified the electromagnetic modes of waveguide structures, according to the symmetry properties of the configuration. This approach was previously exploited by Yamashita *et al.* [78] for a modal analysis of conventional multicore fibres. The point group most often encountered in MOF studies is  $C_{6v}$  since it combines six-fold symmetry with mirror symmetry (symmetries of the hexagonal lattice). This leads immediately to a number of conclusions: any mode belongs to one of eight *classes*, and they are either non-degenerate (classes 1, 2, 7, 8), in which case they exhibit the full symmetry of the structure, or two-fold degenerate (classes 3, 4, 5, 6), in which case they exhibit the full symmetry in an appropriate linear combination. Since the non-degenerate modes have the full symmetry of the structure, their field only needs to be calculated in a *minimum sector* of  $30^\circ$ , the edges of which must coincide with a symmetry axis of the structure, with the field elsewhere following by symmetry. The difference between the modal classes are that different boundary conditions apply to the tangential component of the electric field at the edges of the minimum sector; these are either Neumann ( $\partial E_z / \partial \theta = 0$ ) or Dirichlet ( $E_z = 0$ ) conditions, or combinations of these (see Fig. 4.3). For the degenerate mode classes the minimum sector is  $90^\circ$  (see Fig. 4.3).

Table 4.1 lists the first ten modes for the MOF we are considering, exemplifying all McIsaac's [76] eight mode classes. The losses in dB/m in column 3 are obtained from the imaginary part of  $n_{\text{eff}}$  by

$$\mathcal{L} = \frac{20}{\ln(10)} \frac{2\pi}{\lambda} \Im(n_{\text{eff}}) \times 10^6, \quad (4.1)$$

with  $\lambda$  in  $\mu\text{m}$ . In Table 4.1 the losses are large since more than one ring is necessary to achieve losses compatible with practical usage; this is discussed further in Chapters 6 and 7.

We show the fields of the first three modes from Table 4.1 in Figs. 4.4–4.6. Fig. 4.4 shows a mode with a vertical nodal line for  $E_z$  and a horizontal antinodal line. It must therefore belong to class  $p = 3$  in Fig. 4.3, one of a degenerate pair. Its companion ( $p = 4$ ) is shown in Fig. 4.5. The similarity between  $|E_z|$  in Fig. 4.4 and  $|K_z|$  in Fig. 4.5 is often evident in degenerate MOF modes, but is not exact, since  $E_z$  and  $K_z$  satisfy different boundary conditions. The non-degenerate mode (Fig. 4.6) displays the MOF's full six-fold symmetry and has nodes of

$n_{\text{eff}}$		Loss	Class	Degeneracy
Real	Imaginary	dB/m	$p$	
1.445395345	$3.15 \times 10^{-8}$	1.2	3, 4	2
1.438585801	$4.986 \times 10^{-7}$	20	2	1
1.438445842	$9.929 \times 10^{-7}$	37	5, 6	2
1.438366726	$1.374 \times 10^{-6}$	52	1	1
1.430175	$2.22 \times 10^{-5}$	840	8	1
1.4299694	$1.577 \times 10^{-5}$	590	3, 4	2
1.429255296	$9.337 \times 10^{-6}$	350	7	1

Table 4.1: Effective index, loss, mode class and degeneracy of the first 10 modes of the MOF given in the text, calculated using  $M = 5$ .

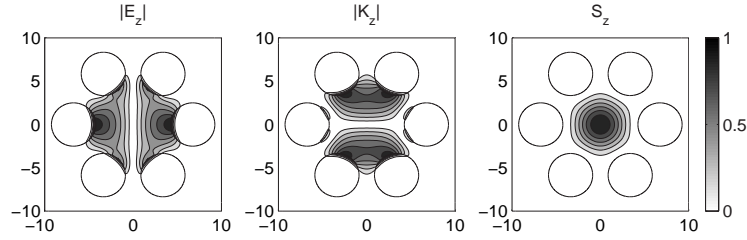


Figure 4.4: Normalized fields  $|E_z|$ ,  $|K_z|$  and energy flow  $\Re(S_z)$  for the degenerate fundamental mode class  $p = 3$  for a six-hole MOF, with data described in the text in regard of Fig. 4.2,  $n_{\text{eff}} = 1.445395345 + 3.15 \times 10^{-8}i$ .

$E_z$  at angles  $0^\circ$  and  $30^\circ$ ; it thus belongs to class  $p = 2$  (Fig. 4.3).

#### 4.5.2 Using the Symmetries

The incorporation of field symmetry in the multipole formulation has two benefits. Firstly, it enables definitive statements to be made about the degeneracy of modes, even in the presence of the accidental degeneracies which arise when normally distinct modal trajectories cross each other. Secondly, it greatly reduces computational burdens, enabling accurate answers for quite large MOF structures to be obtained rapidly on PC's.

In applying the multipole formulation to large six-fold symmetric MOF's, it is highly

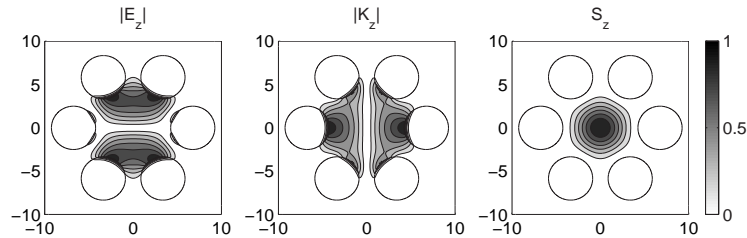


Figure 4.5: Similar to Fig. 4.4, but for degenerate fundamental mode class  $p = 4$ ,  $n_{\text{eff}} = 1.445395345 + 3.15 \times 10^{-8}i$ .

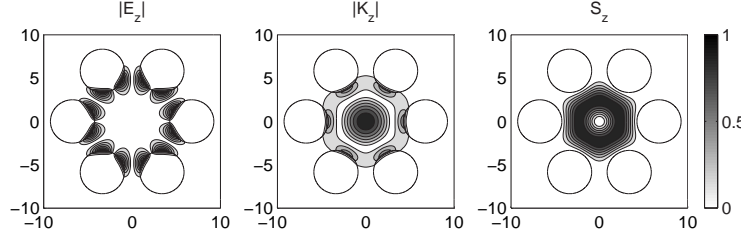


Figure 4.6: Similar to Fig. 4.4, but for nondegenerate mode with  $p = 2$ ,  $n_{\text{eff}} = 1.438585801 + 4.986 \times 10^{-7}i$ .

advantageous to exploit the symmetry properties in Fig. 4.3 to reduce the size of the matrix  $\mathbf{M}$ . This can be achieved since only multipole coefficients for inclusions lying in the minimum sector indicated in Fig. 4.3 need be specified; those for holes outside the minimum sector can be obtained by multiplying by the appropriate geometric phase factor (related to  $\exp(2\pi i/6)$ ). The resulting reduction in the order of the matrix  $\mathbf{M}$  depends on the type of the mode, being maximal for the non-degenerate modes in Fig. 4.3, and still being around 3.5 for degenerate modes, leading to considerable reductions in processing time. See Appendix F for further details.

### 4.5.3 Implementation

Using the symmetry simplifications the search for modes changes slightly. To obtain all the modes we now have to check for each class of modes separately. This implies going through the entire process of evaluating a determinant map and refining each local minimum once per non-degenerate mode class and once for each degenerate pair of mode classes. For a structure with  $C_{6v}$  symmetry, six determinant maps have to be evaluated (classes 1, 2, 3, 5, 7 and 8, the modes of classes 4 and 6 being deduced from those of class 3 and 5, *cf.* Fig. 4.3). But as the matrix size is reduced by a factor ranging from 3.5 to more than 6, and the computations scale as the size of the matrix cubed, the overall efficiency gain of using the symmetries remains high. The gain is even higher when computing dispersion figures for a given mode, as only one symmetry class is then concerned. Note that in many cases only the fundamental and the second mode are of interest, which both belong to specific symmetry classes, so that the scanning of all symmetry classes is often unnecessary.

## 4.6 Software and Computational Demands

We have developed a FORTRAN 90 code to exploit the above considerations.<sup>5</sup> For symmetric structures the suggested optimizations are used and the software can therefore deal, even on PC's, with large structures (modes for fibres with 330 holes have so far been computed on current personal computers). Once the structure has been defined, the software is able to find automatically all the modes within a given region of the complex plane for  $n_{\text{eff}}$  and can optionally track a mode as a function of wavelength (to obtain dispersion characteristics) or continuous changes of the structure (pitch, diameter of holes, refractive index of one or all

<sup>5</sup>Two completely different versions of the code with different, complementary features have been developed separately and simultaneously by T. P. White and the author.

holes...). Material dispersion can be included, if desired.

To validate our software against existing methods, we implemented a slightly more general formulation than the one described here, making it possible to solve external scattering problems as well as computing modes (a right hand term accounting for external sources is then added to Eq. (3.45)). We also included in our implementation the possibility of using jacket reflection matrices resulting from more than one dielectric interface: we can include a cladding layer between the matrix and the jacket, and it would be straightforward to add any dielectric concentric multilayer around the matrix.

Computational demands are relatively modest: the complete set of modes with  $M = 5$  in the region of interest  $1.4 < \Re(n_{\text{eff}}) < 1.45$  for the structure used in Fig. 4.2 and Fig. 4.4– 4.6 can be computed on a Pentium III (733MHz) personal computer in less than 3 minutes using less than 2 Mb of memory. Of course the load rises for larger structures, but computing the complete set of modes for a structure with  $N_r = 3$  takes less than an hour (and about 15 Mb memory) on a Compaq workstation. Note that often the complete set of modes is of little interest and only properties of the fundamental or the second mode are sought. In that case only one or two symmetry classes need to be gone through, and one often has some knowledge of the approximative location of these modes, so that the size of the initial determinant map can be significantly reduced: finding the fundamental mode of the largest structures presented in this thesis has rarely taken more than an hour.<sup>6</sup>

Tracking modes along continuous parameters can be computationally more expensive: some of the curves used in Chapter 7 to derive the phase diagrams have taken up to one day of computation on a Pentium III (1 GHz), and some of the dispersion curves for large structures presented in Chapter 8 where large values of  $M$  were needed for accuracy, have taken several days to be computed on modern Alpha powered workstations.<sup>7</sup>

## 4.7 Validation and Self Consistency

### 4.7.1 Convergence and Wijngaard Test

The formulation of Chapter 3 requires the finding of modes satisfying the field identity (3.45), which expresses the equality of two sets of field representations: a local expansion in the neighbourhood of each cylindrical inclusion in the MOF (3.20) and a global or Wijngaard expansion (3.21). The Wijngaard expansion is expressed in local coordinates using Graf's addition theorem, truncated to the chosen multipole order  $M$  and equated with the local expansion (3.20). The two expansions for  $E_z$  and the corresponding expansions for the scaled magnetic field component  $K_z$  only match perfectly for untruncated fields ( $M \rightarrow \infty$ ), and so their numerical difference on cylinder surfaces can be used as a powerful indicator of truncation errors and the quality of the matrix null vector location. We illustrate this with an example shown in Figs. 4.7 and 4.8 of an air-core MOF. Fig. 4.7 shows significant field errors occurring around the boundary of the larger central air hole. As well, the low frequency modulation of the field discrepancies indicates some imprecision in the minimization of the determinant. In Fig. 4.8, the multipole truncation order on the central hole has been increased<sup>8</sup> to  $M = 19$ ,

<sup>6</sup>Towards the end of the PhD., thanks to a better knowledge of MOF-modes, finding the fundamental mode was rather a matter of minutes.

<sup>7</sup>See the Chapters 7 and 8 for details.

<sup>8</sup>Using different truncation orders for different inclusions is not implemented in the software written by the author, and data and results related to Fig. 4.7 and 4.8 were provided by T. P. White.

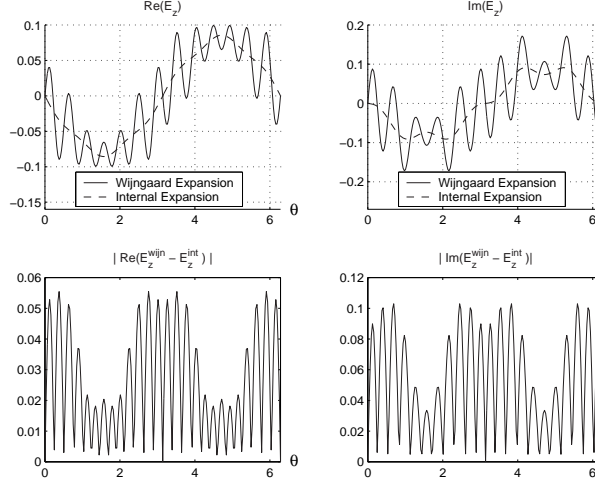


Figure 4.7: In the upper and lower parts of the figure, internal and Wijnngaard expansions are compared for respectively  $E_z$  and  $K_z$ , for an air core MOF, with  $M = 5$  both for the central air hole and all other air holes (54 air holes of diameter  $4.0271 \mu\text{m}$ , core hole diameter  $13.0714 \mu\text{m}$ ,  $n_M = 1.39$ ,  $n_i = 1.00$ ,  $\Lambda = 5.78157 \mu\text{m}$ ,  $\lambda = 3.846 \mu\text{m}$ ).

while the truncation order on the smaller holes has been kept at 5. The decrease in field matching errors is evident (note the change in scale in the lower panels between Figs. 4.7 and 4.8), as is a slight improvement in the quality of the determinant minimization, manifest as a reduction in the low-frequency modulation. One clear sign of adequate convergence in the formulation is obtained from these comparison plots. When enough terms are included, the error term oscillates like the first neglected term in field expansions (i.e., like  $\exp[i(M+1)\theta]$ ).

A second test of convergence is of course provided by the stability of  $n_{\text{eff}}$  with respect to increase of  $M$ . This is illustrated in Table 4.2, where we also introduce

$$W_l^E = \frac{\int_{C_l} |E_z^{\text{local}}(\theta_1) - E_z^{\text{Wijnngaard}}(\theta_1)| d\theta_1}{\int_{C_l} |E_z^{\text{Wijnngaard}}(\theta_1)| d\theta_1}, \quad (4.2)$$

and similarly for  $H_z$ .  $W_l^E$  is a measure of the accuracy of the equality between the local (3.20) and Wijnngaard expansions (3.21) of  $E_z$  around cylinder  $l$ . With increasing  $M$ ,  $W_l^E$  decreases while  $n_{\text{eff}}$  stabilises, as expected. Note that  $W_l^E$  is comparable to a mean relative error of the local expansion, taking as a reference the Wijnngaard expansion of the field around inclusion  $l$ . Assuming that both fields eventually converge to the *true* value of the field, we will occasionally use  $W_l^V$  ( $V = E$  or  $H$ ) as an approximate *a priori* measure of the local relative error of each field expansion on field  $V$ .

We have found that the choice of the truncation parameter  $M$  should be made such that this quantity clearly exceeds (by a factor around 1.5) the largest argument of Bessel functions on the boundary of inclusions. This guarantees that the cylindrical functions of largest order in field expansions behave like the cylindrical multipoles of electrostatics to leading order, and ensures rapid convergence with increasing  $M$ . This criterion is manifest in the case of Figs 4.7 and 4.8 where many more Bessel terms are necessary for the large central hole than for other, smaller holes.

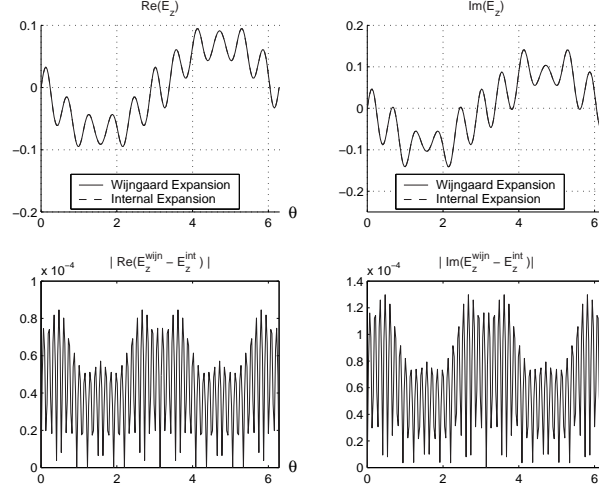


Figure 4.8: As for Fig. 4.7, but with  $M = 19$  for the core hole and 5 for all other holes. Note that the Wijnngaard and internal expansions now match to graphical accuracy.

$M$	$\Re(n_{\text{eff}})$	$\Im(n_{\text{eff}}) \times 10^6$	$W_1^E$
3	1.43852886240663	6.918242988502046	$9.7 \times 10^{-2}$
4	1.43838719374803	1.749096334333127	$4.6 \times 10^{-2}$
5	1.43836672605884	1.373925319699950	$1.5 \times 10^{-2}$
6	1.43836499998690	1.414928166193201	$2.7 \times 10^{-3}$
7	1.43836493475660	1.416468499483090	$9.3 \times 10^{-4}$
8	1.43836493461317	1.416459892560528	$7.7 \times 10^{-4}$
9	1.43836493424529	1.416475747100788	$2.5 \times 10^{-4}$

Table 4.2: Convergence of  $n_{\text{eff}}$  with  $M$ . Results are for the  $p = 1$  mode of the MOF in Table 4.1 at  $\lambda = 1.45 \mu\text{m}$ . Here  $W$  from Eq.(4) gives the degree of accuracy of the equality between Wijnngaard and local expansions. The integrals are taken over the boundary of cylinder 1 situated at  $r = 6.75 \mu\text{m}$ ,  $\theta = 0$ .

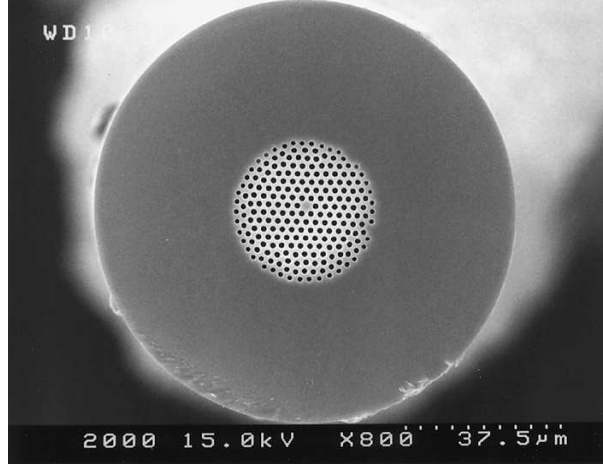


Figure 4.9: Scanning electron micrograph of a cleaved end-face of the MOF fabricated by Kubota *et al.* used in our comparisons. Figure supplied by H. Kubota.

Note that in cases where  $n_{\text{eff}}$  is close to  $n_M$ ,  $k_{\perp}^M$  and therefore arguments in Bessel function can become small even with larger inclusions, and small values of  $M$  can become sufficient. We will see in forthcoming chapters examples where values of  $M$  as small as 2 give results of satisfying accuracy.

#### 4.7.2 Comparison with Other Methods

A powerful way of validating a new formulation is also to compare its results with those of a well-established method. A successful comparison of the results of our method with those of the scalar and vector beam propagation methods, for a MOF fibre having a single ring of inclusions, and with the imaginary part of  $n_{\text{eff}} = \beta/k_0$  of order  $10^{-5}$ , was already presented in previous work [45].

As we also included in our software the extension of the present formalism to simulate the diffraction of incident light by the structure, we were able to validate the code thoroughly against results from other, well established, diffraction codes. Comparisons with a fictitious source code [90] and other multipole like codes [77, 91] in conical incidence with complex or real permittivities in various geometries gave excellent agreement of at least 8 decimal figures on the radar cross section, validating each part of the code separately as well as in its entirety.<sup>9</sup>

#### 4.7.3 Theory and Experiment

We compared results from our simulations with experimental data published by Kubota *et al.* [92]. The MOF used for their experiments was a silica fibre with approximately 7 rings of air holes disposed in a very regular hexagonal lattice, the core being created by a missing hole (Fig. 4.9). For our simulations we used the geometrical data as published, but varied the number of rings from one to seven. We used the Sellmeier approximation for the index of silica.

<sup>9</sup>The description of the examples and methods used as well as the results of these comparisons are available on the enclosed CD-ROM, in French. See validation/validation.ps

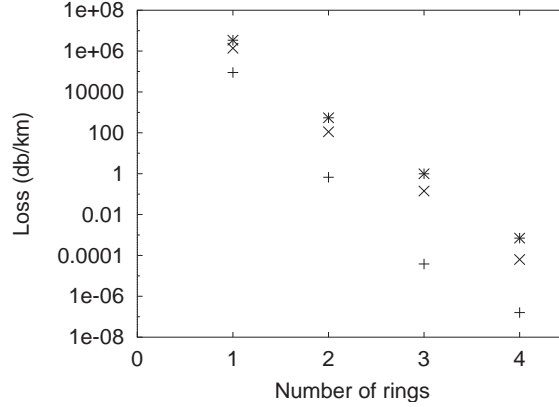


Figure 4.10: Loss of the first three modes as a function of number of rings for the structure published by Kubota *et al.*, at a wavelength of  $0.76 \mu\text{m}$ . Only geometrical losses are included.

A first result is that there is no need to have a large number of rings to reach geometrical losses of the order of losses of conventional fibres. Fig. 4.10 shows the loss figures for the first three modes versus the number of rings at a wavelength of  $0.76 \mu\text{m}$ . These figures only include geometrical losses, absorption or Rayleigh scattering having not been included: they show the limitations due to the confinement by a MOF structure.

With two rings, the fibre has a single-mode behavior for kilometric lengths, as only the fundamental mode propagates without significant losses, but with more than two rings other modes become virtually lossless. This is in agreement with the multi-mode behaviour observed experimentally for seven rings of holes.<sup>10</sup> Clearly, three rings of holes are theoretically enough to ensure a guidance only limited by losses due to absorption or structural imperfections. We confirm that the losses observed by Kubota *et al.* (7.1 dB/km at 850 nm) are not due to the limitation imposed by the MOF geometry of the fibre but mainly to Rayleigh scattering, structural imperfections and absorption.

The imaginary parts of  $n_{\text{eff}}$  corresponding to Fig. 4.10 are well below those able to be determined directly by determinant minimization. Instead we must proceed through its evaluation by an energy flux argument, once the real part of  $n_{\text{eff}}$  has been determined to high accuracy by determinant minimization. This method is discussed in Chapter 5.

We computed dispersion figures for the fundamental mode of the Kubota structure. We first observed that the number of rings has very little influence on the actual dispersion curve, as the fundamental mode is already well confined with one ring.<sup>11</sup> We therefore used a one ring structure in subsequent simulations to improve computational speed, without losing significant accuracy for dispersion parameters. Although we observed a shift of the zero dispersion wavelength to the 800 nm band, we did not find an exact agreement with the experimental zero-dispersion wavelength of 810 nm. With the given geometrical data, we found a zero dispersion wavelength of 889 nm. Kubota *et al.* found similar results with an FDTD method. In order to explain the difference with experimental data, we have computed the zero dispersion wavelength for different hole pitch and diameter: Fig. 4.11 is for varying pitch with constant diameter, Fig. 4.12 is for varying diameter with constant pitch and Fig. 4.13

<sup>10</sup>We will discuss the definition of the number of modes in MOFs in Chapter 7.

<sup>11</sup>The influence of the the number of rings on the dispersion properties will be studied in Chapters 7 and 8

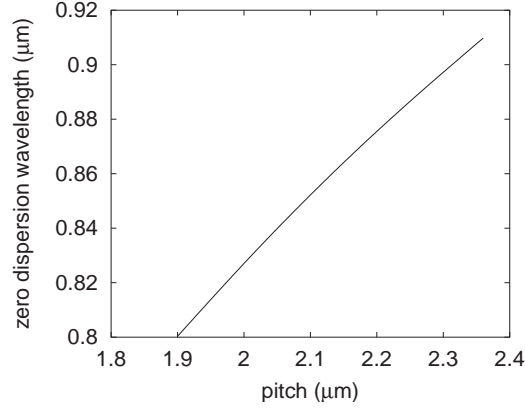


Figure 4.11: Zero dispersion wavelength as a function of pitch for the structure published by Kubota *et al.*, with constant diameter  $d = 1.51 \mu\text{m}$ .

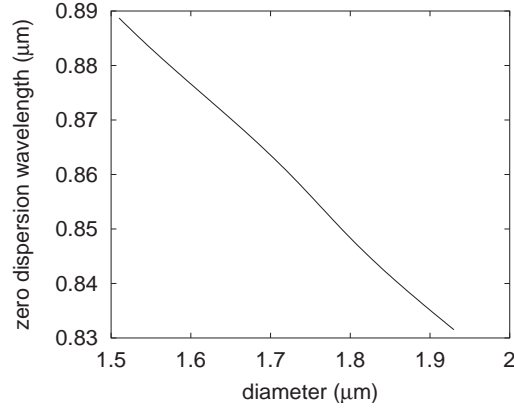


Figure 4.12: Zero dispersion wavelength as a function of hole diameter for the structure published by Kubota *et al.*, with constant pitch  $\Lambda = 2.26 \mu\text{m}$ .

is for varying pitch and diameter with constant pitch/diameter ratio. These figures show that a variation of about 15% in the pitch with constant diameter or 25% in the pitch with constant diameter/pitch ratio is necessary to obtain the experimental zero dispersion wavelength. The experimental fibres shown by Kubota *et al.* do not seem to have such high variations of their geometrical characteristics, and it seems that other reasons for the poor agreement between theory and experiment have to be found. We will discuss this in detail in Chapter 8.

Scientific curiosity encouraged us to simulate, whenever possible, the structures used in every new publication concerning MOFs brought to our knowledge. Out of lack of space, time and interest for the reader these comparisons are not detailed here. The agreement between the multipole method and experimental results or other theoretical models were not always satisfying, which was quite puzzling at the beginning. It appeared later that agreement with some other theories using periodic or closed boundary conditions *can not* be reached in some regions of the parameter space, and that only methods taking into account the finite cross-section and the exact number of inclusions can accurately describe MOF modes in these regions. We will detail this in Chapter 7.

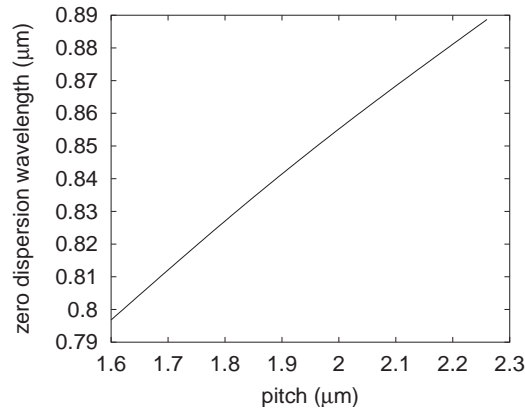


Figure 4.13: Zero dispersion wavelength as a function of pitch for the structure published by Kubota *et al.*, with constant diameter/pitch ratio  $d/\Lambda = 0.67$ .

More disconcerting is the disagreement with experimental results concerning dispersion properties. We have seen in the example described above that experimental inaccuracy is unlikely to explain these discrepancies. It is worth noting that when comparisons with other theoretical models are possible (*i.e.* when the modes are well confined), the agreement between these and the multipole method regarding dispersion characteristics is excellent<sup>12</sup>, so that to our knowledge *no* theoretical tool is able to predict accurately dispersion properties of MOFs to date. This suggests strongly that physical phenomena occur which have not yet been taken into account. These could for example be linked to stress induced changes of refractive indices resulting from the drawing process, or to effects related to the air-silica interfaces, and definitely need further investigation.

---

<sup>12</sup>...*i.e.* all theoretical predictions are consistent, but disagree with the experimental results.

Trou :

## Granité du Vigneron

*Winegrower's Granita*

**Pour 6 personnes :**

*50 cl de vin rouge  
100 à 200 g de sucre glace*

Et, éventuellement :

*cognac  
citron*

**L**ES proportions de cette recette doivent être adaptées au vin utilisé. Nous préconisons un vin d'avantage sur le fruit et le sucre que sur le tanin. L'idéal est un vin dominé par une syrah fruitée, gorgée de soleil. Ainsi la plupart des Shiraz Australiens conviennent à merveille. Du côté de la France, un Côte du Roussillon donnera généralement d'excellents résultats. Enfin on peut également partir de vins doux (Banyuls, Maury, Porto, Madère, Port Australiens), en diminuant la quantité de sucre.

**D**ISSOUDRE du sucre glace dans le vin jusqu'à ce qu'il ait un goût bien sucré (la sensation de sucré s'estompe avec le froid). Ajouter, toujours au goût, jusqu'à quelques centilitres de cognac et ajuster éventuellement l'acidité avec un peu de jus de citron.

**V**ERSER dans un récipient de préférence métallique et à large surface (un moule à gâteau convient bien). Laisser prendre au congélateur. Après une heure, gratter à la fourchette les bords et le fond du moule pour ramener les cristaux en formation vers le centre. Recommencer toutes les demi-heures jusqu'au moment de servir. Compter 4 à 6 heures selon le congélateur pour que la granité ait le temps de prendre. Alternativement on peut aussi placer le mélange en sorbetière, mais éviter alors de le préparer trop à l'avance : Conservé au repos au congélateur il fige en bloc et perd son côté fondant et «volatile».

**R**ÉPARTIR dans six verres à vin et servir.

# Chapter 5

## Tools

A mode found by the multipole method is defined by an effective index and a set of Fourier-Bessel coefficients. We have already seen how to use these to compute the fields in and outside the MOF structure. In this Chapter we introduce other tools we will need to analyse modes further.

### 5.1 Lowering the Loss Limit

As discussed in the previous Chapter, finding the roots of the mode equation (3.45) does not permit an arbitrary precision for the imaginary part of  $n_{\text{eff}}$ . The absolute precision for  $\Im(n_{\text{eff}})$  is ultimately limited by the machine precision around  $\Re(n_{\text{eff}}) \simeq 1$ , which in the current implementation is approximately  $10^{-15}$ . For modes with  $\Im(n_{\text{eff}}) \lesssim 10^{-14}$  the relative precision becomes unacceptable, and for  $\Im(n_{\text{eff}}) \lesssim 10^{-15}$  one often has to set  $\Im(n_{\text{eff}})$  artificially to zero in order to find the mode. In such cases it becomes important to achieve a better estimate of the losses through an indirect method.

Once the real part of  $n_{\text{eff}}$  has been determined to high accuracy by determinant minimization, we can find an estimate of the loss coefficient through an energy flux argument. The loss coefficient  $\alpha$  is obtained through the conservation of the time averaged flux of the Poynting vector  $\mathbf{S}$  through a cylinder of elementary length  $\delta z$  centered at the origin and with a radius  $R$  such that the cylinder includes all inclusions. We have:

$$\iint_{\theta, \rho < R} \Re(\mathbf{S}(\rho, \theta, z)) \cdot \mathbf{u}_z \rho d\rho d\theta = \delta z \oint_{\theta} \Re(\mathbf{S}(R, \theta, z)) \cdot \mathbf{u}_r R d\theta + \iint_{\theta, \rho < R} \Re(\mathbf{S}(\rho, \theta, z + \delta z)) \cdot \mathbf{u}_z \rho d\rho d\theta \quad (5.1)$$

where  $\mathbf{u}_z, \mathbf{u}_r$  are the usual unit vectors of the local basis in cylindrical coordinates. As  $\mathbf{S}$  varies as  $e^{-\alpha z}$ , we have

$$\mathbf{S}(\rho, \theta, z + \delta z) \simeq (1 - \alpha \delta z) \mathbf{S}(\rho, \theta, z) \quad (5.2)$$

so that (5.2) becomes

$$\alpha \iint_{\rho < R, \theta} \Re(\mathbf{S}(\rho, \theta, z)) \cdot \mathbf{u}_z \rho d\rho d\theta = \oint_{\theta} \Re(\mathbf{S}(R, \theta, z)) \cdot \mathbf{u}_r R d\theta . \quad (5.3)$$

Isolating  $\alpha$  gives

$$\alpha = \frac{\oint_{\theta} \Re(S_r(R, \theta, z)) R d\theta}{\iint_{\theta, \rho < R} \Re(S_z(\rho, \theta, z)) \rho d\rho d\theta} \quad (5.4)$$

where we have introduced  $S_z$  and  $S_r$ , components of  $\mathbf{S}$  in cylindrical coordinates. The imaginary part of the effective index is then given by

$$\Im(n_{\text{eff}}) = \frac{\alpha}{2k_0} . \quad (5.5)$$

The integrals in Eq. (5.4) can then be computed numerically from the field expansions.

It is difficult to evaluate the precision of this method. Of course the precision will depend on the precision of the numerical integration (which can be easily evaluated and readily improved), but also on the precision of the field expansions, *i.e.* the accuracy of  $\Re(n_{\text{eff}})$  and the truncation of the Fourier-Bessel series .

When the direct evaluation of  $\Im(n_{\text{eff}})$  through the determinant minimization is accurate ( $\Im(n_{\text{eff}}) \gg 10^{-14}$  and good Wijngaard test), both evaluation methods agree up to the precision of the numerical integration. For  $\Im(n_{\text{eff}}) < 10^{-14}$  we have no direct means to check the accuracy of the results given by (5.4). Nevertheless we can get an estimate of the relative error of the fields through the Wijngaard test, from which we can derive an estimate of the relative error of  $\alpha$ . Eq. (5.4) yields

$$\frac{\delta\alpha}{\alpha} \simeq \frac{\delta I_1}{I_1} + \frac{\delta I_2}{I_2} \quad (5.6)$$

where  $I_1$  and  $I_2$  are the integrals of the numerator and denominator of (5.4) respectively, and  $\delta X$  represents the absolute error of  $X$ . From (5.4) we have

$$\delta I_1 = \oint \delta \Re(S_r(R, \theta, z)) R d\theta \quad (5.7)$$

$$= \oint \frac{\delta \Re(S_r(R, \theta, z))}{\Re(S_r(R, \theta, z))} \Re(S_r(R, \theta, z)) R d\theta . \quad (5.8)$$

In the last equation appears the relative error of  $\Re(S_z)$ , which can be estimated through the Wijngaard test. We have indeed seen that  $W_i^E$  and  $W_i^H$  can be interpreted as the relative precision of  $E_z$  and  $H_z$  respectively, in the vicinity of inclusion  $i$ . Expressing  $S_z$  as a function of  $E_z$  and  $H_z$  results in an expression involving  $n_{\text{eff}}$ , so that  $\delta \Re(S_z)/\Re(S_z)$  will also depend on the precision of  $n_{\text{eff}}$ . The latter being in general much better than the precision of the fields, we will assume the errors come mainly from errors on  $E_z$  and  $H_z$ . Introducing  $W_M = \max\{W_i^E, W_i^H\}_{i=1, N_i}$ , we have

$$\frac{\delta S_z}{S_z} \lesssim 2W_M \quad (5.9)$$

as  $S_z$  is the product of two  $\mathbf{E}$  and  $\mathbf{H}$  components. Eq. (5.8) becomes

$$\delta I_1 \lesssim 2W_M \oint \Re(S_r(R, \theta, z)) R d\theta \quad (5.10)$$

$$\lesssim 2W_M I_1 . \quad (5.11)$$

The same arguments hold when evaluating  $\delta I_2$ , so that the total relative error of  $\alpha$  is

$$\frac{\delta\alpha}{\alpha} \lesssim 4W_M . \quad (5.12)$$

Note that the main hypothesis in this derivation is that the relative errors of the fields are bounded above by  $W$ . This is not strictly true, and therefore Eq. (5.12) should only be used as an estimate of the precision.

Our simulations have shown that errors due to other factors (mainly the numerical evaluation of the Bessel functions) limit the indirect evaluation of  $\Im(n_{\text{eff}})$  to values above  $10^{-20}$ . Note that this extremely low value corresponds to loss coefficients 8 orders of magnitude smaller than the best possible absorption coefficients in silica, so that such small values can only be of theoretical interest.

## 5.2 Bloch Transform

As mentioned in the first Chapter, the revival of interest in MOFs originated from the burgeoning field of Photonic Crystals, and the idea of guiding light through defects in photonic bandgap structures. Even for solid core MOFs, where it is often argued that guidance results from total internal reflection due to the lowered average index in the cladding region, considerations concerning the band structure of the cladding structure prove to be very useful. Here we develop a tool to analyse MOF modes in terms of Bloch modes of the periodic cladding structure.

We first use the properties of an infinite periodic structure to introduce a function - the *Bloch transform* - able to isolate Bloch vectors (see below) associated with a given field. We then generalize the Bloch transform to finite structures and review some of its basic properties. We briefly discuss the numerical implementation of the Bloch transform before showing a few examples. Finally we analyse some of the properties of the Bloch transform in more detail. As we will see in the remaining Chapters, the Bloch transform will enable us to differentiate between two very distinct classes of modes, to gain insight into their physical nature and to follow modes with varying fibre parameters with accuracy.

### 5.2.1 Definition

#### The Infinite Lattice

We consider an infinite 2D-periodic structure of inclusions centered on points of the periodic lattice  $\mathcal{L}$ . Fields propagating in that structure satisfy the Bloch-Floquet theorem, from which there exists a Bloch vector  $\mathbf{k}_B$  such that

$$V(\mathbf{r} + \mathbf{c}_p) = \exp(i\mathbf{k}_B \cdot \mathbf{c}_p) V(\mathbf{r}) \quad (5.13)$$

where  $V$  is either  $E_z$  or  $H_z$  and  $\mathbf{c}_p \in \mathcal{L}$ . We suppose we can expand  $V$  in terms of Fourier-Bessel series centered on each inclusion. In regions where this expansion is valid<sup>1</sup>, we have

$$V(\mathbf{r} + \mathbf{c}_p) = \sum_{\mathbf{c}_l \in \mathcal{L}} \sum_{n \in \mathbb{Z}} B_n(\mathbf{c}_l) H_n^{(1)}(k_\perp |\mathbf{r} + \mathbf{c}_p - \mathbf{c}_l|) \exp(in \arg(\mathbf{r} + \mathbf{c}_p - \mathbf{c}_l)) , \quad (5.14)$$

where  $B_n(\mathbf{c}_l)$  is the  $n^{\text{th}}$  Fourier-Bessel coefficient for the inclusion centered on  $\mathbf{c}_l$ . Using Eq. (5.13) we have

$$V(\mathbf{r} + \mathbf{c}_p) = \sum_{\mathbf{c}_l \in \mathcal{L}} \sum_{n \in \mathbb{Z}} \exp(i\mathbf{k}_B \cdot \mathbf{c}_p) B_n(\mathbf{c}_l) H_n^{(1)}(k_\perp |\mathbf{r} - \mathbf{c}_l|) \exp(in \arg(\mathbf{r} - \mathbf{c}_l)) . \quad (5.15)$$

---

<sup>1</sup>See Chapter 3.

Changing the summation index to  $\mathbf{c}'_l = \mathbf{c}_l - \mathbf{c}_p$  in Eq. (5.14), and then equating the result to Eq. (5.15) yields<sup>2</sup>

$$B_n(\mathbf{c}_l + \mathbf{c}_p) = \exp(i\mathbf{k}_B \mathbf{c}_p) B_n(\mathbf{c}_l) . \quad (5.16)$$

Eq. (5.16) is the equivalent of the Bloch-Floquet theorem for multipole coefficients.

We now introduce the function

$$\mathcal{B}_n(\mathbf{k}) = \sum_{\mathbf{c}_l \in \mathcal{L}} \exp(-i\mathbf{k} \cdot \mathbf{c}_l) B_n(\mathbf{c}_l) . \quad (5.17)$$

If  $V$  satisfies the Bloch-Floquet theorem with Bloch vector  $\mathbf{k}_B$ , we have

$$\mathcal{B}_n(\mathbf{k}) = \exp(-i\mathbf{k} \cdot \mathbf{c}_0) B_n(\mathbf{c}_0) \sum_{\mathbf{c}_l \in \mathcal{L}} \exp(i(\mathbf{k}_B - \mathbf{k}) \cdot (\mathbf{c}_l - \mathbf{c}_0)) , \quad (5.18)$$

with  $\mathbf{c}_0 \in \mathcal{L}$  being an arbitrary vector of the periodic lattice  $\mathcal{L}$ . This function takes the value 0 for  $\mathbf{k} \neq \mathbf{k}_B + \mathbf{G}$  and diverges for  $\mathbf{k} = \mathbf{k}_B + \mathbf{G}$ , where  $\mathbf{G}$  is any vector of the reciprocal lattice, *i.e.* a vector satisfying

$$\forall \mathbf{c}_l \in \mathcal{L}, \mathbf{G} \cdot \mathbf{c}_l \in 2\pi\mathbb{Z} . \quad (5.19)$$

$\mathcal{B}_n(\mathbf{k})$  has many similarities to a spatial Fourier transform, but instead of peaking at the Fourier components of the field  $V$ , it only peaks at its Bloch vectors. We shall therefore call it a *Bloch transform*.<sup>3</sup>

### Finite structures

We have defined a Bloch transform for infinite periodic lattices, but in the case of MOFs we will apply it to finite structures. In that case Bloch-Floquet's theorem is no longer valid, and solutions to propagating waves are not strictly speaking a superposition of Bloch-waves. Indeed, the Bloch waves are not a complete set of functions for a finite structure. A complete set of functions to describe fields in a finite domain with periodically arranged boundary conditions inside that domain can be constructed by adding to the Bloch waves eigenfunctions related to the domain boundaries. In other words surface states are needed in addition to volume states to describe the modes [93]. Nevertheless if we take a large<sup>4</sup> structure of periodically arranged inclusions, we can expect the influence of the boundary states to be small, and the modes of the structure to be predominantly a superposition of Bloch waves.

Similarly to the case of an infinite lattice, we define the Bloch transform for a finite structure with  $N_i$  inclusions centered around  $\mathbf{c}_l$ :

$$\mathcal{B}_n(\mathbf{k}) = \sum_{l=1}^{N_i} \exp(-i\mathbf{k} \cdot \mathbf{c}_l) B_n(\mathbf{c}_l) . \quad (5.20)$$

---

<sup>2</sup>To go from the identity for the fields to the identity for the Fourier-Bessel coefficients we use the same arguments as in Chapter 3.

<sup>3</sup>The term “Bloch transform” has been used in previous work by Allaire *et al.* [93] who developed a complete Bloch transform analysis very similar to the Fourier analysis but using the Bloch functions of a periodic structure as a basis. The Bloch transform we use here is not directly related to the one defined by Allaire *et al.* Its relation to the Fourier transform is analysed in Appendix G.

<sup>4</sup>Compared with the wavelength.

### 5.2.2 Basic Properties

#### Periodicity

We will from now on consider that the inclusions are centered on positions defined by a finite subset of a periodic lattice  $\mathcal{L}$ . In that case the Bloch transform will still have the periodicity of the reciprocal lattice. Indeed the property of Eq. (5.19) will be satisfied by each vector of the subset of  $\mathcal{L}$ . When visualizing the Bloch transform we will therefore need to do so only on the first Brillouin zone associated with the periodic lattice of the structure.

#### Peaks

If a mode is essentially located within the cladding region, *i.e.* does not concentrate on its boundaries, we expect that it can be predominantly decomposed in terms of Bloch waves. We can even expect the number of Bloch waves to be discrete, resulting from a selection effect due to Fabry-Perot resonances from the boundaries. A MOF mode will therefore usually be associated with several Bloch vectors. For each of those Bloch vectors, the Bloch transform will no longer diverge as the sum is now finite. For the same reasons, the Bloch transform will not vanish when  $\mathbf{k}$  is not a Bloch vector. We will rather have peaks of finite width and magnitude around the Bloch vectors. When increasing the number of inclusions, we can expect these peaks to become narrower and larger in magnitude, as the structure becomes closer to the infinite periodic structure. We will derive and quantify those effects in the following subsections.

The most striking property of the Bloch transform is that the geometric distribution of the peaks - the “*shape*” of the Bloch transform - is characteristic of a MOF mode, and is extremely stable when varying the wavelength or the fibre parameters. We will see in the following chapters that the field distributions and the Fourier-Bessel coefficients of the same mode can vary considerably with varying fibre parameters, and that it can become extremely difficult to identify similar modes of different yet comparable structures. Our simulations have shown that the Bloch transform of a given mode keeps its shape regardless of the fibre parameters, and that this shape is indeed the most precise and convenient way to differentiate and define specific modes. It is difficult to prove this property without precisely defining a classification of modes, but it can be understood through the fact that the Bloch transform decomposes each mode in a natural basis for the structure. In fact we will use this property as an axiom, defining the nature of a mode through the properties of its Bloch transform.

#### Bloch transforms of different orders

The Bloch transform defined in Eq. (5.20) is defined for a specific order  $n$ . We have seen that if  $V$  is a Bloch wave associated with the Bloch vector  $\mathbf{k}_B$ , the Fourier-Bessel coefficients of all orders obey Eq. (5.18). Nevertheless this equation does not imply that coefficients of a specific order can not be zero<sup>5</sup>. If  $V$  is a superposition of Bloch waves of different  $\mathbf{k}_B$ , those waves need not have the same relative magnitudes of Fourier-Bessel coefficients of different orders. This leads to the conclusion that Bloch transforms  $\mathcal{B}_n$  of different orders  $n$  do not necessarily peak at the same values of  $\mathbf{k}$ . To get the complete set of Bloch vectors associated with a field,

---

<sup>5</sup>And indeed, for modes of specific symmetry properties it can be shown that most of the Fourier-Bessel coefficients are strictly zero.

one needs to consider the Bloch transform of all orders. We therefore define the *total Bloch transform*, which is the sum of the normalized Bloch transforms of all orders:

$$\mathcal{B}^T(\mathbf{k}) = \sum_n \frac{1}{\sup_{\mathbf{k}' \in \mathbb{R}^2} (|\mathcal{B}_n(\mathbf{k}')|)} |\mathcal{B}_n(\mathbf{k})|, \quad (5.21)$$

where in practice  $n$  takes the values of all available orders, and the sup is taken to be the numerical maximum in the first Brillouin zone. If a field  $V$  has some Bloch wave components,  $\mathcal{B}^T(\mathbf{k})$  will peak at the corresponding Bloch vectors. The Bloch transforms of each order are normalized so that all Bloch vectors can be easily visualized at once on a same plot of the total Bloch transform. The counterpart to this is that the information on the relative importance of the peaks of different orders is lost, and that neighbouring peaks can merge into a larger, blurred peak. It will therefore be sometimes useful to go back to the Bloch transform of a single order  $n$ .

### Effective Angle of Propagation

We consider a mode with propagation constant  $\beta = n_{\text{eff}}k_0$ , having clear Bloch components (such as for example the mode of Fig. 5.1). A peak in the Bloch transform is associated to a Bloch wave  $V$  with Bloch vector  $\mathbf{k}_B$ :

$$V(\mathbf{r}) = \exp(i\mathbf{k}_B \mathbf{r})v(\mathbf{r}) \quad (5.22)$$

where  $v(\mathbf{r})$  has the periodicity of the lattice, and  $\mathbf{r}$  is in the  $xy$  plane. The Bloch wave propagates along the  $z$ -axis with propagation constant  $\beta$ , and perpendicularly to the  $z$ -axis following the Bloch vector. In three dimensions we have:

$$V(\mathbf{r}, z) = \exp(i(\mathbf{k}_B \mathbf{r} + \beta z))v(\mathbf{r}). \quad (5.23)$$

$V$  can be seen as a plane wave with wave vector  $(\mathbf{k}_B, \beta \mathbf{u}_z)$ , modulated by  $v(\mathbf{r})$ . The “effective direction of propagation” of this wave makes an angle with the  $z$ -axis given by:

$$\theta = \tan^{-1} \left( \frac{|\mathbf{k}_B|}{|\beta|} \right). \quad (5.24)$$

We will call this angle *effective angle of propagation* of a Bloch wave. To get an idea of the order of magnitude of the effective angle, we consider  $\mathbf{k}_B$  to be on the top edge of the Brillouin cell, so that we have  $|\mathbf{k}_B| = 2\pi\sqrt{3}/(3\Lambda)$ . In that case

$$\theta_{\text{BZ edge}} = \tan^{-1} \left( \frac{\lambda}{\Lambda} \frac{\sqrt{3}}{3n_{\text{eff}}} \right). \quad (5.25)$$

Note that Bloch peaks on the edge of the Brillouin zone hence have smaller effective propagation angles with decreasing  $\lambda/\Lambda$ .

### 5.2.3 Implementation

The implementation of (5.20) is straightforward. Indeed the sole point which has to be emphasized here is that the Bloch transform only involves complex exponentials, which makes its computation much easier and much faster than the computation of field distributions, involving Bessel functions with complex arguments. Computing the Bloch transform distribution over the first Brillouin zone is therefore extremely fast. The Bloch transform is thus not only the best (in terms of accuracy and ease of identification) but also the computationally most efficient way of identifying modes.

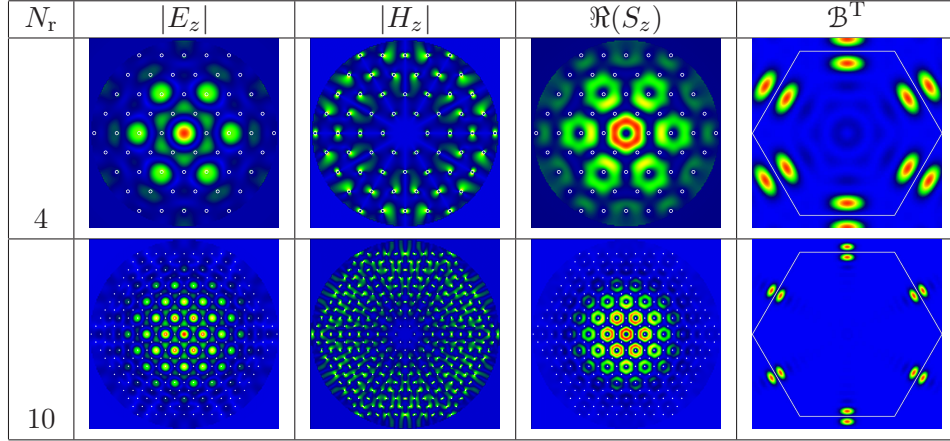


Figure 5.1: Field maps and total Bloch transform of a mode consisting essentially of a superposition of 6 Bloch waves. Note that the fields are depicted in the direct space ( $\mathbf{r}$ -space), whereas the Bloch transform is in the reciprocal space ( $\mathbf{k}$ -space): the white hexagon on the Bloch transform map depicts the edges of the first Brillouin zone.

### 5.2.4 Examples

Before analysing properties of the Bloch transform in greater detail, we illustrate the basic properties seen in the previous sections with two examples. In both examples the MOFs are made out of a cladding of hexagonally packed air inclusions in silica, the core being defined by a missing hole.

Fig. 5.1 shows an example of a mode of symmetry class 1, constituted of a superposition of 6 Bloch waves, for two MOFs with different number of rings  $N_r$  but with same pitch and hole-diameter ( $\Lambda = 2.3\mu\text{m}$ ,  $d/\Lambda = 0.15$ ), and at the same wavelength ( $\lambda = 1.55\mu\text{m}$ ). The total Bloch transform shown was computed with the  $E_z$  Fourier-Bessel coefficients, but the transform is the same to graphical accuracy when computed with the coefficients related to  $H_z$ , as is expected from the interdependence of  $E_z$  and  $H_z$  through the scattering matrices.<sup>6</sup> When analysing the Bloch transform for different orders, it appears that the peaks of the total Bloch transform are essentially due to the orders  $n = -1$  and  $n = 1$ .

We see that for  $N_r = 4$  the peaks are quite broad, and as predicted become much narrower for  $N_r = 10$ . For  $N_r = 4$ , secondary peaks are not negligible; this is partly related to the importance of the surface and defect states for a system consisting of only 4 periodic layers, but we will see in the last section of this Chapter that some of the secondary peaks are a natural feature of the Bloch transform for finite MOFs, even for fields resulting from superposition of sole Bloch modes.

For  $N_r = 10$  on the contrary, peaks are well defined, and the importance of secondary peaks is fading, suggesting that edge effects are becoming negligible. In both cases the main peaks are close to the edge of the first Brillouin zone, indicating that each Bloch component is close to a standing wave. We note that the exact position of the maxima of the peaks is not the same in both cases, but that the “overall shape” remains constant. We further note the predicted periodicity in the reciprocal space of  $\mathcal{B}^T(\mathbf{k})$ : the peaks outside the first

<sup>6</sup> Note that the Fourier Bessel coefficients of order 0 for  $E_z$  and  $H_z$  are not *a priori* related as  $R_0^{\text{EK}+} = R_0^{\text{KE}+} = 0$ . When the total Bloch transform is dominated by the order 0, the total Bloch transforms for  $E_z$  and  $H_z$  can therefore differ substantially. We will see an example of such a case in Chapter 7.

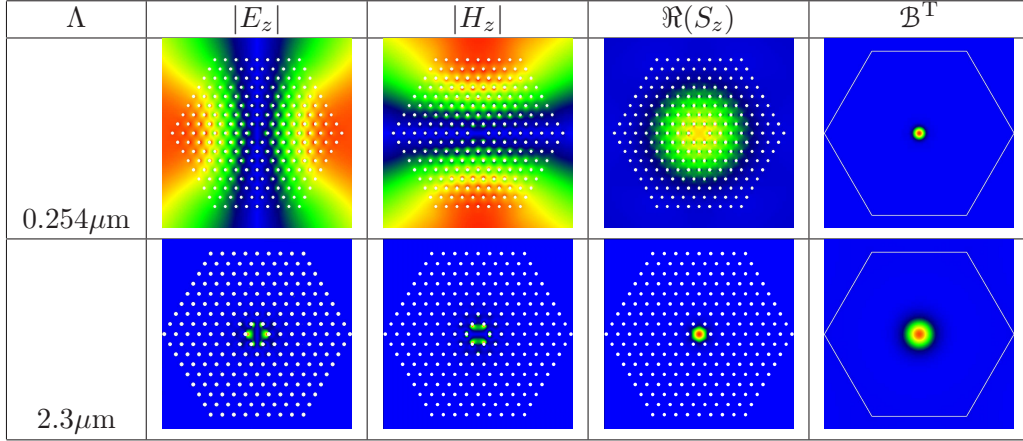


Figure 5.2: Fundamental mode of two MOFs with different pitch, but with same  $d/\Lambda = 0.3$  and  $N_r = 8$ . The field distribution changes considerably between the two values of the pitch, but the Bloch transform remains a single peak centered on the origin.

Brillouin zone are replicates of the peaks inside the first Brillouin zone, and do not contain any additional information. Finally, we note that the Bloch transform has symmetry properties induced by the symmetry properties of the mode.

Fig. 5.2 shows a second example illustrating how helpful the Bloch transform becomes when trying to identify modes of MOFs having different yet comparable structures. Both lines of contour plots shown in Fig. 5.2 relate to the fundamental mode of a MOF with  $N_r = 8$  holes of air inclusions in silica, with the same relative hole size  $d/\Lambda = 0.3$  and at same wavelength  $\lambda = 1.55\mu\text{m}$ , but with different values of the pitch. We see that the field patterns differ considerably, but that the Bloch transform remains similar for the two values of the pitch: there is only one peak centered on  $\mathbf{k} = 0$ , only the width of the peak changes, being much narrower for the wider mode than for the well confined mode. We will see in the next sections that in such a case the width of the mode and the width of the Bloch transform are linked through a Heisenberg-type relation.

### 5.2.5 Advanced Properties

To derive some analytical properties of the Bloch transform, we will consider a mode consisting of a superposition of a finite number  $N_b$  of Bloch waves so that

$$\forall l \in [1, N_i], B_n(\mathbf{c}_l) = \sum_{j=1}^{N_b} \hat{B}_n^j \exp(i\mathbf{k}^j \cdot \mathbf{c}_l), \quad (5.26)$$

where  $\mathbf{k}^j$  is the Bloch vector of Bloch wave  $j$ , whereas  $\hat{B}_n^j$  is the complex amplitude of Bloch wave  $j$  associated with the Fourier-Bessel order  $n$ . We know that this kind of decomposition is not exact in the case of finite structures, as surface states are neglected. To take into account non-Bloch components, a term  $\hat{B}_n^0(\mathbf{c}_l)$  would have to be added to Eq. (5.26).

### Normalizing the Bloch Transform: Bloch Wave Decomposition and Parseval Identity

Until now we have only interpreted the location of peaks of the Bloch transform. Through normalizing the Bloch transform we will also be able to give a meaning to the actual value of  $\mathcal{B}_n(\mathbf{k})$ . Here we give two methods of making such a normalization, the comparison of which will lead to a Parseval-like identity.

First we make explicit the value of the Bloch transform when  $\mathbf{k}$  takes the value of one of the Bloch vectors  $\mathbf{k}^i$  of the field:

$$\mathcal{B}_n(\mathbf{k}^i) = \sum_{l=1}^{N_i} \sum_{j=1}^{N_b} \hat{B}_n^j \exp(i(\mathbf{k}^i - \mathbf{k}^j) \cdot \mathbf{c}_l) \quad (5.27)$$

$$= N_i \hat{B}_n^i + \sum_{j=1, j \neq i}^{N_b} \hat{B}_n^j \sum_{l=1}^{N_i} \exp(i(\mathbf{k}^i - \mathbf{k}^j) \cdot \mathbf{c}_l) . \quad (5.28)$$

Under the rather strong assumptions that no  $\mathbf{k}^i - \mathbf{k}^j$  is *too close* to a vector of the reciprocal lattice and that the number of inclusion is *large enough*,<sup>7</sup> each sum over  $l$  in Eq. (5.28) takes values much smaller than  $N_i$ , so that

$$\mathcal{B}_n(\mathbf{k}^i) \simeq N_i \hat{B}_n^i . \quad (5.29)$$

The value of the Bloch transform taken at a Bloch vector  $\mathbf{k}^i$  gives therefore an approximation of the complex amplitude  $\hat{B}_n^i$  of the associated Bloch wave component in Eq. (5.26). Nevertheless, as because of linearity only relative amplitudes in that decomposition have a physical meaning, it is necessary to be able to compare the amplitudes to each other. Mathematically speaking, we would eventually like to obtain

$$\frac{\hat{B}_n^i}{\left( \sum_{j=1}^{N_b} |\hat{B}_n^j|^2 \right)^{1/2}} . \quad (5.30)$$

One way of computing this would be to isolate and compute all the peaks of the Bloch transform to get the complete set of  $\hat{B}_n^i$ , but this method would numerically be cumbersome and approximate. Indeed isolating the exact position and value of the maximum of the Bloch transform would need a refinement of each peak. Another method to make the normalization would be to find an equivalence between the discrete sum over the values at the peaks and an integral over the whole first Brillouin zone. To do so, we consider the integral

$$A_n = \iint_{\text{FBZ}} |\mathcal{B}_n(\mathbf{k})|^2 d\mathbf{k} \quad (5.31)$$

where the integral is taken over the first Brillouin zone (FBZ). With  $*$  denoting the complex

---

<sup>7</sup>We will see in the next subsection that these two assumptions are connected.

conjugation, we have

$$A_n = \iint_{\text{FBZ}} \left| \sum_{i=1}^{N_b} \sum_{l=1}^{N_i} \hat{B}_n^i \exp(\imath(\mathbf{k}^i - \mathbf{k}) \cdot \mathbf{c}_l) \right|^2 d\mathbf{k} \quad (5.32)$$

$$= \iint_{\text{FBZ}} \left( \sum_{i=1}^{N_b} \sum_{l=1}^{N_i} \hat{B}_n^i \exp(\imath(\mathbf{k}^i - \mathbf{k}) \cdot \mathbf{c}_l) \right) \left( \sum_{j=1}^{N_b} \sum_{m=1}^{N_i} \hat{B}_n^{j*} \exp(-\imath(\mathbf{k}^j - \mathbf{k}) \cdot \mathbf{c}_m) \right) d\mathbf{k} \quad (5.33)$$

$$= \sum_{i,j=1}^{N_b} \sum_{l,m=1}^{N_i} \hat{B}_n^i \hat{B}_n^{j*} \exp(\imath \mathbf{k}^i \cdot \mathbf{c}_l) \exp(-\imath \mathbf{k}^j \cdot \mathbf{c}_m) \iint_{\text{FBZ}} \exp(-\imath \mathbf{k} \cdot (\mathbf{c}_l - \mathbf{c}_m)) d\mathbf{k} . \quad (5.34)$$

As  $(\mathbf{c}_l, \mathbf{c}_m) \in \mathcal{L}^2$ ,  $\mathbf{c}_l - \mathbf{c}_m \in \mathcal{L}$ , so that the exponential in the integral is invariant when adding any vector of the reciprocal lattice to  $\mathbf{k}$ . The domain of integration can be rearranged to a rectangle using this periodicity, and it is then readily shown that the integral takes the value  $\mathcal{A}_{\text{FBZ}} \delta_{l,m}$  where  $\delta$  is the usual Kronecker symbol and  $\mathcal{A}_{\text{FBZ}}$  is the area of the first Brillouin zone. If  $\mathcal{L}$  is a hexagonal lattice with pitch  $\Lambda$  we have

$$\mathcal{A}_{\text{FBZ}} = \frac{8\sqrt{3}\pi^2}{3\Lambda^2} \quad (5.35)$$

so that

$$A_n = \frac{8\sqrt{3}\pi^2}{3\Lambda^2} \sum_{i,j=1}^{N_b} \sum_{l=1}^{N_i} \hat{B}_n^i \hat{B}_n^{j*} \exp(\imath(\mathbf{k}^i - \mathbf{k}^j) \cdot \mathbf{c}_l) \quad (5.36)$$

$$= \frac{8\sqrt{3}\pi^2}{3\Lambda^2} \left[ \sum_{i=1}^{N_b} N_i |\hat{B}_n^i|^2 + \sum_{\substack{i \neq j \\ i,j=1}}^{N_b} \hat{B}_n^i \hat{B}_n^{j*} \sum_{l=1}^{N_i} \exp(\imath(\mathbf{k}^i - \mathbf{k}^j) \cdot \mathbf{c}_l) \right] . \quad (5.37)$$

Under the same assumptions as above (large  $N_i$  and  $\mathbf{k}^i - \mathbf{k}^j$  not too close to a vector of the reciprocal lattice), each sum over  $l$  in Eq. (5.37) takes values much smaller than  $N_i$ , so that

$$A_n \simeq \frac{8\sqrt{3}\pi^2}{3\Lambda^2} N_i \sum_{i=1}^{N_b} |\hat{B}_n^i|^2 . \quad (5.38)$$

We recognize here the denominator of Eq. (5.30), and obtain

$$\frac{\hat{B}_n^i}{\left( \sum_{j=1}^{N_b} |\hat{B}_n^j|^2 \right)^{1/2}} \simeq \frac{2\pi\sqrt{2} 3^{3/4}}{3\Lambda N_i^{1/2}} \frac{\mathcal{B}_n(\mathbf{k}^i)}{\left( \iint_{\text{FBZ}} |\mathcal{B}_n(\mathbf{k})|^2 d\mathbf{k} \right)^{1/2}} , \quad (5.39)$$

which is much more straightforward to implement numerically than the method suggested previously.

It would nevertheless be even easier to normalize the Bloch transform using a normalization in the direct space, *i.e.* using the  $B_n(\mathbf{c}_l)$  coefficients. To do so, we now consider the sum

$$S_n = \sum_{l=1}^{N_i} |B_n(\mathbf{c}_l)|^2 . \quad (5.40)$$

Using Eq. (5.26) we have

$$S_n = \sum_{l=1}^{N_i} \left( \sum_{i=1}^{N_b} \hat{B}_n^i \exp(\imath \mathbf{k}^i \cdot \mathbf{c}_l) \right) \left( \sum_{j=1}^{N_b} \hat{B}_n^{j*} \exp(-\imath \mathbf{k}^j \cdot \mathbf{c}_l) \right) \quad (5.41)$$

$$= \sum_{l=1}^{N_i} \sum_{i,j=1}^{N_b} \hat{B}_n^i \hat{B}_n^{j*} \exp(\imath (\mathbf{k}^i - \mathbf{k}^j) \cdot \mathbf{c}_l). \quad (5.42)$$

The sum is the same as in Eq. (5.36), and with the same assumptions than previously we obtain

$$S_n \simeq N_i \sum_{i=1}^{N_b} |\hat{B}_n^i|^2. \quad (5.43)$$

From Eq. (5.29) and (5.43) we derive

$$\frac{\hat{B}_n^i}{\left( \sum_{j=1}^{N_b} |\hat{B}_n^j|^2 \right)^{1/2}} \simeq \frac{\mathcal{B}_n(\mathbf{k}^i)}{\left( N_i \sum_{l=1}^{N_i} |B_n(\mathbf{c}_l)|^2 \right)^{1/2}}. \quad (5.44)$$

Through Eq. (5.39) and (5.44) we now have two ways of obtaining the normalized coefficients of the Bloch wave decomposition (5.26). Note that both ways are equivalent, as from Eqs. (5.36), (5.42) and (5.43) we obtain Parseval-type identities:

$$\sum_{l=1}^{N_i} |B_n(\mathbf{c}_l)|^2 = \frac{\sqrt{3}\Lambda^2}{8\pi^2} \iint_{\text{FBZ}} |\mathcal{B}_n(\mathbf{k})|^2 d\mathbf{k} \simeq N_i \sum_{i=1}^{N_b} |\hat{B}_n^i|^2, \quad (5.45)$$

where the first identity is rigorous, as we used the assumptions only in deriving the second one.

### Width of the Bloch Transform Peaks: Heisenberg Uncertainty

We have predicted earlier that the width of the peaks centered on the Bloch vectors  $\mathbf{k}^i$  decreases with increasing number of inclusions. Here we analyse this behaviour analytically, and show that the width of the Bloch transform peaks is related to the width of modes through a Heisenberg-type relationship. For this analysis we consider Eq. (5.26) with a single Bloch component, *i.e.*

$$B_n(\mathbf{c}_l) = \hat{B}_n^1 \exp(\imath \mathbf{k}^1 \cdot \mathbf{c}_l). \quad (5.46)$$

The Bloch transform is then

$$\mathcal{B}_n(\mathbf{k}) = \hat{B}_n^1 \sum_{l=1}^{N_i} \exp(\imath (\mathbf{k}^1 - \mathbf{k}) \cdot \mathbf{c}_l). \quad (5.47)$$

For the sake of simplicity we consider that the structure is limited by a parallelogram, so that the set of  $\mathbf{c}_l$  is entirely described by

$$\mathbf{c}_l = \mathbf{c}_{(\alpha,\beta)} \quad (5.48)$$

$$= \alpha \mathbf{u}_1 + \beta \mathbf{u}_2, \quad (\alpha, \beta) \in [1, N_\alpha] \times [1, N_\beta] \quad (5.49)$$

where  $N_\alpha N_\beta = N_i$  and  $\mathbf{u}_1$  and  $\mathbf{u}_2$  are the vectors generating  $\mathcal{L}$  which, in the case of a hexagonal lattice with pitch  $\Lambda$ , are

$$\mathbf{u}_1 = \Lambda \hat{x} \quad (5.50)$$

$$\mathbf{u}_2 = (1/2)\Lambda \hat{x} + (\sqrt{3}/2)\Lambda \hat{y}. \quad (5.51)$$

Introducing  $\delta k_x$  and  $\delta k_y$  as the  $x$  and  $y$  components of  $\mathbf{k}^1 - \mathbf{k}$ , the Bloch transform becomes

$$\mathcal{B}_n(\mathbf{k}) = \hat{B}_n^1 \sum_{\alpha=1}^{N_\alpha} \sum_{\beta=1}^{N_\beta} \exp \left( i(\delta k_x(\alpha\Lambda + \beta\Lambda/2) + \delta k_y(\sqrt{3}\beta\Lambda/2)) \right) \quad (5.52)$$

$$= \hat{B}_n^1 \left( \sum_{\alpha=1}^{N_\alpha} \exp(i\delta k_x \alpha\Lambda) \right) \left( \sum_{\beta=1}^{N_\beta} \exp \left( i\beta(\delta k_x \Lambda/2 + \delta k_y \sqrt{3}\Lambda/2) \right) \right) \quad (5.53)$$

$$= \hat{B}_n^1 \exp(i(3\delta k_x \Lambda/2 + \delta k_y \sqrt{3}\Lambda/2)) \times \frac{1 - \exp(iN_\alpha \delta k_x \Lambda)}{1 - \exp(i\delta k_x \Lambda)} \frac{1 - \exp(iN_\beta(\delta k_x \Lambda/2 + \delta k_y \sqrt{3}\Lambda/2))}{1 - \exp(i(\delta k_x \Lambda/2 + \delta k_y \sqrt{3}\Lambda/2))}. \quad (5.54)$$

As we only consider the magnitude of the peaks, we take the modulus of the previous equation. Through conventional trigonometric transformations we obtain

$$|\mathcal{B}_n(\mathbf{k})| = |\hat{B}_n^1| \left| \frac{\sin(N_\alpha \delta k_x \Lambda/2)}{\sin(\delta k_x \Lambda/2)} \right| \left| \frac{\sin(N_\beta \Lambda(\delta k_x + \sqrt{3}\delta k_y)/4)}{\sin(\Lambda(\delta k_x + \sqrt{3}\delta k_y)/4)} \right|. \quad (5.55)$$

The peaks of the Bloch transform along each direction are therefore of the same type as the function

$$f(x) = \begin{cases} \left| \frac{\sin(ax)}{\sin(x)} \right| & \text{if } x \neq m\pi, m \in \mathbb{Z} \\ |a| & \text{if } x = m\pi, m \in \mathbb{Z} \end{cases} \quad (5.56)$$

This function has main peaks of value  $a$  for  $x = m\pi$ ,  $m \in \mathbb{Z}$ .<sup>8</sup> These become narrower with increasing  $a$ , and for  $a \rightarrow \infty$  their widths tend to zero. We therefore choose to develop the function for small  $x$  to find the value of the half width  $x_0$ , satisfying

$$f(x_0) = a/2. \quad (5.57)$$

We know that  $x_0$  is between 0 and the first zero of  $f(x)$ , which occurs at  $\pi/a$ . With increasing  $a$ ,  $x_0$  tends to zero, but  $ax_0$  remains finite and bound by  $\pi/2$ , and the small argument development must be used with care. Using Taylor series to the 5<sup>th</sup> order for  $\sin(ax)$ , while using a first order expansion for  $\sin(x)$ , we obtain  $x_0$  with sufficient accuracy:

$$f(x_0) = a/2 \quad (5.58)$$

$$\Rightarrow ax_0 - \frac{(ax_0)^3}{6} + \frac{(ax_0)^5}{120} \simeq \frac{ax_0}{2} \quad (5.59)$$

$$\Leftrightarrow 1 - \frac{(ax_0)^2}{3} + \frac{(ax_0)^4}{60} \simeq 0. \quad (5.60)$$

---

<sup>8</sup>Note that the  $f$  also has smaller secondary peaks at  $x \simeq (m + 1/2)\pi/a$ ,  $m \in \mathbb{Z} - \{0, -1\}$  of magnitude decaying as  $a/(\pi|m + 1/2|)$ . The magnitude of the first secondary peak is roughly 1/5 of the magnitude of the main peak, and can barely be seen on the contour plots of section 5.2.4.

Solving the latter equation gives

$$x_0 \simeq \frac{1.91}{a} \quad (5.61)$$

and thus the width of the peak of the Bloch transform is given by

$$\begin{cases} \delta k_x \Lambda & \simeq 2 \frac{1.91}{N_\alpha} \\ \delta k_x \Lambda / 2 + \sqrt{3}/2 \delta k_y \Lambda & \simeq 2 \frac{1.91}{N_\beta} \end{cases} \quad (5.62)$$

The result to be retained from this analysis is that the width along a given direction varies as the inverse of the number of inclusions along that same direction. The exact value of the proportionality constant will depend on the actual shape of the boundaries of the cladding structure, but will remain of the order of 4. For a hexagonal arrangement of inclusions delimited by a hexagonal shape,  $N_\alpha \simeq N_\beta \simeq N_r$  where  $N_r$  is the number of layers of holes. Therefore we obtain

$$\delta k \Lambda N_r \simeq 4. \quad (5.63)$$

Note that  $\Lambda N_r$  represents the spatial width of the fibre, and  $\delta k$  the angular width of the mode. Eq. (5.63) is a Heisenberg-type relation.

In the example chosen for this analysis, the field was a single Bloch wave. The result holds for a superposition of Bloch waves for each peak associated to each Bloch vector. But if the mode is not a superposition of Bloch waves, which is the case for a surface or defect state, the relation has to be modified. In the case of a localized defect mode (*e.g.* the mode for  $\Lambda = 2.3 \mu\text{m}$  in Fig. 5.2), the magnitude of the Fourier-Bessel coefficients decays exponentially away from the defect. In that case only the Fourier-Bessel coefficients associated with inclusions close to the defect contribute significantly to the Bloch transform. In other words the sums of Eq. (5.53) would be reduced to a sum over the inclusions where the field is significant, which would lead to a corrected number of layers  $N'_r$  in the Heisenberg relation (5.63), reflecting the number of rings where the field is significant. The Heisenberg relation is therefore a relation between the spatial extent of the mode and the width of the Bloch transform peaks.

Through the above analysis, we also can quantify the assumptions made when normalizing the Bloch transform. For the sums in Eq. (5.28) to be negligible, we needed a large enough number of inclusions and  $\mathbf{k}_i - \mathbf{k}_j$  not to be too close to a vector of the reciprocal lattice. These sums are similar to the one analysed for extracting the half-width, and using similar arguments to those of this section, it appears that the sums become negligible roughly when

$$\forall \mathbf{G} \in \mathcal{L}^*, \forall i \neq j, |\mathbf{k}^i - \mathbf{k}^j + \mathbf{G}| N_i^{1/2} \Lambda \gtrsim 4 \quad (5.64)$$

where  $\mathcal{L}^*$  is the reciprocal lattice. The width of the first Brillouin zone being of the order of  $2\pi/\Lambda$ , the distance between peaks, normalized to the width of the first Brillouin zone, should therefore be greater than  $2/(\pi N_i^{1/2})$ .

Note that in the first example of Bloch transform we used in section 5.2.4 (Fig. 5.1) this condition is only roughly satisfied.

### 5.2.6 Bloch Transform for Other Methods

The Bloch transform we have defined here is particularly well suited for use in combination with the multipole method. For other MOF simulation models, the Bloch transform has to

be adapted. Any transform able to isolate Bloch components of a mode should be suited, and the simple Fourier transform of the fields is among them. Indeed, if a field has a Bloch component of the form

$$V(\mathbf{r}) = \exp(i\mathbf{k}_B \mathbf{r})v(\mathbf{r}) \quad (5.65)$$

where  $v(\mathbf{r})$  has the periodicity of the lattice  $\mathcal{L}$ , its Fourier transform is given by

$$\tilde{V}(\mathbf{k}) = \delta(\mathbf{k} - \mathbf{k}_B) * \tilde{v}(\mathbf{k}) \quad (5.66)$$

where  $\tilde{V}$  and  $\tilde{v}$  are the Fourier transform of  $V$  and  $v$  respectively, and  $*$  represents the convolution operator. Since  $v$  is  $\mathcal{L}$  periodic, its Fourier transform is a discrete sum over the reciprocal lattice  $\mathcal{L}^*$ :

$$\tilde{v}(\mathbf{k}) = \sum_{\mathbf{k}_p' \in \mathcal{L}^*} A_p \delta(\mathbf{k} - \mathbf{k}_p') . \quad (5.67)$$

The Fourier transform of  $V$  becomes

$$\tilde{V}(\mathbf{k}) = \sum_{\mathbf{k}_p' \in \mathcal{L}^*} A_p \delta(\mathbf{k} - \mathbf{k}_B - \mathbf{k}_p') . \quad (5.68)$$

This distribution has peaks at  $\mathbf{k} = \mathbf{k}_B + \mathbf{k}_p$  where  $\mathbf{k}_p$  is a vector of the reciprocal lattice. Since Bloch vectors are defined to within an arbitrary vector of the reciprocal lattice, all peaks of this distribution correspond to Bloch vectors. It is sufficient to find a vector of the reciprocal lattice  $\mathbf{k}_p$  associated to a non zero value of  $A_p$  to get the full information on the Bloch components of the field.

Initially we wanted to use the Fourier transform of the fields to obtain the mode's Bloch components. It appeared that in order to get the field's Fourier transform with sufficient accuracy to extract the Bloch components, we needed a numerically prohibitive number of points in the field maps. We therefore decided to exploit the analytic expansion we had of the fields (the Wijnngaard expansion, Eq. (3.21)), which led to the definition of the Bloch transform. In cases where the Fourier transform of the fields is easier to obtain than the field maps (*e.g.* plane wave methods), it would nevertheless be a natural choice to use the former. We discuss the relation between Bloch and Fourier transforms further in Appendix G.

Plat de Rôt :

## Filet de Kangourou

### Sauce Poivrade «Oz», Fruits et Légumes Glacés, Rose des Sables

*Kangaroo Loin, "Oz-style" Poivrade Sauce, Glacé Fruits and Vegetables, Gypsum Flower*

#### Pour 6 personnes :

Pour le kangourou :

800 g de filet de kangourou  
50 g de beurre clarifié

Pour la marinade :

*1 L de vin rouge  
25 cl de vinaigre de vin rouge  
1 oignon  
2 échalottes  
1 grosse carotte  
1/2 botte de persil  
5 gousses d'ail  
1 cuillerée à soupe de poivre  
grains  
1/2 cuillerée à soupe de  
grains de coriandre  
2 clous de girofle  
5 baies de genièvre  
1 branche de thym  
1 branche de romarin  
1 feuille de laurier  
1 petite branche de céleri  
2 cuillerées à soupe d'huile  
d'olive  
une petite cuillerée à café de  
paprika  
25 «pepperberries» (baies  
natives d'australie)*

#### La marinade

ÉMINCER grossièrement l'oignon, les échalottes, la carotte et l'ail (sans peler ce dernier). Réunir l'ensemble des ingrédients dans une terrine. Détailler le filet de kangourou en 6 médaillons régulier. Les laisser dans la marinade au moins 24 heures.

#### Les roses des sables [2]

PELER les pommes de terre et les laver, les essuyer, puis les débiter en bouchons de 5 cm de haut environ. À l'aide d'un économe, tourner les bouchons en ruban, si possible sans interruption. Laisser les rubans de pomme de terre reposer dans de l'eau fraîche jusqu'au moment de servir.

AU moment de servir, égouter et essuyer avec du papier absorbant les rubans de pommes de terre. Faire fondre le beurre clarifié, y tremper les rubans de pommes de terre. Enrouler les rubans comme une rose et les déposer dans un plat en Téflon. Glisser au four préchauffé à 220°C, laisser cuire 10 minutes en arrosant fréquemment les rubans de beurre clarifié jusqu'à ce qu'ils deviennent colorés.

#### Les fruits et légumes glacés

ÉPLUCHER puis détailler en carrés de 5 cm de côté et de 6 à 7 mm d'épaisseur les navets, la courge, les pommes et les poires. Arroser d'un peu de jus de citron les morceaux de pommes, de poire et de navet, légèrement saler ceux de navet et de courge. Faire revenir les carrés de pomme et les poire séparément dans une poêle avec un peu de beurre clarifié et une cuillerée à soupe de sucre en poudre d'abord à feu vif pour les colorer puis à feu doux jusqu'à ce qu'ils soient fondant. Maintenir au tiède.

Pour la sauce poivrade  
«Oz» :

*2 cuillerées à soupe de  
confiture de cassis  
1 tomate  
sel  
pepperberries  
30 g de beurre*

Pour les fruits et légumes glacés :

*2 gros navets  
un quart de courge  
2 pommes golden  
2 poires pas trop mûres  
100 g de sucre  
1 dl de vinaigre de vin*

Pour les roses des  
sables :

*6 grosses pommes de  
terre à chair ferme  
125 g de beurre clarifié  
sel fin*

Garniture :

*raisins roses  
fruits rouges  
lanières de zeste  
d'agrumes finement  
prélevées*

Cuire les carrés de courge à la vapeur en les laissant un peu fermes. Cuire les navets dans le vinaigre additionné de trois cuillerées à soupe de sucre à feu très doux. Laisser réduire jusqu'au sirop, ajouter 10 cl d'eau puis laisser réduire à nouveau. Recommencer une ou deux fois, jusqu'à ce que les carrés de navets soient cuits. Quelques minutes avant de servir, ajouter les carrés de courge et réduire le feu au minimum. Tiédir les raisins et les fruits rouges.

### La sauce poivrade «Oz»

**R**ÉCUPÉRER les médaillons de kangourous dans la marinade et les entreposer au froid. Porter la marinade à ébullition avec la tomate coupée en morceaux. Dès le premier bouillon écumer aussi souvent que possible. Une fois réduite de moitié, passer au chinois, puis poursuivre la réduction, jusqu'au sirop. Après la cuisson des médaillons de kangourou, déglacer la poêle avec très peu d'eau et ajouter les sucres de cuisson à la marinade réduite. Laisser réduire à nouveau au sirop. Baisser le feu et incorporer la confiture de cassis et le beurre par petits morceaux en remuant constamment. Ajouter une vingtaine de pepperberries et ajuster l'assaisonnement.

### Le kangourou

**E**SSUYER les médaillons soigneusement avec du papier absorbant. Cuire les médaillons dans une poêle anti-adhésive très chaude avec très peu de beurre clarifié. Juste saisir les médaillons des deux côtés, le kangourou mariné devant être d'une tendreté exceptionnelle, les morceaux doivent rester bleu à saignant. Laisser reposer sous aluminium au four à 60° juste le temps de terminer la sauce, et incorporer le jus résultant du repos à la sauce.

**D**ISPOSER dans chaque assiette un carré de chaque fruit et de chaque légume, en formant un arlequin. Placer la rose des sables, le médaillon de kangourou, un filet de sauce, quelques pepperberries, les fruits rouges et les grains de raisin tièdes. Décorer des quelques fines lanières de zeste d'agrumes.

# Chapter 6

## Modes in MOFs

### 6.1 Introduction

The application of the multipole method as described in Chapters 3 and 4 to a given MOF structure gives a very large number of modes, all of which are generally leaky<sup>1</sup>. Among these, some modes - as for example the fundamental mode - are of much greater importance than others for applications. Others may seem to have no importance at all at certain wavelengths in certain structures, but may become useful, or a nuisance, at other wavelengths or in different structures. In the next Chapters we will investigate this through following mode properties with varying wavelength or fibre parameters, but to be able to do so, it seems a prerequisite that these modes can be identified in a clear, unquestionable manner.

The usual classification for conventional fibres, using the HE, EH, TE and TM denominations, was established for waveguides of  $C_{\infty v}$  symmetry and for perfectly guided modes. The use of this classification can be extended to leaky modes if these are considered as being guided modes below cutoff [3, Sec. 24], but not to guides of symmetries other than  $C_{\infty v}$ .

In this Chapter, we discuss how to distinguish, identify and classify MOF modes, mainly through the Bloch transform. It appears that MOF modes can be divided into two categories: *defect modes* and *edge dominated modes*, having very different properties.

### 6.2 Identifying Modes

#### 6.2.1 Differences to Conventional Fibres

For conventional fibres, modes are labeled  $HE_{\nu,m}$ ,  $EH_{\nu,m}$ ,  $TE_m$  or  $TM_m$ . The two first categories, HE and EH, denote modes which are the  $m^{th}$  solution to a waveguide equation depending on  $\nu$ . This equation factorizes into two independent equations for  $\nu = 0$  and the  $m^{th}$  solutions of these two equations are the  $TM_m$  and  $TE_m$  modes. As a result, the effective indices of modes of the same category and same  $\nu$  follow the same order, regardless of the wavelength. This order is kept for the real part of  $n_{\text{eff}}$  even below cutoff. One could consider classifying modes of a MOF in a similar way, following the order of the real part of  $n_{\text{eff}}$ , but it appears that mode crossing occurs, and that no simple order in the effective indices is preserved when changing the wavelength or MOF parameters.

---

<sup>1</sup>Non-leaky modes can be carried by MOF structures with a low refractive index jacket ( $n_0 < n_M$ ).

In conventional fibres, the  $E_z$  and  $H_z$  fields of a given mode are of the form

$$E_z(r, \theta) = f(\lambda) J_\nu(g(\lambda)r) \exp(i\nu\theta) \quad (6.1)$$

where  $r$  and  $\theta$  are the cylindrical coordinates with origin at the center of the core. For different wavelengths the field maps are therefore related to each other through a simple scaling, and modes can be identified through the scaled field maps. This is no longer possible for MOFs: the relative weight of Fourier-Bessel coefficients of different inclusions can vary through several orders of magnitude with varying wavelength, so that the same mode at different wavelengths has no recognizable specific shape.

### 6.2.2 Similar Modes of Similar Structures

To give an idea of the difficulty of classifying modes *ab initio*, Fig. 6.1 gives a few examples of modes encountered in MOFs. All modes are of symmetry class 1, for a structure with  $d/\Lambda = 0.75$  (frames B and H) or  $d/\Lambda = 0.45$  (all other frames) and  $N_r$  ranging from 1 to 4.

Increasing the number of rings increases the number of modes (the number of possible resonances of the cladding structure increases with the number of inclusions)<sup>2</sup> and modifies the modes, but one would expect that modes confined in the core remain similar with increasing  $N_r$ . Mode A should therefore remain if we increase  $N_r$ , but when considering the modes of the same structural parameters with  $N_r = 2$ , two modes (C and D) are similar to mode A. For  $N_r = 3$  we again have two modes (E and F) which have field distributions comparable to mode A. For  $N_r = 4$ , three modes (G, I and J) could be seen as a generalization of mode A.

If we only consider the field maps, one would be inclined to say that modes C, E and G are the most similar to mode A. This would be supported by considering the similar mode for a structure with  $d/\Lambda = 0.75$ , shown in frames B and H. But if we consider the trajectory of  $n_{\text{eff}}$  with varying  $N_r$  and *expect* a steady behaviour,<sup>3</sup> the choice of mode I instead of G for  $N_r = 4$  seems a more “logical” choice.

Mode A is the mode of symmetry class 1 with the lowest losses for the considered MOF. If this property was to be conserved with increasing  $N_r$ , modes D, F and J would be the candidates for continuing mode A with increasing  $N_r$ .

As shown in this example a simple look at the field distributions and the effective indices does not allow an obvious identification of modes. The increasing number of similar modes with increasing  $N_r$  could lead to the suggestion that the approach of finding similar modes for different values of  $N_r$  is not sensible. There is no obvious reason other than *intuition* that a confined mode will remain confined with increasing  $N_r$ , or that we can define a one to one ascending correspondence of modes with  $N_r$ . Indeed  $N_r$  is a discrete parameter, and it is therefore difficult to see whether two modes for different values of this parameter are in some way related. There could also be a mode splitting between two values of  $N_r$ , so that for example modes G, H and I reduce to mode A if  $N_r$  is decreased.

Note that in the preceding paragraphs we used the notion of “confined modes” in an intuitive way, arguing that a confined mode should remain confined with increasing  $N_r$ . One would indeed expect the losses of a confined mode to decrease with increasing number of

<sup>2</sup>The number of leaky modes being a discrete infinity, it is actually the density of modes in  $n_{\text{eff}}$  space which increases, *cf.* section 2.4.

<sup>3</sup>This might seem slightly arbitrary, but it is *a priori* not more arbitrary than looking at graphic similarities in field maps... Our approach here is to demonstrate that simple arguments for classifying the modes are not suitable.

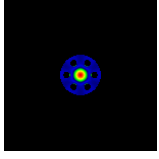
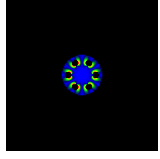
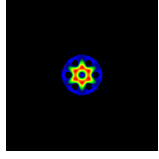
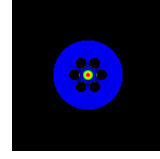
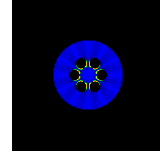
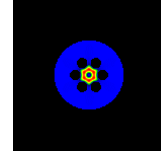
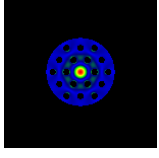
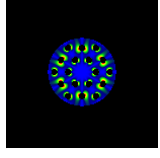
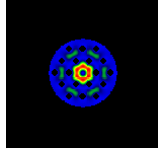
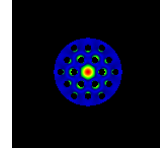
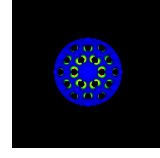
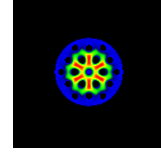
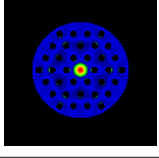
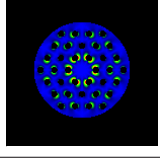
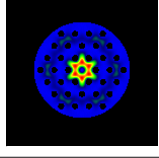
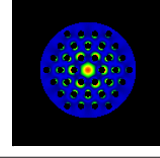
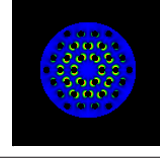
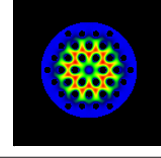
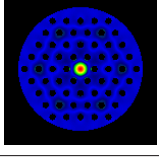
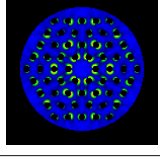
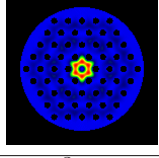
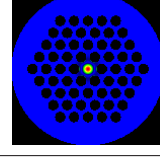
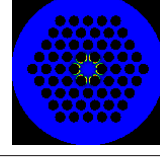
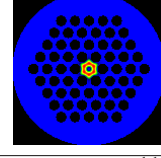
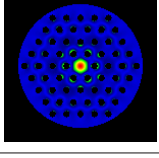
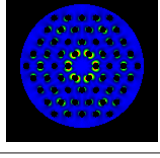
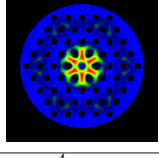
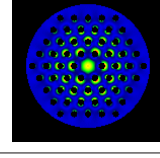
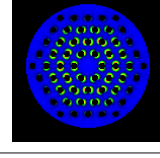
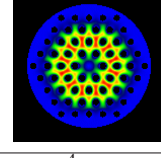
$N_r$	$ E_z $	$ H_z $	$\Re(S_z)$	$ E_z $	$ H_z $	$\Re(S_z)$
1						
	A: $n_{\text{eff}} = 1.38820 + i 5.36^{-3}$			B: $d/\Lambda = 0.75$ , $n_{\text{eff}} = 1.34654 + i 6.47^{-4}$		
2						
	C: $n_{\text{eff}} = 1.38009 + i 3.22^{-3}$			D: $n_{\text{eff}} = 1.39744 + i 1.45^{-3}$		
3						
	E: $n_{\text{eff}} = 1.39117 + i 1.65^{-3}$			F: $n_{\text{eff}} = 1.40110 + i 6.30^{-4}$		
4						
	G: $n_{\text{eff}} = 1.38658 + i 1.54^{-3}$			H: $d/\Lambda = 0.75$ , $n_{\text{eff}} = 1.34668 + i 1.11^{-11}$		
4						
	I: $n_{\text{eff}} = 1.39638 + i 8.89^{-4}$			J: $n_{\text{eff}} = 1.40285 + i 3.23^{-4}$		

Figure 6.1: Selection of MOF modes with increasing number of rings. Except for frames B and H all field maps are for  $d/\Lambda = 0.45$ . All modes belong to the symmetry class 1. ( $\lambda = 1.55\mu\text{m}$ ,  $\Lambda = 2.3\mu\text{m}$ .)

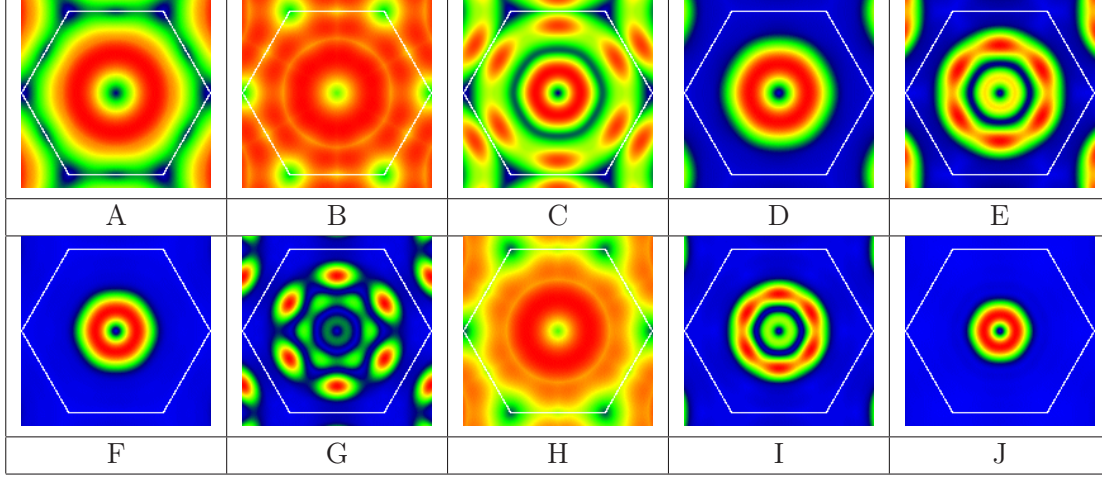


Figure 6.2: Total Bloch transform of the modes of Fig. 6.1.

rings, as the tunneling width increases. “Better confined” modes should therefore somehow be associated with lower losses. The examples of modes G and J contradict this intuition, and raise the question of the definition of a “confined” mode when all modes are leaky.

### 6.2.3 Using the Bloch Transform

Fig. 6.2 shows the total Bloch transform of the modes shown in Fig. 6.1. Admitting that the shape of the Bloch transform is characteristic of a mode, it now appears that modes A, D, F and J are of the same type, and that the modes in frames B and H were indeed of the same type as the one in frame A for a different hole size. Note that in this example the criterion of the mode being the one with the lowest losses within the symmetry class 1 identified the modes correctly, but other examples not shown here have proven that the order of mode losses within a symmetry class is not a reliable criterion for identifying modes. The criterion of field distribution to identify modes, however, seems completely unreliable: as shown in this example, the field distribution of a mode with increasing  $N_r$  can change drastically. To investigate this further and check the validity of the Bloch transform criterion, we attempted to turn  $N_r$  into a continuous parameter (Section 6.3), by adding to a structure with  $N_r$  rings an additional ring with inclusions having a refractive index going progressively from  $n_M$  to 1. Following the modes through this transformation gave us insights in how modes change when rings are added. Two distinct behaviours emerged, leading to the notions of defect modes and space-filling, edge dominated modes.

## 6.3 Continuous Growth of Rings

Starting from an arbitrary<sup>4</sup> structure of air holes in silica, with  $N_r = 1$ ,  $\Lambda = 2.3\mu\text{m}$  and  $d/\Lambda = 0.15$ , we defined structures with increasing  $N_r$ . For each value of  $N_r$  we defined 6 structures differing only by the refractive index of the inclusions of the outer ring, taking the values  $n_i$  with  $i$  ranging from 0 to 5 and the values of  $n_i$  given in Table 6.1. The values

<sup>4</sup>We chose  $d/\Lambda$  to have an *a priori* single-mode fibre, according to Birks *et al.* [60], with the aim of finding a difference in behaviour between the fundamental and the second mode when increasing  $N_r$ .

$n_0$	$n_M (1.444023621818)$
$n_1$	1.428729141173
$n_2$	1.373481986377
$n_3$	1.222011810851
$n_4$	1.070541635325
$n_5$	1.015294480530

Table 6.1: Values of the refractive index of the inclusions of the outer ring.  $n_0$  is the refractive index of silica at  $\lambda = 1.55 \mu\text{m}$ .

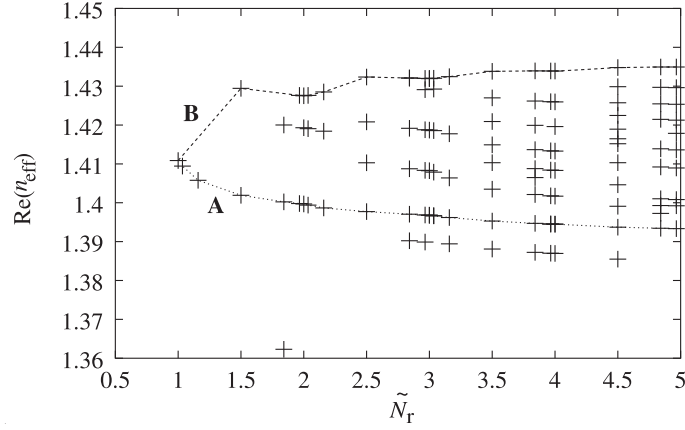


Figure 6.3: Real part of  $n_{\text{eff}}$  of modes of symmetry class 1 as a function of the corrected number of rings  $\tilde{N}_r$

were chosen following a sigmoid distribution between  $n_M$  and 1, so that the steps between refractive indices are smaller near the extrema, as we suspected that the most radical changes would happen when the inclusion “appeared” out of nowhere, the number of inclusions being suddenly increased. We computed the modes for each of these structures at  $\lambda = 1.55 \mu\text{m}$ , and followed the mode trajectories in  $n_{\text{eff}}$  space. To reflect the introduced continuity of  $N_r$ , we define, for a structure with  $N_r$  layers of true holes (having refractive index 1) surrounded by a layer of inclusions with index  $n_i$ , the *corrected number of rings*  $\tilde{N}_r$  as:

$$\tilde{N}_r = N_r + 1 - \frac{n_i - 1}{n_M - 1} . \quad (6.2)$$

### 6.3.1 Mode Trajectories and Identification

Fig. 6.3 and 6.4 show the real and imaginary part respectively of the effective indices of modes of symmetry class 1 as a function of the corrected number of rings. We first note that, as expected, the number of modes found in the  $n_{\text{eff}}$  region used increases with the number of rings. Expecting a smooth behaviour of  $n_{\text{eff}}$  with  $\tilde{N}_r$  for each mode, we also note that some modes seem to be missing for a few values of  $\tilde{N}_r$ , reflecting the fact that the number of points computed in the initial determinant map was not large enough. Refining the determinant map in the regions where modes are missing would give us these modes, but it turned out that the available modes were enough for the intended study. Using figures 6.3 and 6.4 we tried to follow mode trajectories with increasing  $\tilde{N}_r$  to identify modes. This led straightforwardly to

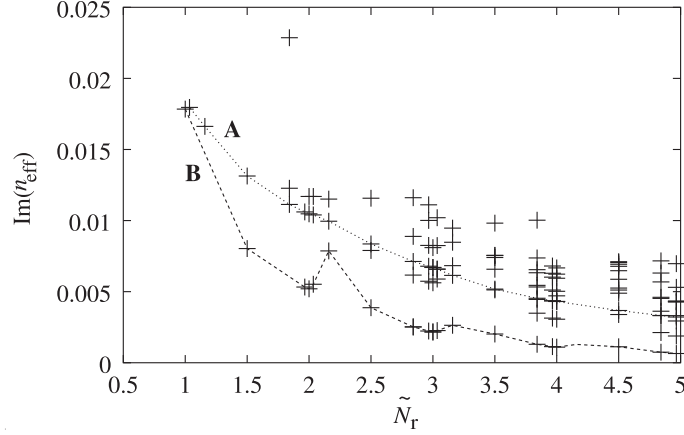


Figure 6.4: Imaginary part of  $n_{\text{eff}}$  of modes of symmetry class 1 as a function of the corrected number of rings  $\tilde{N}_r$

the trajectory marked *A* in both figures, corresponding to modes depicted in Fig. 6.5, which shows clearly that the shape of the total Bloch transform is conserved. From the analysis of the Bloch transform we also established trajectory *B*, which does not seem as “smooth” as trajectory *A*, and would probably not have been found considering solely the mode trajectories. Fig 6.6 shows the modes of trajectory *B*: their Bloch transform is centrosymmetric, showing an annulus around the center. This kind of Bloch transform can not be explained in terms of a mode resulting from a discrete superposition of Bloch waves, and is therefore very likely to be linked to the defect, although it seems not confined in the defect.

Another example of a mode which seems to be linked to the defect is the fundamental mode, shown in Fig. 6.7. The fundamental mode is defined as the one having the largest  $\Re(n_{\text{eff}})$  of all modes, and has also the lowest loss.<sup>5</sup> For the considered structures, it is a degenerate pair of modes of symmetry classes 3 and 4. In contradiction to the previous modes, for which the field distributions were extending over the whole cladding structure regardless of the number of rings, the fundamental mode remains confined near the core with increasing  $N_r$ . Its total Bloch transform shows a single peak centered on the origin, which implies a zero Bloch vector: this implies that all multipolar coefficients are in phase, but as we have seen in Chapter 5, the finite extent of the mode is related to Fourier-Bessel coefficients decaying away from the defect, so that the mode is not a single Bloch wave but must be a defect mode.

### 6.3.2 Evolution of Mode Properties

As mentioned above, the mode trajectories *A* and *B* in Fig. 6.3 and 6.4 differ in the fact that trajectory *A* is relatively smooth, whereas trajectory *B* shows peaks in the real and imaginary parts of  $n_{\text{eff}}$  between two integer values of  $\tilde{N}_r$ . These ripples in the trajectories are also found for the fundamental mode. To investigate this further and analyse the decrease of losses with  $\tilde{N}_r$  we followed the mode of trajectory *A* and the fundamental mode with increasing  $\tilde{N}_r$  up to  $\tilde{N}_r = 10$ . Fig. 6.8 shows the mode trajectories we obtained. Along the whole trajectory the fields of mode *A* extend over the entire cladding region, whereas the fields of the fundamental

<sup>5</sup>The fact that the fundamental mode has the lowest losses was observed in all examples studied. Nevertheless we are not aware of any theorem which would prove that this is the case for all imaginable MOF structures.

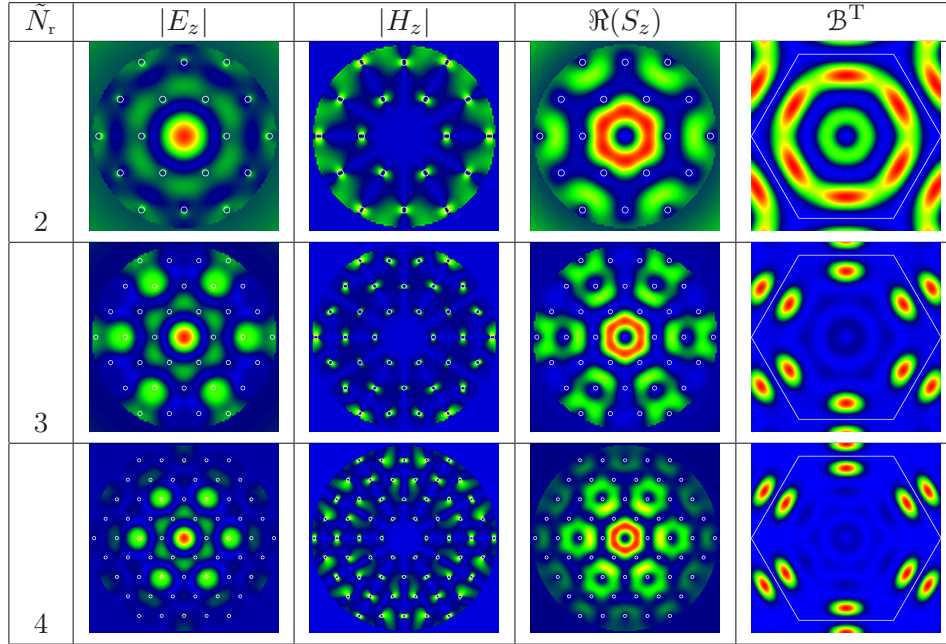


Figure 6.5: Modes of trajectory A of Figs. 6.3 and 6.4.

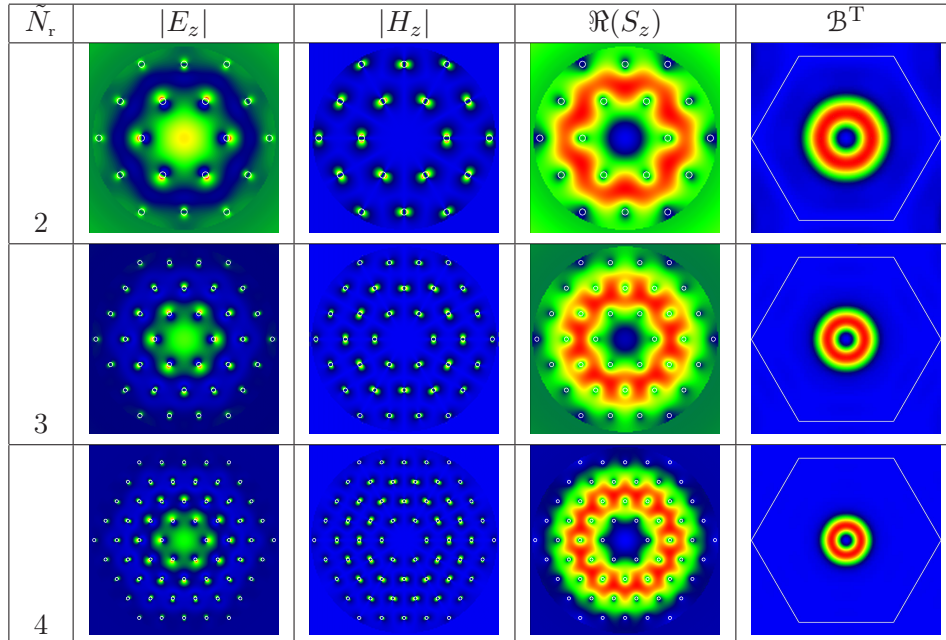


Figure 6.6: Modes of trajectory B of Figs. 6.3 and 6.4.

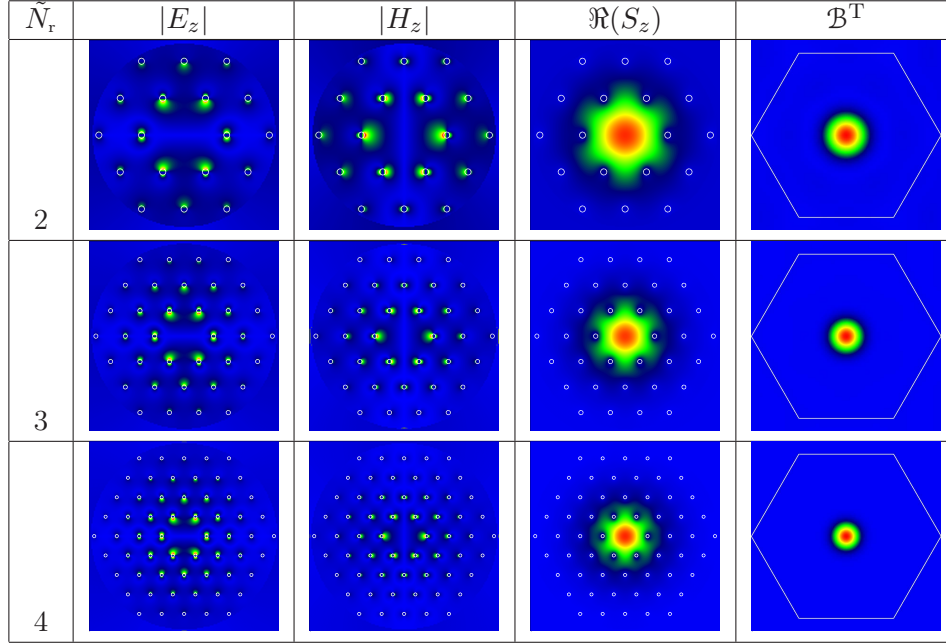


Figure 6.7: Fundamental mode of the same structures as in Figs. 6.5 and 6.6. The modes shown are of symmetry class 4, their degenerate counterpart of symmetry class 3 not being shown.

mode remain confined around the core. For a confined mode one would expect to have an exponential decrease of the losses with  $N_r$ .

First we only take into account integer values of  $\tilde{N}_r$  (in which case  $N_r = \tilde{N}_r$ ). The decrease of the losses with  $N_r$  seems *almost* exponential for both modes for  $N_r > 5$ , where the loss curves in the semi-log plot are almost straight lines. Analyzing the same curves in a log-log plot and fitting them to exponential or power rule functions showed that the decay of losses can not be described by either of these functions. We will understand in Chapter 7 that this results from an unfortunate choice of fibre parameters, but that losses of confined modes generally decay exponentially with  $N_r$ , whereas extended modes have a more complex decay which can locally be approximated by a power law.

We now consider all values of  $\tilde{N}_r$ : The ripples in the trajectories between two integer values of  $\tilde{N}_r$  exist for both modes studied, although they are much stronger for the fundamental mode. It was quite surprising at first to see that adding a layer of lower index inclusions, *i.e.* increasing the effective thickness of the confining structure, results at first in an *increase* of the losses. This effect can be explained invoking an index matching effect: when the outer inclusions have a higher index than air, the outer layer has an averaged index which lies between that of the jacket and that of the cladding, which can result in index matching behaviors similar to anti-reflection coatings. The losses then decrease only if the effect of increasing the thickness of the confining structure is more important than the index matching effect. With the interpretation used, it can be predicted that an exterior layer with smaller holes could also increase the losses. As experimental MOFs tend to have smaller holes in the outer layers because of the drawing process, it is worth checking this effect. To do so, we added to a two layer structure a third layer of holes with different diameters. Fig 6.9 shows the imaginary part of  $n_{\text{eff}}$  as a function of  $d_e/d$ , where  $d_e$  is the diameter of the holes in the outer layer, and  $d$  is the diameter of all

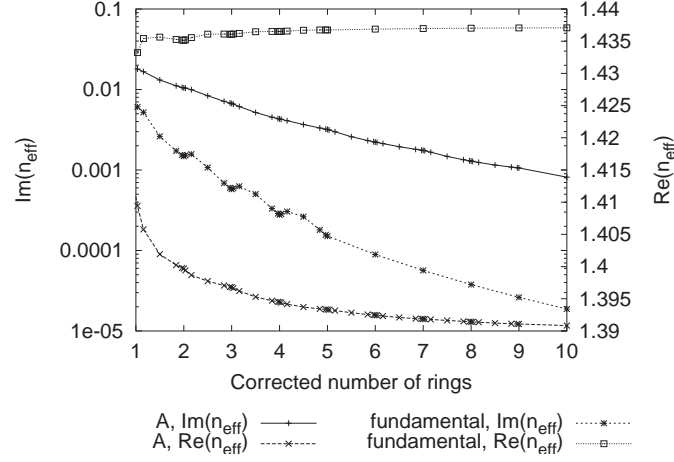


Figure 6.8: Real and imaginary part of  $n_{\text{eff}}$  as a function of the corrected number of rings for the fundamental mode and the mode of trajectory A in Figs. 6.3 and 6.4.

other holes. We see that when adding a ring with increasing hole size, the losses increase at first before decreasing towards the value of the losses for a larger number of rings. It is worth noting that in the case shown, the holes on the outer layer need to be at least half as large as the other holes before an actual decrease of the losses can be expected.

### 6.3.3 Extended and Localized Modes

Other modes found for the fibres all entered in one of the categories illustrated above: they all appeared to be either modes resulting from a discrete superposition of Bloch waves or to be defect modes which could be localized or space filling.

The first kind of modes seems to result from a superposition of Bloch waves selected by resonance conditions between the borders of the cladding structure. The properties of those modes should be largely unaffected by the presence, absence or nature of the defect, but must be sensitive to the exact shape of the cladding structure's boundaries. By increasing the size of the shape by an integer number of layers, these modes remain, although the resonating Bloch vectors can change slightly. The fields of these modes extend over the whole cladding, regardless of the number of layers. These modes will not have an exponential decay of the losses with the number of layers. We will call these modes *extended modes*.

The second kind of modes, the localized defect modes, must be quite sensitive to the nature of the defect. Their fields decay away from the defect, they are likely to have an exponential decay of the losses with increasing number of rings, and if the boundaries of the cladding are *far enough* away from the core, their properties should be largely independent of the shape of the cladding's boundaries.

The remaining modes, appearing to be defect modes from their Bloch transform but which extend in the whole cladding region, seem less well defined; they are certainly dominated by the limits of the MOF structure as their fields reach the cladding boundaries, but it is not clear how far they are indeed defect dependent. We will see in the Chapter 7 that these modes, when varying the MOF parameters, can undergo a cutoff transition to become localized defect modes. We will therefore call these modes *extended transition modes*.

The interpretation of the modes in terms of Bloch waves or defect modes can be easily

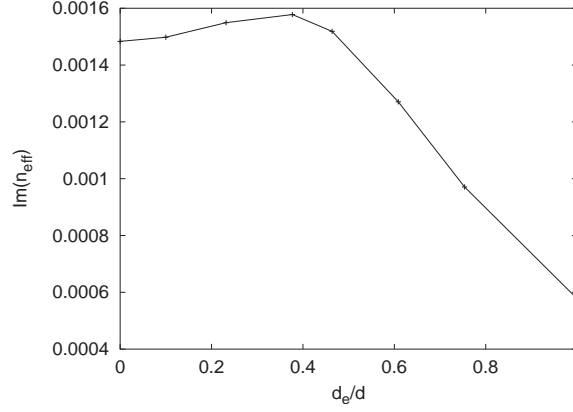


Figure 6.9: Imaginary part of  $n_{\text{eff}}$  for a structure with two rings of holes of diameter  $d = 0.15\Lambda$  and a third ring of holes of diameter  $d_e$ .  $\Lambda = 2.3 \mu\text{m}$ ,  $\lambda = 1.55 \mu\text{m}$ . The point at  $d_e/d = 0$  corresponds to the structure with two rings only.

checked by varying the boundaries of the cladding, or by altering the defect as the following experiments show.

### Shape Dependence

To check the mode dependence on the shape of the boundaries of the cladding structure, we tried to find similar modes to the ones studied above for structures with same fibre parameters but with different cladding boundaries. Fig. 6.10 shows the fundamental mode in a MOF with three different cladding boundaries. Note that in the rectangular and non-symmetric cases the degeneracy is lifted and two almost degenerate fundamental modes coexist, of which only one is shown. As expected for a localized defect mode, the fields, the Bloch transform and the effective index change only slightly for the different cladding shapes.

In contrast, the extended mode A used in the previous paragraphs does not survive intact when the boundaries of the cladding are changed. Fig. 6.11 shows the modes found for the considered structures which are most similar to mode A: note that the peaks of the Bloch transform have similar positions in the Brillouin zone for all modes shown, but that some peaks are missing, and that the new configuration of peaks now respects the symmetry of the cladding boundaries rather than the symmetries of the lattice. For the rectangular cladding boundary we could find two modes for which the Bloch transform peaks are a subset of the Bloch transform peaks of mode A, but as these modes are not degenerate, their superposition is not a mode of the MOF. Note also that the changes in effective index between the modes for the different structures are much more important for these modes than for the fundamental mode.

### Defect Dependence

Fig. 6.12 shows mode A for a MOF with 5 rings of holes, with and without defect: the fields as well as the effective index are only very slightly altered by the presence or absence of the defect. Fig. 6.12 also shows the same mode for a structure with a displaced defect. The mode is not affected by the position of the defect. As predicted, this kind of mode depends mainly

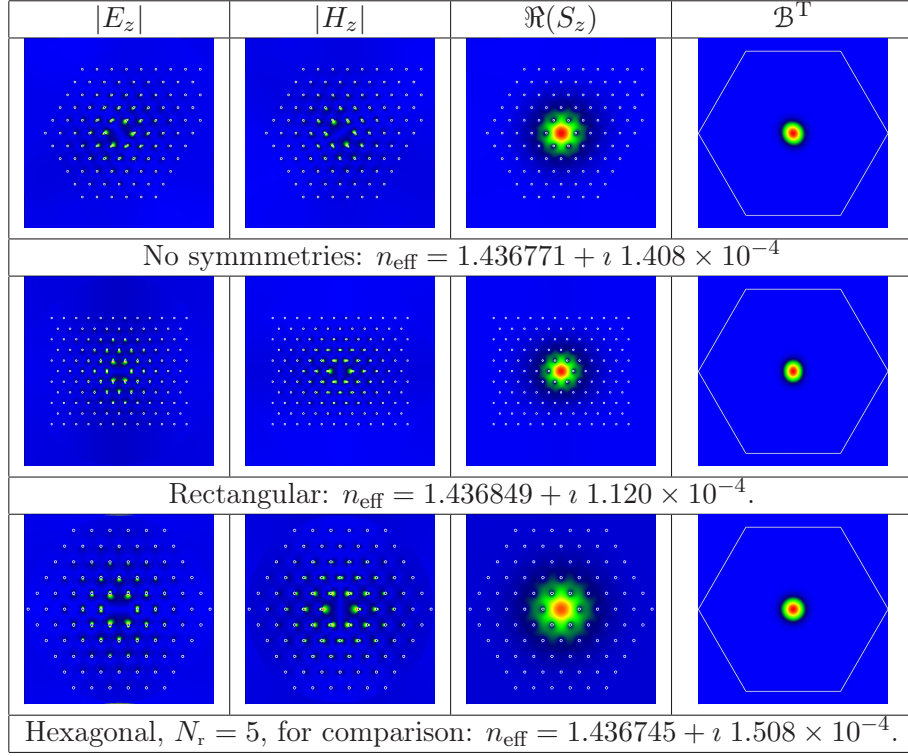


Figure 6.10: Fundamental mode for MOFs with different cladding shapes. For all structures  $\Lambda = 2.3 \mu\text{m}$ ,  $d/\Lambda = 0.15$ ,  $\lambda = 1.55 \mu\text{m}$ .

on the boundaries of the cladding structure, and is only weakly affected by defects.

Fig. 6.13 shows the fundamental mode for a MOF with 5 rings of holes, with and without defect, as well as the fundamental mode of a MOF with 6 rings of holes and a displaced defect. When there is a defect, the mode remains localized around it. In the absence of a defect, the mode fills almost the entire fibre and becomes an extended mode. In this example, the difference in  $n_{\text{eff}}$  between the mode in a MOF with and without defect is surprisingly small for both the real and the imaginary part. As we mentioned earlier the choice of fibre parameters for these example was somewhat unfortunate, and we will see in Chapter 7 that for other fibre parameters the defect becomes vital for defect modes.

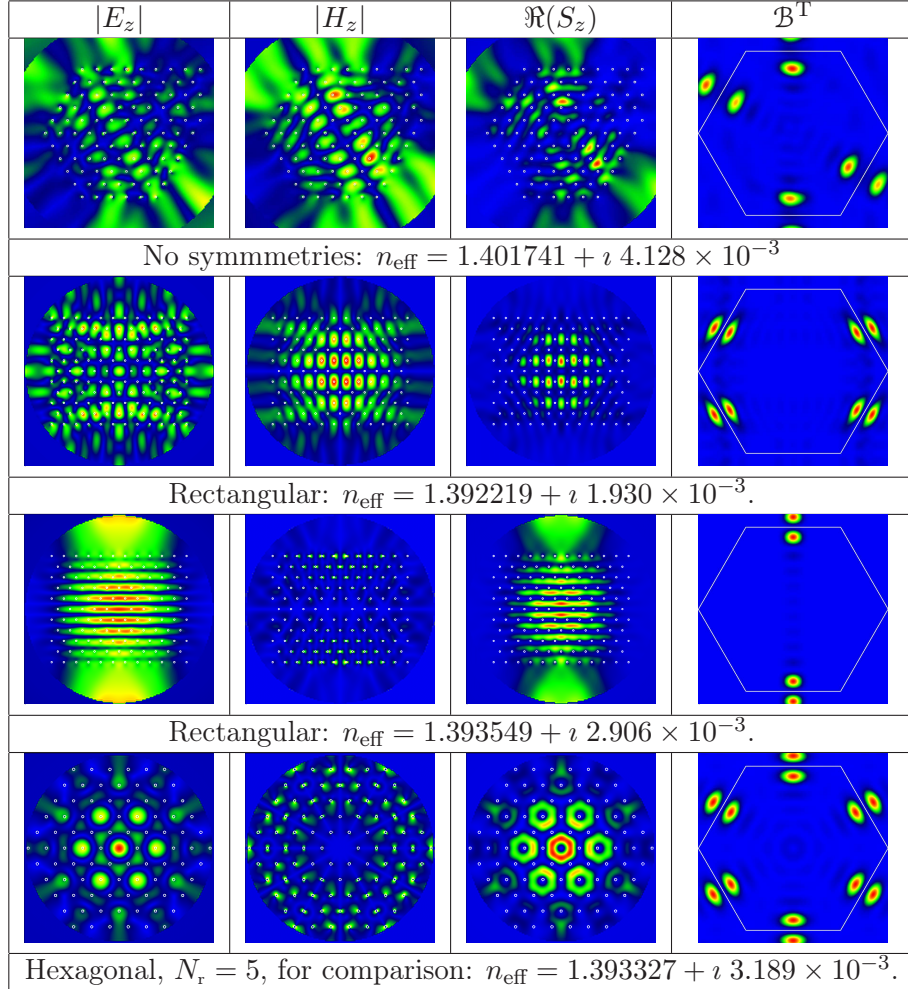


Figure 6.11: Modes equivalent to mode A for MOFs with different cladding shapes. For all structures  $\Lambda = 2.3 \mu\text{m}$ ,  $d/\Lambda = 0.15$ ,  $\lambda = 1.55 \mu\text{m}$ .

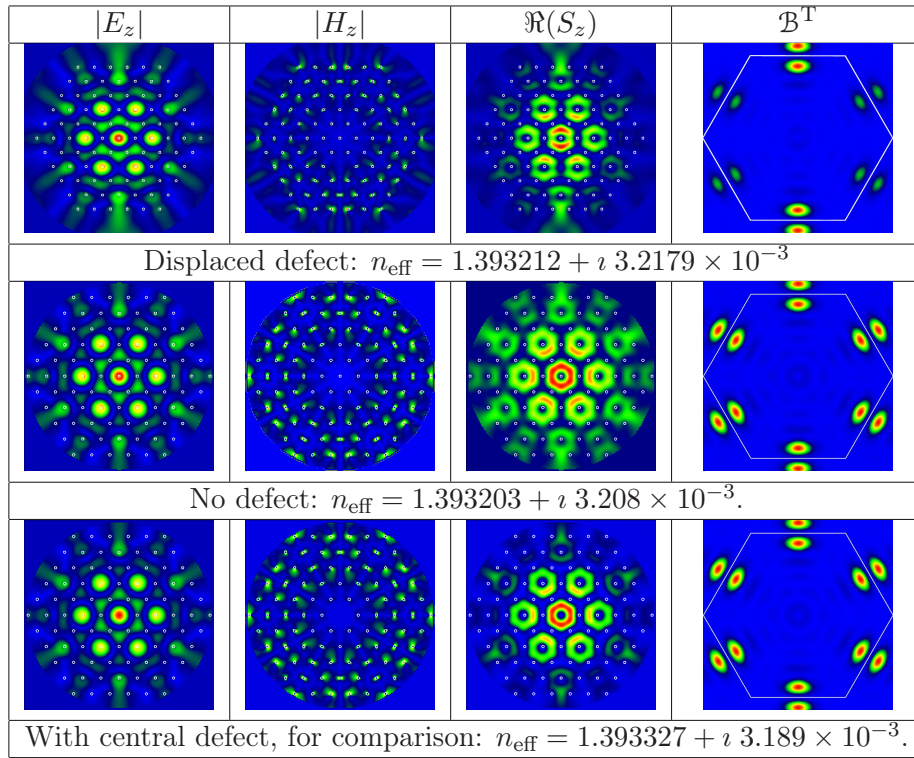


Figure 6.12: Modes equivalent to mode A for MOFs with a central defect, a displaced defect or no defect at all. For all structures  $\Lambda = 2.3 \mu\text{m}$ ,  $d/\Lambda = 0.15$ ,  $\lambda = 1.55 \mu\text{m}$ .

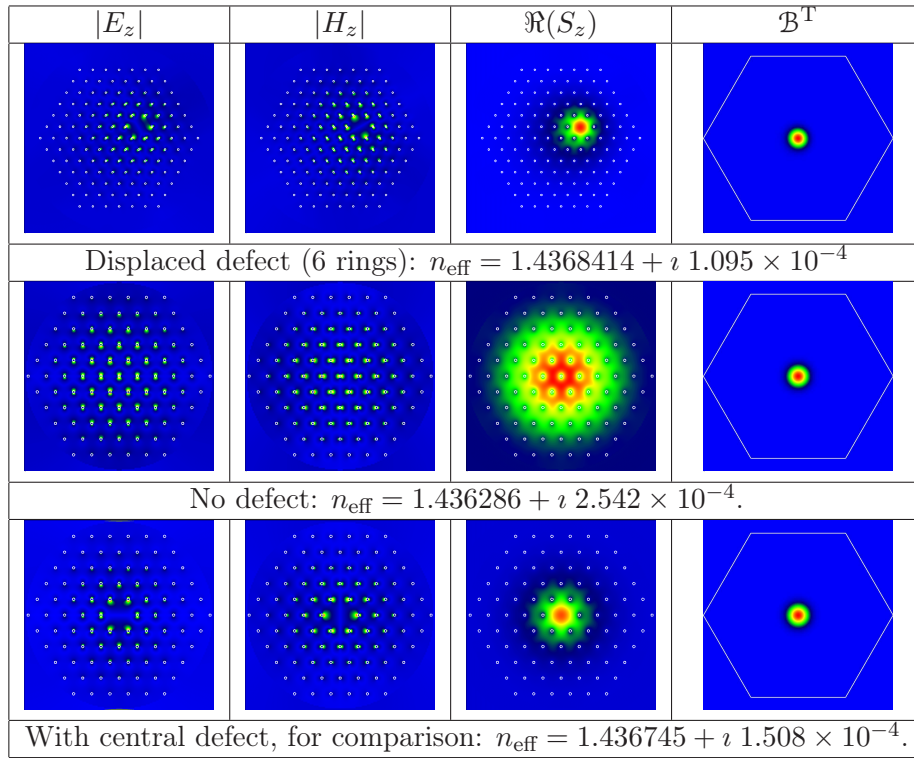


Figure 6.13: Fundamental mode for MOFs with a central defect, a displaced defect or no defect at all. For all structures  $\Lambda = 2.3 \mu\text{m}$ ,  $d/\Lambda = 0.15$ ,  $\lambda = 1.55 \mu\text{m}$ .

Fromage :

## Chèvre Frais, Raisin Chasselas, Tuile au Thé Vert

*Goat's Cheese, Chasselas Grape, Green Tea Tuile*

### Pour 6 personnes :

*500 g de chèvre frais  
500 g de raisins chasselas*

Pour les tuiles

*30 g de farine  
125 g de sucre glace  
50 g de beurre  
15 g d'amandes effilées  
20 g de thé vert*

**P**ELER et épépiner les raisins. Détailler le chèvre frais en 6 tronçons de 8 cm de diamètre et 1 cm de haut. Hacher très grossièrement le raisin.

**H**ACHER finement la moitié du thé vert. Laisser infuser l'autre moitié dans 50 g d'eau frémissante. Laisser refoirir. Faire fondre le beurre. Hacher grossièrement les amandes effilées. Meler la farine et le sucre glace dans une jatte. Ajouter les amandes et le thé vert haché, puis incorporer peu à peu en fouettant l'infusion de thé vert passée au chinois, puis le beurre. Laisser prendre au frais.

**D**ÉPOSER des tas d'une cuillerée à café de cette préparation sur une plaque de cuisson recouverte de papier cuisson. Veiller à bien espacer ces tas. Enfourner au four préchauffé à 160°C. Laisser cuire 7 à 8 minutes, jusqu'à brunissement partiel. Laisser refroidir une dizaine de secondes, puis détailler des disques de 8 cm de diamètre à l'emporte pièce. Conserver au sec.

**R**ECOUVIR chaque disque de fromage de chèvre d'une couche de concassée de chasselas, et disposer par dessus une tuile au thé vert. Servir sans attendre.

## Chapter 7

# Modal Cutoff

*Some results of this Chapter have been published in Refs. [94] and [95].*

### 7.1 Introduction

One of the earliest known and most exciting properties of MOFs is that they can be endlessly single-mode [60]. However, as we have mentioned earlier, a MOF where a finite number of rings of holes is solely responsible for the confinement of light carries an infinite number of modes, all of which are leaky. From the beginning of our work we wanted to understand how this apparent contradiction could be lifted. Our first approach [84] was to consider the relative losses of modes: If losses of the different modes of a MOF are such that after a given length of propagation all modes except for one have faded away, the MOF can be considered to be single-mode for that length of propagation. Such a definition of single modedness was unsatisfactory in several ways: not only does it depend on the actual length of propagation, but it also depends on the number of rings of holes. Indeed we have mentioned (and will study in more detail in the present Chapter) that the losses of all modes decrease with the number of rings, so that for an infinite number of rings no MOF can be single-mode. We have also seen that some modes fill the entire cladding, so that for an infinite number of rings they become completely delocalized, which is far from what is generally understood as being a propagating mode of a fibre. This will lead us to consider a new, more restrictive definition of a MOF mode, taking into account something resembling a “degree of confinement”. Our approach to investigate those concepts was to consider a confined higher order mode of an “obviously” multimode MOF, in which more than two modes having low losses are strongly confined in the core, and track this mode while changing as continuously as possible the MOF parameters towards those of a MOF being endlessly single-mode according to Birks *et al.* [60]. Doing so we were able to identify a cutoff for the second mode, and clarify the endlessly single-mode regime predicted by Birks *et al.* Out of curiosity, we undertook the same kind of study for cladding filling modes and for the fundamental mode, and discovered that the fundamental mode undergoes a cutoff as well. However, the cutoff of the fundamental mode turned out to be somewhat different in nature from the cutoff of the second mode. Using analytic asymptotic models we gained further understanding of the nature and importance of the cutoff, and isolated a subregion of the MOF parameter space in which interesting MOF properties are most likely to be found.

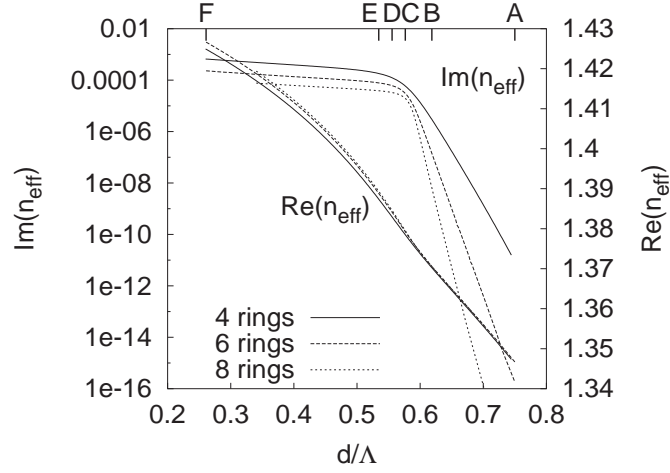


Figure 7.1: Real and imaginary part of the effective index of the first mode of symmetry class 1 as a function of  $d/\Lambda$ . Letters A-F mark the positions of the frames of Fig. 7.2.  $\Lambda = 2.3 \mu\text{m}$ ,  $\lambda = 1.55 \mu\text{m}$ .

## 7.2 Modal Cutoff of the Second Mode

### 7.2.1 Towards the Endlessly Single-Mode Fibre

As mentioned in the introduction, we started our studies through analysing the changes a confined higher order mode of a multimode MOF undergoes when the MOF parameters are continuously modified towards those of a single-mode structure. To do so we considered three structures with  $\Lambda = 2.3 \mu\text{m}$ ,  $d/\Lambda = 0.75$  and  $N_r = 4, 6$  and  $8$ , at a wavelength of  $1.55 \mu\text{m}$ , and followed the first confined mode of symmetry class 1 while reducing  $d/\Lambda$  down to a value of  $0.25$ .<sup>1</sup> By the first mode of symmetry class 1 we mean the mode of symmetry class 1 with the highest real part and lowest imaginary part of  $n_{\text{eff}}$ .<sup>2</sup> When confined in the core, it is similar<sup>3</sup> to the  $\text{TM}_1$  mode of conventional fibres. With all classes of symmetry taken together, it is, for this particular MOF, the third mode in descending order of  $\Re(n_{\text{eff}})$ ,<sup>4</sup> the second mode being a mode of symmetry class 2 we will consider later in this Chapter. Note that according to Birks *et al.* [60] below  $d/\Lambda \simeq 0.4$  the MOF should be endlessly single-mode, so that the mode considered should no longer be guided. Fig. 7.1 shows the real and imaginary parts of  $n_{\text{eff}}$  as a function of  $d/\Lambda$ , while Fig. 7.2 shows the power density plots and total Bloch transforms for  $E_z$  and  $H_z$  for different values of  $d/\Lambda$  for the 6 ring MOF.

Fig. 7.1 shows a dramatic change of slope of the imaginary part of  $n_{\text{eff}}$  as a function of  $d/\Lambda$  around  $d/\Lambda \simeq 0.6$ . This change of slope is accompanied by a sudden increase in the mode

<sup>1</sup>To follow the mode with varying diameter or pitch we used the method described in section 4.4. Particular care was taken to check that the observed behaviour did not result from mode crossing.

<sup>2</sup>We have mentioned earlier that mode crossing does occur in MOFs, so that this definition is ambiguous. Nevertheless it is not ambiguous when the fibre is “obviously multimode”, *i.e.* when several modes are obviously well confined in the core. The mode crossing only occurs between modes which are not well confined. Note that the definition of “confined” is detailed in the present Chapter.

<sup>3</sup>*cf.* Appendix H. Field maps of this mode can be found in Fig. 6.6.

<sup>4</sup>As already mentioned several times, the order of  $\Re(n_{\text{eff}})$  can not be used to classify modes, as mode crossings occur: for the MOF studied in Section 4.5.1 the third mode in order of  $\Re(n_{\text{eff}})$  is of classes of symmetry 5 and 6 (*cf.* Table 4.1).

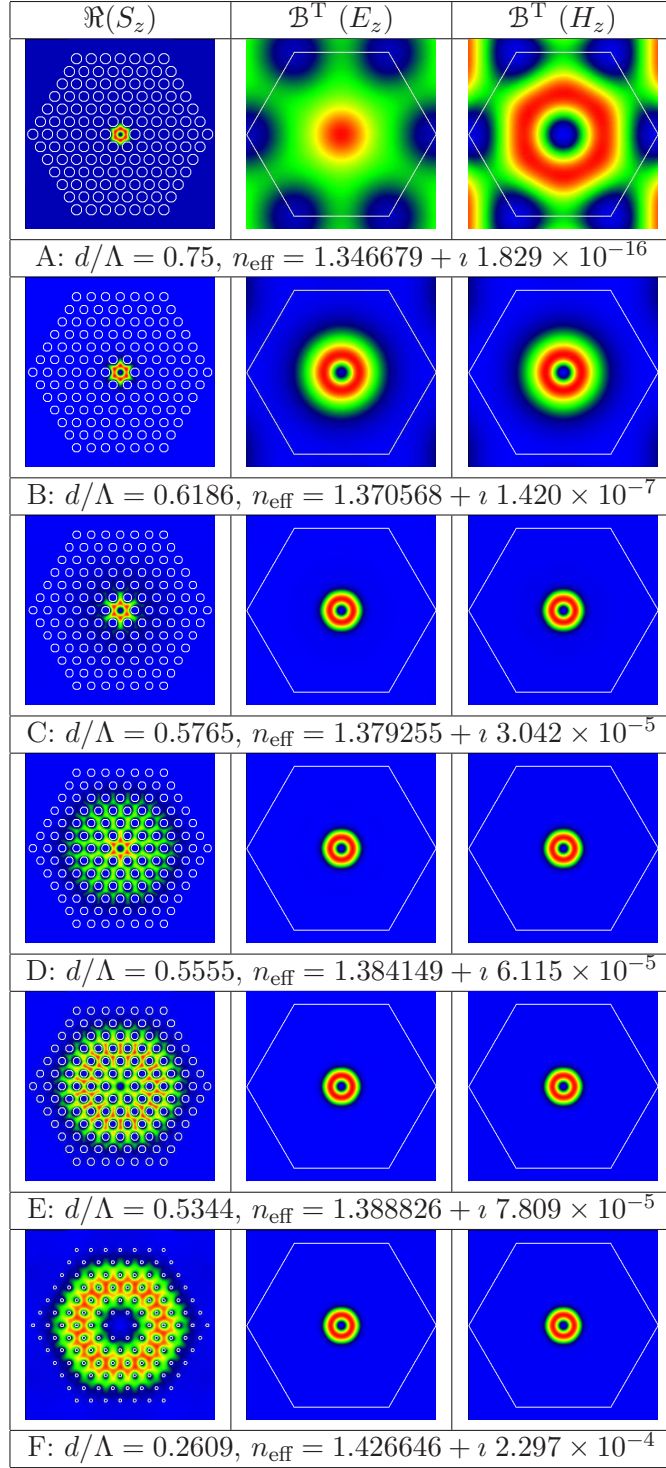


Figure 7.2: Carried power density and total Bloch transforms of the first mode of symmetry class 1 for several values of  $d/\Lambda$  along Fig. 7.1. Letters A-F refer to the points marked on Fig. 7.1. Note that the Bloch transforms for  $E$  and  $H$  are very different in frame A, which results from the fact that, when localized, the mode is monopole dominated (*cf.* Chapter 5, footnote 6).

size (Fig. 7.2, frames B to E), marking a transition between confined and cladding filling states, whereas the mode shape and size remain stable with varying  $d/\Lambda$  on either side of this transition. We note further that for  $d/\Lambda \lesssim 0.6$ , when the mode fills the entire cladding, the real part of  $n_{\text{eff}}$  depends on  $N_r$ , whereas this doesn't seem to be the case when the mode is well confined in the core. The dependence of the imaginary part on  $d/\Lambda$  on the contrary seems less affected by the value of  $N_r$  when the mode fills the cladding than when it is confined in the core, resulting in an increased sharpness of the change of slope with increasing  $N_r$ . Note that the value of  $d/\Lambda$  where the transition occurs doesn't seem to change with  $N_r$  – we will study this in more detail in section 7.2.3.

These observations lead to the hypothesis that going from a “multimode” MOF towards a “single-mode” MOF by reducing  $d/\Lambda$ , the actual total number of modes is not altered, but that confined higher order modes undergo a transition towards an unconfined, cladding filling state. A single-mode MOF would then be a MOF in which only the fundamental mode is confined, all other modes being cladding filling.

### 7.2.2 Characterization of the Transition – Definition of Cutoff

From the preceeding comments it seems that defect modes can be in two states: one in which the fields are confined in the core, and another in which the fields extend over the whole cladding region. The transition occurring between these states is somewhat reminiscent of the modal cutoff of conventional fibres,<sup>5</sup> which occurs either when varying fibre parameters (core size or index) or when varying the wavelength. We have observed the transition when varying  $d/\Lambda$  at fixed  $\lambda/\Lambda$ , but the value of  $d/\Lambda$  at which the transition occurs will depend upon  $\lambda/\Lambda$ . Conversely at fixed  $d/\Lambda$  we expect to observe a similar transition when varying  $\lambda/\Lambda$ , at least when the MOF is not endlessly single-mode.

In this section we study in more detail the transition of the technologically more important *second mode*<sup>6</sup> occurring at fixed  $d/\Lambda$  when varying  $\lambda/\Lambda$ . We vary the latter quantity through changing the pitch and keeping the wavelength constant at  $\lambda = 1.55 \mu\text{m}$  so that the refractive index of silica keeps a constant value of  $n_M = 1.444024$ , and will do so throughout this Chapter. Note that since  $\lambda$  is constant,  $\Im(n_{\text{eff}})$  and the geometric loss coefficient are directly proportional and we will use the word losses as a synonym for  $\Im(n_{\text{eff}})$ .

In Fig. 7.3, we display a number of characteristic fibre parameters as a function of  $\lambda/\Lambda$ , for a geometry with  $d/\Lambda = 0.55$ . First, the loss is shown for 4, 8 and 10 ring geometries (curves (1) to (3)), with the transition becoming more acute with an increasing number of rings, but remaining at a fixed  $\lambda/\Lambda$  ratio. To make the transition more evident, we have calculated the second derivative of the logarithm of the loss with respect to the logarithm of the pitch ( $\mathcal{Q}$ ) (curve 4).

$$\mathcal{Q} = \frac{d^2 \log(\Im(n_{\text{eff}}))}{d \log(\Lambda)^2} \quad (7.1)$$

This exhibits a sharp negative minimum giving an accurate value for the transition. Next, we

<sup>5</sup>Note that this transition also reminded us of Anderson localization transitions in random media and Mott conductor/insulator transitions, but the analogies with these phenomena remain to be elucidated.

<sup>6</sup>Similarly to what we did for the third mode, we define the second mode as the mode which, in an “obviously multimode” MOF (*i.e.* where more than one mode is obviously confined) has second highest  $\Re(n_{\text{eff}})$  and second lowest  $\Im(n_{\text{eff}})$ . The second mode is of class of symmetry 2. When it is confined in the core it is similar to the  $\text{TE}_1$  mode of conventional fibres, *cf.* Appendix H.

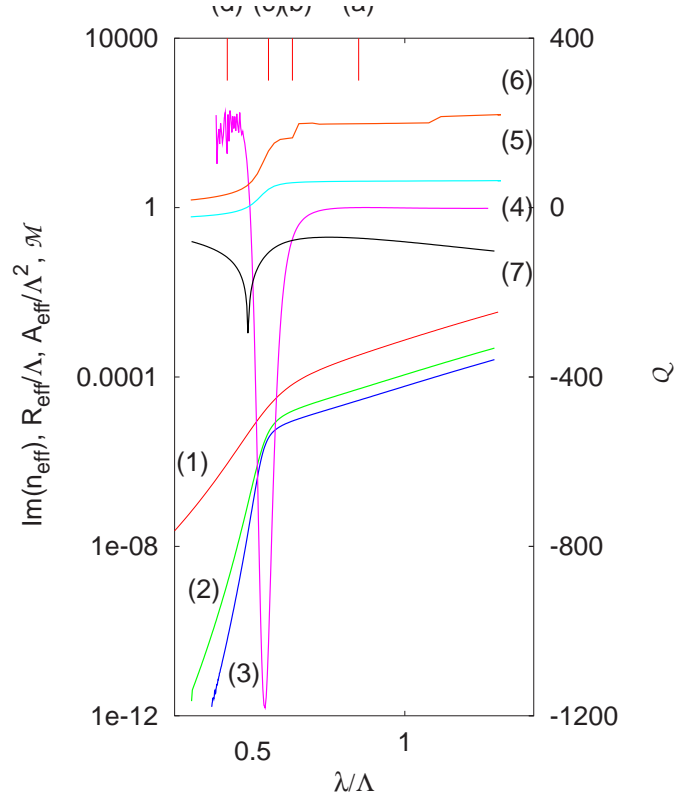


Figure 7.3: Variation of different physical quantities during the transition, for a MOF with  $d/\Lambda = 0.55$  used at  $\lambda = 1.55 \mu\text{m}$ . Curves (1) to (3) are  $\Im(n_{\text{eff}})$  for 4, 8 and 10 rings, curves (4) to (7) are  $Q$ ,  $R_{\text{eff}}/\Lambda$ ,  $A_{\text{eff}}/\Lambda^2$  and  $\mathcal{M}$  as defined in the text, for  $N_r = 8$ . The points (a-d) indicate the position of the field plots of Fig. 7.4.

show the normalized effective radius  $R_{\text{eff}}/\Lambda$  (curve 5) where

$$R_{\text{eff}} = \frac{\iint r^2 S_z(r, \theta) dr d\theta}{\iint r S_z(r, \theta) dr d\theta}, \quad (7.2)$$

with  $S_z$  denoting the real part of the component along the fibre of the Poynting vector, and the normalized effective area [4]  $A_{\text{eff}}/\Lambda^2$  (curve 6), where

$$A_{\text{eff}} = \frac{(\iint |E|^2 d\mathbf{r})^2}{\iint |E|^4 d\mathbf{r}}. \quad (7.3)$$

In both cases the integrals are taken over the structured cross section of the fibre only, because for leaky modes, the fields diverge at infinity [3]. Parameters  $R_{\text{eff}}/\Lambda$  and  $A_{\text{eff}}/\Lambda^2$  change, respectively, by 1 and 2 orders of magnitude at the transition, with the effective area curve being less smooth due to numerical errors.

The last indicative quantity  $\mathcal{M}$  (7) shown in Fig. 7.3 is the ratio of the magnetic field monopole coefficient ( $B_0^{(\text{H})}$ ) to the magnetic field dipole coefficient ( $B_1^{(\text{H})}$ ) for a cylinder in the first ring of the MOF geometry. This exhibits a well defined minimum just below the transition, at which the magnetic field is almost exclusively dipolar.

In Fig. 7.4 we show the spatial variation of the fields for the mode above (a) during (b,c) and below (d) the transition. Above the transition (a), the mode is well described (*cf.* Chapter 6 and Ref. [68]) as a space-filling cladding resonance. Its electric and magnetic fields are predominantly dipolar around each inclusion, and the magnitude of the Poynting vector decreases to small values in smooth fashion both at the center and near the edge of the MOF structure. During the transition, its  $S_z$  distribution rapidly contracts (b,c), before stabilizing in a localized state (d). It is worth noting that when localized, the losses seem to decrease exponentially with the number of rings, whereas when the mode is space-filling, the decrease follows a power law; we will study the dependency of the losses on  $N_r$  in more detail in section 7.2.3.

According to Fig. 7.3, the nature of the mode changes quantitatively and qualitatively in a well defined narrow region. We identify this with the cutoff of the mode.

All the quantities used in Fig. 7.3 can be used to define a cutoff point, either through the locus of their minimum ( $\mathcal{Q}$ ,  $\mathcal{M}$ ) or through the locus of the extrema of their derivatives ( $A_{\text{eff}}/\Lambda^2$ ,  $R_{\text{eff}}/\Lambda$ ). We have found that  $\mathcal{Q}$  is in fact the most sensitive indicator of the transition, and we will keep the locus of this minimum as a definition of the locus of the cutoff; an asymptotic analysis of the transition (section 7.4) will underpin this choice. In what follows the locus of the cutoff will refer to the locus of the  $\mathcal{Q}$  minimum.

### 7.2.3 Scaling Properties

In the previous sections we have seen that the locus in parameter space where the cutoff occurs doesn't seem to depend on  $N_r$ , and further that the width of the transition decreases with increasing  $N_r$ . We also noted that the losses as a function of  $N_r$  follow different rules in the two different states of the mode. In this section we study these observations in more detail.

#### Cutoff Locus

Fig. 7.5 shows the locus of the transition of the second mode of three MOF designs with different  $d/\Lambda$ , as a function of  $N_r^{-b_2}$ .  $b_2$  is an arbitrary positive coefficient adjusted to get

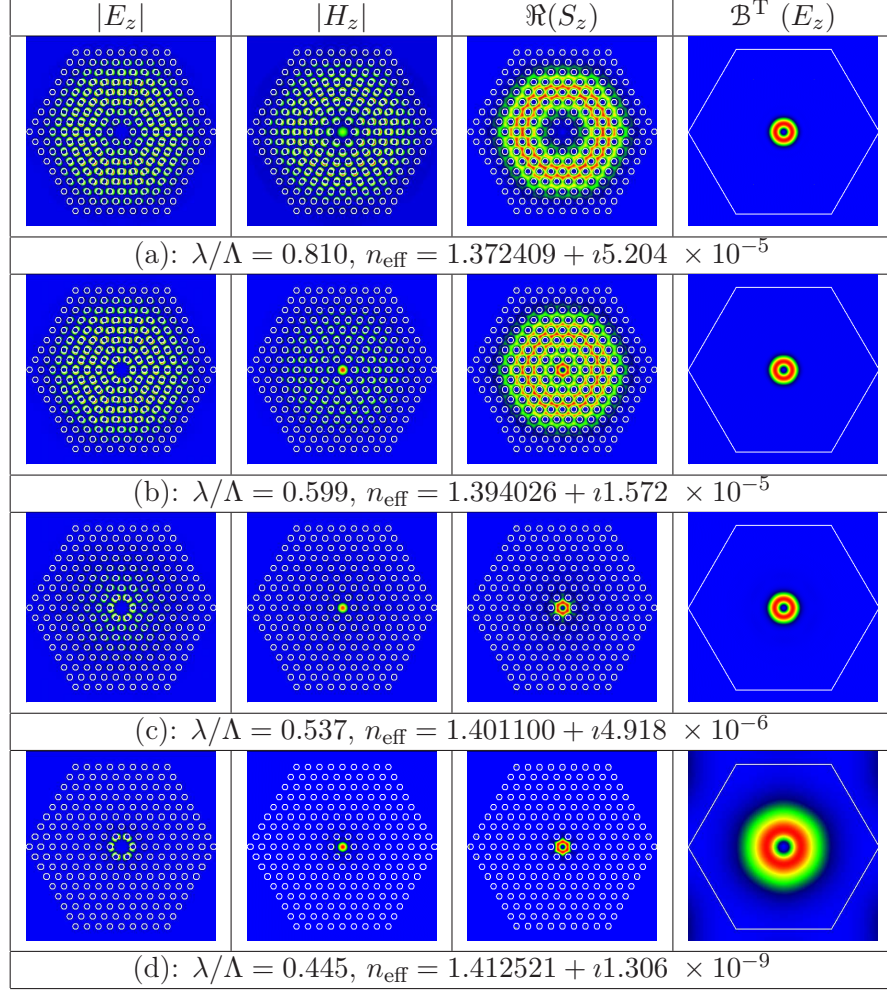


Figure 7.4: Field distributions and total Bloch transform of the second mode across the transition. The letters in brackets refer to the points marked on Fig. 7.3. For all structures  $d/\Lambda = 0.55$ ,  $\lambda = 1.55 \mu\text{m}$ .

the best straight-line behaviour of the datasets. We see that the locus of the cutoff slightly depends on  $N_r$ , but that it seems to converge when  $N_r$  approaches infinity (*i.e.* when  $N_r^{-b_2}$  approaches 0). The conclusion we draw from this observation is twofold: Firstly, the cutoff is not an artefact resulting from the finite cross section of the fibre but an intrinsic property of the mode, secondly the locus of the cutoff obtained for finite values of  $N_r$  is a reasonable approximation for the locus of the cutoff for any value of  $N_r$ .<sup>7</sup>

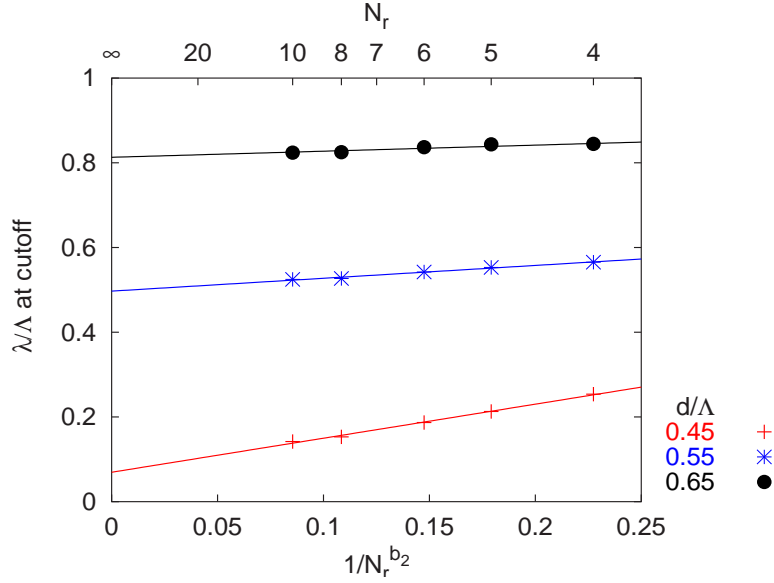


Figure 7.5: Normalized wavelength at cutoff as a function of  $N_r^{-b_2}$  for the second mode, for three values of  $d/\Lambda$ . Here  $b_2 \simeq 1.07$ . The cutoff wavelength clearly converges with increasing  $N_r$ .

### Transition Width and Sharpness

Fig. 7.6 shows, for the same MOF structures as in Fig. 7.5, the half-width of the peak of  $\mathcal{Q}$  as a function of  $N_r^{-b_2^w}$ , where  $b_2^w$  is again an arbitrary positive coefficient adjusted to obtain the best straight-line behaviour of the datasets. Regardless of  $d/\Lambda$ , the peak becomes narrower with increasing  $N_r$  and tends to an infinitely narrow peak when  $N_r$  approaches infinity. Note that simultaneously the magnitude of the peak increases. To illustrate this, we define the quantity  $\mathcal{J}$  as the half-width multiplied by the magnitude of the minimum, a quantity roughly proportional to the area of the peak and therefore to the change of slope of  $\log(\Im(n_{\text{eff}}))$  as a function of  $\log(\Lambda)$  between the confined and unconfined states. Fig. 7.7 shows the inverse of  $\mathcal{J}$  as a function of  $N_r^{-b_2^s}$ , where the positive coefficient  $b_2^s$  has been adjusted for the best straight-line behaviour of the datasets.  $1/\mathcal{J}$  approaches zero when  $N_r$  approaches infinity, in other words the change of slope of the transition becomes infinite when the system size becomes infinite. Fig. 7.8 shows an enlargement of the preceding figure (yet with slightly different  $b_2^s$ ) to demonstrate the divergence of  $\mathcal{J}$  for  $d/\Lambda$  values of 0.55 and 0.65.

<sup>7</sup>Note that conclusions concerning large ( $N_r > 10$ ) and infinite number of rings in this section result from extrapolations and cannot be considered as being rigorously proven.

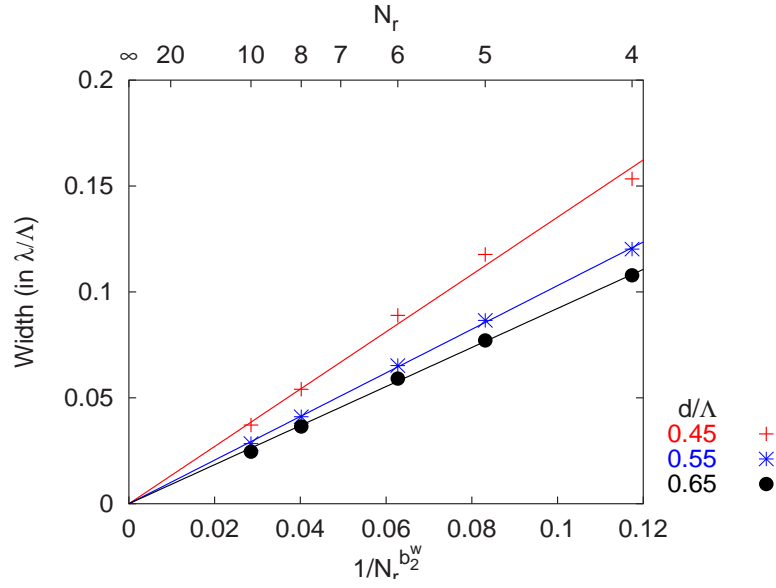


Figure 7.6: Width of the cutoff of the second mode as a function of the number of rings for three different values of  $d/\Lambda$ . The depicted quantity is the half-width of the  $\mathcal{Q}$  peak as a function of  $N_r^{-b_2^w}$ . Here  $b_2^w \simeq 1.55$ . The width of the cutoff transition goes to zero with increasing number of rings.

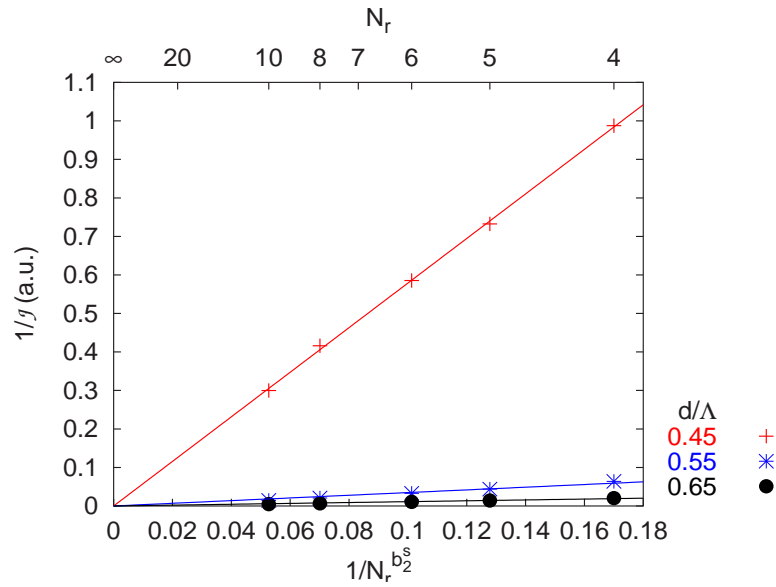


Figure 7.7:  $1/\mathcal{M}$  as a function of  $N_r^{-b_2^s}$  for three different values of  $d/\Lambda$ . Here  $b_2^s \simeq 1.28$ .

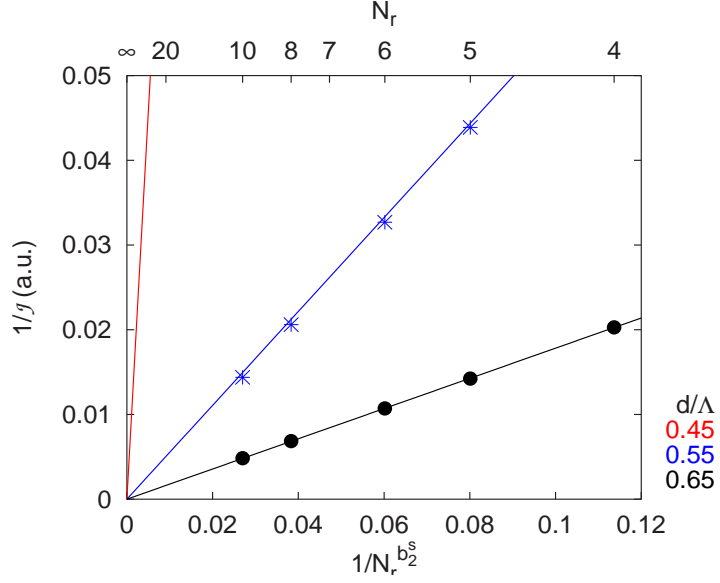


Figure 7.8: Enlargement of an equivalent of Fig. 7.7, but with  $b_2^s \simeq 1.57$ .

### Losses

Figs. 7.9 and 7.10 show the imaginary part of the effective index as a function of the number of rings for the second mode of a MOF with  $d/\Lambda = 0.55$ , for two different values of  $\lambda/\Lambda$ . The values of  $\lambda/\Lambda$  have been chosen so that the mode is clearly in the confined ( $\lambda/\Lambda = 0.378$ ) or unconfined ( $\lambda/\Lambda = 1.50$ ) states. In the confined state, the losses clearly decrease exponentially with  $N_r$  as is illustrated by the straight-line behaviour in the semi-logarithmic plot of Fig. 7.9. The curve superimposed on the data points shows the result of a fit to an exponential decay function

$$\Im(n_{\text{eff}}) = a \exp(-bN_r) . \quad (7.4)$$

The fit is excellent and gives  $a \simeq 9.923 \times 10^{-4} \pm 0.4\%$  and  $b \simeq 2.443 \pm 0.05\%$ . In the unconfined state, the losses do not decay exponentially: the points in the semi-logarithmic plot of Fig. 7.9 are not in a straight line. The fact that they are on a straight line in a logarithmic representation (Fig. 7.10) suggests they follow a power law. The curve superimposed to the data points for the unconfined mode results from a best fit with a power law of the type

$$\Im(n_{\text{eff}}) = cN_r^{-d} . \quad (7.5)$$

The fit is not as good as the previous one but still more than satisfactory (and by far better than a fit with an exponential decay function applied to the same data). We obtain  $c \simeq 0.121 \pm 3.8\%$  and  $d \simeq 2.65 \pm 1\%$ .

### Conclusions and Interpretation in terms of Band Diagrams

In the confined state, the second mode is well localized in the defect and losses decay exponentially with the number of rings. In the cladding filling state the mode extends across the whole structured region of the MOF, and the decay of losses with the number of rings roughly follows a power law. The locus of the transition between these states, which we identify with

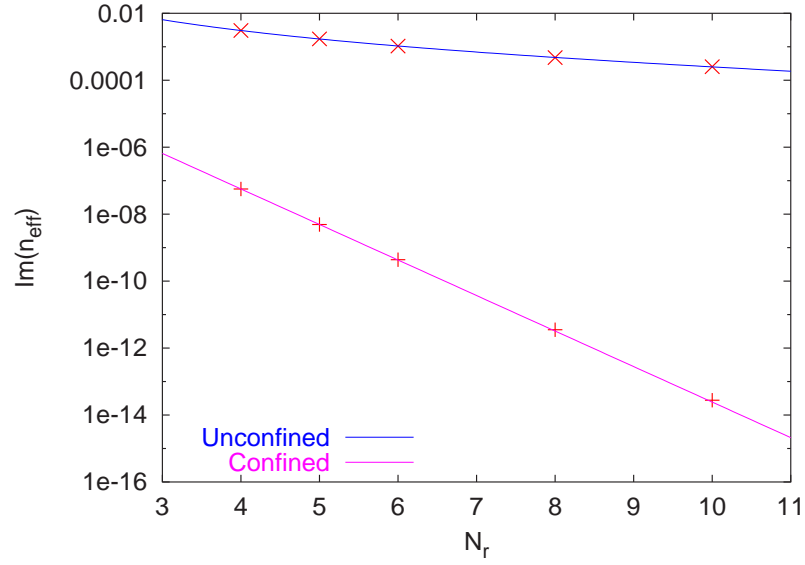


Figure 7.9: Imaginary part of the effective index as a function of the number of rings, for the second mode of a MOF with  $d/\Lambda = 0.55$  in the confined ( $\lambda/\Lambda = 0.378$ ) and unconfined ( $\lambda/\Lambda = 1.50$ ) states with  $\lambda = 1.55 \mu\text{m}$ . The  $y$ -axis is in logarithmic scale, whereas the  $x$ -axis is linear.

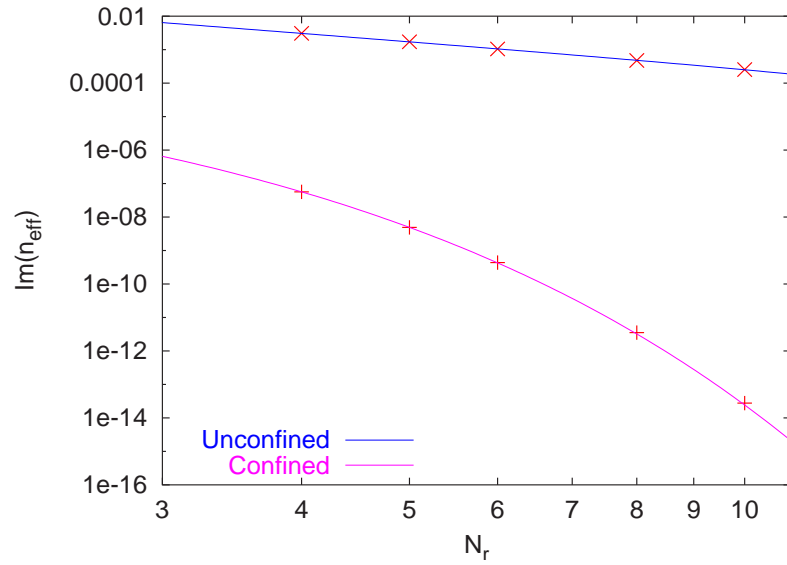


Figure 7.10: Same as Fig. 7.9, but with logarithmic scales on both axes.

the cutoff of the mode, is largely independent of the number of rings, but the transition becomes increasingly sharp when adding rings of holes. The phenomenon we identify as the cutoff is intrinsic to the mode and not due to the finite size of the system. Note that in the case of a MOF with infinite number of rings, *i.e.* a single defect in an infinite photonic crystal, the mode in its extended state would fill the entire photonic crystal, and would therefore be identified with a mode of one of the bands of the photonic crystal, whereas when confined the mode would be identified as a defect mode, its propagation constant being necessarily in a photonic bandgap. In terms of band diagrams, the transition we observe is one between a state with propagation constant in a bandgap and one with propagation constant in a band [96]. Indeed, we could verify that the transition occurs when  $n_{\text{eff}} \simeq n_{\text{FSM}}$ , where  $n_{\text{FSM}}$  is the effective index of the fundamental space filling mode [97] *i.e.* the largest effective index a mode propagating in the infinite photonic crystal can have.

### 7.2.4 Second Mode “Phase Diagram”

Now that we have seen that the cutoff is an intrinsic property of the second mode, it makes sense to try to establish a map of the locus of the cutoff in parameter-space. With that in mind, we carried out the studies introduced in section 7.2.2 for 8-ring MOFs with 14 values of  $d/\Lambda$  ranging from 0.405 to 0.75.<sup>8</sup> The resulting loss curves are shown in Fig. 7.11. The transition remains sharp for  $d/\Lambda > 0.45$ , whereas for  $d/\Lambda < 0.45$  the transition becomes more and more gradual, disappearing entirely at around  $d/\Lambda \simeq 0.40$ . We established the loci of

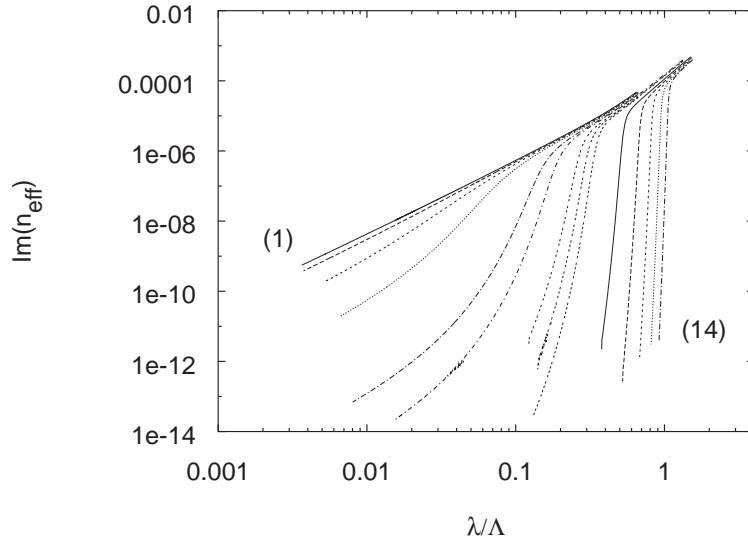


Figure 7.11:  $\Im(n_{\text{eff}})$  as a function of wavelength/pitch, for a structure of 8 rings of holes in silica at a wavelength of  $\lambda = 1.55 \mu\text{m}$  for several diameter-to-pitch ratios.  $\Im(n_{\text{eff}})$  decreases monotonically with increasing  $d/\Lambda$ , as this parameter takes the values 0.40 (1), 0.41, 0.42, 0.43, 0.45, 0.46, 0.48, 0.49, 0.50, 0.55, 0.60, 0.65, 0.70, 0.75 (14).

the transition using all the mentioned criteria; the results are summarized on Fig. 7.12. This

<sup>8</sup>Note that for selected values of  $d/\Lambda$  we also carried out studies with  $N_r$  ranging between 3 and 10, which confirmed the results of the previous section.

figure can be seen as a “*phase diagram*” of the second mode: The  $(d/\Lambda, \lambda/\Lambda)$  parameter space is partitioned by the cutoff curve; the mode is in a confined state in the lower right partition, and in an unconfined state elsewhere.

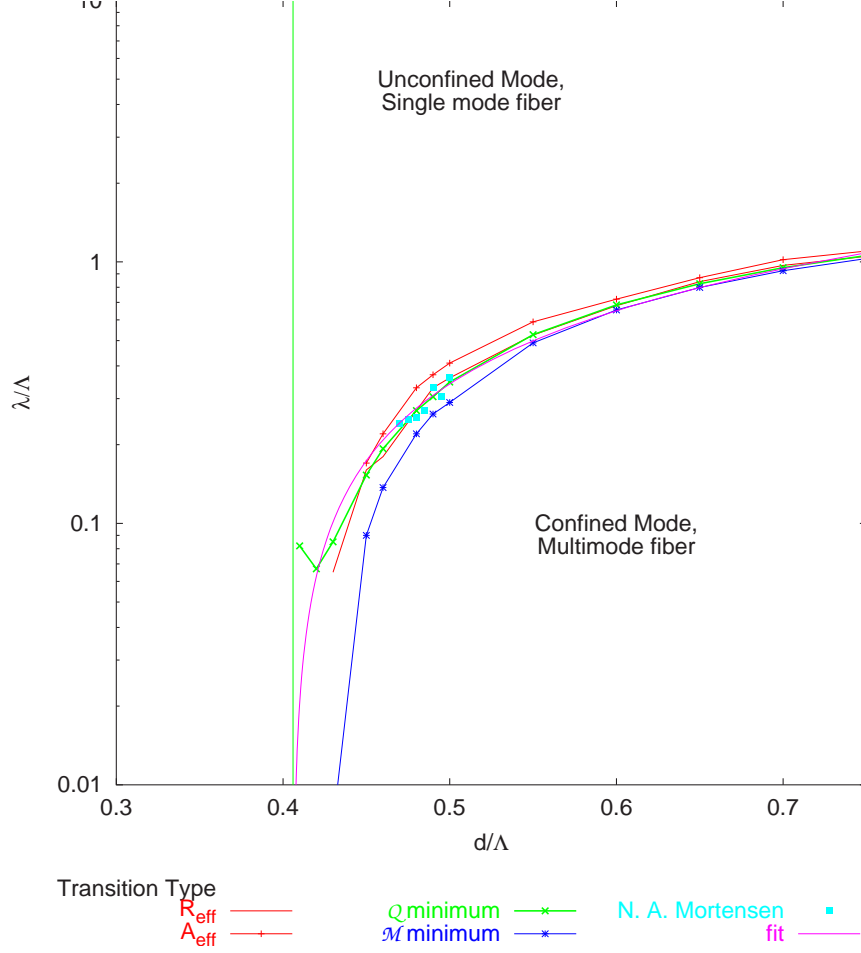


Figure 7.12: Phase diagram of the second mode. The different curves correspond to different definitions of the transition point. The dotted curve shows the fit from Eq. (7.7). The squares represent the values for the cutoff published by N. A. Mortensen in Ref. [98]. In the upper region the fundamental mode is the only one confined in the defect, which corresponds to a single-mode regime. In the lower region the second mode is confined and the fibre is therefore dual moded. For  $d/\Lambda < 0.45$  the increasing discrepancy of the different definitions is due to the decreasing sharpness of the transition for finite systems. The dashed vertical line shows the approximation to the limit of the endlessly single-mode regime. Note that values used to establish this diagram come from simulations with  $N_r = 8$ .

On Fig. 7.12 we also added points N. A. Mortensen found for the cutoff in Ref. [98] (squares between  $d/\Lambda = 0.47$  and  $d/\Lambda = 0.5$ ). His study, the first to analyse modal cutoff in a fully vector treatment in MOFs, used plane wave methods with the supercell approximation and was based on the sudden increase of the effective area of the second mode. Above  $d/\Lambda = 0.45$ , all criteria agree on a tightly defined transition curve. Below 0.45, the different criteria become individually more or less difficult to apply, because of the decreasing sharpness of the transition

for finite systems.

Quantity  $\mathcal{Q}$  remains a sensitive indicator of the transition down to near the value where the transition ceases to occur. Fig. 7.13 shows the value of  $\mathcal{Q}$  at its minimum as a function of  $d/\Lambda$ . To find the intersection of this curve with the  $x$ -axis, *i.e.* the point where the transition ceases to occur, we fit a power law of the form

$$f(x) = a(x - b)^c \quad (7.6)$$

to this data. Although the fit is not exceptionally good, the range of possible values for  $b$  is quite narrow: we find  $b \simeq 0.406 \pm 0.003$ . Below this  $d/\Lambda$  ratio,  $\mathcal{Q}$  remains positive everywhere: there is no negative  $\mathcal{Q}$  peak. The result of the fit is shown in Fig. 7.14, where we depict the value of  $\mathcal{Q}$  at its minimum as a function of  $d/\Lambda - b$  along with  $f(x + b)$  in a log-log scale. For  $d/\Lambda < 0.406 \pm 0.003$  the second mode is always space filling, the fundamental mode is the only one to be confined,<sup>9</sup> and this regardless of the wavelength: the MOF is endlessly single-mode. Mortensen [98, 99] uses a value of  $d/\Lambda = 0.45$  for the limit of the endlessly

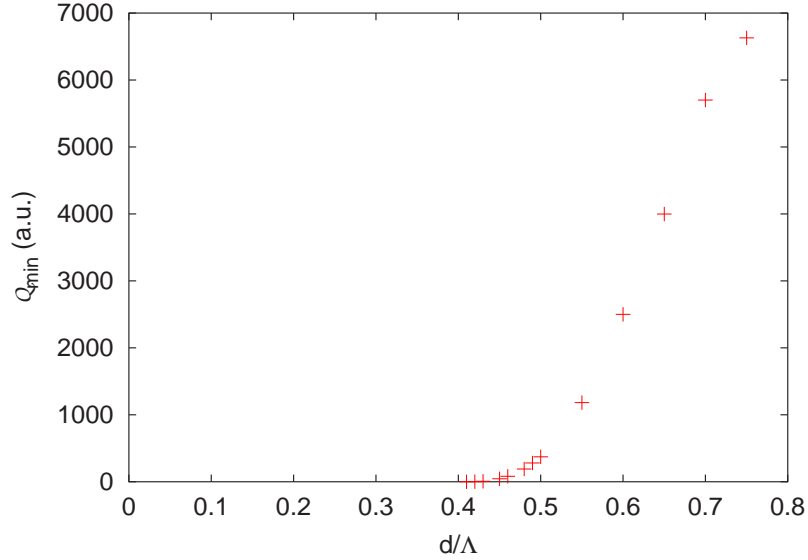


Figure 7.13: Value of  $\mathcal{Q}$  at the cutoff as a function of  $d/\Lambda$ .

single-mode regime, but our investigation is for finite MOF geometries, whereas Mortensen used periodic boundary conditions, and had fewer points to extrapolate this value. A best fit for the data ( $\mathcal{Q}$  minimum) of Fig. 7.12 gives the single mode/dual-mode boundary as

$$\frac{\lambda}{\Lambda} \simeq \alpha(d/\Lambda - 0.406)^\gamma \quad (7.7)$$

with  $\alpha = 2.80 \pm 0.12$  and  $\gamma = 0.89 \pm 0.02$ . Recent experimental work by Folkenberg *et al.* [100] strongly corroborates this cutoff curve. Further, Mortensen *et al.* recently found results in excellent agreement with the above fit using a different theoretical approach, adapting the usual fibre parameter  $V$  to MOFs [101].

<sup>9</sup>The confinement of the fundamental mode will be studied in the next section.

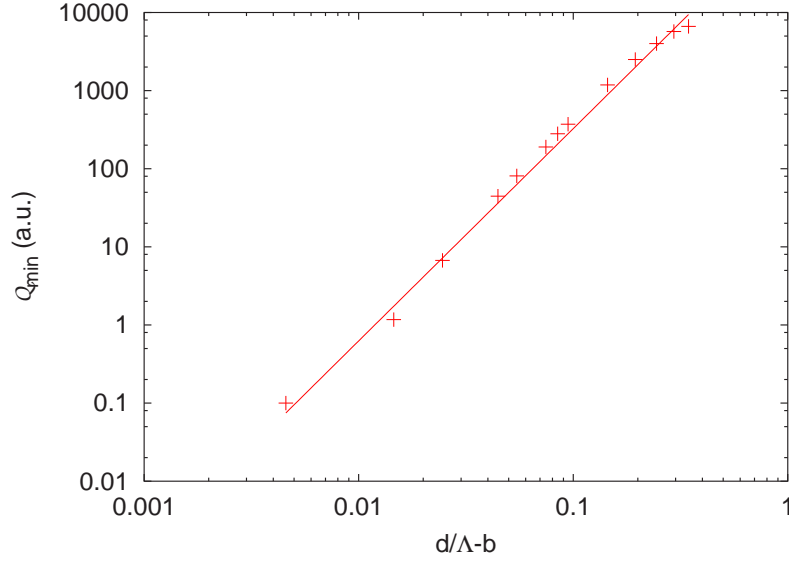


Figure 7.14: Value of  $Q$  at the cutoff as a function of  $d/\Lambda - 0.406$  and corresponding fit.

### 7.3 Modal Cutoff of the Fundamental Mode

Conventional optical fibres are always able to propagate at least one mode: there is no cutoff for the fundamental mode. It is nevertheless a well-known fact that W-fibres can have a cutoff for the fundamental mode [50]. Given the analogies which can be drawn between MOFs and W-fibres, it wouldn't be surprising to find a cutoff for the fundamental mode, at least in MOFs consisting of a finite number of rings of holes. In the case of MOFs with an infinite number of rings (single defect in an infinite photonic crystal) the analogy with W-fibre doesn't hold, and it is difficult to predict *a priori* whether the fundamental mode will undergo a cutoff or not. In this section we show that the fundamental mode undergoes a cutoff at least when  $N_r$  is finite. Using scaling laws we also investigate fundamental mode cutoff properties when  $N_r$  approaches infinity, and find that it is very likely that the fundamental mode undergoes a cutoff even for an infinite number of rings.

#### 7.3.1 Observation of the Cutoff

Figs. 7.15 and 7.16 are the equivalent of Figs. 7.3 and 7.4 for the fundamental mode of a MOF with  $d/\Lambda = 0.3$ . Similarly to what we observed for the second mode, the slope of the curve of the losses as a function of  $\lambda/\Lambda$  in the log-log plot changes rapidly in a narrow region of  $\lambda/\Lambda$  space. This change of slope is accompanied by a rapid variation of the field distributions. For large values of  $\lambda/\Lambda$  the mode has a large effective radius, it is cladding filling, and has high losses only weakly depending on the number of rings. For small values of  $\lambda/\Lambda$  the mode is confined in the core and losses depend more strongly on the number of rings. There are nevertheless differences with the cutoff of the second mode: the dependence of the locus of the transition on the number of rings doesn't seem negligible, and the transition doesn't seem to become infinitely sharp with increasing  $N_r$ . We also observe that quantity  $Q$  goes through a positive peak before having a negative peak. Indeed the slope of the loss curve for  $N_r = 3$  is similar for small (say  $\lambda/\Lambda < 0.2$ ) and large (say  $\lambda/\Lambda > 0.9$ ) values of  $\lambda/\Lambda$ , it is only in the

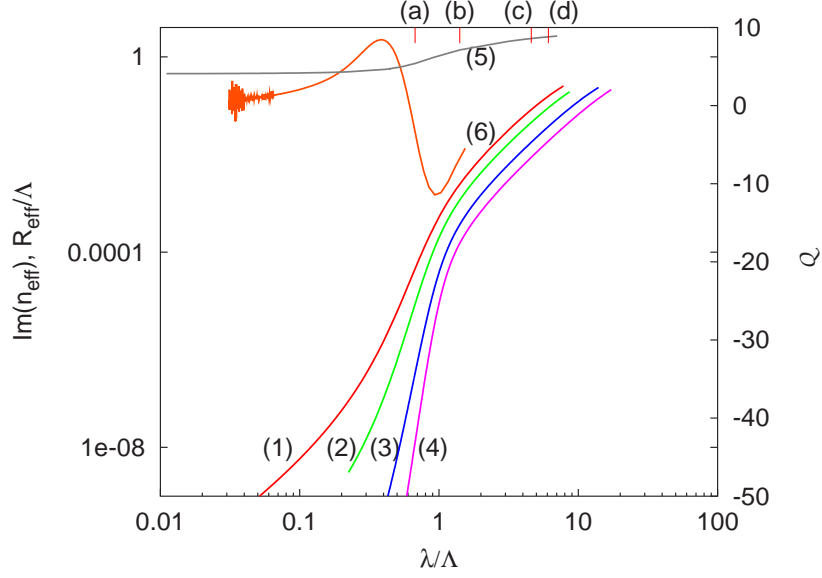


Figure 7.15: Variation of different physical quantities during the transition of the fundamental mode, for a MOF with  $d/\Lambda = 0.3$  used at  $\lambda = 1.55 \mu\text{m}$ . Curves (1) to (4) are  $\Im(n_{\text{eff}})$  for 3, 4, 6 and 8 rings, curves (5) and (6) are  $R_{\text{eff}}/\Lambda$  and  $Q$  for  $N_r = 3$  respectively. The points (a-d) indicate the position of the field plots of Fig. 7.16.

“transition region” (when approximately  $0.2 < \lambda/\Lambda < 0.9$ ) that the slope takes a different, larger value. Note that for the second mode we did not observe this behaviour, but we might have missed a similar phenomenon which could have happened outside the  $\lambda/\Lambda$  domain we investigated in the preceding sections. We will come back to this question in section 7.4.

### 7.3.2 Scaling Properties

Using the same methods as we used for the second mode, we study the behaviour of the locus and sharpness of the transition as well as the losses with increasing number of rings. Similarly to what we have done with the second mode, we concentrate on the negative  $Q$  peak, leaving the study and interpretation of the positive  $Q$  peak to subsequent sections.

#### Locus

We noticed in Fig. 7.15 that the convergence of the locus of the transition with increasing number of rings is not obvious. Indeed, applying the same methods as in Section 7.2.3 doesn’t lead to straightforward conclusions. The locus of the minimum of the negative  $Q$  peak doesn’t seem to converge *a priori* for an infinite number of rings, but the available data doesn’t prove that this locus diverges either. To be able to conclude as to the convergence or divergence of the locus of the  $Q$  peak, we would need the complete  $Q$  curves for values of  $N_r$  larger than 8. Unfortunately these become increasingly difficult to get since losses become so small that the direct evaluation of  $\Im(n_{\text{eff}})$  through the multipole method is impossible, and the indirect evaluation of the losses (*cf.* Ch. 5) doesn’t give a sufficient precision to get an unbiased second derivative. Instead of concentrating solely on the locus of the minimum, we therefore also analysed the behaviour of the loci of the points at which the value of  $Q$  is half the value of

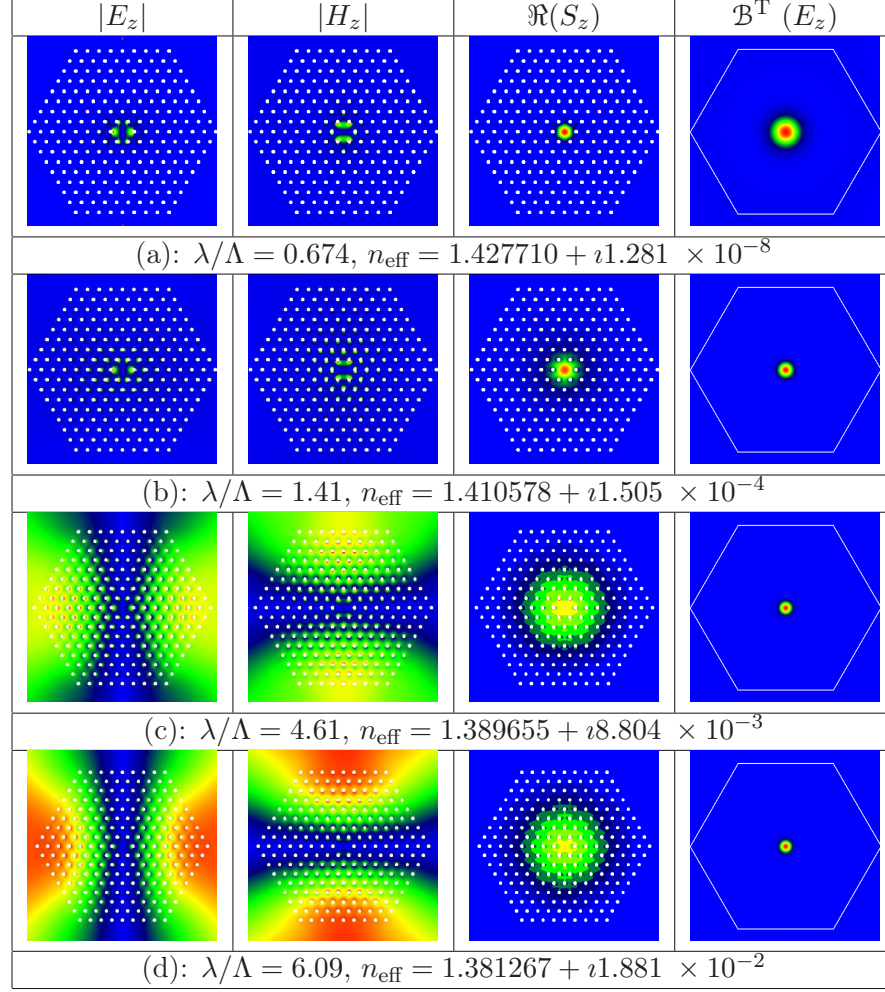


Figure 7.16: Field distributions and total Bloch transform of the fundamental mode across the transition. The letters in brackets refer to the points marked on Fig. 7.15. For all structures  $d/\Lambda = 0.3$ ,  $\lambda = 1.55 \mu\text{m}$ . The divergence of  $E_z$  and  $H_z$  outside the MOF in frames (c) and (d) is due to the high imaginary part of  $n_{\text{eff}}$ .

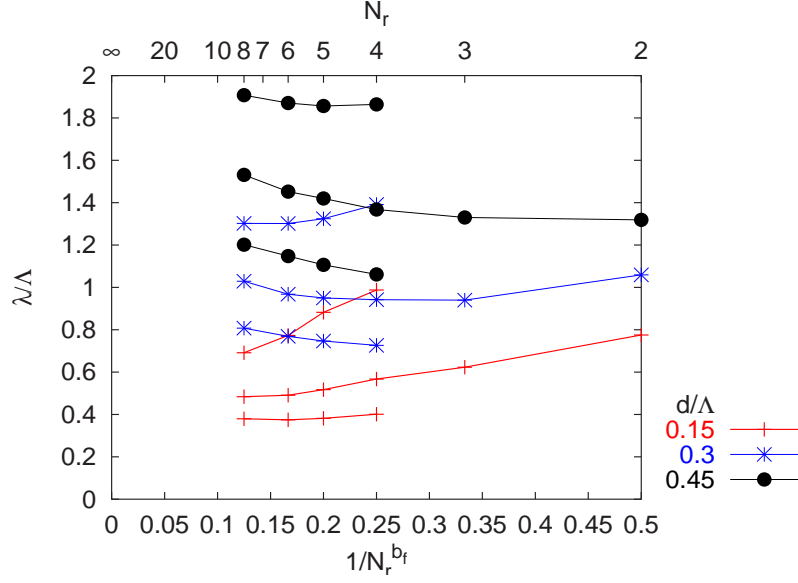


Figure 7.17: Loci of the minimum and half-width points of the negative  $Q$  peak as a function of the inverse of the number of rings ( $b_f = 1$ ), for three values of  $d/\Lambda$ . The curve showing the locus of the  $Q$  minimum is between the two half-width point curves for the same value of  $d/\Lambda$ .

the  $Q$  extremum of the peak (*half-width points*). Fig 7.17 shows the locus of the  $Q$  minimum along with the loci of the half-width points of the peak as a function  $1/N_r^{b_f}$  for several values of  $d/\Lambda$ .<sup>10</sup> Fitting the data to obtain a value of  $b_f$  resulting in a straight-line behaviour of the data sets didn't give satisfying results; the plot has been done with  $b_f$  arbitrarily set to 1. For  $d/\Lambda = 0.15$  the loci of the minimum and of the half width points seem to converge when  $N_r$  approaches infinity. For  $d/\Lambda = 0.3$  and  $d/\Lambda = 0.45$  the convergence of the locus of the minimum is far from being obvious, but the loci of the half-width points seem<sup>11</sup> to converge to finite values, and since the minimum has to be located between the half-width points, it seems that the locus of the transition does converge, *i.e.* there is a cutoff even for infinite systems.

### Transition Width and Sharpness

Fig. 7.18 shows, for the same MOFs as in Fig. 7.17, the width of the transition (defined by the half width of the negative  $Q$  peak) as a function of  $N_r^{-b_f}$  for three values of  $d/\Lambda$ . Again,  $b_f$  is an arbitrary positive coefficient adjusted to obtain the best straight-line behaviour of the datasets. Unlike what we have seen in Fig. 7.6 for the second mode, for which the transition-width becomes infinitely small when  $N_r$  approaches infinity, the width of the transition of the fundamental mode converges to a finite value.

Fig. 7.19 shows quantity  $1/\mathcal{J}$  –as defined in Section 7.2.3– for the fundamental mode of MOFs, for three different values of  $d/\Lambda$ . As for the second mode,  $\mathcal{J}$  diverges with increasing  $N_r$ : the change of slope of  $\Im(n_{\text{eff}})$  as a function of  $\lambda/\Lambda$  in a log-log plot during the transition

<sup>10</sup>For  $N_r \leq 3$  the  $Q$  peaks are too asymmetric to allow an easy definition of a half-width and accordingly we left out the corresponding points on Fig. 7.17 .

<sup>11</sup>There is an apparent convergence, but without more data we cannot be definitive about our conclusions.

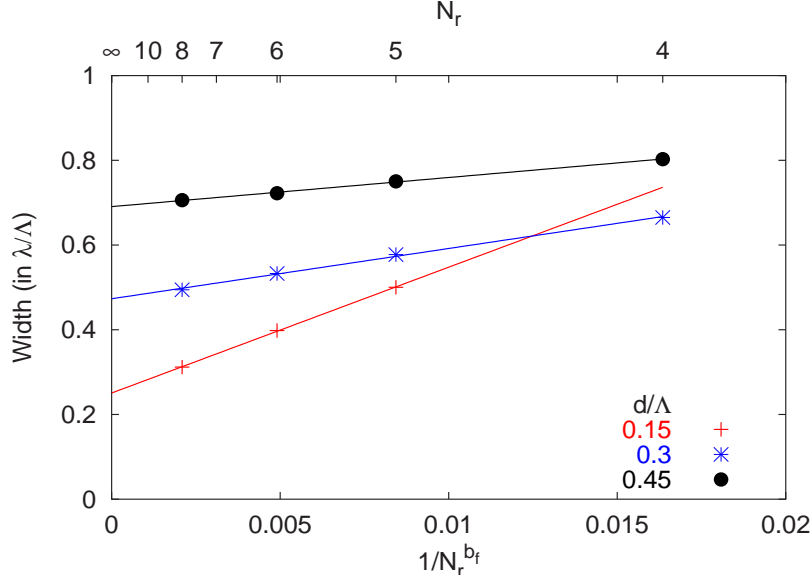


Figure 7.18: Half-width of the negative  $Q$  peak as a function of  $1/N_r^{b_f}$ . The width of the peak converges to a finite value. Here  $b_f \simeq 2.97$ .

becomes infinite for infinite  $N_r$ . We will discuss the meaning of this in connection with the finite transition width for infinite systems in Section 7.5 once we have gained a better understanding of the cutoff-transition through asymptotic models.

### Losses

Fig. 7.20 and Fig. 7.21 show the imaginary part of  $n_{\text{eff}}$  as a function of the number of rings for the fundamental mode of a MOF with  $d/\Lambda = 0.45$ , for two different values of  $\lambda/\Lambda$ . The values of  $\lambda/\Lambda$  have been chosen on each side of the negative  $Q$  peak, so that the mode is clearly in the confined ( $\lambda/\Lambda = 1.01$ ) or unconfined ( $\lambda/\Lambda = 3.1$ ) states. In the confined state, the losses decrease exponentially with  $N_r$  as is illustrated by the straight-line behaviour in the semi-logarithmic plot of Fig. 7.20. The curve superimposed on the data points shows the result of a fit to the exponential decay function given in Eq. (7.4). As for the second mode, the fit is excellent and we obtain  $a \simeq 2.092 \times 10^{-2} \pm 0.9\%$  and  $b \simeq 2.162 \pm 0.1\%$ . In the unconfined state, the losses as a function of the number of rings are a straight line in full logarithmic scale (Fig. 7.21), and fitting the data to the power law of Eq. (7.5) results in  $c \simeq 0.402 \pm 6\%$  and  $d \simeq 2.57 \pm 1.6\%$ .

As for the second mode, losses of the fundamental mode decay exponentially with the number of rings when the mode is confined, whereas they decay following an approximate power law when the mode is cladding filling.

### Conclusion

The fundamental mode of MOFs undergoes a transition between confined and unconfined states, which we identify with the cutoff of the mode. The locus in parameter space of the cutoff depends on the number of rings, but it seems that this locus converges with increasing number of rings. In the confined state, losses decrease exponentially with the number of

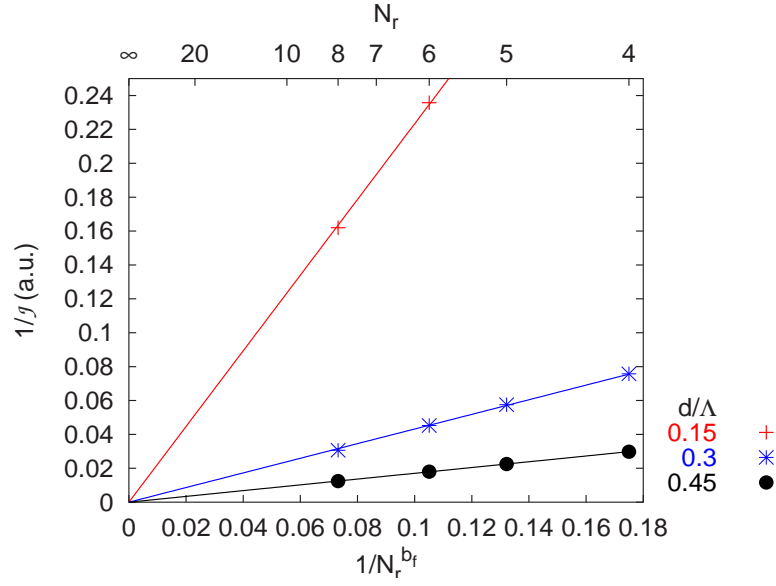


Figure 7.19:  $1/g$  as a function of  $1/N_r^{b_f}$  for three different values of  $d/\Lambda$ . Here  $b_f \simeq 1.26$ .

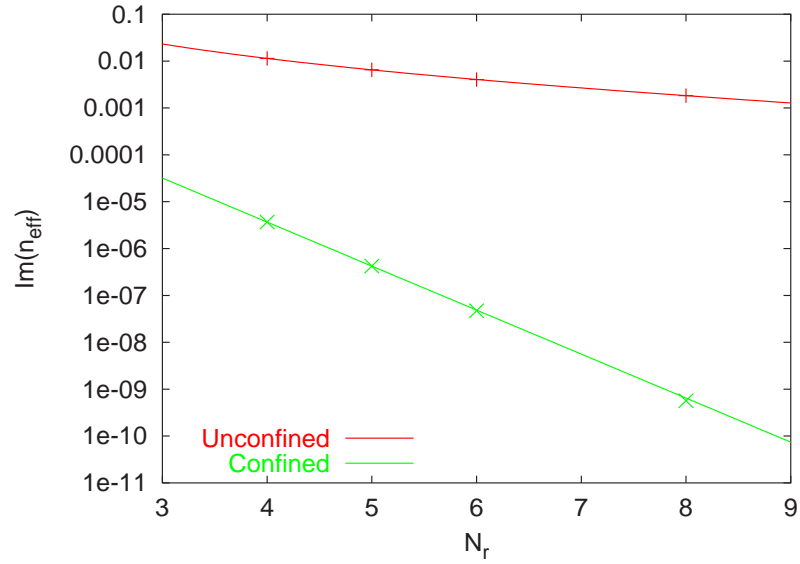


Figure 7.20: Imaginary part of the effective index as a function of the number of rings, for the fundamental mode of a MOF with  $d/\Lambda = 0.45$  in the confined ( $\lambda/\Lambda \simeq 1.01$ ) and unconfined ( $\lambda/\Lambda = 3.1$ ) states with  $\lambda = 1.55\mu\text{m}$ . The  $y$ -axis is in logarithmic scale, whereas the  $x$ -axis is linear.

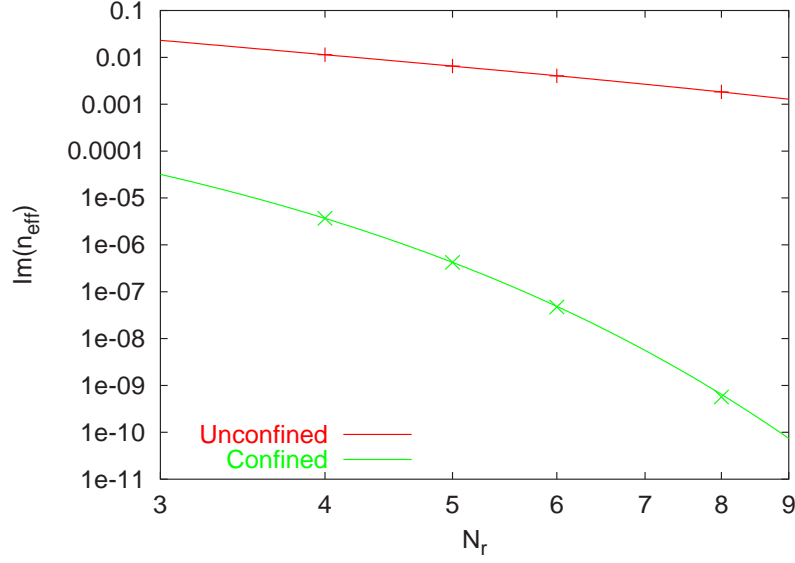


Figure 7.21: Same as Fig. 7.20, but with logarithmic scales on both axes.

rings, whereas is the unconfined cladding filling state, losses decrease with the number of rings following an approximate power law.

For the second mode we identified the locus of the cutoff with the negative  $Q$  peak. This made sense since the width of this peak approaches zero for infinite number of rings. For the fundamental mode, the width of the negative  $Q$  peak remains finite for infinite  $N_r$  and it becomes difficult to define a cutoff point. The cutoff transition spreads on a range of  $\lambda/\Lambda$ , and it would be more accurate to speak of a transition region.

Moreover, we have observed another, positive, peak preceding the negative peak on the  $Q$  curves. We haven't studied the properties of this second peak yet, nor have we been able to give a satisfying interpretation of either of the peaks.

## 7.4 Asymptotic Analysis of Cutoffs

With the aim of obtaining better insights into the physics of the cutoff, we develop asymptotic models of the guidance in MOFs for large and small values of the normalized wavelength  $\lambda/\Lambda$ . The qualitative predictions we will obtain from these models will allow us to understand the meaning of both the  $Q$  peaks marking the cutoff, to explain the scaling properties of the transition and to give a definition of a cutoff point for the fundamental mode. The latter will enable us to establish the “phase-diagram” of the fundamental mode.

The asymptotic models will also enable us to conclude as to the evolution of numerous modes properties with increasing number of rings. Notably, we will establish that mode properties as for example chromatic dispersion converge with increasing  $N_r$  for confined modes, but diverge for unconfined modes, that the decay of losses with  $N_r$  is exponential for confined modes whereas it follows an approximate power law for unconfined modes. The better understanding of the physical nature of the unconfined and confined modes will also lead us to predictions concerning mode sensitivity to structural flaws or bend losses. Finally, we will see that the fundamental mode “phase-diagram” can be used to predict properties of more

complex MOFs, *e.g.* with cores consisting of more than one missing inclusion or with hole sizes differing from one layer to another.

#### 7.4.1 Asymptotic Model for Long Wavelengths: CF1 Model

##### Homogenization

When the wavelength is much longer than all characteristic lengths of the MOF microstructure, homogenization arguments can be used: For  $\lambda \gg \Lambda$  the structured part of the MOF behaves like a homogenous uniaxial material, the extraordinary axis being parallel to the axis of the fibre. Indeed, homogenization theory predicts an effective dielectric constant given by the mean of the dielectric constants of air and silica for the electric field parallel to the fibre axis, whereas the Maxwell-Garnett formula can be used to derive effective constants for the transverse electric field component [102, 103]. With  $f$  being the air filling fraction of the fibre we have:

$$\bar{n}_z = (fn_i^2 + (1-f)n_M^2)^{1/2} \quad (7.8)$$

$$\bar{n}_\perp \cong n_M \left( \frac{T-f}{T+f} \right)^{1/2} \quad (7.9)$$

$$\text{where } T = \frac{n_M^2 + n_i^2}{n_M^2 - n_i^2}.$$

Note that (7.9) results from the Maxwell-Garnett formula, which is accurate only for small  $d/\Lambda$ . For larger  $d/\Lambda$  values, better approximations can be derived *e.g.* from homogenization theories using higher order multipolar expansions of the fields [104, 105].

##### Equivalent MOF

In the frame of homogenization, the exact position of the inclusions becomes irrelevant, and likewise the central defect loses its importance: the light doesn't "resolve" the exact structure, but "sees" only averages. The equivalent structure of a MOF is therefore a single rod of uniaxial material with refractive index tensor  $[\bar{n}]$  following from Eqs. (7.8) and (7.9), surrounded by an infinite jacket of index  $n_J = n_M$ . The shape and size of the equivalent rod result from the outer contour of the microstructured region of the MOF: In our examples the cross section of the rod would be hexagonal with corners situated at a distance of approximately  $N_r\Lambda$  from the center. We will try an even simpler approximation, using a rod of circular cross section with radius  $\rho$  defined by the distance from the MOF's center to the edge of the outermost inclusion:

$$\rho = N_r\Lambda + d/2. \quad (7.10)$$

To be consistent with the approximation of the rod shape, we use the filling fraction defined by the ratio of the total areas of all inclusions divided by the area of the equivalent rod:

$$f = \frac{N_i\pi(d/2)^2}{\pi\rho^2}, \quad (7.11)$$

where  $N_i$  is the number of inclusions.

Note that, in our case, where  $n_J = n_M$ , the components of the refractive index tensor of the homogenized rod are smaller than the refractive index of the jacket. The equivalent waveguide

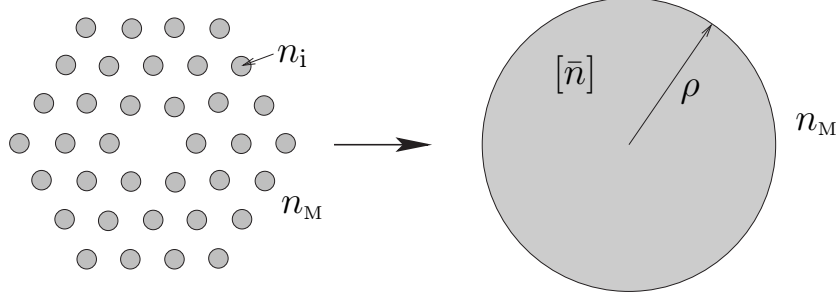


Figure 7.22: CF1 model geometry: conventional step index fibre equivalent to a MOF at long wavelengths.

consequently doesn't guide any strictly bounded mode,<sup>12</sup> but only leaky, quite lossy modes. Fig. 7.22 summarizes the model we use for the asymptotic study of MOFs at long wavelengths. Henceforth we will call this model of an equivalent conventional fibre *CF1*.

### Mode Equation

The equations to find the modes of the resulting uniaxial step index fibre are well established [3, 106]:<sup>13</sup> Introducing the usual fibre parameters

$$U = \rho k_0 (\bar{n}_\perp^2 - n_{\text{eff}}^2)^{1/2} \quad (7.12)$$

$$W = \rho k_0 (n_J^2 - n_{\text{eff}}^2)^{1/2} \quad (7.13)$$

$$V = \rho k_0 (n_J^2 - \bar{n}_\perp^2)^{1/2} \quad (7.14)$$

$$\kappa = \bar{n}_z / \bar{n}_\perp \quad (7.15)$$

the eigenvalue equation is

$$XY = \left( \frac{\nu n_{\text{eff}}}{\bar{n}_\perp} \right)^2 \left( \frac{V}{UW} \right)^4 \quad (7.16)$$

where

$$X = \frac{1}{U} \frac{J'_\nu(U)}{J_\nu(U)} - \frac{1}{W} \frac{H_\nu^{(1)'}(W)}{H_\nu^{(1)}(W)} \quad (7.17)$$

$$Y = \frac{\kappa}{U} \frac{J'_\nu(\kappa U)}{J_\nu(\kappa U)} - \frac{1}{W} \left( \frac{n_J}{\bar{n}_\perp} \right)^2 \frac{H_\nu^{(1)'}(W)}{H_\nu^{(1)}(W)}. \quad (7.18)$$

$\nu$  is any positive integer; the fundamental mode is the first (in order of  $\Re(n_{\text{eff}})$ ) solution of Eq. (7.16) with  $\nu = 1$ , whereas the second mode is the first solution of Eq. (7.16) with  $\nu = 0$  (which, in that case, factorizes into  $X = 0$  or  $Y = 0$ ). Note that all modes being leaky, we look for complex values of  $n_{\text{eff}}$  satisfying (7.16). There is no easy asymptotic simplification of these equations for large wavelengths; we will solve them numerically.

<sup>12</sup>*i.e.* modes with  $\Im(n_{\text{eff}}) = 0$ .

<sup>13</sup>Table 12-12 of Ref. [3] summarizes the necessary equations, but contains several typographical errors, which we have corrected here. Note that, rather than introducing modified Hankel functions, we use the usual Hankel functions of the first kind with complex argument, which has led us to redefine  $W$ . As a consequence, the usual relationship  $V^2 = U^2 + W^2$  is not satisfied by the fibre parameters we use here.

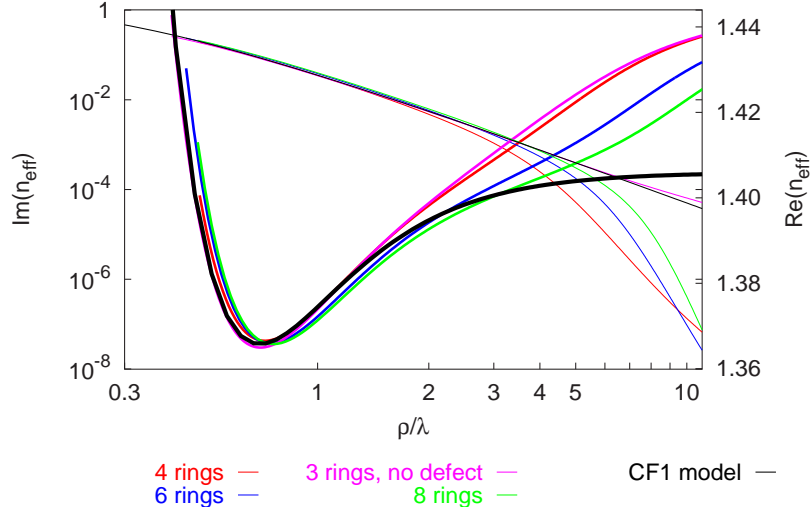


Figure 7.23: Real (thick curves) and imaginary part of  $n_{\text{eff}}$  as a function of normalized fibre radius  $\rho/\lambda$  for MOFs with  $d/\Lambda = 0.3$  and  $N_r$  ranging from 4 to 8. The results for a similar MOF design with  $N_r = 3$  but without central defect and the results for an equivalent CF1 fibre are shown as well.

## Results

In the CF1 model, as soon as  $N_r \gtrsim 2$ , the filling fraction  $f$  and hence the homogenized refractive indices become almost independent of  $N_r$ . At fixed wavelength and  $d/\Lambda$ , Eq. (7.16) then only depends on the total MOF size  $\rho$ . In the domain of validity of the CF1 model, we should therefore find modes with  $n_{\text{eff}}$  almost exclusively depending on  $N_r\Lambda + d/2$ . Further, with a sufficient number of rings, the presence or absence of a defect only slightly affects  $f$  and  $[\bar{n}]$ . At long wavelengths, the modes should become largely unaffected by the presence, absence, or position of a defect in the lattice. In Fig. 7.23 we show the real and imaginary part of the effective index of the fundamental mode of several MOF structures with same  $d/\Lambda = 0.3$  but different  $N_r$ , with and without a defect, as a function of  $\rho/\lambda$ , along with the values of  $n_{\text{eff}}$  resulting from Eq. (7.16). Here we used  $N_r = 8$  to compute the equivalent filling fraction  $f$  in Eq. (7.11). The agreement between the CF1 model and the individual MOFs is excellent for the real and imaginary parts of  $n_{\text{eff}}$  as soon as  $\lambda/\Lambda \gtrsim 2$ . For shorter wavelengths, the losses for the MOF without defect remain close to the losses computed from the CF1 model, while all other MOFs start to have significantly smaller losses. Discrepancies in the real part of  $n_{\text{eff}}$  for  $\lambda/\Lambda \lesssim 2$  become noticeable even for the MOF without defect: the homogenization argument doesn't hold for short wavelengths. Note that the value of  $\lambda/\Lambda$  at which homogenization starts to give accurate results is remarkably small, but it should be kept in mind that the important quantity for homogenization arguments in the CF1 model is the perpendicular wavelength-to-pitch ratio:

$$\frac{\lambda_{\perp}}{\Lambda} = \frac{2\pi}{\Re(k_{\perp}\Lambda)} = \frac{1}{\Re((n_M^2 - n_{\text{eff}}^2)^{1/2})} \frac{\lambda}{\Lambda}, \quad (7.19)$$

where  $k_{\perp} = (2\pi/\lambda)(n_M^2 - n_{\text{eff}}^2)^{1/2}$  is the perpendicular wavenumber in the core. In Fig. 7.24 we show the perpendicular wavelength as a function of the normalized fibre size  $\rho/\lambda$  for the

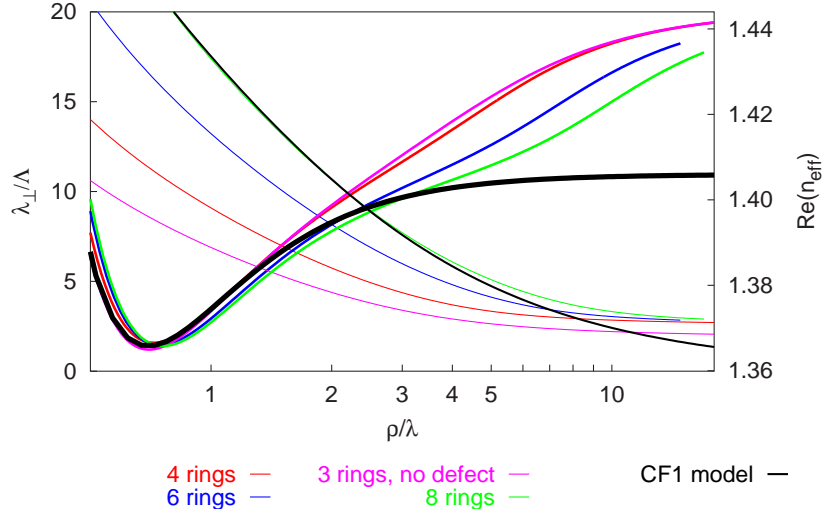


Figure 7.24: Real part of  $n_{\text{eff}}$  (thick curves) and normalized perpendicular wavelength  $\lambda_{\perp}/\Lambda$  in the core as a function of normalized fibre radius  $\rho/\lambda$  for the same structures than in Fig. 7.23.

same structures as in Fig. 7.23, along with the real part of  $n_{\text{eff}}$ : Agreement between the homogenized model and the MOFs with a central defect is reached when  $(\lambda_{\perp}/\Lambda) \gtrsim 7$ . For the  $\lambda_{\perp}/\Lambda$  curve given for the CF1 model, we used the value of the pitch derived from Eq. (7.10) with  $N_r = 8$ . Similar studies for other values of  $d/\Lambda$ , for the fundamental as well as the second mode, confirmed the validity of the CF1 model at long wavelengths; results remain accurate with the Maxwell-Garnett approximation for values of  $d/\Lambda$  at least up to 0.45. Higher order estimates of  $\bar{n}_{\perp}$  can be used for larger values of  $d/\Lambda$ . Note that the value of  $\bar{n}_{\perp}$  is only important for quantitative studies; qualitative results are not affected by errors on  $\bar{n}_{\perp}$ . One of the qualitative results of the CF1 model is that, as suggested by the straight-line behaviour of the loss curve for the CF1 model in Fig. 7.23, the loss as a function of fibre size follows an approximate power law. When the CF1 model is valid,  $\mathcal{Q}$  therefore takes a near zero value. Conversely, the negative peak observed for  $\mathcal{Q}$  before this quantity takes a near zero value for large  $\lambda/\Lambda$  indicates the limit of validity of the CF1 model. We shall call  $\mu_{\text{CF1}}$  the value of  $\lambda/\Lambda$  at which the CF1 model becomes valid.<sup>14</sup>

We emphasize that the main result of the CF1 model is that mode properties at fixed wavelength and  $d/\Lambda$  depend solely on the total fibre size  $\rho$  for large wavelengths: for the same values of  $\Lambda$  and  $d$ , mode properties will therefore be sensitive to the number of rings; mode properties such as dispersion will not converge with increasing number of rings. Losses are generally very high since guidance results from a rod of lowered index in a matrix of larger refractive index. They decrease with the number of rings, but they do so following an approximate power law. Note that for conventional fibres at long wavelengths bend-loss can become a limitation. Since in the frame of the CF1 model geometric losses are already prohibitive, the bend-loss should not be the limiting factor.

Finally, note that although agreement is generally good between results from the CF1

<sup>14</sup>Since a quantitative definition of  $\mu_{\text{CF1}}$  would necessarily be arbitrary, we choose not to give such a definition. Nevertheless, we assume that a coherent, unique definition of  $\mu_{\text{CF1}}$  is used throughout the remainder of this thesis. Qualitatively we associate  $\mu_{\text{CF1}}$  with the upper bound of the  $\lambda/\Lambda$  region supporting the negative  $\mathcal{Q}$  peak. For small transition widths it is therefore close to the upper half-width point of the negative  $\mathcal{Q}$  peak.

model and simulations using the multipole method for large wavelengths, one should not expect to obtain accurate results – especially for second order quantities such as the dispersion – from the CF1 model since the approximations made, in particular as to the shape of the equivalent rod, are quite coarse.

### 7.4.2 Asymptotic Model for Short Wavelengths: CF2 Model

#### Fundamental Space-Filling Mode

For short wavelengths, MOFs have already been successfully modeled by several authors as step index fibres with varying cladding index [60–62, 97]. In the so-called effective index model, a solid core MOF is modeled by an equivalent circular step index fibre consisting of a core (refractive index  $n_M$ ) of radius  $\rho_c$  surrounded by a cladding extending to infinity with refractive index  $n_{\text{FSM}}$ .  $n_{\text{FSM}}$  is defined by

$$n_{\text{FSM}} = \beta_{\text{FSM}}/k_0 \quad (7.20)$$

where  $\beta_{\text{FSM}}$  is the largest propagation constant allowed in the cladding<sup>15</sup> or equivalently the propagation constant of the fundamental space-filling mode (FSM).

The idea behind this model is to draw analogies between total reflection at the interface between two dielectrics and at the interface between a 2D-photonic crystal and a dielectric. If we consider a plane interface perpendicular to  $Ox$  between two dielectrics 1 and 2 with refractive index  $n_1$  and  $n_2$  respectively, a plane wave in region 1 with wave vector  $\mathbf{k}_1 = n_1 k_0 \hat{u}_1 = \alpha \hat{e}_x + \beta \hat{e}_z$  can propagate in region 2 only if  $\beta \leq n_2 k_0$ .  $n_2 k_0$  is the largest allowed propagation constant for a plane wave in region 2. If  $\beta > n_2 k_0$ , the wave in region 1 is totally reflected. In the case of a plane interface perpendicular to  $Ox$  between a dielectric and a periodic array of cylinders parallel to  $Oz$ , the situation is very similar: the band structure of the photonic crystal determines all possible modes propagating in it, the one with the largest component along  $Oz$  is the fundamental space-filling mode; its propagation constant is  $\beta_{\text{FSM}}$ . If a plane wave in the dielectric has a component of the wave vector along  $Oz$  which is larger than  $\beta_{\text{FSM}}$  it cannot couple to any propagating mode in the photonic crystal: the wave in the dielectric is totally reflected.  $\beta_{\text{FSM}}/k_0$  therefore determines the “effective index” of the photonic crystal for total reflection. The guiding mechanism in step index fibre being total internal reflection, choosing  $n_{\text{FSM}}$  as the cladding index is a natural choice.

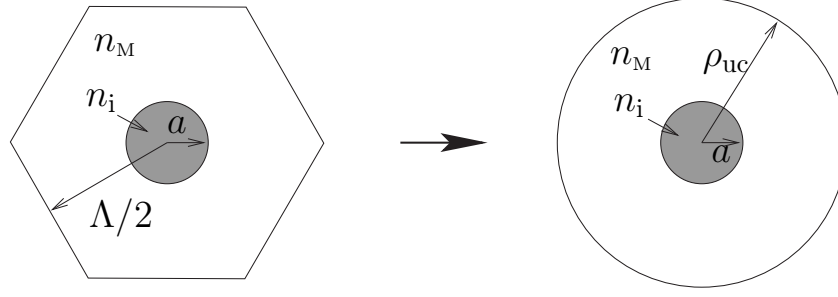
The accurate value of  $n_{\text{FSM}}$  can be extracted from the band diagrams for the infinite lattice computed *e.g.* through multipole [107, 108] or plane wave methods [64]. Birks et al. [60] suggested a simplified model to compute  $n_{\text{FSM}}$ , illustrated by Fig. 7.25:

The method results from the geometric properties of the FSM. The FSM’s wavevector is parallel to the cylinders. Its Bloch vector is zero, it has the same symmetries as the photonic crystal itself. There must therefore be field components which are symmetric along the borders of the Wigner-Seitz unit cell. Using a scalar approximation with wavefunction  $\psi$  this results in

$$\frac{\partial \psi}{\partial s} = 0 \quad (7.21)$$

where  $s$  is a coordinate perpendicular to the border of the unit cell. We approximate the

<sup>15</sup>Or rather in the infinite photonic crystal consisting of the array defined by the cladding: In our case an infinite hexagonal array of circular holes with same  $d$  and  $\Lambda$ .

Figure 7.25: Computing  $n_{\text{FSM}}$  for the CF2 model: Equivalent unit cell.

hexagonal border of the unit cell by a circle with radius  $\rho_{\text{uc}}$  (see Fig. 7.25), so that we have

$$\left. \frac{\partial \psi}{\partial r} \right|_{r=\rho_{\text{uc}}} = 0, \quad (7.22)$$

where we use cylindrical coordinates centered on the inclusion under consideration. We choose  $\rho_{\text{uc}}$  to keep the original filling fraction of the array of cylinders, which results in

$$\rho_{\text{uc}} = \Lambda \left( \frac{\sqrt{3}}{2\pi} \right)^{1/2}. \quad (7.23)$$

We can now attempt to justify the scalar approximation: the equivalent geometry we use is similar to a coaxial guide (light is guided between a perfect reflector at  $r = \rho$  and a lower refractive index core). The fundamental mode of this kind of structure is transverse electric (TE) (*i.e.*  $E_z = 0$  everywhere), and for TE modes of circularly symmetric step index guides, the transverse components  $\mathbf{E}_t$  of  $\mathbf{E}$  satisfy the scalar wave equation everywhere, which notably implies the continuity of  $\mathbf{E}_t$  and its first derivatives everywhere, including at the interface between two regions of different refractive indices. For a detailed discussion, see Sec. 11-16 of [3] and references cited therein. Note that this clarifies that  $\psi$  is a transverse component of  $\mathbf{E}$ .

The above justification of the scalar approximation<sup>16</sup> might leave the alert reader rightly suspicious. Although this model has been widely used, Midrio and coworkers have shown [61] that it is quite approximate, that the fundamental mode of the unit cell is generally *not* TE, and that a full vector treatment is needed to get accurate results for  $n_{\text{FSM}}$ . We nevertheless chose to use this model for its analytic simplicity. Our aim is to get an asymptotic approximation of  $n_{\text{FSM}}$  in order to bring out qualitative properties of MOFs, especially concerning the losses. If one was to consider getting quantitative results from this kind of model, the asymptotic treatment we apply below to the scalar equations can be applied to the analytic full vector treatment suggested by Midrio *et al.* [61]. However, even in the full vector case, approximations and arbitrary parameters (such as the choice of  $\rho_{\text{uc}}$ ) remain, so that results could only be semi-quantitative.

To find the equation satisfied by  $n_{\text{FSM}}$ , we expand the fields in Fourier-Bessel series around the center of the inclusion. Inside the inclusion we have

$$\psi = \sum_n A_n^- J_n(k^- r) \exp(in\theta) \quad (7.24)$$

<sup>16</sup>...and of the external boundary conditions.

and outside the inclusion we have

$$\psi = \sum_n \left( A_n^+ J_n(k^+ r) \exp(in\theta) + B_n^+ H_n^{(1)}(k^+ r) \right) \exp(in\theta), \quad (7.25)$$

with

$$k^+ = k_0(n_M^2 - n_{\text{FSM}}^2)^{1/2} \quad (7.26)$$

$$k^- = ik_0(n_{\text{FSM}}^2 - n_i^2)^{1/2}. \quad (7.27)$$

Given the symmetries of the sought mode, the sums are over multiples of 6 only:  $n \in 6\mathbb{Z}$ . Since we look for an approximate value of  $n_{\text{eff}}$  and have approximated the boundaries of the unit cell by a circle, it is sensible to neglect values of  $n \geq 6$ , so that only Bessel and Hankel functions of order 0 remain. Eq. (7.22) together with the continuity of  $\psi$  and  $\partial\psi/\partial r$  at  $r = a = d/2$  give the eigenvalue equation of the FSM:

$$\frac{k^+ J_0(k^- a)}{k^- J'_0(k^- a)} = \frac{J'_0(k^+ \rho_{\text{uc}}) H_0^{(1)}(k^+ a) - H_0^{(1)'}(k^+ \rho_{\text{uc}}) J_0(k^+ a)}{J'_0(k^+ \rho_{\text{uc}}) H_0^{(1)'}(k^+ a) - H_0^{(1)'}(k^+ \rho_{\text{uc}}) J'_0(k^+ a)} \quad (7.28)$$

### Asymptotic Value of $n_{\text{FSM}}$

Knowing that  $n_{\text{FSM}}$  approaches  $n_M$  when  $\lambda$  approaches 0,<sup>17</sup> we look for an asymptotic expansion of  $n_{\text{FSM}}$  for short wavelengths taking the form

$$n_{\text{FSM}} \simeq n_M - \nu_{\text{FSM}} \left( \frac{\lambda}{\rho_{\text{uc}}} \right)^2. \quad (7.29)$$

Note that for reasons of time symmetry, odd orders in such an expansion are absent, so that Eq. (7.29) is the lowest order expansion of  $n_{\text{FSM}}$ .

Using Eq. (7.29) we find asymptotic values of  $k^+$  and  $k^-$ :

$$k^- = i \frac{2\pi}{\lambda} \delta + O\left(\frac{\lambda}{\rho_{\text{uc}}}\right) \quad (7.30)$$

$$k^+ = \frac{2\pi}{\rho_{\text{uc}}} (2\nu_{\text{FSM}} n_M)^{1/2} + O\left(\left(\frac{\lambda}{\rho_{\text{uc}}}\right)^2\right), \quad (7.31)$$

where  $\delta = (n_M^2 - n_i^2)^{1/2}$ . Consequently  $-ik^- a$  approaches  $\infty$  when  $\lambda$  approaches 0. We use asymptotic expansion of the Bessel and Hankel functions [82] to simplify the left hand side of Eq. (7.28) and find

$$\frac{k^+ J_0(k^- a)}{k^- J'_0(k^- a)} \simeq \lambda \frac{\sqrt{2n_M \nu_{\text{FSM}}}}{\delta \rho_{\text{uc}}}. \quad (7.32)$$

The left hand side of Eq. (7.28) hence approaches 0 when  $\lambda$  approaches zero. On the contrary,  $k^+$  approaches a constant finite value when  $\lambda$  approaches zero, so that the right hand side of Eq. (7.28) also approaches a finite limit when  $\lambda$  tends to zero. Equating the limits, we obtain

$$H_0^{(1)}((a/\rho_{\text{uc}})2\pi\sqrt{2n_M \nu_{\text{FSM}}}) J'_0(2\pi\sqrt{2n_M \nu_{\text{FSM}}}) - H_0^{(1)'}(2\pi\sqrt{2n_M \nu_{\text{FSM}}}) J_0((a/\rho_{\text{uc}})2\pi\sqrt{2n_M \nu_{\text{FSM}}}) = 0. \quad (7.33)$$

<sup>17</sup>Indeed at short wavelengths the light tends to become completely confined in the high index region.

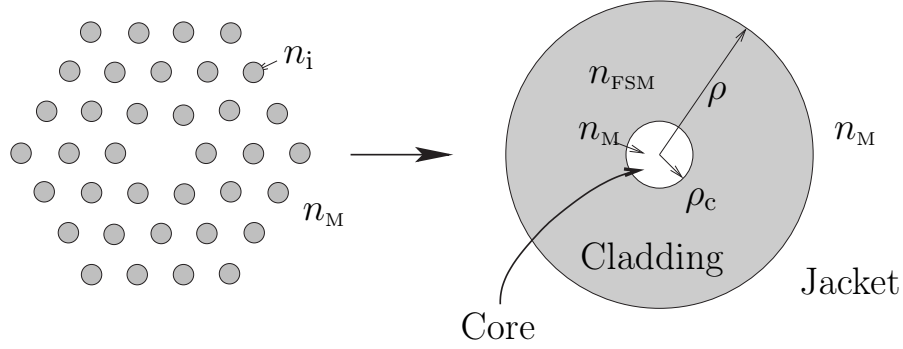


Figure 7.26: CF2 model: Geometry of the conventional W-step index fibre equivalent to MOFs at short wavelengths.

Introducing  $x = 2\pi\sqrt{2n_M\nu_{\text{FSM}}}$  and  $q = a/\rho_{\text{uc}}$  and using the differentiation formulas for Hankel and Bessel functions, Eq. (7.33) can be written

$$\frac{H_0^{(1)}(qx)}{J_0(qx)} = \frac{H_1^{(1)}(x)}{J_1(x)}. \quad (7.34)$$

The smallest real positive root of this equation gives us the sought value of  $\nu_{\text{FSM}} = (x/2\pi)^2/(2n_M)$ .

We compared  $n_{\text{FSM}}$  obtained through the asymptotic model to exact computations of  $n_{\text{FSM}}$  resulting from rigorous band diagram computations, and to solutions of the scalar model described above without the asymptotic approximations.<sup>18</sup> It appears that the scalar model without asymptotic approximations gives satisfactory values of  $n_{\text{FSM}}$  for  $\Lambda/\lambda \gtrsim 3$ ,<sup>19</sup> and that the asymptotic scalar model gives correct values of  $n_{\text{FSM}}$  within a few percent compared to the exact value of  $n_{\text{FSM}}$  as soon as the scalar model becomes valid.

### Equivalent MOF: the CF2 Model

Fig. 7.26 summarizes the model we use for MOFs at short wavelengths: a solid rod with circular cross section (radius  $\rho_c$ ) and refractive index  $n_M$  (the core) is surrounded by a homogeneous annulus with refractive index  $n_{\text{FSM}}$  (the cladding). Brechet *et al.* [62] studied the best value for the radius of the rod to obtain most accurate results and found that  $\rho_c$  should be taken to be  $0.64\Lambda$ . For the outer radius of the annulus we use the radius used in the CF1 model  $\rho = N_r\Lambda + d/2$ . Outside the annulus the refractive index is  $n_M$  and extends to infinity (jacket). The equivalent CF2 fibre is similar to a W-fibre with same refractive index for the core and the jacket. Note that with decreasing wavelength the difference between all refractive indices becomes arbitrarily small, so that we can use the scalar approximation. We take the scalar mode eigenvalue equation and estimate the losses of the equivalent fibre from Ref. [50] and apply an asymptotic treatment similar to the one used to find  $n_{\text{FSM}}$ .

**Eigenvalue equation** We use an asymptotic estimate of  $n_{\text{eff}}$  similar to Eq. (7.29):

$$n_{\text{eff}} \simeq n_M - \nu_f \left( \frac{\lambda}{\rho_c} \right)^2. \quad (7.35)$$

<sup>18</sup>*i.e.*  $n_{\text{FSM}}$  obtained through solving directly Eq. (7.28).

<sup>19</sup>Note that the value of  $\Lambda/\lambda$  from which the model becomes valid depends on  $d/\Lambda$ . We will detail this in subsequent sections.

The transverse wavenumbers in the core and the jacket ( $k_{\perp}^M$ ), and in the cladding ( $k_{\text{clad}}$ ) become

$$k_{\perp}^M = k_0(n_{\text{M}}^2 - n_{\text{eff}}^2)^{1/2} = \frac{2\pi}{\rho_c} (2n_{\text{M}}\nu_{\text{f}})^{1/2} + O\left((\lambda/\rho_c)^2\right) \quad (7.36)$$

$$k_{\text{clad}} = k_0(n_{\text{FSM}}^2 - n_{\text{eff}}^2)^{1/2} = -i\frac{2\pi}{\rho_c} (2n_{\text{M}}(\tilde{\nu}_{\text{FSM}} - \nu_{\text{f}}))^{1/2} + O\left((\lambda/\rho_c)^2\right), \quad (7.37)$$

where we have introduced  $\tilde{\nu}_{\text{FSM}} = (\rho_c/\rho_{\text{uc}})^2\nu_{\text{FSM}}$ . Note that both transverse wavenumbers are independent of  $\lambda$  to the first order in  $\lambda/\Lambda$ . Replacing the transverse wavenumbers in the scalar eigenvalue equation for HE modes of W-fibres in the scalar approximation (Eq.(23) of Ref. [50]) by their asymptotic values, we find the eigenvalue equation satisfied by  $\nu_{\text{f}}$ :

$$\begin{aligned} \frac{H_1^{(2)}(sw)}{H_1^{(2)}(w)} \left[ J(u) - H^{(1)}(w) \right] \left[ H^{(2)}(su) - H^{(2)}(sw) \right] \\ - \frac{H_1^{(1)}(sw)}{H_1^{(1)}(w)} \left[ J(u) - H^{(2)}(w) \right] \left[ H^{(2)}(su) - H^{(1)}(sw) \right] = 0, \end{aligned} \quad (7.38)$$

where

$$u = 2\pi(2n_{\text{M}}\nu_{\text{f}})^{1/2} \quad (7.39)$$

$$w = -i2\pi [2n_{\text{M}}(\tilde{\nu}_{\text{FSM}} - \nu_{\text{f}})]^{1/2} \quad (7.40)$$

$$s = \frac{\rho}{\rho_c} \quad (7.41)$$

$$J(z) = \frac{J_0(z)}{zJ_1(z)} \quad (7.42)$$

$$H^{(i)}(z) = \frac{H_0^{(i)}(z)}{zH_1^{(i)}(z)}. \quad (7.43)$$

Note that this equation is valid for  $\text{HE}_{1,\mu}$  modes only, and consequently cannot be used for the second mode. Eq. (7.38) can be solved numerically with conventional equation solvers. The smallest  $\nu_{\text{f}}$  found will be the one for the fundamental mode. Given that we do not aim to obtain quantitative results, we will not study comprehensively the solutions to this equation.<sup>20</sup>

We can nevertheless use the eigenvalue equation (7.38) to analyse the behaviour of modes with increasing number of rings  $N_{\text{r}}$ , *i.e.* with increasing  $s$ . Using asymptotic expansions of the Bessel and Hankel functions for large arguments, it is straightforward to show that Eq. (7.38) becomes independent of  $s$  for large values of  $s$ : the first term of the sum approaches zero exponentially for large  $s$ , whereas the second term diverges exponentially with increasing  $s$ , so that only the second term remains for large  $s$ . The second term is already factorized; removing the trivial solutions, the mode equation becomes:<sup>21</sup>

$$J(u) - H^{(2)}(w) \simeq 0. \quad (7.44)$$

<sup>20</sup>Out of curiosity we have solved this equation, along with the asymptotic model to compute  $\nu_{\text{FSM}}$ , and found  $\nu_{\text{f}}$  to be accurate to about 20%. For the estimate of the losses (Eq.(7.45)) the inaccuracies are accentuated and the value of  $\Im(w)$  – which determines the rate of exponential decay of the losses with  $N_{\text{r}}$  – we found is accurate to only  $\sim 40\%$ , which is not really surprising given the numerous approximations made.

<sup>21</sup>Note that this equation is the eigenvalue equation of a simple step index fibre in the weak guidance approximation, which indeed is identical to a W-fibre with infinite  $s$ .

The first conclusion we can draw from the CF2 model is therefore that at short wavelengths  $n_{\text{eff}}$  converges with increasing number of rings.

**Losses** In the previous paragraph we have seen how to obtain an asymptotic estimate of the real part of  $n_{\text{eff}}$ . To obtain the imaginary part of  $n_{\text{eff}}$  we use the perturbative estimation of the attenuation coefficient found by Maeda *et al.* (Eq. (28-29) of Ref. [50]). Note that the method used by Maeda *et al.* to derive the estimate is very similar to the one described in Sec. 5.1. Using the asymptotic approximation and the coefficients defined in Eqs.(7.39-7.43) we find to the lowest order in  $\lambda/\Lambda$

$$\Im(n_{\text{eff}}) = \frac{2}{\pi \rho_c^2 n_M k_0^2} \left| \frac{X}{H_0^{(2)}(su)} \right|^2 \left[ 1 + \left( \frac{J_1(u)}{J_0(u)} \right)^2 \right]^{-1}, \quad (7.45)$$

where

$$X = \frac{J(u) - H^{(1)}(w)}{J(u)} \frac{sH^{(2)}(sw)}{H^{(2)}(su) - H^{(1)}(sw)} \frac{H^{(1)}(sw) - H^{(2)}(sw)}{H^{(1)}(w) - H^{(2)}(w)} \frac{H_1^{(2)}(sw)}{H_1^{(2)}(w)}. \quad (7.46)$$

Note that  $u$  and  $w$  being independent of the wavelength in our asymptotic approximation [see Eqs.( 7.39-7.40)], the sole dependence of  $\Im(n_{\text{eff}})$  on  $\lambda$  lies in  $k_0$  in the denominator of the first fraction of Eq.(7.45). All other terms are wavelength independent. At fixed  $d/\Lambda$  they nevertheless depend on the number of rings. With the aim of bringing out the dependence on the number of rings, we consider an asymptotic expansion of Eq.(7.45) for large  $s$  (*i.e.* large  $N_r$ ) and obtain:

$$\Im(n_{\text{eff}}) \simeq A \left( \frac{\lambda}{\rho_c} \right)^2 \exp \left[ 2 \frac{\rho}{\rho_c} \Im(w) \right], \quad (7.47)$$

where  $A$  depends on  $\nu_f$ ,  $\nu_{\text{FSM}}$ ,  $n_M$  but not on  $\rho$  or  $\lambda/\Lambda$ .

At short wavelengths the imaginary part of the effective index of the fundamental mode is proportional to the square of the wavelength, and at short wavelengths *and* large number of rings  $\Im(n_{\text{eff}})$  decays exponentially with the number of rings.

**Bend loss** When the CF2 model is valid, the critical bend radius  $R_c$  at which bend loss becomes large varies as [60]

$$R_c \propto \frac{\rho_c^3}{\lambda^2}. \quad (7.48)$$

$R_c$  increases with decreasing wavelength, so that in practice the fibre becomes useless for wavelengths shorter than a short wavelength bend-loss edge. Note that for conventional fibres – where the difference between cladding and core refractive indices is constant – bend-loss is a limiting factor at long wavelengths, but not at short wavelengths. In the frame of the short wavelengths CF2 approximation, no long wavelength bend-loss edge can be predicted. Using the scalar model without asymptotic approximation leads to a long-wavelength bend-loss edge [60,109,110] but it appears that this edge is found in a region of parameter space where the approximation of assimilating a MOF to a conventional fibre becomes questionable.<sup>22</sup>

<sup>22</sup>In the examples we have studied, the large wavelength bend-loss edge found with the scalar approximation was found to be very close to the cutoff. Indeed the long wavelength bend-loss edge is linked to an increase in the effective area, which occurs at the cutoff.

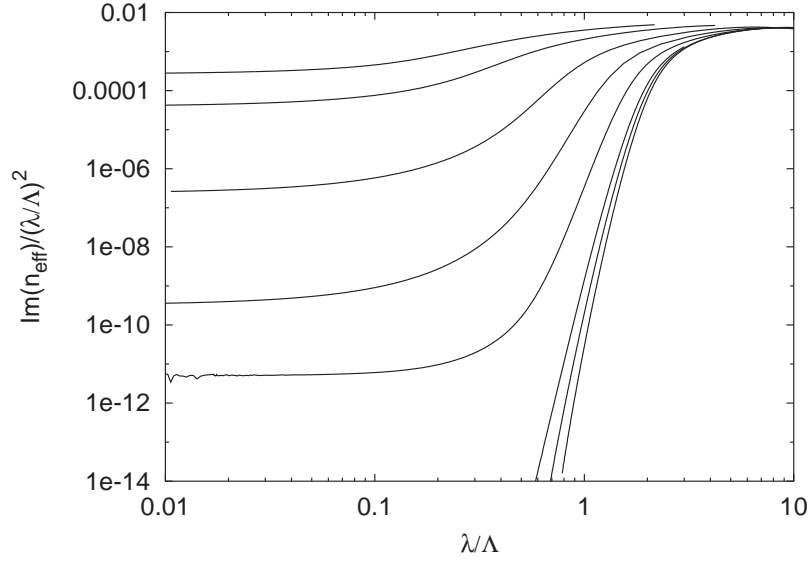


Figure 7.27: Imaginary part of  $n_{\text{eff}}$  as a function of wavelength on pitch, rescaled by  $(\lambda/\Lambda)^2$ , for a silica structure with 3 rings of holes, with  $d/\Lambda$  taking the values 0.075 (top curve), 0.15, 0.3, 0.45, 0.6, 0.75, 0.8 and 0.85. (Figure obtained by varying  $\Lambda$ , with  $\lambda = 1.55 \mu\text{m}$  for silica MOFs.)

### Region of validity

Given the numerous approximations needed to establish the CF2 model, it is difficult to predict *a priori* the value  $\mu_{\text{CF2}}$  of  $\lambda/\Lambda$  from which the model becomes qualitatively valid.<sup>23</sup> We here adopt a heuristic approach.

When the CF2 model is valid,  $\Im(n_{\text{eff}})$  is proportional to the square of the wavelength and therefore  $\mathcal{Q} = 0$ . Fig. 7.27 shows  $\Im(n_{\text{eff}})/(\lambda/\Lambda)^2$  as a function of  $\lambda/\Lambda$  in a log-log plot, for MOFs with  $N_r = 3$  and several values of  $d/\Lambda$ . The curves tend to a constant for approximately  $\lambda/\Lambda < 0.3$ , indicating clearly that the asymptotic dependence becomes valid for reasonable wavelength to pitch ratios.<sup>24</sup> In Fig. 7.15, curve (6), representing  $\mathcal{Q}$ , approaches zero after a positive peak with decreasing  $\lambda/\Lambda$ : the lower limit of the peak corresponds to the limit of validity of the CF2 model.

We have seen that the imaginary and real parts of  $n_{\text{eff}}$  converge with increasing  $N_r$ . The model actually gets more accurate with increasing  $N_r$ , since  $n_{\text{FSM}}$  is a value coming from infinite photonic crystal properties. Hence, not only should  $\mu_{\text{CF2}}$  converge with increasing  $N_r$ , but it should even do so towards a larger domain of validity of the CF2 model. Unfortunately it is difficult to verify this assertion directly through analysing loss curves computed through the multipole method. Indeed losses are already extremely small at  $\lambda/\Lambda = \mu_{\text{CF2}}$  for small values of  $N_r$ : for  $N_r > 3$  they rapidly become smaller than what can numerically be estimated through the multipole method. We could nevertheless verify directly (through analysing the positive  $\mathcal{Q}$  peak) that  $\mu_{\text{CF2}}$  slightly increases with  $N_r$  and eventually seems to converge for

<sup>23</sup>Again we do not give a quantitative definition of  $\mu_{\text{CF2}}$ . See, *mutatis mutandis*, footnote 14.

<sup>24</sup>Note that what we have shown is that  $\Im(n_{\text{eff}})$  varies as  $(\lambda/\Lambda)^2$  when the CF2 model is valid. Here we assume that the CF2 model is valid when  $\Im(n_{\text{eff}})$  varies as  $(\lambda/\Lambda)^2$ , but we haven't rigorously proven this reciprocal assertion.

values of  $d/\Lambda < 0.15$ . For  $d/\Lambda > 0.15$  losses are too small to obtain a complete positive  $\mathcal{Q}$  peak for  $N_r > 4$ .

### CF2 model and long wavelengths

We have derived the CF2 model using asymptotic expansions for short wavelengths and obviously cannot use it for long wavelengths. The model, without the asymptotic approximations, has nevertheless been used for long wavelengths (*e.g.* in Refs. [60, 97] and many others) and it was argued that for long wavelengths  $n_{\text{FSM}}$  should converge to  $\bar{n}_z$  given by Eq. (7.8). This is true for the same homogenization reasons we used in Section 7.4.1 for the CF1 model. It is however arguable to use the geometry of Fig. 7.26 at long wavelengths, since the core is connected to the matrix and homogenization arguments must be applied to the whole structure, including the core (which leads to the CF1 model).

### CF2 Model for the Second Mode

The CF2 model was established and detailed for the fundamental mode. For the second mode, the eigenvalue equation (7.38) and the loss formula (7.45) have to be adapted. The correct equations for the second mode nevertheless keep similar asymptotic behaviour for small  $\lambda/\Lambda$  and large  $N_r$ , so that qualitative results such as the exponential decay of  $\Im(n_{\text{eff}})$  with  $N_r$  and the proportionality of  $\Im(n_{\text{eff}})$  to  $(\lambda/\Lambda)^2$  remain valid.

## 7.5 Interpretation of the Cutoff

### 7.5.1 Fundamental Mode

We have now acquired sufficient knowledge to try to explain the features observed in Fig. 7.15 (see also Fig. 7.28):

#### Loss and $\mathcal{Q}$ Curves Revisited

At short wavelengths (CF2 model),  $\Im(n_{\text{eff}})$  varies as  $(\lambda/\Lambda)^2$ . The curve of  $\Im(n_{\text{eff}})$  as a function of  $\lambda/\Lambda$  is therefore a straight line in the log-log plot, and  $\mathcal{Q} = 0$ . For large wavelengths the CF1 model becomes valid and  $\Im(n_{\text{eff}})$  as a function of  $\lambda/\Lambda$  is an approximate power law: the  $\Im(n_{\text{eff}})$  curve again becomes an approximate straight line and  $\mathcal{Q} \simeq 0$ . There is nevertheless a remarkable difference between the CF1 and CF2 models: in the former, losses vary following an approximate power law dependence on  $N_r$ , whereas in the latter case, losses decrease exponentially with  $N_r$ .<sup>25</sup> The difference in losses between the two asymptotic regimes therefore increases nearly exponentially with increasing  $N_r$ . Since  $\mu_{\text{CF2}}$  and  $\mu_{\text{CF1}}$  converge with increasing  $N_r$ ,<sup>26</sup> the region of  $\lambda/\Lambda$  in which the losses have to go from those of the CF2 model to those of the CF1 model keeps a finite width, whereas the range covered by the losses in that region diverges in the log-plot with increasing  $N_r$ : The slope of the loss versus normalized wavelength curve has to diverge at least at one point between  $\mu_{\text{CF2}}$  and  $\mu_{\text{CF1}}$  with increasing

<sup>25</sup>Note that we have already directly observed this behaviour in Section 7.3.2.

<sup>26</sup>We remind the reader that we could only conclude as to the convergence of  $\mu_{\text{CF1}}$  and  $\mu_{\text{CF2}}$  for values of  $d/\Lambda < 0.15$ . We assume here that there is convergence for larger values of  $d/\Lambda$  as well. See the disclaimer at the end of the section.

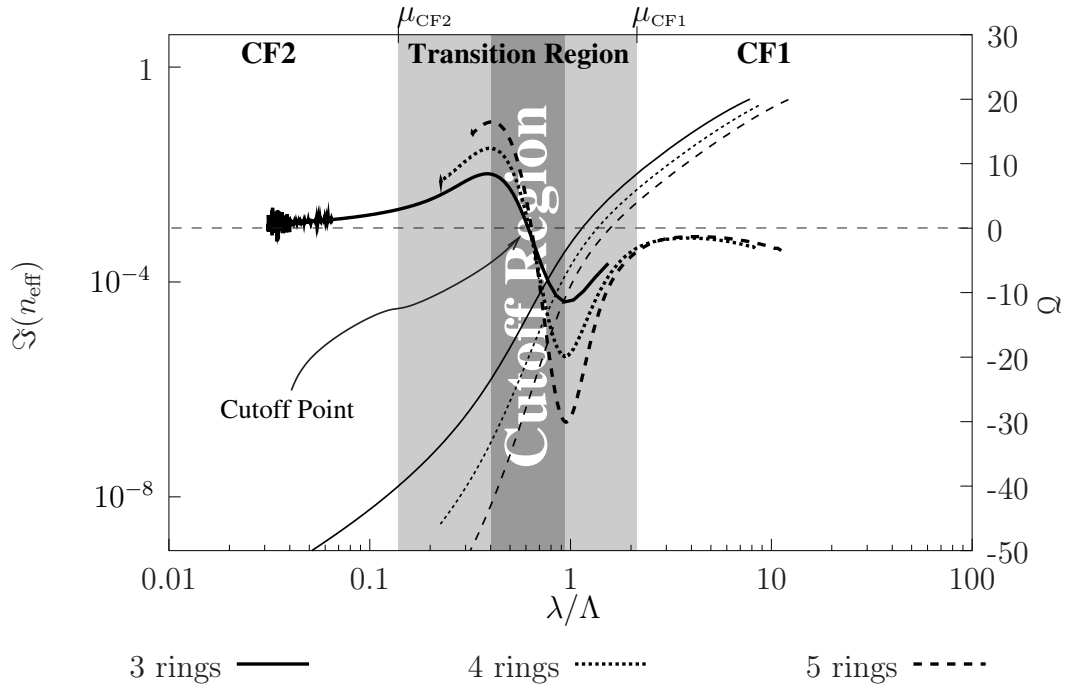


Figure 7.28: The different operation regions of a MOF. The curves show  $Q$  and  $\Im(n_{\text{eff}})$  for MOFs with 3 to 5 rings of inclusions and  $d/\Lambda = 0.3$ . The locus of the  $Q$  extrema delimit the cutoff region. The boundaries of the transition region are determined by the limit of validity of the CF1 and CF2 models.

$N_r$ .<sup>27</sup> This is reflected in quantity  $\mathcal{Q}$ : When in the region of validity of the CF2 model,  $\mathcal{Q} \simeq 0$ . With increasing  $\lambda/\Lambda$ , the slope of  $\Im(n_{\text{eff}})$  versus  $\lambda/\Lambda$  increases when leaving the CF2 regime, resulting in  $\mathcal{Q}$  taking positive values. When entering the CF1 regime the slope has to decrease rapidly, resulting in a negative  $\mathcal{Q}$  peak. Between the positive and the negative peaks, the slope of  $\Im(n_{\text{eff}})$  versus  $\lambda/\Lambda$  is maximum at the point where  $\mathcal{Q} = 0$ .

### Transition Region

The region where  $\mathcal{Q}$  takes values differing significantly from 0 is a region where neither the CF1 nor the CF2 models are valid. In that region, which we define to be the transition region, mode properties cannot be explained in terms of simple step index fibres.

### Width of the Transition Region

Further, we have seen that the width of the negative  $\mathcal{Q}$  peak keeps a finite non-zero value when  $N_r$  approaches infinity. This implies that the transition region keeps a finite, non-zero width, even for a single defect in an infinite photonic crystal.

In that region mode properties are fundamentally different from those of conventional step index fibres. The further away we are from the regions of validity of the CF1 and CF2 models, the more non-conventional, potentially interesting mode properties we can expect. It is between the two  $\mathcal{Q}$  extrema that the difference from conventional fibres is most important, and we will show in section 7.6.1 that it is indeed in that region that most interesting MOF properties have been found or predicted.

### Cutoff Point and Cutoff Region

Between the  $\mathcal{Q}$  peaks, at the point where  $\mathcal{Q} = 0$ , the slope of  $\Im(n_{\text{eff}})$  versus  $\lambda/\Lambda$  in a log-log plot diverges with increasing  $N_r$ . This implies a discontinuity in mode properties for infinite systems, and can be used to define a cutoff-point for infinite MOFs. Since we haven't done so earlier, we will study the convergence of this important point with  $N_r$  in Section 7.5.3. For finite MOFs the cutoff is nevertheless blurred, and it makes more sense to speak of a cutoff region. Rather than using what we have called so far the transition region, extending from  $\mu_{\text{CF2}}$  to  $\mu_{\text{CF1}}$ , we arbitrarily define the limits of the cutoff region by the locus of the extrema of the two  $\mathcal{Q}$  peaks. This is indeed the region of most drastic changes in modal properties. Fig. 7.28 summarizes the different operation regions defined above superimposed on loss and  $\mathcal{Q}$  curves for a MOF with  $d/\Lambda = 0.3$ .

### Mode Properties in the Cutoff Region

Since the cutoff-region seems to be the most interesting for MOFs, it is worth considering a few properties we can expect in that region.

**Convergence of properties with  $N_r$**  At the long wavelengths end of the transition region, mode properties derived from  $\Re(n_{\text{eff}})$  (*e.g.* dispersion) depend on  $N_r$ , so that we can expect mode properties to become increasingly sensitive to the actual number of rings when approaching the long wavelength limit of the cutoff region. When simulating MOFs in the cutoff

---

<sup>27</sup>But the slope doesn't need to diverge *everywhere* between  $\mu_{\text{CF2}}$  and  $\mu_{\text{CF1}}$ .

region it is therefore crucial to use methods which are able to deal with MOFs of finite cross section. In particular methods using supercell approximations –which should give accurate results in the whole CF2 region– should be used with care in the cutoff region.

**Confinement** It is in the cutoff region that the effective mode area increase with  $\lambda/\Lambda$  is most accentuated. In the CF2 region the mode is well confined in the core. Entering the cutoff region, the field distribution starts to expand; this implies that the fields start to become sensitive to the details of the structure beyond the core. When approaching the long wavelengths end of the cutoff region the field distribution covers the whole microstructured region of the MOF, and when entering the CF1 region the mode becomes exclusively confined by the boundaries of the microstructured region.

**Geometric losses** The losses are strongly wavelength dependent in the cutoff region. If MOFs are designed to operate in the cutoff region it becomes very important to check that geometric losses are acceptable for the whole wavelength range. Since in the transition region losses are dragged down at the short wavelengths end by the exponential decay of losses with  $N_r$  in the CF2 region, losses decrease (almost) exponentially with  $N_r$  in the whole cutoff region.

**Bend-loss** The effective area increasing abruptly around the cutoff-point, we can expect bend-loss to become important for the long wavelengths part of the cutoff-region. Nevertheless, in that region geometric loss generally becomes prohibitive, so that the bend-loss might not be the limiting factor. This question remains to be studied in detail in connection with the cutoff.

**Sensitivity to structural flaws** We have seen that in the CF1 region mode properties are mainly dictated by the average air filling fraction and by the boundaries of the microstructured region of the MOF, but are largely insensitive to the exact position and size of inclusions. In the CF2 region, the mode being well confined, mode properties are quite sensitive to the geometry of the first ring of inclusions, but *a priori* are largely unaffected by defects in the periodicity beyond the first ring of inclusions. In contrast, in the cutoff-region fields extend beyond the core, but homogenization is not yet effective. Propagation properties become sensitive to the exact position and size of inclusions beyond the first ring: the sensitivity to structural flaws is exacerbated, which renders the fabrication of MOFs designed to operate in that regime particularly challenging. Comparisons between theory and experiments also become delicate, since smallest differences in the geometry (exact size, shape and position of each hole) and refractive index distribution between experimental and simulated MOFs could affect results.

Table 7.1 summarizes mode properties for the fundamental mode in the different parameter space regions of MOFs. In the transition region, excluding the now well defined cutoff region, properties can not be predicted by either of the asymptotic models, but properties are not as dramatically different from those predicted by these models as in the cutoff-region: Between  $\mu_{CF2}$  and the lower edge of the cutoff region (maximum of the positive  $Q$  peak) properties can not be predicted by the CF2 model, but properties are still globally similar to those found in the strict region of validity of the CF2 model. The same applies for the upper part of the transition region, between the minimum of the negative  $Q$  peak and  $\mu_{CF1}$ , where mode

Properties	CF2	Cutoff Region	CF1
Mode properties depend on	$\lambda/\text{Core size}$	Detailed MOF geometry	$\lambda/\text{Fibre size}$
Convergence with $N_r$ of $\Re(n_{\text{eff}})$ and derived properties	Exponential convergence	Almost exponential convergence	No convergence
$\Im(n_{\text{eff}})$ decrease with $N_r$	Exponential	Almost exponential	Power law
Geometric Loss	Arbitrarily Small $\Im(n_{\text{eff}}) \sim (\lambda/\Lambda)^2$	Highly wavelength dependent	Very Large $\Im(n_{\text{eff}}) \sim (\lambda/\rho)^\alpha$
Bending loss	Short wavelength bend-loss edge	Long wavelength bend loss edge	
Mode confinement	In core	In core and cladding	In cladding
Sensitivity to structural flaws	High for flaws concerning the first ring of inclusions, relatively small beyond the first ring	High	Small

Table 7.1: Summary of mode properties in the different parameter space regions.

properties are globally similar to those predicted by the CF1 model. For simplicity we will henceforth denote by “CF1 region” and “CF2 region” the whole parameter-space regions where mode properties are similar to those predicted by the CF1 or the CF2 models respectively, including the tails of the transition region, so that we will only distinguish between CF1-, cutoff- and CF2-regions.

### 7.5.2 Second Mode

Most considerations concerning the fundamental mode can be applied directly to the second mode. However, we draw attention to a few differences between the fundamental mode and the second mode cutoffs:

The convergence of the locus of the negative  $Q$  peak is much clearer for the second mode than for the first mode. Further, we have seen that the negative  $Q$  peak for the second mode becomes infinitely narrow when  $N_r$  approaches infinity, whereas this peak remains of finite width for the fundamental mode. The fact that the negative  $Q$  peak determining the limit of the CF1 regime becomes infinitely narrow implies that the point of maximum slope, where  $Q = 0$  in the transition region, is getting infinitely close to  $\mu_{\text{CF1}}$ . This means that in the case of infinite  $N_r$  the CF1 model becomes valid “instantly” at  $\lambda/\Lambda = \mu_{\text{CF1}}$ , and the cutoff-point coincides with  $\mu_{\text{CF1}}$  for infinite  $N_r$ . In Section 7.2.2 we identified the locus of the cutoff with the locus of the  $Q$  minimum. It appears that the two definitions are equivalent for the second mode for infinite  $N_r$ . We can therefore keep the phase diagram of the second mode we established in Section 7.2.4 without any changes.<sup>28</sup>

<sup>28</sup>Further, since  $\mu_{\text{CF1}}$ , the cutoff-point and the locus of the minimum of negative  $Q$  peak coincide for infinite  $N_r$ , we are also exempt from studying the convergence of the cutoff-point defined by  $Q = 0$ .

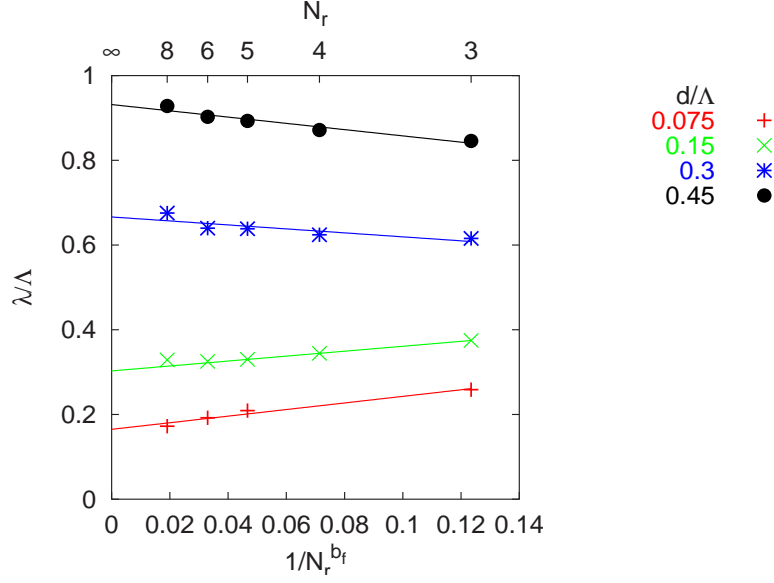


Figure 7.29: Points of maximum slope ( $\mathcal{Q} = 0$ ) of the logarithmic loss plots as a function of  $1/N_r^{b_f}$ . Here  $b_f \simeq 1.90$ .

We did not study the behaviour of the positive  $\mathcal{Q}$  peak when we were studying the cutoff of the second mode, because we hadn't discovered it at that time. Looking at Fig. 7.11, it becomes now obvious that there is a positive  $\mathcal{Q}$  peak for the second mode as well. Indeed the slope of the  $\Im(n_{\text{eff}})$  versus  $\lambda/\Lambda$  curve in the log-log plot decreases with decreasing wavelength before stabilizing when the CF2 regime becomes valid. Although we are confronted with the same limitations as when studying the evolution of the positive  $\mathcal{Q}$  peak for the fundamental mode, from the limited data we have gathered it appears that the locus of the maximum of the positive  $\mathcal{Q}$  peak converges with increasing  $N_r$ , and also that the width of this peak remains finite. Hence, even if the portion of the transition region lying between the cutoff point and  $\mu_{\text{CF1}}$  collapses for infinite  $N_r$ , a finite transition region remains between  $\mu_{\text{CF2}}$  and the cutoff-point, even for infinite  $N_r$ .

### 7.5.3 Study of the Cutoff-Point and Disclaimer

Fig 7.29 shows  $\mu_C$ , the locus of the points where  $\mathcal{Q} = 0$  between peaks, as a function of  $1/N_r^{b_f}$  for different values of  $d/\Lambda$ , for the fundamental mode.  $b_f$  is a positive parameter which has been optimized to obtain a straight line behaviour of the dataset for  $d/\Lambda = 0.15$ . A rapid look at the figure could lead to the conclusion that convergence is obvious. On the contrary, the figure is a perfect example of how choosing the right representation can show exactly what one wants to see. In fact, fits of the data with power laws are very poor and don't allow any extrapolation for infinite  $N_r$ . It appeared nevertheless that for  $d/\Lambda = 0.075$  and  $d/\Lambda = 0.15$  the data can be fit to an exponentially converging function of the type

$$\mu_C = a \exp(-bN_r) + c \quad (7.49)$$

with very satisfying accuracy. Such a function cannot be represented by a straight line in the kind of plots used for Fig.7.29. Nevertheless, the fit from Eq. (7.49) leads to the conclusion

that  $\mu_C$  does converge, and that is all we wanted to prove. But for  $d/\Lambda = 0.3$  and  $d/\Lambda = 0.45$  we could fit converging, diverging or constant functions with the same degree of unacceptable inaccuracy. We encounter the same difficulties in concluding about the convergence or divergence of the locus of the cutoff as we run into in Section 7.3.2. To be able to conclude definitively we would need data for values of  $N_r$  larger than 8.

Further we emphasize that there is no argument to prove *a priori* that  $\mu_C$  has to converge with  $N_r$ : For very large values of  $d/\Lambda$ , the inclusions eventually intersect and fill the whole microstructured part of the MOF. What remains is a single silica rod in vacuum, for which it is well established that there is no cutoff for the fundamental mode. It might well be possible that beyond a certain value of  $d/\Lambda$  the fundamental mode remains confined for  $N_r = \infty$  regardless of the wavelength. The only thing we can be sure of is that this value of  $d/\Lambda$  would be greater than 0.15.

Having mentioned that, we reassure the reader that, except in the counter-example of Fig. 7.29, whenever we have used the scaling law diagrams with  $1/N_r^{-b}$  in abscissa, we have done so in all conscience and with the best intentions. Nevertheless, one should keep in mind that all results we have mentioned concerning an infinite number of rings ensue from extrapolations and should not be considered as being unalterable truth.<sup>29</sup>

To end this disclaimer on a more positive note, we would like to remind the reader that, although it would have been quite satisfying to find properties intrinsic to a single defect in an infinite lattice, all experimental MOFs have a finite number of rings.

## 7.6 MOF Phase Diagrams

### 7.6.1 Fundamental Mode Phase Diagram

#### Establishing the Phase Diagram

Fig. 7.30 shows the phase diagram for the fundamental mode. It is somewhat more complicated than the phase diagram for the second mode, since it includes the curve of cutoff points along with the boundaries of the cutoff region. We also added the cutoff-curve of the second mode established in Section 7.2.4, and the locus in parameter space of MOFs with experimentally established or theoretically predicted interesting properties, which we will discuss in the next section.

We established the upper limit of the cutoff-region, which corresponds to the locus of the minimum of the  $Q$  curves for different  $d/\Lambda$ , in exactly the same way as we did for the second mode phase diagram. The corresponding curve in Fig. 7.30 [curve (1)] is the result of a best fit of the  $Q$  minimum data for<sup>30</sup>  $N_r = 4$  with a function similar to Eq. (7.6). We find

$$\frac{\lambda}{\Lambda} = \alpha(d/\Lambda - b)^\gamma \quad (7.50)$$

where  $0 < b < 0.06$ ,  $\alpha \simeq 2.63 \pm 0.03$  and  $\gamma \simeq 0.83 \pm 0.02$ . With increasing  $N_r$  this curve shifts slightly towards larger values of  $\lambda/\Lambda$  for  $d/\Lambda \gtrsim 0.3$  and towards smaller values of  $\lambda/\Lambda$  for  $d/\Lambda \lesssim 0.3$ .

<sup>29</sup>Incidentally, we do not have the pretension of believing that any of the results in this thesis is unalterable truth.

<sup>30</sup> $N_r = 4$  is the largest number of rings for which we could extract the locus of the minimum of  $Q$  for values of  $d/\Lambda$  up to 0.75.



Data set 2 shows the location of experimental zero-dispersion wavelength measures, which were compared to theoretical values from a CF2 model in the original publication [37]. For the two lower points (b and d) which lie in the CF2 region, comparison with the CF2 model gave good agreement, for point c agreement was approximate and for point a, lying in the cutoff region, the agreement was unsatisfactory.

The third data set, which we will study in more detail in Chapter 8, consists of regions of observed or predicted flat or oscillating chromatic dispersion, taken from Refs. [35, 36, 38, 62, 66]. All data points herein are located exactly in the cutoff region, using the increased and highly configurable wavelength dependence of structural dispersion to compensate material dispersion. The consequences of being in the cutoff region are that confinement losses are highly wavelength dependent, and that the waveguide dispersion is sensitive to the actual fibre geometry. Such high sensitivity to structural imperfections was observed by Monro et al. [111], and indeed the fibre parameters used by these authors are in the cutoff region (data line 4).

In studying the influence of the number of rings on dispersion (Ref. [35] and Chapter 8), we observed that the dispersion does not necessarily converge with the number of rings. Data set 5 shows the location of an example where the dispersion converges with  $N_r$  in a limited wavelength range before diverging with  $N_r$ . The wavelength range where dispersion properties diverge crosses the transition line from the cutoff region to the CF1 region, where we have seen  $N_r$  dictates mode properties.

Although we tried to map as many published MOF designs as possible onto Fig. 7.30, a few were omitted: some were overlapping the cutoff region and the CF2 region and had more conventional dispersion properties, while others were beyond the scope of this study (e.g. grossly non-circular holes). One theoretical study by Monro et al. [66] had two examples of MOFs lying in the CF1 region, with both displaying conventional dispersion. It should be emphasized that no experimental MOF has been published with parameters in the CF1 region.

### Phase Diagram and Geometric Losses

We have mentioned that in the CF1 region geometric losses are “high” while they are “small” in the CF2 region, but haven’t quantified this assertion yet. Indeed, even in the CF2 region, losses can be large if the number of rings is insufficient; in the cutoff region losses vary very quickly, and it is important to know how many rings of inclusions are needed for losses to be acceptable. Fig. 7.31 shows the curves defined by the  $\lambda/\Lambda$  values from which losses are larger than 1 dB/m, as a function of  $d/\Lambda$  for several values of  $N_r$ , for the fundamental as well as the second mode. The curves get closer to the cutoff-point curve with increasing  $N_r$ , which is consistent with the fact that the slope of the loss versus  $\lambda/\Lambda$  diverges with increasing  $N_r$  at the cutoff point. It appears that for small values of  $d/\Lambda$ , more than 8 rings are needed to achieve acceptable losses in the cutoff-region.

We have continued the 1dB/m curve for the second mode of the 4 ring MOF beyond cutoff: on the left hand side of the second mode cutoff curve, the mode is cladding filling, but losses can still be small.

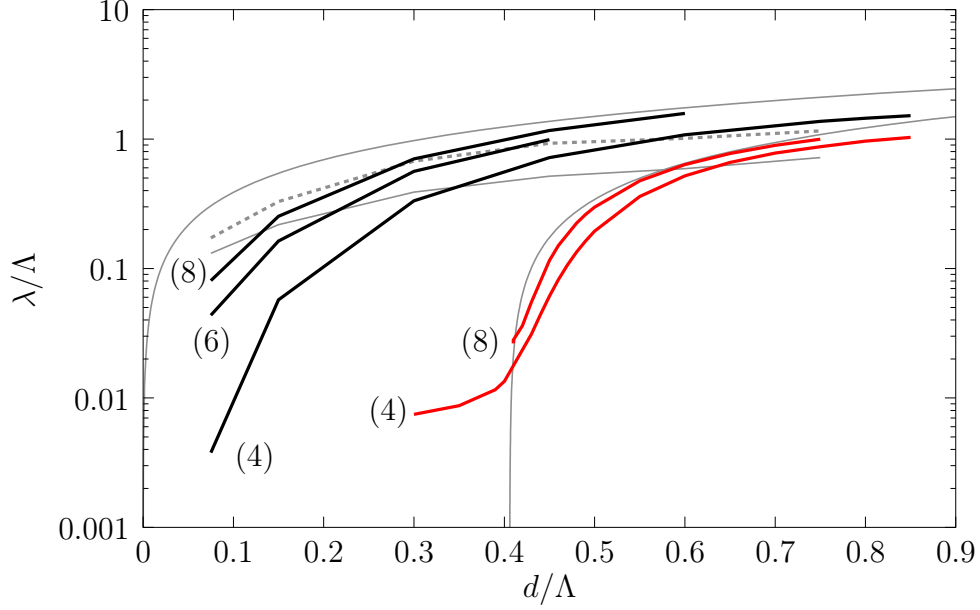


Figure 7.31: 1 dB/m loss curves for the fundamental (upper three black thick three curves) and second (lower two curves) mode for several values of  $N_r$  (in brackets): Above each curve, losses are larger than 1 dB/m for the given MOF. In the background is the phase diagram from Fig. 7.30. Losses were computed for  $\lambda = 1.55 \mu\text{m}$ .

### 7.6.2 Using the Phase Diagram

The phase diagram of Fig. 7.30 already gives an idea of the region of parameter space in which specific mode properties of MOFs consisting of a core surrounded by a hexagonal periodic arrangement of holes can be found. It could also be used to understand and design MOFs with more complex cladding or core structures, as we suggest here:

#### Changing the Core Size

In the CF2 region mode properties are dictated by the core size and we have

$$n_{\text{eff}} \simeq n_M - \nu_f \left( \frac{\lambda}{\rho_c} \right)^2 \quad (7.51)$$

where, for large number of rings,  $\nu_f$  depends only on  $d/\Lambda$  but not on  $\rho_c$ .<sup>32</sup> A necessary condition for CF1 to be valid is that  $n_{\text{eff}} < \bar{n}_z$ , so if we consider the cutoff to occur in the vicinity of the point where  $n_{\text{eff}} = \bar{n}_z$ ,<sup>33</sup> we have,  $\lambda_c$  being the wavelength at cutoff<sup>34</sup>

$$\lambda_c \simeq \left( \frac{n_M - \bar{n}_z}{\nu_f} \right)^{1/2} \rho_c. \quad (7.52)$$

<sup>32</sup>This follows from Eqs.(7.39-7.44).

<sup>33</sup>This is coherent with the observation that the cutoff occurs at  $n_{\text{eff}} \simeq n_{\text{FSM}}$ , see Section 7.2.3.

<sup>34</sup>Note that we use the asymptotic expansion of  $n_{\text{eff}}$  near the cutoff, where we know it is not valid. The result is therefore very approximate, and should only give an idea of the direction of change in  $\lambda_c$  with varying  $\rho_c$ .

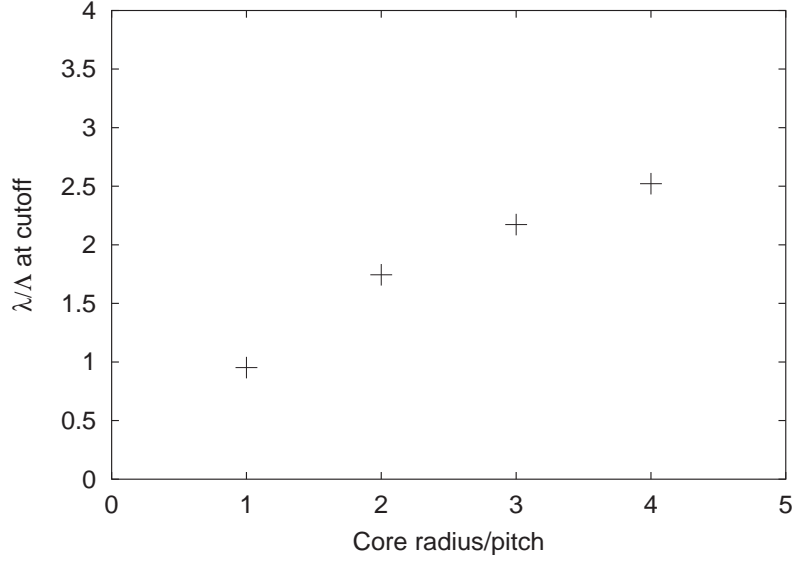


Figure 7.32:  $\lambda/\Lambda$  at cutoff with varying core radius, for the fundamental mode of MOFs with  $d/\Lambda = 0.3$ . The core radius is defined by the distance from origin to the center of the first inclusion. We used structures with  $N_r = 5$  for MOFs with cores consisting of up to two missing rings and  $N_r = 6$  for the core constituted by 3 missing rings, so that there are always at least 3 rings of holes around the core.

If one increases the core size, for example through leaving out more than one central inclusion, the CF1 model will therefore start to become valid at longer wavelengths, and the cutoff can be expected to be shifted towards longer wavelengths. This is indeed the case as can be seen in Fig. 7.32 showing  $\lambda/\Lambda$  at cutoff as a function of core radius for an example of MOFs with  $d/\Lambda = 0.3$ .

### Rings with Inclusions of Different Sizes

We consider a MOF with a first ring of inclusions with diameter  $d_1$  and further rings of inclusions with diameter  $d_2$  (Fig. 7.33). The cutoff wavelength  $\lambda_1$  of a MOF where all inclusions have diameter  $d_1$  can be extracted from the phase diagram, and we suppose we have a good estimation of the cutoff wavelength  $\lambda_2$  of the MOF consisting of inclusions with diameter  $d_2$  and a core extended to a whole missing ring. We suppose that the values of  $\lambda_2$  and  $\lambda_1$  are not “too close”, and that  $\lambda_1 < \lambda_2$ . If the wavelength  $\lambda$  of the guided light is smaller than  $\lambda_1$ , the light will be confined in the core consisting of the missing central inclusion. If with increasing  $\lambda$  we enter the cutoff region of the first ring, the first ring doesn’t confine the light anymore, and the mode starts to leak beyond it. The CF1 model becomes valid for the first ring, and the MOF can now be seen as a core consisting of one missing ring surrounded by rings of inclusions with diameter  $d_2$ .<sup>35</sup> Since the wavelength is at this stage still shorter than  $\lambda_2$ , the mode is now confined by the cladding of the new equivalent MOF. If  $\lambda$  increases further, the mode will eventually undergo the cutoff for the second structure around  $\lambda_2$  (see

<sup>35</sup>The core has a homogenized index which is slightly lower than the matrix, but as long as this index is initially larger than  $n_{\text{FSM}}$  for  $d_2/\Lambda$  this shouldn’t be of concern for the confinement.

Fig. 7.33). We could imagine to use this kind of design –similar to double clad fibres [112]– to separate the confinement regions of a mode at two different wavelengths, or equivalently to increase the numerical aperture at one wavelength while keeping a good confinement at another wavelength. Note that the wavelength with a better confinement is necessarily the shorter wavelength, so that this design couldn't for example be used as is in fibre lasers with the idea of having a large numerical aperture at the shorter pump wavelength while keeping the longer lasing wavelength well confined.<sup>36</sup> The effect could nevertheless be used *e.g.* for frequency doubling.

As an example of the use of cutoff considerations for the design of double clad MOFs, we consider a MOF with  $N_r = 5$ , the inclusions of the three first rings being of diameter  $d_1 = 0.15\Lambda$  and the inclusions of the two outer rings of diameter  $d_2 = 0.45\Lambda$  [MOF (3) on Fig. 7.34]. From the phase diagram, we know the cutoff region associated with the first few rings of holes. When well below cutoff, the CF2 model is valid for the first few rings: the mode is confined and the influence of the exterior rings is limited to an overall decrease of losses, so that mode properties are very similar to the usual MOF with 5 rings of inclusions having same  $d/\Lambda = 0.15$  [MOF (1) in Fig. 7.34]. Beyond cutoff, the CF1 model becomes valid ( $\lambda/\Lambda \gtrsim 0.5$ ) for the first few rings: the outer rings will now become of importance. Using the scaling law of the cutoff wavelength with core size given in the previous section [Eq. (7.52)], we expect the cutoff of the MOF made out of the two exterior rings [MOF (2) in Fig. 7.34] to be around  $\lambda/\Lambda \simeq 3$ , so that for  $0.5 < \lambda/\Lambda < 3$  the mode will be confined by the two outer rings of inclusion. Since the CF1 model is valid for the first few rings, the refractive index of the core of the equivalent fibre in this regime is not  $n_M$ , but  $[\bar{n}]$  [MOF (2)], which slightly modifies the cutoff wavelength. Fig. 7.35 shows  $Q$  as a function of  $\lambda/\Lambda$  for the double clad MOF [MOF (3)], the equivalent MOF for short wavelength [MOF (1)] and the equivalent MOF between both cutoffs [MOF (2)]. For the double clad MOF, quantity  $Q$  no longer has two simple peaks marking the cutoff region. At short wavelengths its value follows  $Q$  for the short wavelength equivalent model MOF (1), while at longer wavelengths its value is dictated by  $Q$  of MOF (2). For intermediate wavelengths  $Q$  has a more complex behaviour. We also added the normalized mode radius for the double clad MOF, defined here as  $(A_{\text{eff}}/\pi)^{1/2}/\Lambda$  on Fig. 7.35: It is remarkable how the mode is indeed confined in the core delimited by the first ring at short wavelength ( $(A_{\text{eff}}/\pi)^{1/2}/\Lambda \simeq 1$ ) approximately until the cutoff associated with MOF (1), then fills the region defined by the three first rings ( $(A_{\text{eff}}/\pi)^{1/2}/\Lambda \simeq 3$ ), and around the cutoff of the second equivalent MOF starts to diverge.

Note that we have chosen this example for its didactic simplicity, but since the wavelength range covers almost two orders of magnitude it shouldn't be of immediate interest in practice. Although increasing the number of rings sharpens the cutoff, it is unlikely phenomena of the order described here could happen in a much narrower wavelength range. In general the cutoff wavelengths associated with the different equivalent MOFs will not be well separated, so that the cutoff regions overlap. Nevertheless, this can be used to broaden or narrow the cutoff region and more generally to tailor the cutoff region properties, for example to adjust dispersion properties while keeping low losses, as we will show in Chapter 8.

<sup>36</sup>To get a good pump injection efficiency with a good confinement in MOF lasers, one can nonetheless use similar designs, using higher order modes of the inner cladding (region with small holes) confined by an outer cladding (region with bigger holes). See for example Refs. [113, 114].

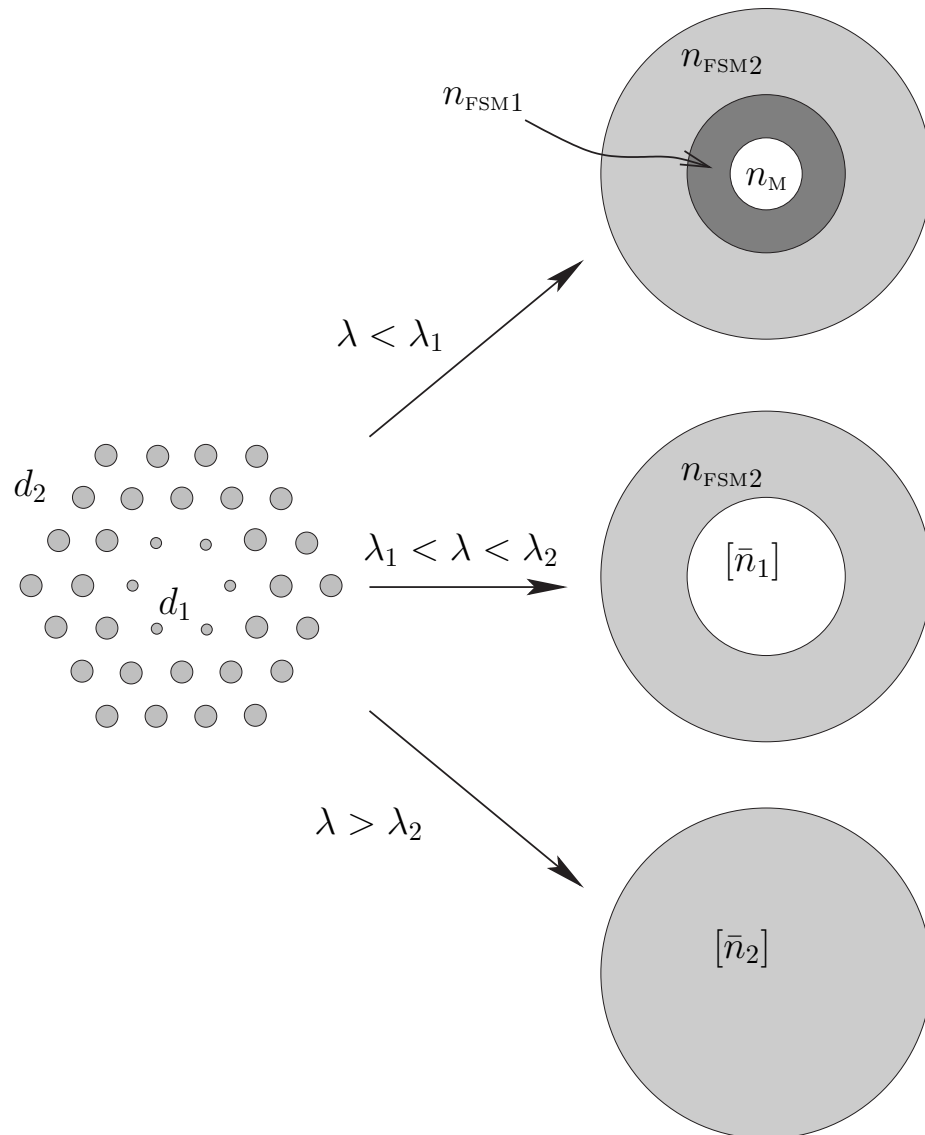


Figure 7.33: Example of wavelength dependent equivalent fibres for MOFs with ring dependent inclusion diameters.

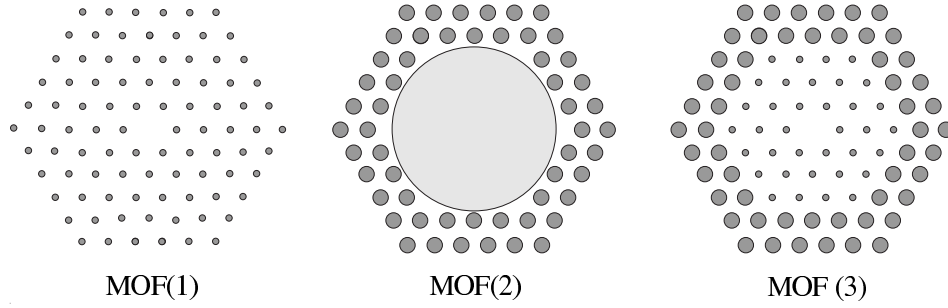


Figure 7.34: Designs used for the double clad MOF example of Fig. 7.35. MOF (3) is the studied double clad MOF:  $d/\Lambda = 0.15$  for the three inner rings and  $d/\Lambda = 0.45$  for the two exterior rings. MOF (1) is the usual MOF design with  $d/\Lambda = 0.15$ , and MOF (2) is a MOF equivalent to the double clad MOF (3) beyond the cutoff of MOF (1).

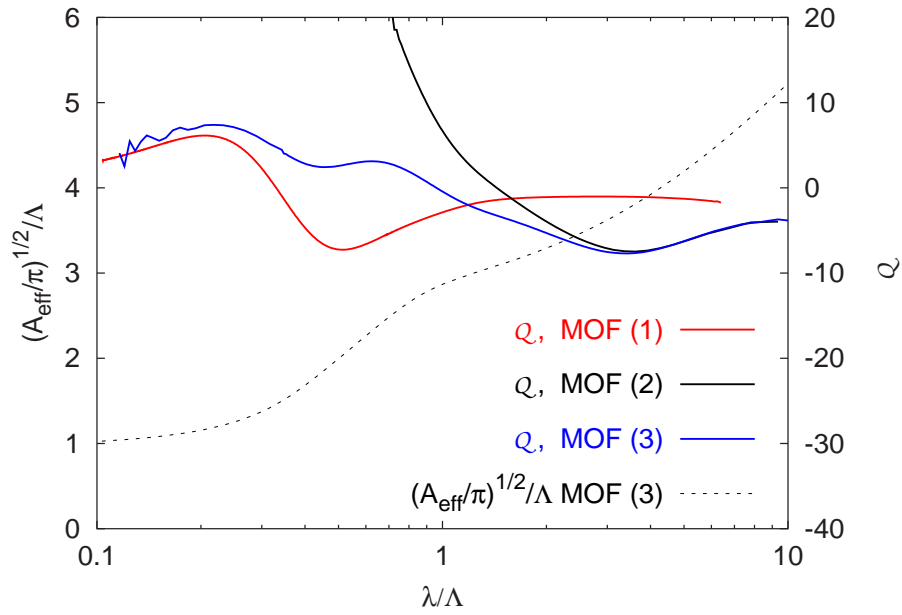


Figure 7.35: Designing double clad MOFs:  $Q$  curves and mode radius as a function of  $\lambda/\Lambda$  for the double clad MOF (3) and the two wavelength dependent equivalent MOFs (1) and (2). The geometry of MOFs (1-3) is detailed in Fig. 7.34.

### 7.6.3 Towards Other Phase Diagrams and Charts of Operation

We have established Fig. 7.30 using the cutoff criterion defined through slope properties of the loss curves associated to geometric confinement properties. However, in some cases other criteria might be more pertinent. For example when working at short wavelengths, the short wavelength bend loss edge must be considered, and delimits a lower region to the useful part of the CF2 region in Fig. 7.30.

In cases where single modedness is important yet not vital, the cutoff curve of the second mode might not be the only one of interest: Even when multimoded, the beat length between the first and second mode can be so small that mode conversion between confined modes is negligible [69], so that MOFs can be operated as if they were single-mode fibres. On the contrary, when strict single modedness is crucial, even in the endlessly single-mode region cladding modes can become a nuisance: For  $d/\Lambda < 0.406$  and at very small  $\lambda/\Lambda$  ratios ( $\lambda/\Lambda \ll 0.1$ ) the second mode, although not undergoing a cutoff as we have defined it here, becomes slowly and gradually confined near the core region.<sup>37,38</sup> Further, scattering of the fundamental mode into higher order, lossy cladding modes can occur through inevitable imperfections in the structure, increasing geometric losses [115] and potentially causing pulse spreading.

For efficient MOF design, it would be useful to draw charts of the parameter space showing the degree of nuisance (or benefit) of the mentioned phenomena. Figs. 7.30 and 7.31 are a first step towards this collection of charts.

### 7.6.4 Impact on Results of the Previous Chapters

#### Extended Modes

Extended modes as we have defined them in Sec. 6.3.3 are resonances of Bloch waves. The asymptotic model for the confinement derived here can not be applied to these modes: the CF2 model uses the fundamental space filling mode to define the effective index of the cladding, but Bloch modes are by definition band modes, *i.e.* modes with an effective index lower than  $n_{\text{FSM}}$ . Hence, they can not be reflected through the mechanisms responsible for confinement in the CF2 model, and can not undergo a localization transition.

#### Defect and Extended Transition Modes

These are the modes for which we have demonstrated the cutoff. In the examples studied in Chapter 6, the Bloch transform of these modes was observed to be essentially circularly symmetric and close to the origin. This can be understood in the frame of the CF1 model. When in the homogenization regime the perpendicular wavelength is set by the outer radius of the cladding region so that the fields are globally in phase everywhere in the cladding. The Fourier-Bessel coefficients for all inclusions are therefore in phase as well and the Bloch vector associated with the field distribution is a peak centered on zero.

#### Numerical Examples of Previous Chapters

We have mentioned several times in the previous Chapters that the choice of parameters was “unfortunate”, leading to results lacking in generality. What we meant was that the parameters

<sup>37</sup>This is accompanied by the geometric losses of the second mode becoming small, see Fig. 7.31.

<sup>38</sup>Nevertheless bend-loss becomes a serious problem at such small  $\lambda/\Lambda$  ratios, so that this region of parameter space should rarely be of interest.

were in a specific region of the phase diagram, and that a correct interpretation of results is impossible without knowing whether the mode is well confined, in the cutoff region or beyond cutoff. In Section 6.3.2 for example we studied the losses of the fundamental mode as a function of  $N_r$  and mentioned that the decay was neither a power law nor exponential. If we locate the parameters used for the study ( $d/\Lambda = 0.15$ ,  $\lambda/\Lambda = 0.674$ ) it appears that we are at the edge of the CF1 region, very close to the cutoff region. Note that we used these parameters throughout Chapter 6, and were actually quite lucky to find a confined mode at all. Results of Chapter 6 regarding the evolution of mode properties with increasing  $N_r$  have naturally to be put into the perspective of the region of parameter space for which they were established.

When we were comparing experimental results by Kubota *et al.* [92] with results found through the multipole method (Section 4.7.3) we claimed that the influence of  $N_r$  on the dispersion properties was negligible and that the decay of losses with  $N_r$  was exponential for the first three modes. This is coherent with the locus of the used parameters ( $d/\Lambda = 0.668$ ,  $\lambda/\Lambda \simeq 0.3 - 0.4$ ) in the phase diagram, but one should not claim that these results are general.

At the end of the same Section, we mentioned that agreement between the multipole method and other simulation tools was sometimes quite unsatisfactory. The examples where this occurred were always either in the cutoff or in the CF1 region, and the methods with which agreement wasn't good were using supercell approximations, which, as we have shown in this Chapter, can not give accurate results in the CF1 and in the cutoff region.

Finally, in Section 4.3.1 we used an absorbing jacket, initially for “mathematical convenience” and claimed that the imaginary part of the jacket's index didn't have much effect on the modes. We were quite lucky again to have used fibre parameters which were well inside the CF2 region ( $d/\Lambda = 0.775$ ,  $\lambda/\Lambda = 0.22$ ), so that modes were indeed well confined and the jacket didn't have much effect. Our conclusions would certainly have been different if the parameters had been in the CF1 region.

Dessert :

## Dessert : Stratifié de Chocolat, de Pralin et d'Orange

*Chocolate, Pralin and Orange Gradation*

**Pour 6 personnes :**

Pour le biscuit chocolat :

6 œufs  
225 g de chocolat à pâtisserie  
à 64%  
150 g de sucre  
150 g de beurre pommade  
75 g de farine tamisée  
50 g de cacao en poudre  
1/2 cuillerée à café de café  
soluble  
1 cuillerée à soupe rase  
d'extrait de vanille  
1 cuillerée à soupe de Kirsch

Pour le pralin :

150 g de noisette en poudre  
75 g de sucre en poudre  
1 cuillerée à café d'extrait  
naturel de vanille

Pour la ganache :

200 g de chocolat à pâtisserie  
à 64%  
20 cl de crème fleurette  
100 g de sucre  
1 cuillerée à café de fleur  
d'oranger

**Le granité à l'orange**

**D**ISSOUDRE les trois-quarts du sucre glace dans le jus d'orange et verser la moitié du jus de citron. Ajuster le sucre et le jus de citron au goût, la quantité exacte dépendant du degré de maturité des oranges. Le résultat doit être bien sucré et légèrement acidulé. Verser en moule métallique (moule à gâteau) puis procéder de la même façon que pour la recette du trou du vigneron (*cf.* p.69).

**Le biscuit chocolat**

**F**ONDRE le chocolat au bain-marie, une fois fondu y ajouter le cacao, l'extrait de vanille, le Kirsch et le café soluble. Hors du feu, ajouter le beurre pommade par parcelles. Battre les œufs entiers avec le sucre jusqu'à ce qu'ils moussent. Incorporer le chocolat fondu puis la farine tamisée. Couler l'appareil en ramequins tapissés de papier cuisson ou en moules à muffin Flexipan. Cuire 9 minutes au four préchauffé à 220°C. Laisser refroidir, démouler, couper en deux disques de même épaisseur.

**Le pralin**

**C**HAUFFER dans une poêle la noisette en poudre, le sucre et l'extrait de vanille en remuant fréquemment à l'aide d'une spatule en bois. Lorsque le tout prend une coloration dorée et tend à s'agglomérer, arrêter la cuisson. Laisser refroidir en remuant de temps en temps.

**La ganache**

**P**ORTER la crème à ébullition, hors du feu, ajouter le sucre. Verser la crème sur le chocolat coupé en petits morceaux. Homogénéiser. Ajouter la fleur d'oranger. Une fois tiède, incorporer la moitié du pralin, laisser reposer.

Pour le granité à l'orange :

*500 cl de jus d'oranges  
Navel fraîchement  
pressées  
le jus d'un citron  
environ 150 g de sucre  
glace*

La garniture :

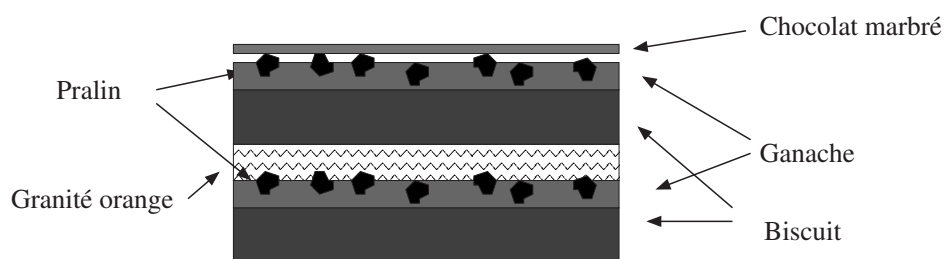
*500 g de couverture  
noire amère  
100 g de couverture  
blanche*

### La garniture

FONDRE et tempérer la couverture ivoire et noire séparément. À l'aide d'un cornet, déposer sur Rhodoïd la couverture ivoire, puis recouvrir de couverture noire et lisser en une couche d'un millimètre d'épaisseur en donnant un effet marbré. Laisser prendre un peu puis détailler à l'emporte-pièces en disques de même taille que les disques de biscuit au chocolat. Enfin laisser prendre complètement.

### Montage

LE cas échéant, sortir du froid la ganache une heure au moins avant le service. Au moment de servir, recouvrir les disques de biscuit d'une couche de 4 mm de ganache. Saupoudrer de pralin. Déposer une couche de 7 mm de granité à l'orange sur six des disques de biscuit, puis recouvrir des six autres disques de biscuit. Déposer un disque de couverture marbré par dessus, servir sans attendre.



Montage du stratifié

## Chapter 8

# Dispersion Properties

### 8.1 Introduction

In this Chapter we discuss dispersion properties of MOFs through the example of two recent papers the author of the present thesis has co-authored. We have included the two papers nearly as is, with only minor copy-editing to ensure the notations, bibliography and layout are consistent with the rest of the thesis. We have left the content untouched although with the results from Chapter 7 – most of which were established after the two papers were submitted – we would now certainly approach things differently. We have added comments in a separate section following each paper, highlighting how the knowledge of results from Chapter 7 leads to a new interpretation of results, or how it could have been used to direct our research. We hope this approach to be didactic in that it shows the advantage one can gain from using the phase diagram given in Fig. 7.30, while giving new insights on dispersion properties of MOFs.

The first article [35] was submitted before we fully understood the cutoff of the second mode, and well before we were aware of the fundamental mode cutoff and hence the existence of an *a priori* interesting cutoff-region in parameter space. Its aim was to establish the dependence of dispersion properties on all MOF parameters, including the number of rings, in connection with structural losses. Dispersion properties of solid core MOFs had already been studied extensively previously (see *e.g.* [116]), but with models using super-cell methods, which didn't take into account the finite size of the MOF cross section, and couldn't give the confinement losses. In our study, we show that dispersion generally *is* sensitive to the number of rings.

The second paper [117] was submitted after we had determined the first and second mode cutoff-diagrams, however not all results of Chapter 7, in particular those of Sec. 7.6.2, were yet established. Extending the study of the influence of the number of rings on dispersion properties, the study reported in the paper leads to two conceptually different MOF designs with very desirable dispersion properties. The first design, a usual endlessly single-mode solid core MOF with identical air holes forming a triangular lattice, yields ultra-flat near-zero normal or anomalous group velocity dispersion (GVD) over a very wide range of wavelengths. However the fundamental mode of that structure has relatively large effective area, and to achieve acceptable losses, at least 18 rings of holes have to be used. The second, innovative, design uses air holes of different diameters in successive rings and yields similarly interesting dispersion properties but with very low losses and reasonable effective area, compatible with usual optical fibres.

Finally, in a last section, we come back to the discussion we started at the end of Sec. 4.7.3 regarding the unsatisfactory agreement between theory and experiment as far as dispersion properties are concerned.

## 8.2 Chromatic Dispersion and Losses of Microstructured Optical Fibers

Authors: B. Kuhlmei, G. Renversez, and D. Maystre

*Date of submission: 26 July 2002*

Published in Applied Optics OT, Vol. 42, No. 4, 1 February 2003, pp. 634-639.

### 8.2.1 Introduction and Background

Microstructured optical fibers (MOFs) are generally made of a regular lattice of cylindrical inclusions, for example air holes, in a dielectric matrix. MOF cores usually consist of a defect of the lattice which can be an inclusion of different type or size or, in bulk core MOFs, a missing inclusion. In recent publications [37, 39], attention was drawn to the peculiar and interesting dispersion properties that MOFs can exhibit, and which indicate that MOFs may be good candidates for dispersion management in optical communication systems. In this paper, we use a fully vector and rigorous multipole method [1, 84], which we have recently co-developed with the group of R.C. McPhedran at the University of Sydney in order to explore the dependence of chromatic dispersion upon wavelength and MOF geometry. We here concentrate on silica bulk core MOFs with a triangular lattice of air holes (see Fig. 8.1). The most important point in which this work contrasts with previous publications concerning MOF dispersion is that the multipole method used herein is able to deal with the finite cross-section of MOFs. We could therefore study the influence of the extent of the confining air-hole region on dispersion *and* on associated losses.

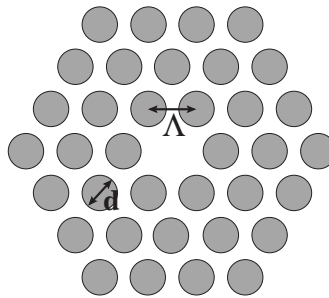


Figure 8.1: Cross-section of the modeled MOF with 3 rings of holes (holes are in grey),  $N_r = 3$ .  $\Lambda$  is the pitch of the triangular lattice, and  $d$  is the hole diameter. The solid core is formed by one missing hole in the center of the structure.

Our multipole method is a standard multipole method extended to conical mounts. It is based on local expansions of the vector fields in Fourier Bessel series and uses addition theorems to link these local expansions. Boundary conditions are implemented analytically for circular inclusions, so that the only approximations are the truncation of the Fourier Bessel series (see references [84] and [45] for a complete study) as well as the fundamental hypothesis of the

invariance of the fiber along its axis. If the inclusions overlap, our method is not appropriate. With the MOF geometry and the wavelength as inputs, the method gives the modes of the MOF as an output. Material dispersion can thus be included in a natural way in the MOF geometry, using for example Sellmeier expansions [4, 118].

A mode of a MOF is characterized by its field pattern and propagation constant  $\beta$  (or equivalently by its effective index  $n_{\text{eff}} = \beta/k_0$  where  $k_0$  is the free space wavenumber). Due to the losses resulting from the finite transverse extent of the confining structure, the effective index is a complex value, its imaginary part  $\Im(n_{\text{eff}})$  being related to the losses  $\mathcal{L}$  in  $\text{dB.m}^{-1}$  through the relation

$$\mathcal{L} = \frac{20}{\ln(10)} \frac{2\pi}{\lambda} \Im(n_{\text{eff}}) \times 10^6 \quad (8.1)$$

where  $\lambda$  is in  $\mu\text{m}$ . The dispersion parameter  $D$  is computed through the usual formula from the real part of the effective index  $\Re(n_{\text{eff}})$  [4]:

$$D = -\frac{\lambda}{c} \frac{\partial^2 \Re(n_{\text{eff}})}{\partial \lambda^2} \quad (8.2)$$

As in ordinary waveguides, dispersion of guided modes results from both material and waveguide dispersions. The remarkable feature of MOFs is that the waveguide dispersion can be modified significantly via a wide range of geometrical parameters, namely the positions and sizes of the different holes. The behavior of waveguide dispersion can be understood from effective-media heuristic considerations: at short wavelengths, light can distinguish the details of the structure, resulting in a greater concentration in the high index region (*i.e.* the core whose index is that of the matrix). In this situation, the effective index is smaller than the refractive index of the matrix. At longer wavelengths, the structure tends to a homogeneous one, and the effective index of the mode will consequently be bounded from above by the homogenized refractive index of the structure, which is much lower than the refractive index of the matrix, due to the air-inclusions. These heuristic considerations are unable to precisely predict MOF chromatic dispersion: a precise numerical study is required. Moreover, in practical applications, the losses have a vital importance. Detailed studies of losses in MOFs versus the pitch of air holes lattice, the hole diameter, and the hole ring number have already been carried out using the multipole method [84, 119]. A vector method using periodic boundary conditions [63] has already been used to study dispersion in MOFs [38], but in this model the influence of the number of hole rings cannot be investigated, and above all, the losses cannot be computed.

### 8.2.2 Validation

The method has been checked thoroughly via comparison with other numerical methods: fictitious source [90], other multipole methods [77, 91] (more details on these comparisons can be found in our previous article [84]).

Symmetry properties of fibers are accurately satisfied [45]: for a MOF with a rotational symmetry of order 6, the fundamental mode is twofold degenerate as expected by Mc Isaac's theory [76].

The method we co-developed and its numerical implementation have also been compared with plane-wave method for a microstructured optical fiber with a ring of six air holes of

Dispersion		Dispersion Slope	
Measured	Calculated	Measured	Calculated
-77.7	-77	0.464	
	-78.6		0.450
-76.78 ( $N_r = 3$ ); -76.95 ( $N_r = 4$ )		0.458 ( $N_r = 3$ ); 0.455 ( $N_r = 4$ )	

Table 8.1: Comparison of the dispersion  $D$  and its slope measured and calculated by Gander *et al.* at  $\lambda = 0.813 \mu\text{m}$  (they did not compute the dispersion slope and  $N_r$  value is not given in their text so only a estimated value can be deduced from the scanning electron micrograph of the MOF they give in Fig. 2 of their article [120]), the results obtained by Brechet *et al.* with a finite element method [62] at  $\lambda = 0.813 \mu\text{m}$  and the results obtained with our multipole method for two values of  $N_r$  at the same wavelength. Unit for dispersion:  $\text{ps.nm}^{-1}.\text{km}^{-1}$ , unit for dispersion slope:  $\text{ps.nm}^{-2}.\text{km}^{-1}$ .

diameter  $d = 5 \mu\text{m}$  with a pitch  $\Lambda = 6.75 \mu\text{m}$  and a fixed background index  $n = 1.45$  at  $\lambda = 1.55 \mu\text{m}$ , the computed value  $\Re(n_{\text{eff}})$  of the fundamental mode is 1.4447672 [45].

Concerning chromatic dispersion, our results are in good agreement (see Table 8.1) both with the dispersion and its slope measured by Gander and his colleagues, and with the dispersion calculated by the same authors [120] using an expansion of the fields in terms of Hermite-Gaussian functions [39] for a microstructured optical fiber ( $d = 0.621 \mu\text{m}$  with a pitch  $\Lambda = 2.3 \mu\text{m}$ ) at  $\lambda = 0.813 \mu\text{m}$ . Our results are also in good agreement (see Table 8.1) with the dispersion and slope dispersion calculated by Brechet *et al.* for the same structure with a finite element method [62].

### 8.2.3 Results

In the examples given in the following, we simulate a MOF made out of a triangular array of cylindrical air-inclusions ( $n_i = 1$ ) of lattice pitch  $\Lambda$ . The inclusions have identical circular cross-sections of diameter  $d$ , the core being formed by a missing inclusion (see Fig. 8.1). The finite thickness of the hole region around the core can be described by the number of rings of holes  $N_r$ . The matrix and the jacket are made of silica, so that the guiding structure is formed by a finite number of low-index inclusions in infinite silica bulk (the Sellmeier expansion is taken from reference [7]). Since the hole region surrounding the core is bounded, it is clear that propagating modes are leaky.

We limit our study to the fundamental mode dispersion properties, and the wavelengths that we consider here are included in the range  $[0.6, 3] \mu\text{m}$ . As shown in Fig. 8.2 for a fixed hole diameter, a small pitch provokes oscillations of the dispersion, several zero-dispersion wavelengths can be found. With a larger pitch, the dispersion increases monotonously with wavelength. This property can be understood as follow: for large pitch, the MOF core is large too and waveguide effects on dispersion are therefore weak, and the material dispersion dominates. Conversely, for smaller pitches the waveguide dispersion takes over, and we observe oscillations of the dispersion curve, the amplitude of which increases as the pitch decreases. In the short wavelength limit, material dispersion is so negative that waveguide dispersion cannot compensate its effect. This remark explains why for sub-micrometric wavelengths, all the dispersions tend toward material dispersion.

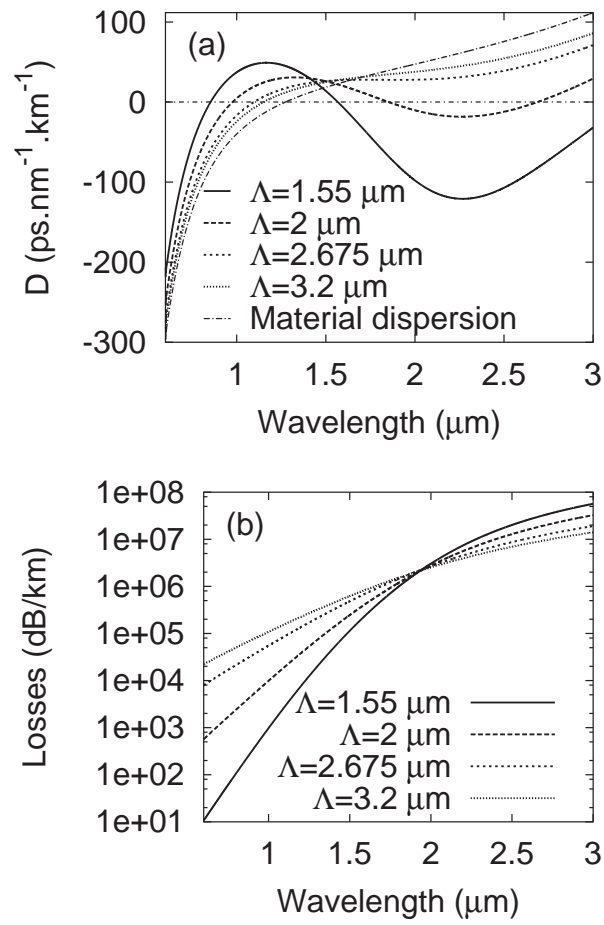


Figure 8.2: Dispersion (a) and losses (b) for a 3 ring MOF as a function of wavelength and pitch  $\Lambda$ . The material dispersion is also shown. Holes diameter  $d$  is equal to  $0.8 \mu\text{m}$ .

In Fig. 8.2, it can be noticed that there exists a pitch value ( $\Lambda = 2.675 \mu\text{m}$ ) for which the dispersion curve is flat over a large range of wavelengths taking the average value  $27.9 \text{ ps.nm}^{-1}.\text{km}^{-1}$  around  $1.85 \mu\text{m}$  with the amplitude of dispersion oscillation equal to  $0.2 \text{ ps.nm}^{-1}.\text{km}^{-1}$  in a wavelength interval of  $0.3 \mu\text{m}$ . For the same pitch but with  $N_r = 4$  (data not shown), the dispersion curve is much less flat than with  $N_r = 3$  and the average level of the dispersion has decreased, taking an average value of  $23.7 \text{ ps.nm}^{-1}.\text{km}^{-1}$  around  $1.85 \mu\text{m}$  with the amplitude of oscillation of  $3.8 \text{ ps.nm}^{-1}.\text{km}^{-1}$  in a wavelength interval of  $0.5 \mu\text{m}$ . In both cases, it must be noticed that the corresponding losses ( $5.9 \times 10^5 \text{ dB.km}^{-1}$  for  $N_r = 3$  and  $6.1 \times 10^4 \text{ dB.km}^{-1}$  for  $N_r = 4$ ) prohibit the use of these MOFs for practical applications. One can try to overcome this drawback by increasing again the number of rings but this change entails a new change of the dispersion curve as it will be shown in detail in the following. This example clearly shows the necessity of studying both losses and dispersion in order to realize a realistic dispersion engineering.

Another remark to draw from figure 8.2 is the existence of a wavelength  $\lambda_{\text{cross}} \simeq 1.93 \mu\text{m}$  for which the losses are almost independent of the pitch  $\Lambda$ , at least in the range of  $\Lambda$  from  $1.55 \mu\text{m}$  to  $3.2 \mu\text{m}$ . This phenomena occurs for other values of  $N_r$ : for  $N_r = 4$ ,  $\lambda_{\text{cross}}$  is around  $2.15 \mu\text{m}$  (see Fig. 8.3), for  $N_r = 2$ ,  $\lambda_{\text{cross}}$  is around  $1.63 \mu\text{m}$  (data not shown), and so the  $\lambda_{\text{cross}}$  value increases slowly with  $N_r$ . A straight scaling-law argument cannot be used since the hole diameter is kept constant for the different structures. Besides, material dispersion depends on the actual wavelength, and so care must be taken when using scaling arguments to try to explain this behaviour. Material dispersion could also have an influence on the extent of the crossing region. Currently, the crossing region is approximatively  $0.1 \mu\text{m}$  wide. From a mathematical point of view, for a fixed value of  $N_r$  the crossing phenomena corresponds to the point  $(\lambda_{\text{cross}}, \Lambda_{\text{cross}})$  of the surface  $\mathcal{L}(\lambda, \Lambda)$  where the curve defined by  $\frac{\partial \mathcal{L}}{\partial \Lambda} = 0$  crosses the curve given by  $\frac{\partial^2 \mathcal{L}}{\partial \Lambda^2} = 0$ . It seems more difficult to give its physical meaning.

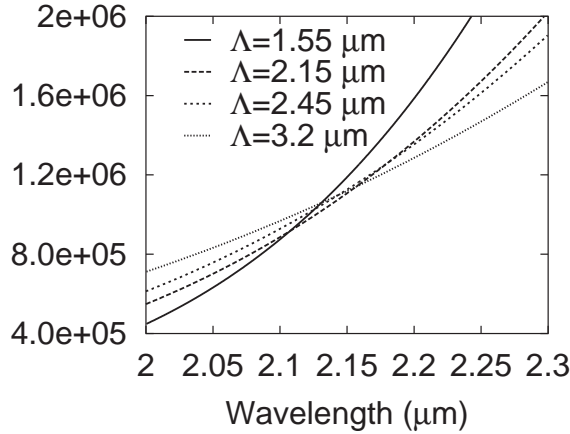


Figure 8.3: Losses for a 4 ring MOF as a function of wavelength and pitch  $\Lambda$ . Hole diameter  $d$  is equal to  $0.8 \mu\text{m}$ . The  $y$ -scale is linear contrary to the Fig. 8.2(b).

It can be seen in Fig. 8.4, that the oscillation amplitudes in dispersion curves increase with hole diameter (for  $d = 1.00 \mu\text{m}$ , i.e.  $d/\Lambda = 0.645$ , the oscillation amplitude exceeds  $300 \text{ ps.nm}^{-1}.\text{km}^{-1}$ ). This behavior can be explained by considerations of MOF core size, and a competition between material dispersion and waveguide dispersion, similar to that given previously for the influence of the pitch. It is worth noting that the value  $D_{\text{max}}$  of

the dispersion local maximum increases with hole diameter for all dispersion curves that we have computed. For three ring MOFs with a fixed pitch  $\Lambda = 1.55 \mu\text{m}$ , the wavelength  $\lambda_{D_{\max}}$  associated with the local maximum  $D_{\max}$  of dispersion increases with the diameter of the holes. This property can be used to efficiently shift the dispersion curves in order to obtain the required  $\lambda_{D_{\max}}$ .

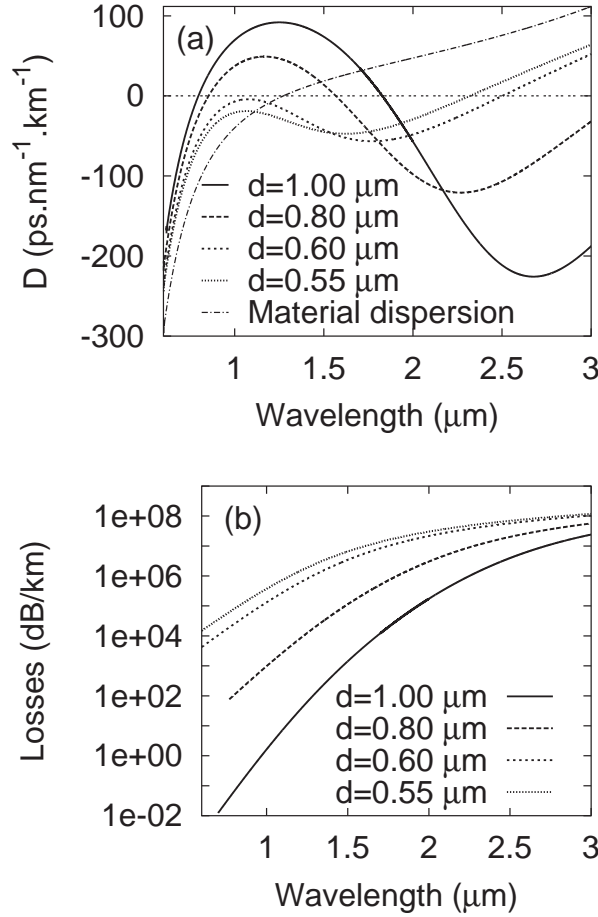


Figure 8.4: Dispersion (a) and losses (b) for a 3-rings MOF as a function of wavelength and hole diameters  $d$ . The material dispersion is also shown. The pitch is equal to  $1.55 \mu\text{m}$ .

One can try to reduce the large losses (above  $1.0 \times 10^2 \text{dB}\cdot\text{km}^{-1}$  around  $\lambda = 1.3 \mu\text{m}$  for all the plotted curves of Fig. 8.4(a)) by increasing the number of hole rings  $N_r$  but once again dispersion profiles are modified. We now describe the influence of this crucial parameter. As shown in Fig. 8.5(a), in the case where there is no local maxima of dispersion for MOFs with few rings, the dispersion decreases as the number of rings is increased. The difference between successive dispersion curves of two MOFs decreases as the number of rings increases, as shown in Fig. 8.5(c). This figure clearly shows that the dispersion converges to a limit when the number of rings is increased, the convergence speed depending on the wavelength: the larger the wavelength, the slower the convergence (in Fig. 8.5(c) for  $\lambda = 1.52 \mu\text{m}$  the limit is not yet reached with 8 rings). It is worth noting that the losses associated with the flattened dispersion curve obtained with the 7-rings MOF of Fig. 8.5(a) are still large (above

$1.0 \times 10^4 \text{dB.km}^{-1}$  around  $\lambda = 1.3 \mu\text{m}$ ). This influence of  $N_r$  on dispersion can be understood in the following way: when losses are weak, a supplementary ring will not change the mode drastically. In contrast, when the mode is not well confined in the core, a supplementary ring will modify the mode significantly. We can thus assume that the field pattern associated with the mode converges with increasing  $N_r$ , the convergence being slower for larger wavelengths since modes are less confined for these wavelengths. As opposed to the example of Fig. 8.5(a), for structures which do exhibit an oscillatory behavior of the dispersion (*e.g.* structures of small pitch in Fig. 8.2(a) *i.e.* high diameter/pitch ratio), an increase of  $N_r$  results in an amplification of the oscillations amplitudes (see Fig. 8.6).

### 8.2.4 Conclusion and Discussion

As shown in the previous section, one cannot keep the flattened dispersion with a fixed  $D$  value obtained for certain MOFs, and at the same time reduce their losses through a simple increase of their number of air hole rings.

It must also be pointed out that an increase of the number of rings can reduce the losses of higher order modes. As a consequence, a monomode fiber may become multimode for some configurations. Nevertheless, if large differences between the real parts of  $n_{eff}$  for the modes are found then mode coupling between the fundamental mode and the higher order mode should be negligible. These effects and the influence of the jacket on dispersion will be studied in a future work.

The high loss figures we showed throughout the article might give the wrong impression that low losses are not feasible in microstructured fibers, but low loss MOFs are possible with appropriate geometric parameters [119] (see also the loss curve at small wavelengths for  $d = 1.0 \mu\text{m}$  in Fig. 8.4(b)). For example, with  $\Lambda = 2.26 \mu\text{m}$ ,  $d = 1.51 \mu\text{m}$ , and  $N_r = 3$ , the losses we compute are below  $1 \times 10^{-4} \text{dB.km}^{-1}$  at a wavelength of  $0.76 \mu\text{m}$ . The same structure with  $N_r = 7$  corresponds to that studied experimentally by Kubota and his colleagues [92]. The measured global losses at a wavelength of  $0.85 \mu\text{m}$  are  $7.1 \text{dB.km}^{-1}$ , this clearly shows that the losses in MOFs can be limited by Rayleigh scattering, structural imperfections and absorption and not by the geometrical losses. But interesting dispersion properties seem to imply geometrical parameters which are not necessarily compatible with low losses and few air hole rings.

The issue for dispersion engineering applications is to find MOF parameters giving both ultraflattened dispersion curves (either negative, positive, or nearly zero) around the specified wavelength (for example  $1.3 \mu\text{m}$  or  $1.55 \mu\text{m}$ ) and low losses (around or below  $1 \text{dB.km}^{-1}$ ). Consequently, for such engineering, the finite size of the fiber cross-section must be considered. Accurate design of such MOFs is currently in progress.<sup>4</sup>

## 8.3 “Chromatic Dispersion and Losses of MOFs”: Comments

Fig. 8.7 locates the MOF parameters used in Figs. 8.2 and 8.4 as well as in Table 8.1 in the phase diagram. In Table 8.1, we compared results concerning the dispersion and its slope, resulting from an experimental study on one hand, and simulations using a Hermite-Gaussian expansion method, a finite element method and the multipole method on the other hand. The point in parameter space at which the dispersion and its slope were estimated, is at the

---

<sup>4</sup>The design of such MOFs is reported in Sec. 8.4.

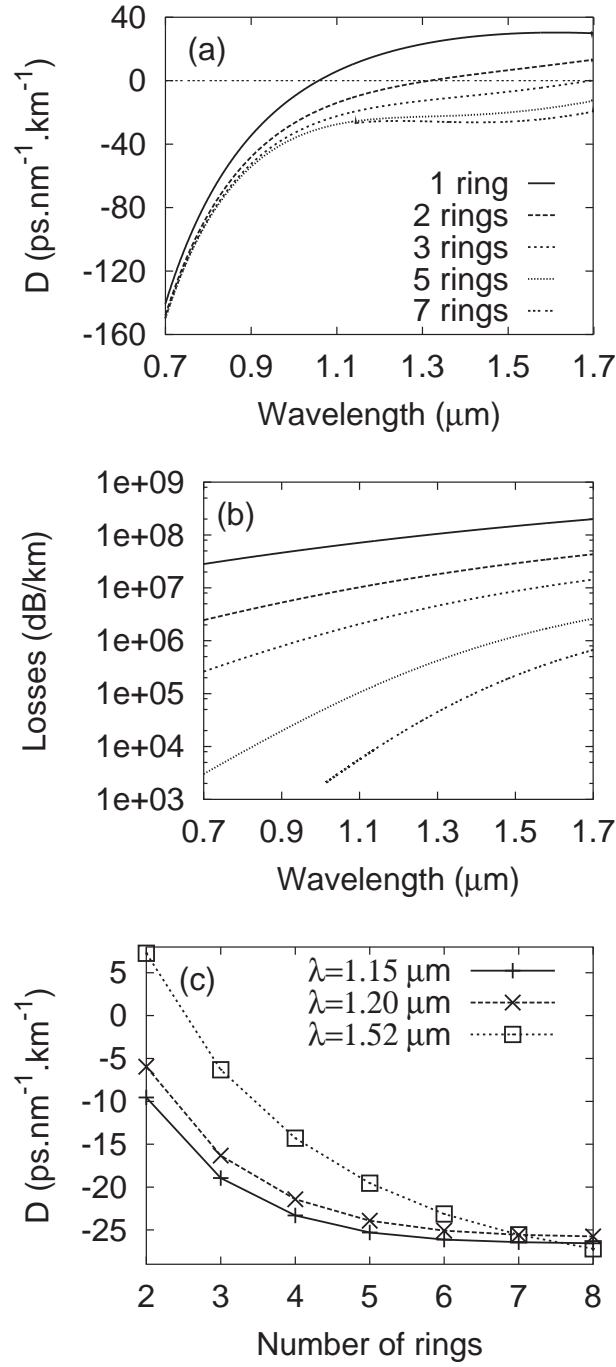


Figure 8.5: Dispersion (a) and losses (b) as a function of the wavelength and number of rings  $N_r$  (the line styles are the same in the two figures). The pitch is  $2.0 \mu\text{m}$ . Holes diameter is  $0.5 \mu\text{m}$ . (c) Dispersion for three different wavelengths as a function of the number of rings  $N_r$  for the same MOF.

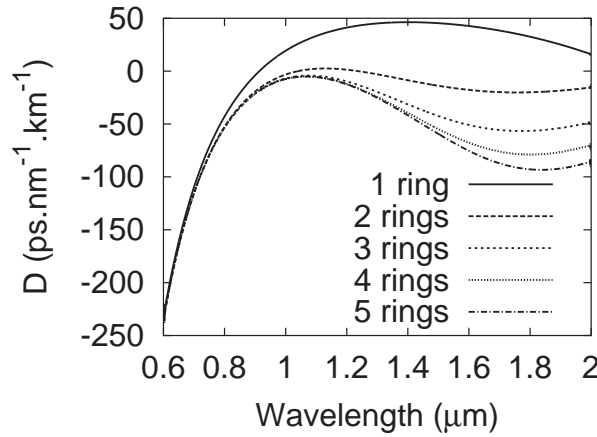


Figure 8.6: Dispersion as a function of the wavelength and number of rings  $N_r$ . The pitch is  $1.55 \mu\text{m}$ . Holes diameter is  $0.6 \mu\text{m}$ .

boundary of the CF2 region: the mode is well confined, convergence of modal properties is exponential and the number of rings has little influence on results. It is hence not surprising to find good agreement, even without knowing the number of rings used in simulations from other authors.

In Figs. 8.2 and 8.4 we studied the dispersion properties for various values of the diameter and the pitch. It appears in Fig. 8.7 that the parameters used to establish those figures extend over the whole cutoff region, with a few values being in the CF1 or CF2 region. It is indeed in the cutoff region that most interesting dispersion properties can be found. When explaining Figs. 8.2 and 8.4 we mentioned that at short wavelengths, the chromatic dispersion of MOFs is very close to the material dispersion. This occurs in the CF2 regime, where light is well confined in the core and dispersion properties are similar to those of conventional step index fibres. Similarly, at long wavelengths, dispersion curves become monotonic, being roughly parallel to the material dispersion. This is in agreement with the fibre parameters approaching or entering the CF1 region, where again modal properties are similar to those of a conventional step-index fibre. The region where dispersion properties are most different from conventional fibres and hence of greatest potential interest, corresponds to the cutoff region. This explains the prohibitive confinement losses encountered throughout Figs. 8.2 and 8.4, as well as the large dependence of losses on wavelength, and the slow convergence of dispersion properties with increasing  $N_r$ .

In Fig. 8.8 we show the position in the phase diagram of the parameters used in Figs. 8.5 and 8.6, in which we were studying the convergence of dispersion properties with the number of rings. Parameters used in Fig. 8.5 extend from one edge of the cutoff region to the other. It is hence not surprising for the dispersion to converge, but to do so with a slower convergence rate towards the long wavelength end of the cutoff region. Parameters used in Fig. 8.6 also cover a whole section of the cutoff region, but extend a bit further, entering the CF2 and CF1 regions.<sup>5</sup> At short wavelengths, the dispersion is independent of  $N_r$  to graphical accuracy, in agreement with the mode being in the CF2 regime. At long wavelengths, for  $\lambda > 1.8 \mu\text{m}$  (dashed line on Fig. 8.8), the dispersion no longer converges with increasing number of rings,

<sup>5</sup>With the wavelength range used in Fig. 8.6, the CF1 region is actually not entered, we have here used data from the original version of the same figure in which the wavelength range extended up to  $\lambda = 3 \mu\text{m}$ .

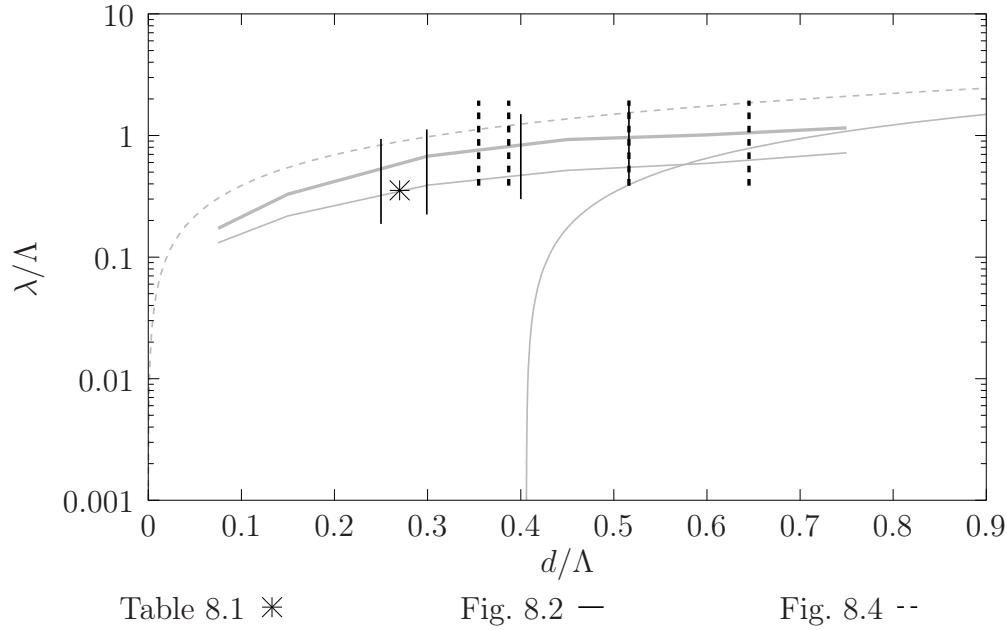


Figure 8.7: Position in the phase-diagram of the parameters used in Table 8.1, Fig. 8.2 and Fig. 8.4.

as expected from MOFs in the CF1 regime.

Finally, we concluded the article by mentioning that for the MOFs studied, increasing the number of rings could render guidance in the MOFs multimode. This was based on our former conception of number of modes in MOFs, based on the difference of losses between modes, and has become obsolete with regard of the results presented in Ch. 7. Note that we also made a somewhat prophetic comment in the last sentence of the third paragraph, Sec. 8.2.4.

## 8.4 Dispersion management with microstructured optical fibers: Ultra-flattened chromatic dispersion with low losses

Authors: G. Renversez, B. Kuhlmeier, and R. McPhedran

*Date of submission: 7 January 2003*

To be published in Optics Letters, Vol. 28, No. 12, June 2003.

Microstructured Optical Fibers (MOFs) have been proposed as a new tool for dispersion management in optical communication systems since 1998 [39]. Several studies [38, 116] using a vector method with periodic boundary conditions [63] have been made in order to design such MOFs, nevertheless as recently shown [35] the finite cross-section of MOFs must be taken into account in order to describe accurately the chromatic dispersion properties of such fibers and to compute the losses. Moreover it must be pointed out that the comparison between the computed dispersion curves and the experimental results is still a difficult issue [36].

A mode of a MOF is characterized by its field pattern and its effective index  $n_{\text{eff}} = \beta/k_0$  where  $\beta$  is its propagation constant and  $k_0 = 2\pi/\lambda$  is the free space wavenumber. Due to the finite transverse extent of the confining structure, the effective index is a complex

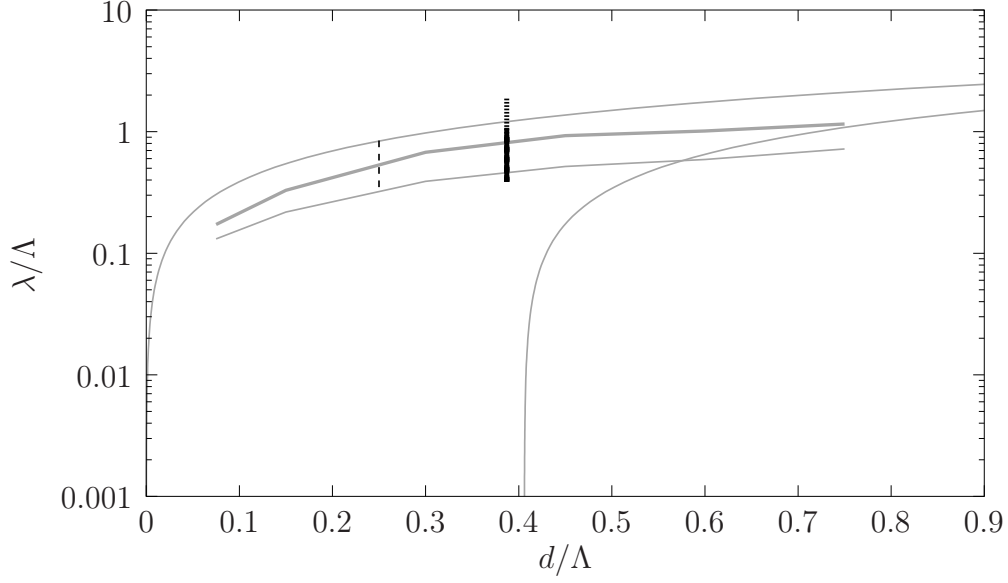


Fig. 8.5 --

Fig. 8.6: D .....

Fig. 8.6: C —

Figure 8.8: Position in the phase-diagram of the parameters used in Fig. 8.5 and Fig. 8.6. For Fig. 8.6, C denotes the range where dispersion converges with  $N_r$ , D denotes the range where dispersion diverges with  $N_r$ .

value, its imaginary part  $\Im(n_{\text{eff}})$  being related to the losses  $\mathcal{L}$  in dB/m through the relation:  $\mathcal{L} = 40\pi\Im(n_{\text{eff}}) \times 10^6/(\lambda \ln(10))$ , where  $\lambda$  is given in micrometers. The dispersion parameter D is computed through the usual formula from the real part of the effective index  $\Re(n_{\text{eff}})$  [4]:  $D = -(\lambda/c)\partial^2\Re(n_{\text{eff}})/\partial\lambda^2$ . We have developed a multipole method [1] which allows us to compute accurately the complex effective index of the modes of a wide variety of MOFs. Our method has been checked via comparison with other numerical methods [35, 45, 84].

In the following, we simulate plain core MOFs made from a subset of a triangular array of cylindrical air-inclusions ( $n_i = 1$ ). The inclusion spacing or pitch is denoted by  $\Lambda$  (see inset in Fig. 8.10). The inclusions are circular with possibly varying diameters, and lie around a core formed by a missing central inclusion. The matrix and the jacket are made of silica, so that the guiding structure is formed by a finite number  $N_r$  of rings of air holes in infinite bulk silica whose Sellmeier expansion (which does not include material losses) is taken from reference [4]. Our aim in this work is to establish MOF designs which combine ultra-flattened chromatic dispersion together with low losses around the telecommunication wavelength  $\lambda = 1.55 \mu\text{m}$ . We exhibit two designs which achieve this. The first contains air-holes of one diameter and requires 18 rings of holes in order to attain losses smaller than 1 dB/m. The second utilizes air-holes with three different diameters which results in ultra-flat dispersion and even lower loss levels with only seven rings.

The chromatic dispersion in MOFs arises from that of the silica ( $D_{\text{mat}}$ ) and also from waveguide dispersion ( $D_W$ ) associated with the structure of the confining region. Note that our multipole method provides directly the total dispersion ( $D$ ), so we deduce  $D_W$  from the relation  $D_W \simeq D - D_{\text{mat}}$ . As pointed out by Ferrando *et al.* [38] it is convenient to achieve a specified total dispersion by controlling  $D_W$  to make it follow a trajectory parallel to that of  $-D_{\text{mat}}$  in the target wavelength interval. The parameters one has to achieve this are the hole

diameter  $d$ , the pitch  $\Lambda$  and the number of rings  $N_r$  [35].

From a previous theoretical work [95], we have defined the region in the design space  $(d/\Lambda, \lambda/\Lambda)$  for usual MOFs where they will behave in a way markedly and controllably different from conventional step-index or graded-index fibers. This defines the range of hole diameters of interest, given the telecommunication wavelength range. From the same study we also choose  $d/\Lambda < 0.406$  in order to guarantee single-mode operation of the MOF design.

In Fig. 8.9 we show the variation of the total dispersion  $D$  with the number of rings for six different usual MOF geometries, all located in the region of stable dispersion. All curves show a simple variation with  $N_r$ , which can be modeled accurately by an exponential form  $D_1 \exp(-\kappa N_r) + D_{\text{lim}}$ . Such a fitting form has three parameters  $(D_1, \kappa, D_{\text{lim}})$ , which can be determined accurately using results from  $N_r = 3$  to 6. This procedure has important advantages, since MOFs with relatively small numbers of rings are relatively quickly modeled, and yet we have established that the exponential fit thereafter accurately describes the dispersion of much larger structures, and even the limiting parameter  $D_{\text{lim}}$ , the dispersion of the mode pinned by a single defect in an infinite lattice. In fact, using the limit dispersion  $D_{\text{lim}}$  determined numerically for a set of values of wavelength  $\lambda$  we can also determine  $S_{\text{lim}} = \partial D_{\text{lim}} / \partial \lambda$ , the limit dispersion slope. These two quantities describe the chromatic dispersion of the defect mode for the infinite lattice, and naturally tell us the chromatic variation of dispersion for large MOF structures.

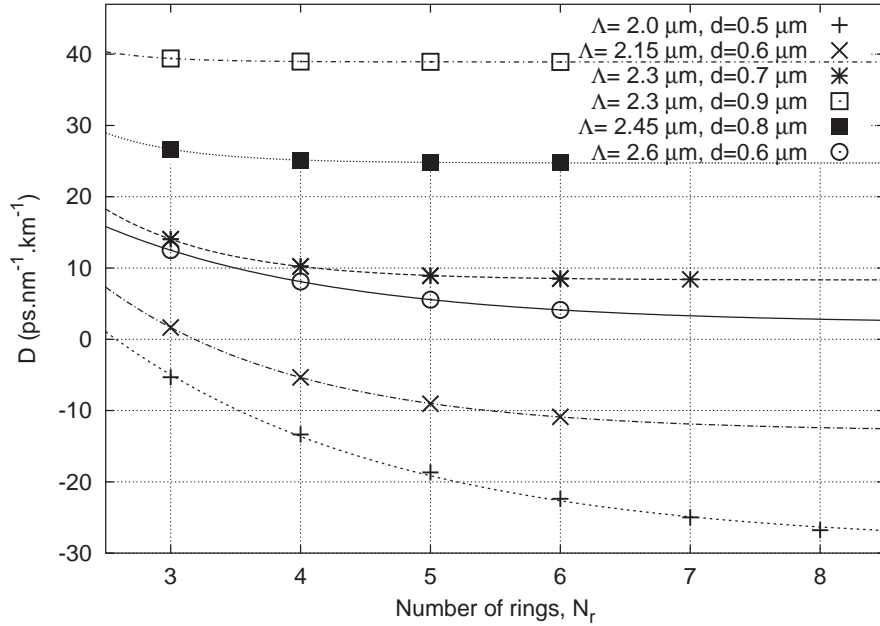


Figure 8.9: Dispersion decay at  $\lambda = 1.55 \mu\text{m}$  as a function of the total number of hole rings  $N_r$  for different microstructured optical fiber (MOF) structures.  $\Lambda$  is the pitch of the triangular lattice of holes, and  $d$  is the hole diameter. The points correspond to the computed numerical dispersion, and the lines to exponential based fits (see the text for more details).

In Fig. 8.10 we show the variations of these important parameters  $D_{\text{lim}}$  and  $S_{\text{lim}}$  as a function of the hole diameter  $d$  for different pitches  $\Lambda$ . This figure illustrates well how one can isolate a MOF exhibiting a target dispersion value for a sufficiently large number of rings  $N_r$ ,

which is flat over a range about the chosen wavelength value. Indeed such a MOF will have the desired value of  $D_{\text{lim}}$  and simultaneously a value of  $S_{\text{lim}}$  close to zero. Note that the pitches exhibited in Fig. 8.10 were chosen carefully to exemplify this desirable behavior. We have also shown that, for the data of Fig. 8.10, the minima of  $S_{\text{lim}}$  as a function of  $d$  occur in the same diameter interval  $[0.65; 0.7]$  micrometers for all MOFs having  $N_r \geq 6$ . From Fig. 8.10, if one requires a positive nearly-zero flat chromatic dispersion then, using these curves, one should start its dispersion engineering with a MOF such that  $\Lambda = 2.45 \mu\text{m}$  and  $d = 0.6 \mu\text{m}$ . Of course, Fig. 8.10 can be used to isolate MOF geometries having different characteristics, such as a prescribed slope with a fixed average value of dispersion over a wavelength range.

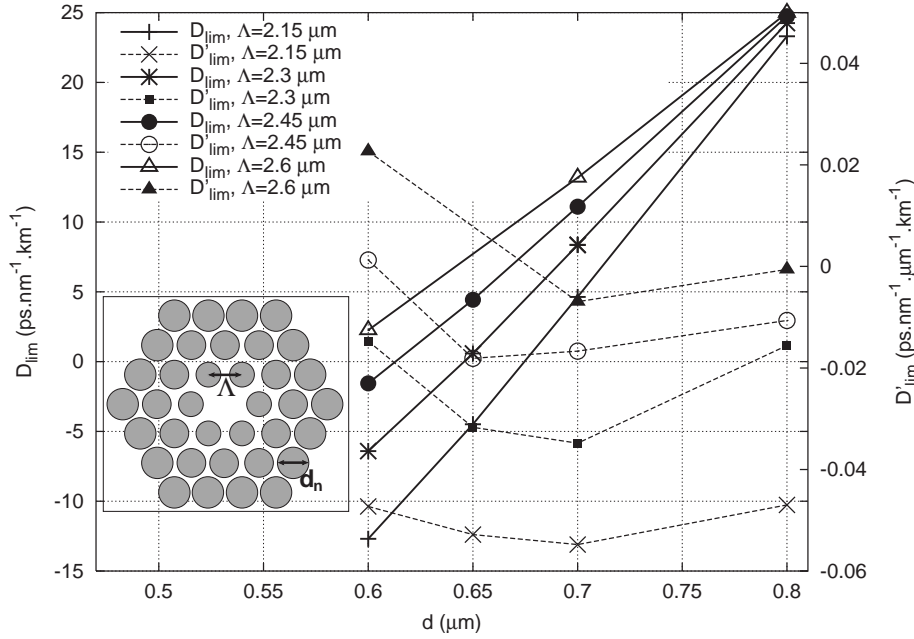


Figure 8.10: Limit dispersion (plain thick lines, left y-scale) and limit dispersion slope (dashed lines, right y-scale) at  $\lambda = 1.55 \mu\text{m}$  as a function of the hole diameter  $d$  for several pitches. The chosen parameter values for  $\Lambda$  and  $d$  correspond to the small limit slope region. Inset: Cross-section of the modeled MOF with 3 rings of holes (holes are in grey),  $N_r = 3$ .  $\Lambda$  is the hole spacing, and  $d_n$  is the hole diameter of the  $n^{\text{th}}$  ring. The solid core is formed by one missing hole in the center of the structure.

In Fig. 8.11 we show dispersion characteristics for three MOF designs. At the top, the total dispersion is linear with negative slope  $[D(a)]$ , constant near zero  $[D(b)]$  and nearly constant near  $-5 \text{ ps/nm/km}$   $[D(c)]$ . These arise because of the balance between the waveguide dispersion  $D_W$  curves and that of the  $-D_{\text{mat}}$  shown in the bottom part of the figure. Note that, while these designs have appropriate dispersion characteristics for  $N_r \geq 6$ , their geometric losses impose much more stringent requirements upon the number of rings, and the effective area of the fundamental mode  $A_{\text{eff}}$  is around  $36.5 \mu\text{m}^2$  for  $N_r = 6$ . For example, for the MOF with ultra-flat dispersion close to zero, it requires  $N_r \geq 18$  (1026 holes) to deliver losses below 1 dB/km at  $\lambda = 1.55 \mu\text{m}$ . Even though several laboratories have already drawn 7-ring fibers [92] (around 168 holes) or even 11-ring fibers [36] (around 396 holes), there is clearly a technological interest in investigating designs which can deliver tailored dispersion

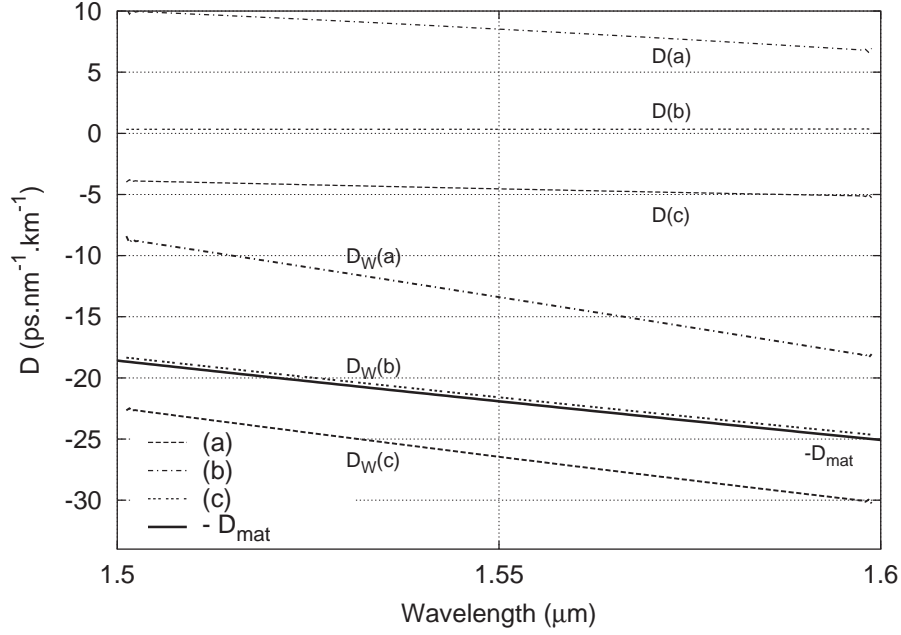


Figure 8.11: Waveguide dispersion  $D_W$  (thick lines), dispersion  $D$  (normal lines), and sign-changed material dispersion  $-D_{mat}$  (thick black line) for three different 6-ring MOF structures. The line style of a MOF structure is identical for  $D_W$  and for  $D$ .  $\Lambda$  and the diameters are given in  $\mu\text{m}$ . (a) :  $\Lambda = 2.3, d = 0.7$ , (b) :  $\Lambda = 2.45, d = 0.6$ , (c) :  $\Lambda = 2.3, d = 0.6$ .

characteristics with many fewer MOF rings.

In order to provide MOF designs displaying the desirable combination of ultra-flat dispersion, low loss and quasi-single mode operation with a practicable value of  $N_r$ , a natural strategy is to allow the hole diameter to differ from one ring to another ( $d_n$  is the hole diameter of the  $n^{\text{th}}$  ring, see inset in Fig. 8.10), with exterior rings having large holes to lower the losses. We start the design process with a three-ring MOF,  $d_1$  being arbitrarily set to  $d_1 = 0.5 \mu\text{m}$ . In pursuing designs of this sort it is advantageous to employ the following scaling relation for waveguide dispersion (this is a generalization of a result given in reference [38]):

$$D_W(\lambda, \Lambda/\Lambda_{ref}, f_1, f_2, \dots, f_n) \simeq \frac{\Lambda_{ref}}{\Lambda} D_W(\lambda \Lambda_{ref}/\Lambda, 1, f_1, f_2, \dots, f_n) \quad (8.3)$$

where  $\Lambda_{ref}$  is the pitch of a reference lattice and  $f_n$  is the ratio  $d_n/\Lambda$ . Using the above scaling law and a rough optimization process on  $d_2, d_3$ , and  $\Lambda$ , we found an ultra-flat dispersion over a long wavelength interval (approximately  $[1.45, 1.65] \mu\text{m}$ ) for  $d_2 = 0.7 \mu\text{m}$ ,  $d_3 = 0.8 \mu\text{m}$ , and  $\Lambda = 1.7 \mu\text{m}$  ([D(3)] in Fig. 8.12). It must be pointed out that the MOF design can be started from other values of  $d_1$ : for example with  $d_1 = 0.6 \mu\text{m}$ , we found  $d_2 = 0.8 \mu\text{m}$ , and  $d_3 = 1.0 \mu\text{m}$ , and  $\Lambda = 2.0 \mu\text{m}$  (data not shown).

Using the scaling law (8.3), we can easily derive other structures having ultra-flattened chromatic dispersion, but around a different value of  $D$ . Three examples of such structures, derived from the reference configuration ( $d_1 = 0.5 \mu\text{m}$ ,  $d_2 = 0.7 \mu\text{m}$ ,  $d_3 = 0.8 \mu\text{m}$ , and  $\Lambda = 1.7 \mu\text{m}$ ), are given in Fig. 8.12 ( $\Lambda = 1.65 \mu\text{m}$  [D(5)],  $1.8 \mu\text{m}$  [D(2)],  $1.9 \mu\text{m}$  [D(1)]). Note that varying the pitch too far results in structures which no longer exhibit ultra-flat dispersion, this

is due to the finite length of the ultra-flat region in the chosen reference MOF design (data not shown).

We now control losses by adding further rings of holes with fixed diameter  $0.8\mu\text{m}$ . As can be seen in Fig. 8.12, adding rings 4 to 7 has almost no effect on the dispersion properties of the MOF  $[D(4)]$ , but results in acceptably low values of geometric loss for technological applications: with  $N_r = 6$ , the losses are below  $10\text{ dB.km}^{-1}$ , and with  $N_r = 7$  the losses are below  $0.2\text{ dB.km}^{-1}$ . For  $N_r = 6$ , the amplitude of dispersion variation is less than  $3.0 \cdot 10^{-2}\text{ ps.nm}^{-1}.\text{km}^{-1}$  in the wavelength interval  $[1.5; 1.6]\mu\text{m}$ . These designs thus attain our goal of ultra-flat dispersion combined with very low geometric loss in a MOF feasible with current fabrication technology. Note that one can use designs in which the outer boundary of the confining region is either hexagonal or circular. For the well confined modes we deal with here ( $A_{\text{eff}} \simeq 10.5\mu\text{m}^2$  for  $N_r = 6$ ), this difference has no practical effect on dispersion (data not shown). One interesting consequence of using three different hole diameters is that the possibility arises of having modes higher than the fundamental confined between rings of holes with different diameters. Indeed the second mode in the seven ring structure of Fig. 8.12 is confined between the first and second rings of holes and has losses around ten thousand times larger than that of the fundamental. This mode would not couple readily to the fundamental mode in the design, because mode energy is concentrated in different regions for the two modes and the real parts of their effective indices are quite different.

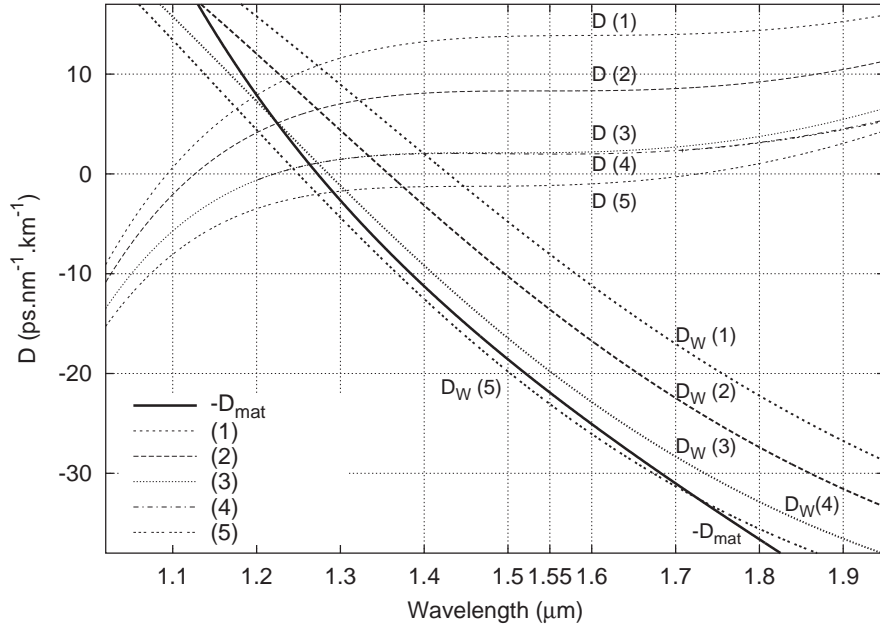


Figure 8.12: Waveguide dispersion  $D_W$  (thick lines), dispersion  $D$  (normal lines) for the MOF structures we proposed, and sign-changed material dispersion  $-D_{\text{mat}}$  (thick black line).  $d_n$  is the hole diameter of the  $n^{\text{th}}$  ring and  $d_{n_1-n_2}$  denotes the hole diameter of the  $n_1^{\text{th}}$  to  $n_2^{\text{th}}$  rings. Unless stated the total number of rings  $N_r$  in the MOF is equal to three. The line style of a MOF structure is identical for  $D_W$  and for  $D$ .  $\Lambda$  and the diameters are given in  $\mu\text{m}$ . (1) :  $\Lambda = 1.9, d_1 = 0.559, d_2 = 0.782, d_3 = 0.894$ , (2) :  $\Lambda = 1.8, d_1 = 0.529, d_2 = 0.741, d_3 = 0.847$ , (3) :  $\Lambda = 1.7, d_1 = 0.5, d_2 = 0.7, d_3 = 0.8$ , (4) :  $N_r = 4 - 7; \Lambda = 1.7, d_1 = 0.5, d_2 = 0.7, d_{3-7} = 0.8$ , (5) :  $\Lambda = 1.65, d_1 = 0.485, d_2 = 0.679, d_3 = 0.776$ .

In conclusion, we have numerically demonstrated that nearly-zero or non-zero ultra-flattened chromatic dispersion with low-loss is feasible using two different types of MOF designs. The more complex design, proposed in this letter, with three different hole diameters used allows us to achieve low losses with many fewer air holes than the conventional design. The design principles introduced here, together with the powerful control on dispersion given by the MOF geometry should enable effective chromatic dispersion management over a wide spectral range in optical fibers.

## 8.5 “Dispersion management with MOFs...”: Comments

### 8.5.1 Conventional MOF Designs

Fig. 8.13 shows the locus in the phase diagram of all MOFs studied in Figs. 8.9, 8.10 and 8.11. Since we are looking for non conventional dispersion properties, it is not surprising to find all the parameters in the cutoff-region.

In Fig. 8.9 we studied the convergence of the dispersion with  $N_r$  and successfully fitted an exponentially-converging function to the data. This is consistent with the –almost– exponential convergence of mode properties in the cutoff region, but we can also see that the point closest to the CF1 region ( $d = 0.5 \mu\text{m}$ ,  $\Lambda = 2.0 \mu\text{m}$ ) has a very slow convergence. The data point for  $N_r = 8$  for this MOF in Fig. 8.9 is slightly under what is expected from an exponential convergence, in agreement with the fact that the parameters are very close to the CF1 region where dispersion properties don’t converge. In fact, it appears that the three upper curves of Fig. 8.9, for which convergence is extremely rapid, correspond in Fig. 8.13 to points below the cutoff-curve<sup>6</sup>, whereas the three lower curves of Fig. 8.9, for which convergence is much slower, correspond to points above the cutoff-curve in the phase-diagram.

The MOFs used in Fig. 8.11 were optimized to obtain flat near-zero dispersion, but suffer from a slow decrease of losses with  $N_r$  and a large effective area. This can be understood from their position in the phase diagram (Points (a-c)): they all are above (or, for point (a), almost exactly on) the cutoff-curve. This implies that the growth of the effective area has already become substantial, and that the decrease of losses and convergence of mode properties with  $N_r$  is slower.

### 8.5.2 New MOF Designs

For the MOFs from Fig. 8.12 using different hole sizes in successive rings, we use considerations from Sec. 7.6.2 to locate the parameters associated with each ring. From Eq. (7.52) we know that the cutoff wavelength  $\lambda_c$  is shifted towards larger values with increasing core size. For a core consisting of a missing central inclusion and  $N$  missing rings, we have

$$\frac{\lambda_c(N)}{\Lambda} \simeq (N + 1) \frac{\lambda_c(0)}{\Lambda} . \quad (8.4)$$

Conversely,

$$\frac{\lambda_c(N)}{(N + 1)\Lambda} \simeq \frac{\lambda_c(0)}{\Lambda} , \quad (8.5)$$

so that in order to keep the same location of the cutoff region in the phase diagram for the three different rings, we have used  $\lambda/[(N + 1)\Lambda]$  as the normalized wavelength in Fig. 8.14, where we

<sup>6</sup>Recall the cutoff point is defined by the point of steepest slope of losses versus wavelength.

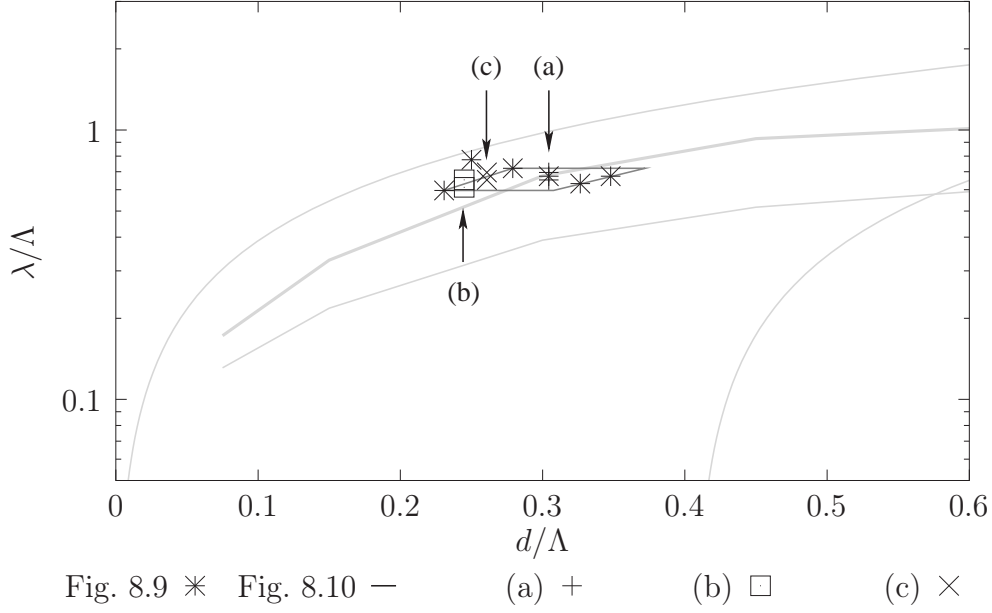


Figure 8.13: Position in the phase-diagram of the parameters used in Figs. 8.9, 8.10 and 8.11. For the latter, the position of the three different MOFs is detailed (a-c). All parameters are in the cutoff region.

show the parameters of the different rings of all MOFs used in Fig. 8.12. We emphasize that this method is approximate: we have seen (Fig. 7.32) that the shift of the cutoff wavelength with increasing core size is not perfectly linear. Further, we neglect the decrease in effective refractive index of the equivalent larger core due to the presence of inner rings (*cf.* Sec. 7.6.2).

Fig. 8.14 shows that the first ring of inclusions is associated with parameters in the endlessly single-mode part of the cutoff region, beyond the cutoff-curve. We have already seen that in this region interesting dispersion properties can be found, with the drawback of relatively large mode area and high losses. The second ring has parameters at the edge of the CF2 region, and still corresponds to single-mode operation. The third ring has parameters in the CF2 region for the fundamental mode, and crosses the second mode cutoff-curve.

From the above considerations, we expect the fundamental mode to be slightly confined by the first ring of inclusions, then strongly confined by the second ring of inclusions. This is in agreement with the effective area of the fundamental mode ( $A_{\text{eff}} \simeq 10.5 \mu\text{m}^2$ ) being slightly larger than the area delimited by the first ring (approximately  $7.5 \mu\text{m}^2$ ), although, the parameters of the first ring being very close to the CF1 region, we would have expected a mode area closer to the area delimited by the second ring (about  $30 \mu\text{m}^2$ ).

From Fig. 8.14, we would expect the second mode to be confined by the third ring. This is not in direct agreement with the results mentioned in the paper, where we indicated that the second mode is already confined by the second ring,<sup>7</sup> and shows the limit of the use of Eq. (8.5) to locate parameters in an unified phase diagram. In fact, with a core larger than a single missing inclusion, the second mode cutoff curve changes more than by a sole

<sup>7</sup>More precisely, we mentioned that the second mode is confined between the first and second ring; in fact the second mode having a power distribution in form of an annulus (*cf.* *e.g.* Fig. 7.4), the fact that its power distribution lies between the first and second ring doesn't imply that it is confined between these. Note that for the second mode,  $A_{\text{eff}} \simeq 38.9 \mu\text{m}^2$ .

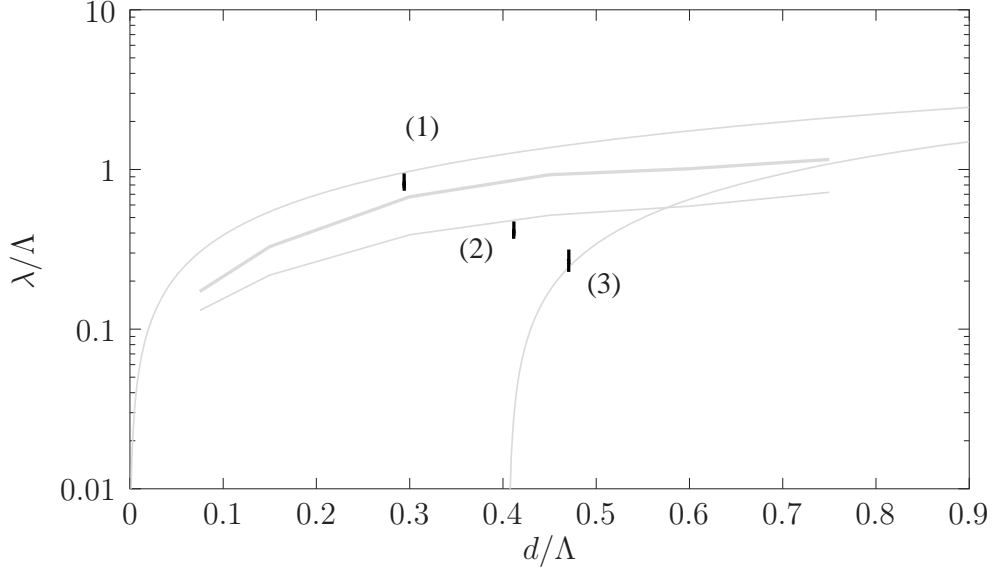


Figure 8.14: Position in the phase-diagram of the parameters used in Fig. 8.12. The figure shows the position of the parameters for each ring, the ring number being in brackets. Since the different MOFs have been designed using the scaling law Eq. (8.3), all MOFs have similar normalized parameters, so they can not be distinguished in the figure. For the second and third ring, we have corrected the position in parameter space taking into account the increased equivalent core size.

translation in  $\lambda/\Lambda$  space. Notably, the endlessly single-mode region becomes narrower, and the second mode can be confined for  $d/\Lambda < 0.406$  [121]. Further, recall that the use of the phase diagram for MOFs with inclusions of different sizes can only be accurate if the cutoff regions associated with different rings are disjoint (*cf.* Sec. 7.6.2), and that in that case one has to use a homogenized refractive index for the equivalent core. None of these conditions were satisfied here: it is remarkable how a quick look at the phase diagram could nevertheless give a general idea of what to expect from such a complex MOF structure. Indeed, using the phase diagram we could predict the MOF would have a well confined fundamental mode, with *a priori* interesting dispersion properties, and that the second mode would be confined, at least by the third ring. Further, since the second mode is in the CF2 region for the third ring (and probably close to it for the second ring), we can expect its losses to decrease exponentially with  $N_r$ : the fibre is strictly multimode, but higher order modes extend over a wider spatial region than the fundamental mode.

## 8.6 Theory and Experiment

In Table 8.1 we presented a comparison between experimental and simulated values of the group velocity dispersion, and agreement was satisfactory. However, as we mentioned earlier (Sec. 4.7.3), GVD curves computed using different numerical models are in good agreement at least when MOF parameters are in the CF2 region, but they generally fail to match measured dispersion curves. This fact was also observed by other authors: in Ref. [36], published a week before we submitted our first study on dispersion in MOFs, Reeves and coworkers

report spectacular experimental results concerning MOFs with ultra-flat dispersion. However, although the measured pitch and hole sizes were within a few percent of values used by Ferrando *et al.* in a theoretical study [38, 116], the experimental data did not agree with the theoretical GVD curves published by Ferrando. The fibre parameters being in the cutoff region,<sup>8</sup> the authors were right to argue that convergence with the number of rings might explain discrepancies. Although increasing the number of rings of the experimental MOF changed the dispersion curves substantially, it didn't bring the anticipated agreement with the theoretical GVD. We could argue that the dispersion curves published by Ferrando *et al.* were computed using a super-cell approximation, and that their validity in the cutoff-region is hence to be verified,<sup>9</sup> but simulations we have undertaken taking into account the finite cross section of the MOF don't give much better agreement. The problem of the bad agreement between theoretical and experimental dispersion curves lies elsewhere. Reeves *et al.* suggest that the observed differences could be explained by unavoidable variations in fibre diameter along the length of the fibre. In Sec. 4.7.3 we mentioned that, in the case of our comparison with experimental results from Kubota *et al.*, variations of 25% on the pitch were needed to account for the difference between computed and measured zero-dispersion wavelength. Although we can not exclude this amount of variation, we should keep in mind that other reasons for the poor agreement between theory and experiment might have to be found. We recently became aware that state of the art experimental MOFs have a much larger dispersion in hole size than we thought [122]; preliminary studies [111] have shown qualitatively that group velocity dispersion is very sensitive to randomness in the hole distribution, but realistic quantitative studies have yet to be undertaken.

If studying the effects of the two preceding geometrical perturbations were to fail in explaining discrepancies between theoretical and experimental GVD, other effects would have to be investigated. These could *e.g.* be unknown refractive index variations due to stress appearing during the drawing process or surface phenomena at the hole/silica boundaries (roughness, contamination...).

---

<sup>8</sup>The location of the MOFs used by Reeves *et al.* in the phase diagram can be found in Fig. 7.30: the four left-most vertical data lines from data set 3 correspond to MOFs from Ref. [36].

<sup>9</sup>The doubt we express here only concerns a limited range of parameters (those in the cutoff and CF1 regions) used in Ferrando's studies, and shouldn't hide our deepest respect and admiration for Ferrando's well thought approach of the issue of dispersion management with MOFs.

# Conclusion

We presented what we believe to be the first systematic theoretical and numerical study of finite cross-section solid core MOFs over a wide range of parameters. This study was only possible through the formulation and implementation of an efficient method well suited to the specific case of MOFs with circular inclusions, and through the development of appropriate tools to analyse results. The systematic study enabled us to develop or adapt simple physical models of light-guidance in MOFs, leading to a better understanding of the physics of MOFs and to charts letting us predict mode properties, even for MOFs with complex geometries.

Numerous properties we have established were probably somewhat intuitive for workers familiar with the field of MOFs, and the latter might only have found confirmation of knowledge they already gained through their own research. Nevertheless we believe that our work clarifies and gives a sounder base to some of the “intuitive” properties of MOFs. In particular, we believe that we have lifted the ambiguity related to the notion of guided leaky modes, establishing a clear distinction between confined and unconfined leaky modes.

The result we attach the most importance to is of course the fundamental mode cutoff and the fundamental mode phase-diagram. In our study of non conventional MOF designs achieving ultra-flat near-zero dispersion, we had a glimpse on how helpful the phase diagram is in understanding properties of complex MOF geometries, and we are confident the phase diagram will prove useful in guiding further innovative MOF applications.

In our work, the MOFs we considered were mostly infinitely long, with perfectly smooth circular inclusions having rigorously the same diameter in each ring, without non-linearity, tension, torsion or bends. Such ideal fibres are closer to a *Gedankenexperiment* than to the reality of experimental fibres, and we have indeed seen that agreement between numerical and experimental results, especially regarding chromatic dispersion, is not always totally satisfactory. Now that properties of “perfect” solid core MOFs are understood, it is time to tackle the study of imperfect MOFs, the first step certainly being to investigate the effect of realistic (longitudinal and transversal) random perturbations in the hole distribution. However, given that exceptional properties of MOFs have already been demonstrated numerous times experimentally, we can predict that taking into account perturbations of the ideal MOFs is unlikely to defeat predicted MOF properties on a fundamental level. We can merely expect a slight shift of the regions of parameter space in which they occur.

# Appendix A

## Choice of the Square Roots

In the multipole method, we encounter mainly two perpendicular wave numbers:  $k_{\perp}^{\text{M}}$  associated with the refractive index  $n_{\text{M}}$  of the matrix, and  $k_{\perp}^{\text{i}}$  associated with the refractive index  $n_{\text{i}}$  of inclusions:

$$k_{\perp}^{\text{i}} = \sqrt{k_0^2 n_{\text{i}} - \beta^2} = k_0(n_{\text{i}}^2 - n_{\text{eff}}^2)^{1/2} \quad (\text{A.1})$$

$$k_{\perp}^{\text{M}} = \sqrt{k_0^2 n_{\text{M}}^2 - \beta^2} = k_0(n_{\text{M}}^2 - n_{\text{eff}}^2)^{1/2} . \quad (\text{A.2})$$

Given that the square root function is double valued, we have to justify which square root we choose. We consider here the case of the solid core MOF of Fig. 2.2, with the jacket consisting of the same material as the matrix. Following the spectral considerations of Sec. 2.4.5, we look for values of  $n_{\text{eff}}$  satisfying

$$n_{\text{i}} < \Re(n_{\text{eff}}) < n_{\text{M}} \quad (\text{A.3})$$

$$0 < \Im(n_{\text{eff}}) \lesssim \Re(n_{\text{eff}}) . \quad (\text{A.4})$$

Fig. A.1 shows the considered region of  $n_{\text{eff}}$  in the complex plane, along with the images of this region through the different transformations leading to  $k_{\perp}^{\text{M}}/k_0$ . Fig. A.2 is the equivalent of Fig. A.1 but for  $k_{\perp}^{\text{i}}/k_0$ .

Since the jacket is made out of the matrix material, the fields in the jacket can be expressed in the cylindrical coordinates  $(r, \theta)$  with origin at the center of the fibre as the Fourier-Bessel series

$$V(r, \theta) = \sum_{n \in \mathbb{Z}} B_n^0 H_n^{(1)}(k_{\perp}^{\text{M}} r) \exp(in\theta) . \quad (\text{A.5})$$

The asymptotic expansion for large arguments of  $H_n^{(1)}$  being

$$H_n^{(1)}(k_{\perp}^{\text{M}} r) \simeq \frac{2}{\sqrt{(\pi k_{\perp}^{\text{M}} r)}} \exp[i(k_{\perp}^{\text{M}} r - n\pi/2 - \pi/4)] \quad (\text{A.6})$$

for the fields to have the correct behaviour of carrying energy away from the fibre (*i.e.* diverging with  $r$ , as explained in Sec. 2.4.3),  $k_{\perp}^{\text{M}}$  must have a negative imaginary part. This leads us to choose the lower right region of possible values for  $k_{\perp}^{\text{M}}/k_0$  in Fig. A.1.

We cannot use the same kind of argument for the choice of the square root leading to  $k_{\perp}^{\text{i}}$ . Indeed, given the size of the inclusions, asymptotic expansions wouldn't make sense, and we

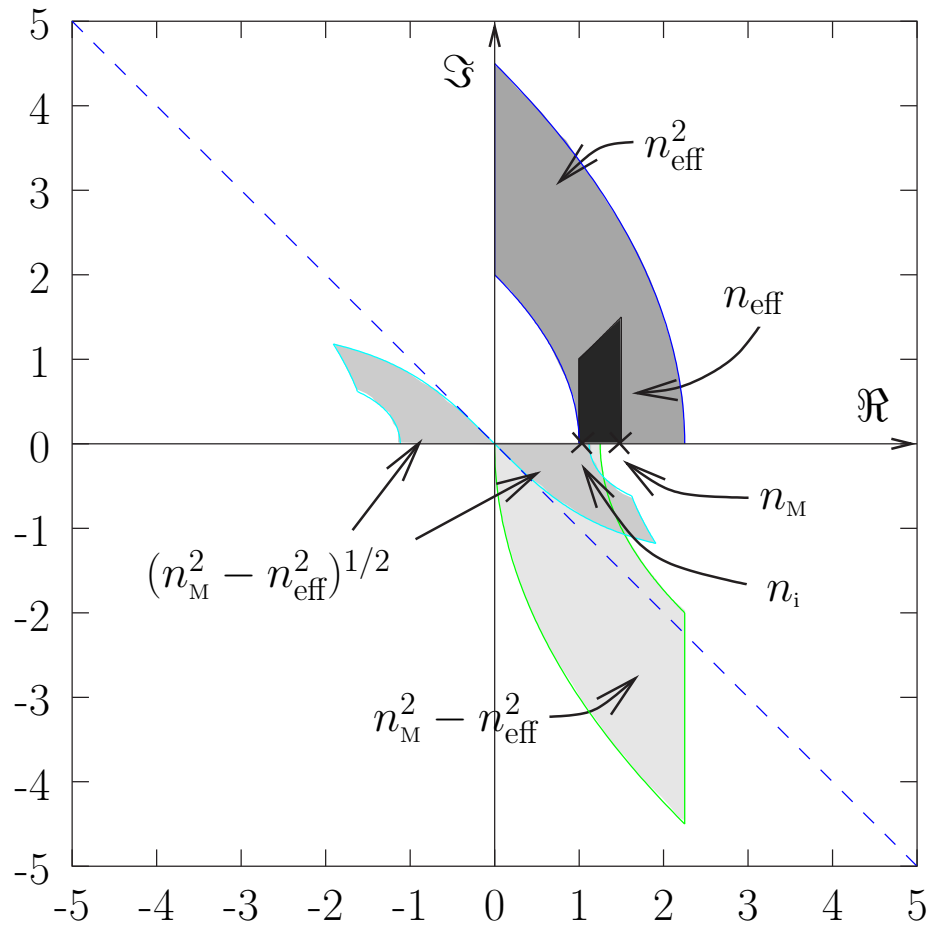


Figure A.1: Choice of the square root for  $k_{\perp}^M$ : regions of possible values of various functions of  $n_{\text{eff}}$ . Here  $n_M = 1.5$  and  $n_i = 1$ .

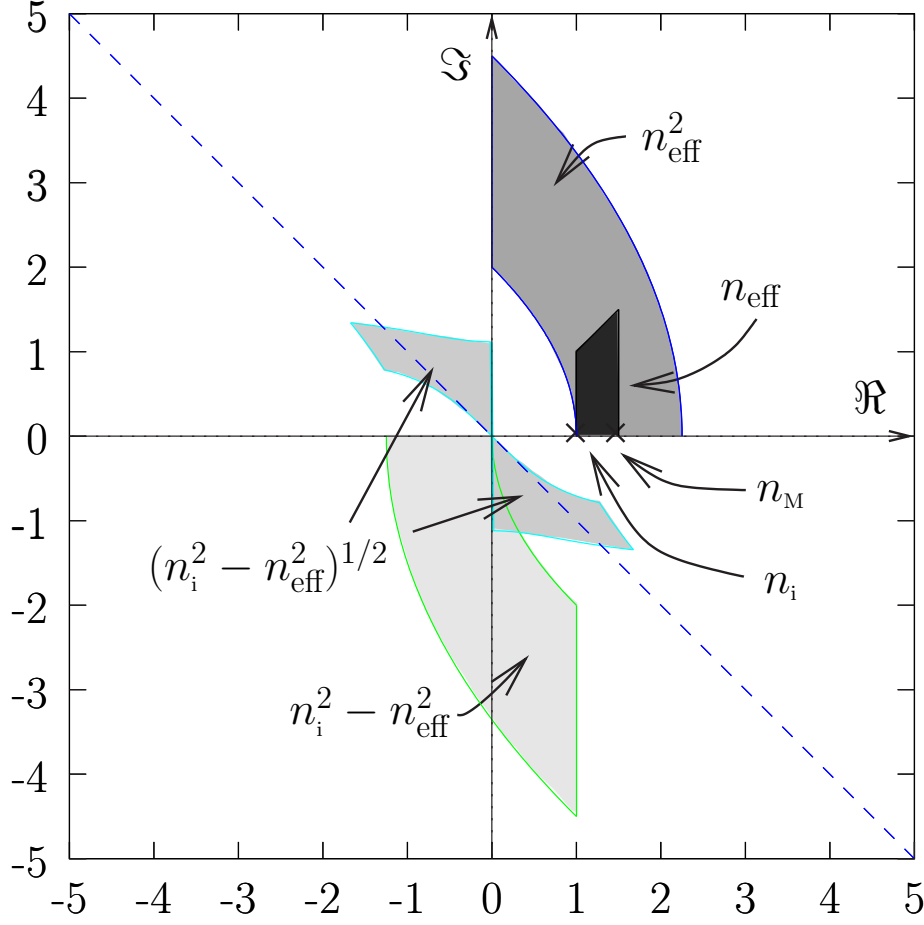


Figure A.2: Choice of the square root for  $k_{\perp}^i$ : regions of possible values of various functions of  $n_{\text{eff}}$ . Here  $n_M = 1.5$  and  $n_i = 1$ .

have no *a priori* knowledge of the behaviour of the fields in the inclusion. We can assume that the fields would be evanescent in the inclusions for well confined modes, but they could become non-evanescent for very leaky modes. This would lead to two different choices of the square root depending on how leaky the mode is. The problem of the choice of the physically correct square root in such a case is not new and has already occurred in the case of gratings. Considerations on continuity of the solutions with varying parameters have led to a cutoff curve for the square root which can be approximated near the origin by the second bisector of the complex plane we have added to Fig. A.2 [123]: the correct square root is the one above the bisector. Given the small imaginary parts we will deal with, we will use the bisector as the cutoff for the square root and choose the value of  $k_{\perp}^i$  satisfying  $\Re(k_{\perp}^i) + \Im(k_{\perp}^i) > 0$ .

## Appendix B

# Derivation of the Wijnngaard expansion

To generalize the Wijnngaard expansion of the field to MOF, we define a function  $U(x, y)$  as

$$U(x, y) = \begin{cases} E_z, & r < R_0, \\ 0, & \text{elsewhere.} \end{cases} \quad (\text{B.1})$$

Thus  $U$  is continuous inside the hole region, because of the continuity of the tangential field component, while its normal derivative is discontinuous at the boundaries of the inclusions. Both  $U$  and its normal derivative are discontinuous at the jacket boundary  $C$  ( $r = R_0$ ). As a consequence, it can be deduced from (3.3) and (3.4) that  $U$  satisfies, in the sense of distributions [124],

$$\nabla^2 U + k_\perp^2 U = s \quad (\text{B.2})$$

where  $k_\perp = k_\perp^i$  in inclusion  $i$ , and  $k_\perp = k_\perp^M$  elsewhere. Source  $s$  is a singular distribution given by

$$s = \sum_{j=1}^{N_i} S_j \delta_{C_j} - T \delta_C - \nabla \cdot (\mathbf{n} Q \delta_C) \quad (\text{B.3})$$

with  $S_j$  defined at the boundary  $C_j$  of the  $j$ -th hole as the jump of the normal derivative of  $U$ . Further,  $Q$  and  $T$  are, respectively, the limits of  $U$  and its normal derivative at  $r = R_0$ , where the normal  $\mathbf{n}$  is outwardly oriented. The distribution  $A \delta_C$  is defined by [124]

$$\langle A \delta_C, \varphi \rangle = \int_C A(M) \varphi(M) dM \quad (\text{B.4})$$

$M$  being a point of  $C$ ,  $dM$  the length of an elementary segment of  $C$  and  $\varphi$  an infinitely differentiable function with bounded support.

Equation (B.2) can be rewritten as

$$\nabla^2 U + (k_\perp^M)^2 U = [(k_\perp^M)^2 - (k_\perp)^2] U + s \quad (\text{B.5})$$

and so in the hole region  $U$  follows from the convolution

$$U = G_e \star [s + ((k_\perp^e)^2 - (k_\perp)^2) U], \quad (\text{B.6})$$

where  $G_e$  is the Green function of the Helmholtz equation:  $G_e = -iH_0^{(1)}(k_\perp^M r)/4$ . From (B.3) and (B.6)  $U$  can be reexpressed as

$$U = \sum_{j=1}^{N_i} G_e \star D_j + G_e \star D, \quad (\text{B.7})$$

with

$$D_j = S_j \delta_{C_j} + \left[ (k_\perp^e)^2 - (k_\perp^j)^2 \right] U_j \quad (\text{B.8})$$

$$D = -T \delta_C - \nabla \cdot (\mathbf{n} Q \delta_C), \quad (\text{B.9})$$

$$U_j = \begin{cases} U & \text{in the } j\text{-th inclusion} \\ 0 & \text{elsewhere.} \end{cases} \quad (\text{B.10})$$

Each term  $V_j = G_e \star D_j$  of the sum on the right-hand side of (B.7) is generated by sources placed inside or at the boundary of the  $j$ -th inclusion and satisfies a radiation condition outside this hole. It can be identified at any point outside this inclusion as the field scattered by it. Of course, since it satisfies the homogeneous Helmholtz equation outside the  $j$ -th inclusion, in the sense of distributions, it can be represented in the entire matrix region as a Fourier Bessel series

$$V_j = \sum_m B_m^{Ej} H_m^{(1)}(k_\perp^M r_j) e^{im\theta_j}. \quad (\text{B.11})$$

The term  $G_e \star D$  on the right-hand member of (B.7) is generated by sources outside or on the jacket boundary and it thus has no singularity inside this boundary. It can be identified as the incident field generated by the jacket and illuminating the matrix-inclusion region. It can also be represented in a Fourier-Bessel expansion

$$V_{\text{inc}} = \sum_m A_m^{\text{E0}} J_m(k_\perp^M r) e^{im\theta}. \quad (\text{B.12})$$

From equations (B.7), (B.11) and (B.12), it can now be shown that in the entire matrix region, the field  $E_z$  can be represented by the Wijnngaard expansion (3.21). The same argument can be used for the  $z$  component of the magnetic field  $H_z$ .

# Appendix C

## Change of basis

Three changes of basis transformations are required: (i) conversion of outgoing fields sourced on one cylinder to regular fields in the basis of another cylinder; (ii) conversion of the regular field sourced on the jacket boundary to a regular field in the basis of each cylinder; and (iii) conversion of outgoing fields sourced at the cylinders to an outgoing field close to the jacket boundary. These are considered separately below.

### C.1 Cylinder to Cylinder Conversion

Here we consider an outgoing cylindrical harmonic wave sourced from cylinder  $j$  and derive its regular representation in the coordinate system of cylinder  $l$ . From Graf's Theorem [82] we derive

$$\begin{aligned} H_m^{(1)}(k_{\perp}^e r_j) e^{im \arg(\mathbf{r}_j)} &= \sum_{n=-\infty}^{\infty} J_n(k_{\perp}^e r_l) e^{in \arg(\mathbf{r}_l)} \\ H_{n-m}^{(1)}(k_{\perp}^e c_{lj}) e^{-i(n-m) \arg(\mathbf{c}_{lj})}, \end{aligned} \quad (\text{C.1})$$

so that the total field due to cylinder  $j$  is expressed as

$$\sum_{m=-\infty}^{\infty} B_m^j H_m^{(1)}(k_{\perp}^e r_j) e^{im \arg(\mathbf{r}_j)} = \sum_{n=-\infty}^{\infty} A_n^{lj} J_n(k_{\perp}^e r_l) e^{in \arg(\mathbf{r}_l)}, \quad (\text{C.2})$$

where  $A_n^{lj}$ , defined in Eqs (3.24) and (3.25), denotes the contribution to the  $n$ th multipole coefficient at cylinder  $l$  due to cylinder  $j$ .

### C.2 Jacket to Cylinder Conversion

From Graf's Theorem [82] we now have

$$\begin{aligned} J_m(k_{\perp}^e r) e^{im\theta} &= \sum_{n=-\infty}^{\infty} J_n(k_{\perp}^e r_l) e^{in \arg(\mathbf{r}_l)} (-1)^{n-m} \\ &\quad J_{n-m}(k_{\perp}^e c_l) e^{-i(n-m) \arg(\mathbf{c}_l)}, \end{aligned} \quad (\text{C.3})$$

and from this, the change of basis transform is

$$\sum_{m=-\infty}^{\infty} A_m^0 J_m(k_{\perp}^e r) e^{im\theta} = \sum_{n=-\infty}^{\infty} A_n^{l0} J_n(k_{\perp}^e r_l) e^{in \arg(\mathbf{r}_l)}, \quad (\text{C.4})$$

where  $A_n^{l0}$  denotes the multipole coefficient in the basis of cylinder  $l$  due to the regular field radiating from the jacket. Equation (3.28) is the matrix form of (C.4).

### C.3 Cylinder to Jacket Conversion

The relevant transformation from Graf's theorem [82] is now

$$\begin{aligned} H_m^{(1)}(k_{\perp}^e r_l) e^{im \arg(\mathbf{r}_l)} &= \sum_{n=-\infty}^{\infty} H_n^{(1)}(k_{\perp}^e r) e^{in\theta} \\ &\quad J_{n-m}(k_{\perp}^e c_l) e^{-i(n-m) \arg(\mathbf{c}_l)}. \end{aligned} \quad (\text{C.5})$$

The contribution from cylinder  $l$  to the outgoing field near the jacket boundary is

$$\sum_{m=-\infty}^{\infty} B_m^l H_m^{(1)}(k_{\perp}^e r_l) e^{im \arg(\mathbf{r}_l)} = \sum_{n=-\infty}^{\infty} B_n^{0l} H_n^{(1)}(k_{\perp}^e r) e^{in\theta}, \quad (\text{C.6})$$

which can be written in the matrix notation (3.32).

## Appendix D

# Scattering Matrices in Conical Incidence

We consider a cylinder centered at the origin of refractive index  $n_-$  and radius  $a$  embedded in a medium of refractive index  $n_+$ . To derive the reflection matrices of this cylinder we express the  $E_z$  and  $H_z$  fields in terms of Fourier-Bessel series in the local cylindrical coordinates  $(r, \theta)$  inside and outside the cylinder (*c.f.* Eq. (3.20)),

$$E_z^\mp(r, \theta) = \sum_{m=-\infty}^{\infty} \left[ A_m^{\text{E}\mp} J_m(k_\perp^\mp r) + B_m^{\text{E}\mp} H_m^{(1)}(k_\perp^\mp r) \right] e^{im\theta}, \quad (\text{D.1})$$

for  $r < a$  ( $-$ ) and  $r > a$  ( $+$ ), with similar expressions for  $K_z$ . Here,  $k_\perp^\pm = (k^0{}^2 n_\pm^2 - \beta^2)^{1/2}$  are the transverse wave numbers inside (outside) the cylinder. We introduce the vectors  $\mathbf{A}^{\text{E}\pm} = [A_m^{\text{E}\pm}]$  and  $\mathbf{B}^{\text{E}\pm} = [B_m^{\text{E}\pm}]$ , as well as their  $K$  counterparts, and the condensed notation introduced in Eqs (3.37) and (3.38) for  $\tilde{\mathbf{A}}^\pm$  and  $\tilde{\mathbf{B}}^\pm$ . The interpretation of the  $J$  and  $H$  terms was given in Chapter 3. At the cylinder boundary, reflection and transmission occurs and the waves mix with each other, which, because of the linearity of the Maxwell equations, can be expressed as a matrix relation between the various coefficients, as

$$\begin{cases} \tilde{\mathbf{A}}^- = \tilde{\mathbf{T}}^- \tilde{\mathbf{A}}^+ + \tilde{\mathbf{R}}^- \tilde{\mathbf{B}}^-, \\ \tilde{\mathbf{B}}^+ = \tilde{\mathbf{R}}^+ \tilde{\mathbf{A}}^+ + \tilde{\mathbf{T}}^+ \tilde{\mathbf{B}}^-. \end{cases} \quad (\text{D.2})$$

Here,  $\mathbf{R}^-$  and  $\mathbf{R}^+$  are referred to as interior and exterior *reflection matrices* of the cylinder, whereas  $\mathbf{T}^+$  and  $\mathbf{T}^-$  are transmission matrices, which do not matter in the analysis below. Note that the first of (D.2) leads to Eq. (3.39), whereas the second leads to (3.38).

The  $\mathbf{R}^\pm$  matrices can be derived from the continuity of the tangential field components at the cylinder boundary. To do this we need the expressions for the  $\theta$  components of the fields, which can be expressed as a function of the  $z$  components as [3]

$$E_\theta(r, \theta) = \frac{i}{k_\perp^2} \left( \frac{\beta}{r} \frac{\partial E_z}{\partial \theta} - k \frac{\partial K_z}{\partial r} \right), \quad (\text{D.3})$$

$$K_\theta(r, \theta) = \frac{i}{k_\perp^2} \left( \frac{\beta}{r} \frac{\partial K_z}{\partial \theta} + k n^2 \frac{\partial E_z}{\partial r} \right), \quad (\text{D.4})$$

where  $n$  is the refractive index. The partial derivatives that appear straightforwardly follow from (D.1).

We can now write the continuity conditions for the  $z$  components by equating Eqs (D.1) on the boundary.

$$\begin{aligned} E_z(a) &= \sum_{m=-\infty}^{\infty} \left[ A_m^{\text{E}-} J_m(k_{\perp}^{-} a) + B_m^{\text{E}-} H_m^{(1)}(k_{\perp}^{-} a) \right] e^{im\theta}, \\ &= \sum_{m=-\infty}^{\infty} \left[ A_m^{\text{E}+} J_m(k_{\perp}^{+} a) + B_m^{\text{E}+} H_m^{(1)}(k_{\perp}^{+} a) \right] e^{im\theta}. \end{aligned} \quad (\text{D.5})$$

Since the resulting equation is valid for all  $\theta$ , terms with different  $m$  decouple and we find for each  $m$

$$A_m^{\text{E}-} J_m^{-} + B_m^{\text{E}-} H_m^{-} = A_m^{\text{E}+} J_m^{+} + B_m^{\text{E}+} H_m^{+}, \quad (\text{D.6})$$

with the same result for  $K_z$ . Here we introduced the condensed notation  $J_m^{\pm} = J_m(k_{\perp}^{\pm} a)$ , etc.

In the same way we can equate the interior and exterior expressions for  $E_{\theta}$  and  $K_{\theta}$ . We then obtain two equalities of Fourier series in  $e^{im\theta}$ , in which, again, terms with different  $m$  decouple. We finally obtain a set of equations valid for all  $m$ :

$$\begin{aligned} &k_{\perp}^{-2} \left\{ \frac{i\beta m}{a} (A_m^{\text{E}+} J_m^{+} + B_m^{\text{E}+} H_m^{+}) - k_0 k_{\perp}^{+} (A_m^{\text{K}+} J_m'^{+} + B_m^{\text{K}+} H_m'^{+}) \right\} \\ &- k_{\perp}^{+2} \left\{ \frac{i\beta m}{a} (A_m^{\text{E}-} J_m^{-} + B_m^{\text{E}-} H_m^{-}) - k_0 k_{\perp}^{-} (A_m^{\text{K}-} J_m'^{-} + B_m^{\text{K}-} H_m'^{-}) \right\} = 0 \end{aligned} \quad (\text{D.7})$$

$$\begin{aligned} &k_{\perp}^{-2} \left\{ \frac{i\beta m}{a} (A_m^{\text{K}+} J_m^{+} + B_m^{\text{K}+} H_m^{+}) + n_+^2 k_0 k_{\perp}^{+} (A_m^{\text{E}+} J_m'^{+} + B_m^{\text{E}+} H_m'^{+}) \right\} \\ &- k_{\perp}^{+2} \left\{ \frac{i\beta m}{a} (A_m^{\text{K}-} J_m^{-} + B_m^{\text{K}-} H_m^{-}) + n_-^2 k_0 k_{\perp}^{-} (A_m^{\text{E}-} J_m'^{-} + B_m^{\text{E}-} H_m'^{-}) \right\} = 0 \end{aligned} \quad (\text{D.8})$$

Here we have extended our condensed notation for the derivatives introducing  $J_m'^{-} = J_m'(k_{\perp}^{-} a)$  and  $J_m'^{+} = J_m'(k_{\perp}^{+} a)$  with similar definitions for  $H_m'^{-}$  and  $H_m'^{+}$ . These equations, in combination with (D.6) and its  $K_z$  counterpart are sufficient to obtain the  $\mathbf{R}$  matrices.

We first concentrate on the interior reflection matrix  $\tilde{\mathbf{R}}^{-}$ ; we obtain its coefficients by setting the exterior incoming field to zero:  $\tilde{\mathbf{A}}^{+} = \mathbf{0}$ . It is now straightforward to solve, for a given  $m$ , the linear set of equation given to express  $A_m^{\text{E}-}$  and  $A_m^{\text{K}-}$  in terms of  $B_m^{\text{E}-}$  and  $B_m^{\text{K}-}$  by eliminating  $B_m^{\text{E}+}$  and  $B_m^{\text{K}+}$ . We obtain

$$\begin{cases} A_m^{\text{E}-} &= R_m^{\text{EE}-} B_m^{\text{E}-} + R_m^{\text{EK}-} B_m^{\text{K}-}, \\ A_m^{\text{K}-} &= R_m^{\text{KE}-} B_m^{\text{E}-} + R_m^{\text{KK}-} B_m^{\text{K}-}, \end{cases} \quad (\text{D.9})$$

with

$$\begin{aligned}
R_m^{\text{EE}-} &= \frac{1}{\delta_m} \left\{ (\alpha_{J^-H^+}^+ - \alpha_{H^+J^-}^-) \times \right. \\
&\quad \left. (n_-^2 \alpha_{H^-H^+}^+ - n_+^2 \alpha_{H^+H^-}^-) - m^2 J_m^- H_m^- H_m^{+2} \tau^2 \right\}, \\
R_m^{\text{EK}-} &= \frac{1}{\delta_m} \left\{ \frac{2m\tau}{\pi k_0 a} \frac{k_\perp^+}{k_\perp^-} H_m^{+2} \right\}, \\
R_m^{\text{KE}-} &= -n_-^2 R_m^{\text{EK}-}, \\
R_m^{\text{KK}-} &= \frac{1}{\delta_m} \left\{ (\alpha_{H^-H^+}^+ - \alpha_{H^+H^-}^-) \times \right. \\
&\quad \left. (n_-^2 \alpha_{J^-H^+}^+ - n_+^2 \alpha_{H^+J^-}^-) - m^2 J_m^- H_m^- H_m^{+2} \tau^2 \right\},
\end{aligned} \tag{D.10}$$

where

$$\alpha_{J^\pm H^\pm}^\pm = \frac{k_\perp^\pm}{k_0} J_m'^\pm H_m^\pm \tag{D.11}$$

with other  $\alpha$  coefficients defined analogously. Further

$$\begin{aligned}
\delta_m &= (\alpha_{H^+J^-}^- - \alpha_{J^-H^+}^+) (n_-^2 \alpha_{J^-H^+}^+ - n_+^2 \alpha_{H^+J^-}^-) \\
&\quad + (m J_m^- H_m^+ \tau)^2
\end{aligned} \tag{D.12}$$

and

$$\tau = \frac{\beta}{a k_\perp^- k_\perp^+} (n_+^2 - n_-^2). \tag{D.13}$$

To obtain the exterior reflection matrix  $\tilde{\mathbf{R}}^+$  we set  $\tilde{\mathbf{B}}^- = \mathbf{0}$ , and eliminate the  $A_m^-$  coefficients. This yields

$$\begin{aligned}
R_m^{\text{EE}+} &= \frac{1}{\delta_m} \left\{ (\alpha_{J^-H^+}^+ - \alpha_{H^+J^-}^-) \times \right. \\
&\quad \left. (n_-^2 \alpha_{J^-J^+}^+ - n_+^2 \alpha_{J^+J^-}^-) - m^2 J_m^+ H_m^+ J_m^{-2} \tau^2 \right\}, \\
R_m^{\text{EK}+} &= \frac{1}{\delta_m} \left\{ \frac{2m\tau}{\pi k_0 a} \frac{k_\perp^-}{k_\perp^+} J_m^{-2} \right\}, \\
R_m^{\text{KE}+} &= -n_+^2 R_m^{\text{EK}+}, \\
R_m^{\text{KK}+} &= \frac{1}{\delta_m} \left\{ (\alpha_{J^-J^+}^+ - \alpha_{J^+J^-}^-) \times \right. \\
&\quad \left. (n_-^2 \alpha_{J^-H^+}^+ - n_+^2 \alpha_{H^+J^-}^-) - m^2 J_m^+ H_m^+ J_m^{-2} \tau^2 \right\}.
\end{aligned} \tag{D.14}$$

## Appendix E

# Algorithm

We compute the determinant for a number of points  $0 \leq i_r \leq N_{\Re}$  over  $0 \leq i_i \leq N_{\Im}$  lines parallel to the real axis, with imaginary parts varying exponentially with  $i_i$ . The exponential variation of the imaginary part is necessary as different modes can have losses differing by several orders of magnitude. Local minima of this array are computed through simple data analysis, and better initial guesses of the minima are estimated through interpolation of the points adjacent to each minimum. This guess is used as a starting point for a Broyden-like algorithm. If the algorithm fails, a new map of the determinant is computed over the region in which the first mapping showed there is a local minimum. This refinement map uses a region of  $5 \times 5$  points, with a linear scale for both real and imaginary parts. If the only minima of the refined region are on its border, the region is extended until a minimum lies inside the region. During the enlargement of the region, care is taken to avoid regions overlapping with regions in which computing errors can occur (negative or excessive imaginary or real part). If a minimum is found in the refined region (excluding the borders), the routine tries the Broyden-like algorithm again. If multiple minima are found in the region, each minimum is added to the initial minima list and is treated separately: missing a zero thus becomes very unlikely. During the Broyden algorithm a calculation of singular values is performed (see Section 4.3.1) each time the modulus of the determinant for the current point is less than a parameterized threshold, and the modules of the eigenvalues are analysed to determine whether an acceptable solution has been found (see the discussion in Section 4.3.1).

The routine continues to alternate Broyden and zooming algorithms until one of the following occurs:

- an acceptable solution is found,
- the extended mapping region concentrates near a border of the initial region,
- the refined region becomes too small,
- the extended mapping region includes a minimum of the initial determinant map which has already been treated,
- a maximum number of iterations is reached.

Depending on the width of the initial scanning region and the complexity of the structure, the pertinent choice of  $N_{\Re}$  varies from about 50 to several hundreds: structures with a substantial number of cylinders have a higher density of modes and therefore need a better

resolution on the initial determinant map. The value of  $N_{\mathfrak{S}}$ , even for intricate structures, does not need to be high, and is usually taken between 4 and 8: as shown by Fig. 4.2, zeros are usually associated with valleys parallel to the imaginary axis, so that precise maps parallel to the real axis for a few values of the imaginary part are sufficient to find a first estimate of the zeros.

## Appendix F

# Symmetrization of modes

We consider waveguides with  $C_{6v}$  symmetry, such as the structures in Fig. 4.9. From McIsaac [76], such structures have 8 mode classes, with 4 of these occurring as 2 degenerate pairs, as shown in Fig. 4.3. For the purpose of this example we are interested in the degenerate fundamental modes  $p = 3$  and  $p = 4$  and the lowest order non-degenerate modes  $p = 1$  and  $p = 2$ . The minimum waveguide segments illustrated in Fig. 4.3 represent the smallest segment of the fibre required to define fully the modal fields of the complete structure. We relate the multipole coefficients for a secondary cylinder outside the minimum segment to those of the corresponding primary cylinder inside the segment.

From Fig. 4.3 the non-degenerate mode classes 1 and 2 have minimum waveguide segments of  $\pi/6$ , so 3 primary cylinders are required to describe the 18 hole structure shown in Fig. F.1. The holes are labeled as  $P_S$  where  $P$  is the primary cylinder and  $S$  the label given to the secondary cylinder. Hole  $1_1$  is the primary cylinder 1 and lies in the inner shell, while the other primary cylinders  $2_1$  and  $3_1$  lie in the second shell. As they are not degenerate, these modes must exhibit the full 6-fold symmetry of the structure.

In terms of the multipole coefficients of the electric field  $b_m^E$ , the relation between those on secondary cylinders to those on primary cylinders can be expressed in the form

$$b_m^{E(P_S)} = b_m^{E(P_1)} e^{im(S-1)\pi/3},$$

and similarly for the magnetic field coefficients.

For the degenerate mode classes 3 and 4, the number of secondary cylinders corresponding to a given primary cylinder depends on the position of the primary cylinder. If the primary cylinder lies on a symmetry axis of the mode, in this case either the  $x$  or  $y$  axis, then only one other cylinder is related to it. A primary cylinder not on a symmetry axis has 3 associated secondary cylinders. A cylinder positioned at the center of the structure has no secondary cylinders. The related primary and secondary cylinders are shown in Fig. F.2.

For classes 3 and 4, the fields are either symmetric or anti-symmetric about the transverse axes. The relation between primary and secondary cylinders is obtained by appropriate combinations of reflections and inversions to give the correct symmetry properties.

For mode  $p = 3$ , the multipole coefficients on a secondary cylinder lying on the  $x$ -axis are related to those on the corresponding primary cylinder by a simple reflection of  $E_z$  and anti-reflection of  $K_z$  across the  $y$ -axis:

$$b_m^{E(P_2)} = -b_{-m}^{E(P_1)}, \quad b_m^{K(P_2)} = b_{-m}^{K(P_1)}.$$

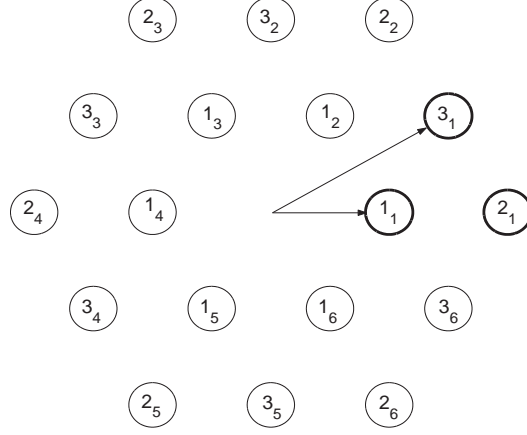


Figure F.1: Primary (bold) and secondary cylinders of the non-degenerate  $p = 1$  and  $p = 2$  mode classes of a 2-ring MOF structure.

Similarly, for a secondary cylinder on the  $y$ -axis, the relations are

$$b_m^{E(P_2)} = (-1)^m b_{-m}^{E(P_1)}, b_m^{K(P_2)} = (-1)^{m+1} b_{-m}^{K(P_1)}.$$

As mentioned, a primary cylinder that does not lie on either axis has three associated secondary cylinders. The relations are again combinations of reflections and anti-reflections about the axes:

$$\begin{aligned} b_m^{E(P_2)} &= -b_{-m}^{E(P_1)}, \\ b_m^{E(P_3)} &= (-1)^{m+1} b_m^{E(P_1)}, \\ b_m^{E(P_4)} &= (-1)^m b_{-m}^{E(P_1)}, \end{aligned}$$

$$\begin{aligned} b_m^{K(P_2)} &= b_{-m}^{K(P_1)}, \\ b_m^{K(P_3)} &= (-1)^{m+1} b_m^{K(P_1)}, \\ b_m^{K(P_4)} &= (-1)^{m+1} b_{-m}^{K(P_1)}. \end{aligned}$$

The relations for the second degenerate mode class  $p = 4$  are simply obtained by swapping the  $b_m^E$  and  $b_m^K$  coefficients in the equations above.

These symmetry relations are used in our method to re-express the field identity (3.45) in terms of the primary cylinders only. This reduces the matrix dimensions by a factor between 3.5 and 6, depending on the mode class, thus greatly increasing the calculation speed and allowing larger structures to be studied.

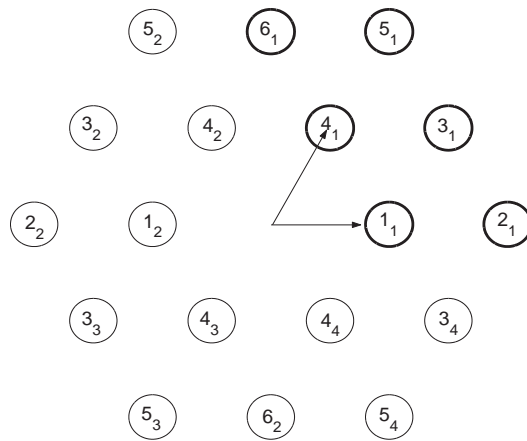


Figure F.2: Primary (bold) and secondary cylinders of the degenerate  $p = 3$  and  $p = 4$  mode classes of a 2-ring MOF structure.

## Appendix G

# Bloch Transform and Fourier Transform

In this appendix we investigate how the Fourier transform and the Bloch transform are related, in the case of a periodic lattice of circular inclusions. Using the multipole expansion, the Fourier transform  $\tilde{V}$  of a field  $V$  in such a structure is

$$\begin{aligned} \tilde{V}(\mathbf{k}) = & \frac{1}{2\pi} \iint_{\mathbf{r} \in \mathbb{R}^2 - \bigcup_{\mathbf{r}_p \in \mathcal{L}} \mathcal{D}(\mathbf{r}_p)} \sum_{\mathbf{r}_l \in \mathcal{L}} \sum_{n \in \mathbb{Z}} B_n(\mathbf{r}_l) H_n^{(1)}(k_\perp |\mathbf{r} - \mathbf{r}_l|) \times \\ & \exp(in \arg(\mathbf{r} - \mathbf{r}_l)) \exp(-i\mathbf{k} \cdot \mathbf{r}) d\mathbf{r} \\ & + \frac{1}{2\pi} \sum_{\mathbf{r}_l \in \mathcal{L}} \iint_{\mathcal{D}(\mathbf{r}_l)} \sum_{n \in \mathbb{Z}} A_n(\mathbf{r}_l) J_n(k_\perp |\mathbf{r} - \mathbf{r}_l|) \exp(in \arg(\mathbf{r} - \mathbf{r}_l)) \exp(-i\mathbf{k} \cdot \mathbf{r}) d\mathbf{r} , \quad (\text{G.1}) \end{aligned}$$

where  $\mathcal{D}(\mathbf{r}_p)$  is the interior of the inclusion centered on  $\mathbf{r}_p$ . Interchanging the summation and integration leads to

$$\begin{aligned} \tilde{V}(\mathbf{k}) = & \frac{1}{2\pi} \sum_{\mathbf{r}_l \in \mathcal{L}} \sum_{n \in \mathbb{Z}} B_n(\mathbf{r}_l) \iint_{\mathbf{r} \in \mathbb{R}^2 - \bigcup_{\mathbf{r}_p \in \mathcal{L}} \mathcal{D}(\mathbf{r}_p)} H_n^{(1)}(k_\perp |\mathbf{r} - \mathbf{r}_l|) \times \\ & \exp(in \arg(\mathbf{r} - \mathbf{r}_l)) \exp(-i\mathbf{k} \cdot \mathbf{r}) d\mathbf{r} \\ & + \frac{1}{2\pi} \sum_{\mathbf{r}_l \in \mathcal{L}} \sum_{n \in \mathbb{Z}} A_n(\mathbf{r}_l) \iint_{\mathcal{D}(\mathbf{r}_l)} J_n(k_\perp |\mathbf{r} - \mathbf{r}_l|) \exp(in \arg(\mathbf{r} - \mathbf{r}_l)) \exp(-i\mathbf{k} \cdot \mathbf{r}) d\mathbf{r} . \quad (\text{G.2}) \end{aligned}$$

Changing the origin in the integrals using  $\mathbf{r}' = \mathbf{r} - \mathbf{r}_l$  yields

$$\begin{aligned} \tilde{V}(\mathbf{k}) = & \frac{1}{2\pi} \sum_{\mathbf{r}_l \in \mathcal{L}} \sum_{n \in \mathbb{Z}} \exp(-i\mathbf{k} \cdot \mathbf{r}_l) B_n(\mathbf{r}_l) \times \\ & \iint_{\mathbf{r} \in \mathbb{R}^2 - \bigcup_{\mathbf{r}_p \in \mathcal{L}} \mathcal{D}(\mathbf{r}_p)} H_n^{(1)}(k_\perp |\mathbf{r}|) \exp(in \arg(\mathbf{r})) \exp(-i\mathbf{k} \cdot \mathbf{r}) d\mathbf{r} \\ & + \frac{1}{2\pi} \sum_{\mathbf{r}_l \in \mathcal{L}} \sum_{n \in \mathbb{Z}} \exp(-i\mathbf{k} \cdot \mathbf{r}_l) A_n(\mathbf{r}_l) \iint_{\mathcal{D}(\mathbf{r}_l)} J_n(k_\perp |\mathbf{r}|) \exp(in \arg(\mathbf{r})) \exp(-i\mathbf{k} \cdot \mathbf{r}) d\mathbf{r} , \quad (\text{G.3}) \end{aligned}$$

where we have used the periodicity of the integration domains. The integrals no longer depend on  $\mathbf{r}_l$  and we have

$$\begin{aligned} \tilde{V}(\mathbf{k}) = & \sum_{n \in \mathbb{Z}} \left( \sum_{\mathbf{r}_l \in \mathcal{L}} \exp(-i\mathbf{k} \cdot \mathbf{r}_l) B_n(\mathbf{r}_l) \right) \times \\ & \left( \frac{1}{2\pi} \iint_{\mathbf{r} \in \mathbb{R}^2 - \bigcup_{\mathbf{r}_p \in \mathcal{L}} \mathcal{D}(\mathbf{r}_p)} H_n^{(1)}(k_\perp |\mathbf{r}|) \exp(in \arg(\mathbf{r})) \exp(-i\mathbf{k} \cdot \mathbf{r}) d\mathbf{r} \right) \\ & + \sum_{n \in \mathbb{Z}} \left( \sum_{\mathbf{r}_l \in \mathcal{L}} \exp(-i\mathbf{k} \cdot \mathbf{r}_l) A_n(\mathbf{r}_l) \right) \times \\ & \left( \frac{1}{2\pi} \iint_{\mathcal{D}(\mathbf{r}_0)} J_n(k_\perp |\mathbf{r}|) \exp(in \arg(\mathbf{r})) \exp(-i\mathbf{k} \cdot \mathbf{r}) d\mathbf{r} \right) . \quad (\text{G.4}) \end{aligned}$$

In this equation we recognize two Fourier integrals on a restricted domain of local functions, and two sums related to the Bloch transform. The sum over  $\exp(-i\mathbf{k} \cdot \mathbf{r}_l) A_n(\mathbf{r}_l)$  is very similar to the Bloch transform, except that  $A_n$  coefficients are used instead of  $B_n$  coefficients. Since, except for  $n = 0$ ,  $A_n$  and  $B_n$  are linearly related through the boundary conditions, we can expect the same behaviour for both sums. The two integrals depend on the lattice structure only through the integration domain, whereas the Bloch transform type sums are, as we have shown earlier, extremely sensitive to the lattice structure and to the actual Bloch vector of the field. The Bloch transform extracts the important information relative to the lattice, whereas the Fourier transform also incorporates the Fourier components of the field around each inclusion.

## Appendix H

# Modes and Mode Classes

The well established classification of guided modes in conventional fibres in  $\text{HE}_{\nu,m}$ ,  $\text{EH}_{\nu,m}$ ,  $\text{TE}_m$  and  $\text{TM}_m$  modes was defined using the  $\text{C}_{\infty v}$  property of those fibres, and is therefore not *a priori* applicable to guides of other symmetries<sup>1</sup>. Nevertheless, some modes of MOFs can be very similar to conventional fibre modes, and it is often useful for comparison purposes to know the conventional fibre equivalent of certain MOF modes. Especially when asymptotic models such as CF1 or CF2 become valid, strong parallels can be drawn between conventional fibre modes and MOF modes.

In a  $\text{C}_{\infty v}$  waveguide, the HE/EH classification uses modes such that the  $E_z$  and  $H_z$  components are given, in the coordinates with origin at the center of the fibre, by a single Fourier-Bessel component  $\nu, -\nu$  in the core. In MOFs the field result from the superposition of multiple Fourier-Bessel series centered around each inclusion. We have seen (*cf.* Appendix C) how to transform these into a single Fourier-Bessel series centered at the origin: these coefficients are given by the Fourier-Bessel coefficients  $\tilde{\mathbf{A}}^0$  and  $\tilde{\mathbf{B}}^0$ . If for a given  $\nu$  components  $A_{\nu}^{\text{E}0}$ ,  $A_{-\nu}^{\text{E}0}$ ,  $A_{\nu}^{\text{K}0}$  and  $A_{-\nu}^{\text{K}0}$  are much larger in magnitude than all other Fourier-Bessel components,  $E_z$  and  $H_z$  in the core and outside the inclusion region can be approximated by a single Fourier-Bessel component. The correspondence to the HE/EH modes of a conventional fibre is then straight-forward.

In the general case of MOF modes, no  $\tilde{\mathbf{A}}^0$  component is clearly higher in magnitude than others, and no corresponding HE/EH mode can be found. At the best the MOF mode could be seen as a superposition of HE/EH modes, but the interest of such a decomposition becomes doubtful.

The analysis of particular single MOF modes in the CF2 regime showed that the first 3 modes of MOFs are among the few modes to which conventional fibre modes can be associated, but that for higher order modes no one to one relationship can be found. Table H.1 summarizes the first few modes of MOFs and their conventional fibre counterparts.

A more general analysis can be done by comparing the general form of the fields of HE and EH modes as can be found in Ref. [3][Table 12-3] and the field expansions of table IV in Ref. [76]. Equating the angular Fourier components of these expansions shows that MOF modes of a given class may correspond to the superposition of specific HE/EH modes. Conversely, some HE/EH modes can only be of specific symmetry classes. Nevertheless no general one to one relationship can be deduced from these results, summarized in table H.2.

---

<sup>1</sup>Note that the HE/EH nomenclature can be extended to leaky modes [3].

Conventional Fibres	MOF		
Mode	Symmetry Class	Mode number	Notes
HE <sub>1,1</sub>	3,4	1	Fundamental, degenerate
TE <sub>1</sub>	2	1	2 <sup>nd</sup> mode, non degenerate
TM <sub>1</sub>	1	1	3 <sup>rd</sup> mode, non degenerate

Table H.1: Correspondence between main C<sub>6v</sub> MOF modes and conventional fibres modes.

Symmetry Class	Modes resulting from a superposition of
1	TM <sub>m</sub> , HE <sub>6ν,l</sub> , EH <sub>6μ,k</sub>
2	TE <sub>m</sub> , HE <sub>6ν,l</sub> , EH <sub>6μ,k</sub>
3,4	HE <sub>6ν±1,l</sub> , EH <sub>6μ±1,k</sub>
5,6	HE <sub>6ν±2,l</sub> , EH <sub>6μ±2,k</sub>
7	HE <sub>3ν,l</sub> , EH <sub>3μ,k</sub>
8	HE <sub>3ν,l</sub> , EH <sub>3μ,k</sub>

Table H.2: Correspondence between C<sub>6v</sub> classes of symmetry and conventional fibres modes.  $k, l, m, \nu, \mu$  are integers with  $k, l, m \geq 1$  and  $\mu, \nu \geq 0$ .

# Appendix I

## Publications

### Journal Papers:

1. Multipole Method for Microstructured Optical Fibers I : Formulation, *T. P. White, B. T. Kuhlmei, R. C. McPhedran, D. Maystre, G. Renversez, C. Martijn de Sterke, and L. C. Botten*, J. Opt. Soc. B. **19**, pp. 2322-2330 (2002).
2. Multipole Method for Microstructured Optical Fibers II : Implementation and Results, *B. T. Kuhlmei, T. P. White, G. Renversez, D. Maystre, L. C. Botten, C. Martijn de Sterke, and R. C. McPhedran*, J. Opt. Soc. B. **19**, pp. 2331-2340 (2002).
3. Modal "Cutoff" in Microstructured Optical Fibers, *B. T. Kuhlmei, R. C. McPhedran, and C. M. de Sterke*, Opt. Lett. **27**, pp. 1684-1686 (2002).
4. Microstructured Optical Fibers: Where's the Edge ?, *B. T. Kuhlmei, R. C. McPhedran, C. M. de Sterke, P. A. Robinson, G. Renversez, and D. Maystre*, Opt. Express **10**, pp. 1285-1290 (2002), <http://www.opticsexpress.org/abstract.cfm?URI=OPEX-10-22-1285>.
5. Chromatic Dispersion and Losses of Microstructured Optical Fibers, *B. Kuhlmei, G. Renversez, and D. Maystre*, Applied Optics OT **42**, pp. 634-639 (2003).
6. Dispersion Management with Microstructured Optical Fibers: Ultra-flattened Chromatic Dispersion with Low Losses, *G. Renversez, B. Kuhlmei, and R. McPhedran*, Opt. Lett. **28**, June, to be published (2003).

### Communications with Proceedings:

7. Rigorous Electromagnetic Theory of Microstructured Optical Fibers, *B. T. Kuhlmei, G. Renversez, D. Maystre*, European Symposium on Numerical Methods in Electromagnetics, JEE 2002 March – Toulouse, France.
8. Photonic Crystals: Modal Theory of PC Optical Fibers and Numerical Application, *B. T. Kuhlmei, G. Renversez, D. Maystre*, 3rd ISAAC Congress, August 2001 – Berlin, Germany.
9. Multipole Study of Dispersion and Structural Losses of Photonic Crystal Fibers, *B. T. Kuhlmei, G. Renversez, D. Maystre, T. P. White, R. C. McPhedran, L. C. Botten, C. M. de Sterke*, SPIE Photonics West, January 2002 – San Jose, California, USA;

Proc. SPIE Vol. 4655, "Photonic Bandgap Materials and Devices", Ali Adibi; Axel Scherer; Shawn-Yu Lin; Eds. p. 114-123 (2002).

10. Numerical Investigation of Photonic Crystal Fibers by Means of Finite Element and Matrix of Diffraction methods, *A. Nicolet, S. Guenneau, F. Zolla, C. Geuzaine, B. Kuhlmei, G. Renversez*, IUTAM Symposium 02/4, July 2002 – Liverpool, UK.
11. Losses and Dispersion of Microstructured Optical Fibre, *B. Kuhlmei, G. Renversez, D. Maystre, T. White, R. McPhedran, L. Botten, and M. de Sterke*, Progress in Electromagnetics Research Symposium 2002. The Electromagnetics Academy (2002).

#### Other Conferences and Communications:

12. Modes and their Transitions in Microstructured Optical Fibers, *R. C. McPhedran, C. M. de Sterke, P. A. Robinson, B. T. Kuhlmei, G. Renversez and D. Maystre*, IEEE LEOS Summer Topicals Meeting Series 2003 – Holey Fibers and Photonic Crystals, Vancouver, British Colombia, Canada, July 2003 (Invited).
13. Losses and dispersion of microstructured optical fibers: a rigorous vector modeling. *G. Renversez, B. Kuhlmei, D. Maystre, T. White, R. C. McPhedran and L. C. Botten.*, FiberComm 2003, Munich, Germany, June 2003 (Invited).
14. Study of the Number and Nature of Modes of Microstructured Optical Fibers, *B. T. Kuhlmei, C. M. de Sterke, R. C. McPhedran, L. C. Botten, G. Renversez*, OSA Annual Meeting 2002, Orlando, Florida.
15. Photonic Crystal Fibers, *C. M. de Sterke, L. C. Botten, B. T. Kuhlmei, D. Maystre, R. C. McPhedran, G. Renversez , T. P. White*, Photonic Crystals Down Under, Canberra, Australia, August 2002.
16. Modelling of photonic crystal fibers, *B. T. Kuhlmei, G. Renversez, D. Maystre*, EOS Electromagnetic Optics 2nd Topical Meeting – Paris, France, August 2001.
17. Electromagnetic theory of optical fibers made with photonic crystals, *B. T. Kuhlmei, G. Renversez, D. Maystre*, PIERS 2001 – Osaka, Japan, July 2001.
18. Théorie des fibres optiques à cristaux photoniques, *B. T. Kuhlmei, D. Maystre, G. Renversez*, Optix – Marseille, France, November 2001.
19. Fibres optiques microstructurées : étude numérique des pertes et de la dispersion *B. T. Kuhlmei, G. Renversez, D. Maystre*, GdR Cristaux Photoniques – Montpellier, France, December 2001.
20. Confinement losses in microstructured optical fibres, *B. T. Kuhlmei, T. P. White, M. de Sterke, R. McPhedran, L. Botten, D. Maystre, G. Renversez*, Proceedings of the Australian Conference on Optics, Lasers and Spectroscopy 2001 – Brisbane, Queensland, Australia, paper Th(d)2, p. 86, (2001).

**Books:**

21. Photonic Crystal Optical Fibres: Theoretical Analysis and Numerical Modelling, *F. Zolla, G. Renversez, A. Nicolet, B. Kuhlmey, S. Guenneau, D. Felbacq*, Imperial College Press, London, to be published (2003).

# Appendix J

## Notations

### Fourier-Bessel Coefficients

Notation	relating to	Field	Comments
$A_n^{\text{El}}$	$J_n$	$E_z$	If $l > 0$ , local expansion around inclusion $l$ . If $l = 0$ the coefficient refers to the jacket.
$B_n^{\text{El}}$	$H_n^{(1)}$	$E_z$	
$A_n^{\text{Kl}}$	$J_n$	$K_z$	
$B_n^{\text{Kl}}$	$H_n^{(1)}$	$K_z$	
$\tilde{A}_n^l$	$J_n$	$E_z$ and $K_z$	
$\tilde{B}_n^l$	$H_n^{(1)}$	$E_z$ and $K_z$	
$\mathcal{H}, \mathcal{J}$	Change of basis matrices		

### Refractive Indices and Related Quantities

Notation	Description
$n_{\text{eff}}$	effective index of a mode
$n_{\text{FSM}}$	effective index of the fundamental space filling mode of an infinite photonic crystal
$n_i$	refractive index of inclusion $i$
$n_{\text{i}}$	Common refractive index of all inclusions where applicable
$n_0$	Refractive index of the jacket for MOFs
$n_{\text{J}}$	Refractive index of the jacket in the CF1 and CF2 models
$n_{\text{M}}$	Refractive index of the matrix.

### MOF Geometry

Notation	Description
$N_{\text{i}}$	Number of inclusions
$N_{\text{r}}$	Number of rings or layers of a MOF with hexagonally packed inclusions
$\Lambda$	Pitch of a hexagonal lattice
$d$	inclusion diameter
$\mathbf{c}_i$	center of inclusion $i$

## Fields, Bloch Transform and related Quantities

Notation	Description
$\beta$	propagation constant of a mode
$N_b$	Number of Bloch components
$\omega$	angular frequency
$\lambda$	vacuum wavelength
$\mathcal{B}^T$	total Bloch transform, Eq. (5.21)
$\mathcal{B}_n$	Bloch transform of order $n$ , Eq. (5.20)
$k_0$	vacuum wavenumber $2\pi/\lambda$
$\mathcal{E}$	Electric field with its complete spatial and temporal dependence
$\mathcal{K}$	Scaled magnetic field with its complete spatial and temporal dependence
$\mathbf{E}$	Electric field, without its $z$ and temporal dependence
$\mathbf{H}$	Magnetic field, without its $z$ and temporal dependence
$\mathbf{K}$	Scaled magnetic field, without its $z$ and temporal dependence
$\hat{B}_n^i$	Amplitude associated with Bloch component $i$ of the Fourier-Bessel coefficients of order $n$ .

## Miscellany

Notation	Description
$\Im$	Imaginary part
$\Re$	Real part
$\text{diag}[a_1, a_2, \dots, a_n]$	The diagonal matrix with diagonal elements $a_i$ . If $a_i$ are matrices, the block-diagonal matrix with blocks $a_i$ .
$M$	Truncation order of Fourier-Bessel series.

# Bibliography

- [1] T.P. White, B.T. Kuhlmey, R.C. McPhedran, D. Maystre, G. Renversez, C.M. de Sterke, and L. C. Botten. Multipole method for microstructured optical fibers. I. Formulation. *J. Opt. Soc. Am. B*, 19(10):2322–2330, 2002.
- [2] Pierre et Michel Troisgros. *Cuisine de famille chez les Troisgros*. Flammarion, 1998.
- [3] A.W. Snyder and J.D. Love. *Optical waveguide theory*. Chapman & Hall, London, 1996.
- [4] G.P. Agrawal. *Nonlinear fibre optics*. Academic Press, San Diego, 1995.
- [5] D. B. Keck, R. D. Maurer, and P.C. Schultz. Ultimate lower limit of attenuation in glass optical waveguides. *Appl. Phys. Lett.*, 22:307–309, 1973.
- [6] G. A. Thomas, B. I. Shraiman, P. F. Glodis, and M. J. Stephen. Towards the clarity limit in optical fibre. *Nature*, 404:262–264, 2000.
- [7] S. C. Rashleigh and R. Ulrich. Polarization mode dispersion in single-mode fibres. *Opt. Lett.*, 3:60–62, 1978.
- [8] I. M. Jauncey R. J. Mears, L. Reekie and D. N. Payne. Low-noise Erbium-doped fiber amplifier operating at 1.54  $\mu\text{m}$ . *Electron. Lett.*, 23(17):884–885, 1987.
- [9] J. K. Ranka, R. S. Windeler, and A. J. Stentz. "visible continuum generation in air-silica microstructure optical fibers with anomalous dispersion at 800 nm. *Opt. Lett.*, 25:25–27, 2000.
- [10] S. Coen, A. Hing Lun Chau, R. Leonhardt, J. D. Harvey, J. C. Knight, W. J. Wadsworth, and Ph. St. J. Russell. White-light supercontinuum generation with 60-ps pump pulses in a photonic crystal fiber. *Opt. Lett.*, 26:1356–1358, 2001.
- [11] J. P. Dudley, L. Provino, N. Grossard, H. Maillotte, R. S. Windeler, B. J. Eggleton, and S. Coen. Supercontinuum generation in air-silica microstructured fibers with nanosecond and femtosecond pulse pumping. *J. Opt. Soc. Am. B*, 19:765–771, 2002.
- [12] A. V. Husakou and J. Herrmann. Supercontinuum generation of higher-order solitons by fission in photonic crystal fibers. *Phys. Rev. Lett.*, 87:203901, 2001.
- [13] S. John. Strong localization of photons in certain disordered dielectric superlattices. *Phys. Rev. Lett.*, 58:2486–2489, 1987.
- [14] E. Yablonovitch. Inhibited spontaneous emission in solid-state physics and electronics. *Phys. Rev. Lett.*, 58:2059–2062, 1987.

- [15] Y. Fink, J. N. Winn, S. Fan, C. Chen, J. Michel, J. D. Joannopoulos, and E. L. Thomas. A dielectric omnidirectional reflector. *Science*, 282:1679–1682, 1998.
- [16] R. Ulrich. Far-infrared properties of metallic mesh and its complementary structure. *Infrared Phys.*, 7:37–55, 1967.
- [17] R. Ulrich. Interference filters for the far infrared. *Appl. Optics*, 7:1987–1996, 1968.
- [18] H. Sami. Sözüer and J. P. Dowling. Photonic band calculations for woodpile structures. *Journal of Modern Optics*, 41(2):231–239, 1994.
- [19] K. M. Ho, C. T. Chan CT, C. M. Soukoulis, R. Biswas, and M. Sigalas. Photonic bandgaps in 3-dimensions - new layer-by-layer periodic structures. *Solid State Commun.*, 89(5):413–416, 1994.
- [20] J. G. Fleming and S.-Y. Lin. Three-dimensional photonic crystal with a stop band from 1.35 to 1.95  $\mu\text{m}$ . *Optics Letters*, 64:49–51, 1999.
- [21] S. Y. Lin, J. G. Fleming, D. L. Hetherington, B. K. Smith, R. Biswas, K. M. Ho, M. M. Sigalas, W. Zubrzycki, S. R. Kurtz, and J. Bur. A three-dimensional photonic crystal operating at infrared wavelengths. *Nature*, 394:251–253, 1998.
- [22] S. Noda, K. Tomoda, N. Yamamoto, and A. Chutinan. Full three-dimensional photonic bandgap crystal at near-infrared wavelengths. *Science*, 289:604, 2000.
- [23] B. Gralak, M. de Dood, G. Tayeb, S. Enoch, and D. Maystre. Theoretical study of photonic bandgaps in woodpile crystals. *Phys. Rev. E*, 2003. accepted for publication.
- [24] Y. A. Vlasov, X.-Z. Bo, J. C. Sturm, and D. J. Norris. On-chip natural assembly of silicon photonic bandgap crystals. *Nature*, 414:289–293, 2001.
- [25] A. Blanco, E. Chomski, S. Grabtchak, M. Ibisate, S. John, S. W. Leonard, C. Lopez, F. Meseguer, H. Miguez, J. P. Mondia, G. A. Ozin, O. Toader, and H. M. van Driel. Large-scale synthesis of a silicon photonic crystal with a complete three-dimensional bandgap near 15 micrometres. *Nature*, 405:437–440, may 2000.
- [26] F. Benabid, J. C. Knight, and P. St. J. Russell. Particle levitation and guidance in hollow-core photonic crystal fiber. *Opt. Express*, 10(21):1195–1203, 2002. <http://www.opticsexpress.org/abstract.cfm?URI=OPEX-10-21-1195>.
- [27] J. N. Winn, Y. Fink, S. Fan, and J. D. Joannopoulos. Omnidirectional reflection from a one-dimensional photonic crystal. *Opt. Lett.*, 23(20):1573–1575, 1998.
- [28] B. Temelkuran, S. D. Hart, G. Benoit, J. D. Joannopoulos, and Y. Fink. Wavelength-scalable hollow optical fibres with large photonic bandgaps for  $\text{CO}_2$  laser transmission. *Nature*, 420:650–653, 2002.
- [29] A. Argyros. Guided modes and loss in Bragg fibres. *Opt. Express*, 10(24):1411–1417, 2002. <http://www.opticsexpress.org/abstract.cfm?URI=OPEX-10-24-1411>.
- [30] I. M. Bassett and A. Argyros. Elimination of polarization degeneracy in round waveguides. *Opt. Express*, 10(23):1342–1346, 2002. <http://www.opticsexpress.org/abstract.cfm?URI=OPEX-10-23-1342>.

- [31] R. F. Cregan, B. J. Mangan, J. C. Knight, T. A. Birks, P. St. J. Russell, P. J. Roberts, and D. C. Allan. Single-mode photonic band gap guidance of light in air. *Science*, 285:1537–1539, 1999.
- [32] A. Ferrando, E. Silvestre, J.J. Miret, P. Andres, and M. V. Andres. Donor and acceptor guided modes in photonic crystal fibers. *Opt. Lett.*, 25(18):1328–1330, 2000.
- [33] P. Kaiser and H. W. Astle. Low-loss single-material fibers made from pure fused silica. *Bell Syst. Tech. J.*, 53(6):1021–1039, 1974.
- [34] J. C. Knight, T. A. Birks, P. St. J. Russell, and D. M. Atkin. All silica single-mode optical fiber with photonic crystal cladding. *Opt. Lett.*, 21(19):1547–1549, 1996.
- [35] B. Kuhlmeiy, G. Renversez, and D. Maystre. Chromatic dispersion and losses of microstructured optical fibers. *Appl. Optics*, 42:634–639, 2003.
- [36] W. H. Reeves, J. C. Knight, and P. St. J. Russell. Demonstration of ultraflattened dispersion in photonic crystal fibers. *Opt. Express*, 10:609–613, 2002. <http://www.opticsexpress.org/abstract.cfm?URI=OPEX-10-14-609>.
- [37] J. C. Knight, J. Arriaga, T. A. Birks, A. Ortigosa-Blanch, W. J. Wadsworth, and P. S. Russell. Anomalous dispersion in photonic crystal fiber. *IEEE Photonic Tech. Lett.*, 12:807–809, 2000.
- [38] A. Ferrando, E. Silvestre, J. J. Miret, and P. Andrés. Nearly zero ultraflattened dispersion in photonic crystal fibers. *Opt. Lett.*, 25:790–792, 2000.
- [39] D. Mogilevtsev, T.A. Birks, and P. St. J. Russell. Group-velocity dispersion in photonic crystal fibres. *Opt. Lett.*, 23:1662–1664, 1998.
- [40] J. H. V. Price, W. Belardi, T. M. Monro, A. Malinowski, A. Piper, and D. J. Richardson. Soliton transmission and supercontinuum generation in holey fiber, using a diode pumped ytterbium fiber source. *Opt. Express*, 10(8):382–387, 2002. <http://www.opticsexpress.org/abstract.cfm?URI=OPEX-10-8-382>.
- [41] J. Herrmann, U. Griebner, N. Zhavoronkov, A. Husakou, D. Nickel, J. C. Knight, P. St. J. Russell W. J. Wadsworth, and G. Korn1. Experimental evidence for supercontinuum generation by fission of higher-order solitons in photonic fibers. *Phys. Rev. Lett.*, 88(17):173901, 2002.
- [42] X. Liu, C. Xu, W. H. Knox, J. K. Chandalia, B. J. Eggleton, S. G. Kosinski, and R. S. Windeler. Soliton self-frequency shift in a short tapered air-silica microstructure fiber. *Opt. Lett.*, 26(6):358–360, 2001.
- [43] B. R. Washburn, S. E. Ralph, and R. S. Windeler. Ultrashort pulse propagation in air-silica microstructure fiber. *Opt. Express*, 10(13):575–580, 2002. <http://www.opticsexpress.org/abstract.cfm?URI=OPEX-10-13-575>.
- [44] A. Ferrando, M. Zacarés, P. Fernández de Córdoba, D. Binosi, and J. A. Monsoriu. Spatial soliton formation in photonic crystal fibers. *Opt. Express*, 11(5):452–459, 2003. <http://www.opticsexpress.org/abstract.cfm?URI=OPEX-11-5-452>.

- [45] M.J. Steel, T. P. White, C.M. de Sterke, R.C. McPhedran, and L.C. Botten. Symmetry and degeneracy in microstructured optical fibres. *Opt. Lett.*, 26:488–490, 2001.
- [46] K. Suzuki, H. Kubota, S. Kawanishi, M. Tanaka, and M. Fujita. Optical properties of a low-loss polarization-maintaining photonic crystal fiber. *Opt. Express*, 9(13):676–680, 2001. <http://www.opticsexpress.org/abstract.cfm?URI=OPEX-9-13-676>.
- [47] M. J. Steel and Jr. R. M. Osgood. Polarization and dispersive properties of elliptical-hole photonic crystal fibers. *J. Lightwave Technol.*, 19(4):495–503, 2001.
- [48] P. M. Blanchard, J. G. Burnett, G. R. G. Erry, A. H. Greenaway, P. Harrison, B. Mangan, J. C. Knight, P. S. Russell, M. J. Gander, R. McBride, and J. D. C. Jones. Two-dimensional bend sensing with a single, multi-core optical fibre. *Smart Mater. Struct.*, 9(2):132–140, 2000.
- [49] B. J. Eggleton, C. Kerbage, P. S. Westbrook, and R. S. Windeler and A. Hale. Microstructured optical fiber devices. *Opt. Express*, 9(13):698–713, 2001. <http://www.opticsexpress.org/abstract.cfm?URI=OPEX-9-13-698>.
- [50] M. Maeda and S. Yamada. Leaky modes on W-fibers: mode structure and attenuation. *Appl. Optics*, 16:2198–2203, 1977.
- [51] P. L François and C. Vassallo. Finite caldding effects in W-fibers: a new interpretation of leaky modes. *Appl. Optics*, 22(19):3109–3120, 1983.
- [52] P. T. Leung and K. M. Pang. Completeness and time-independent perturbation of morphology-dependent resonances in dielectric spheres. *J. Opt. Soc. Am. B*, 13(5):805–817, 1996.
- [53] P. T. Leung, S. S. Tong, and K. Young. Two-component eigenfunction expansion for open systems described by the wave equation i: completeness of expansion. *J. Phys. A: Math. Gen.*, 30:2139–2151, 1997.
- [54] P. T. Leung, S. S. Tong, and K. Young. Two-component eigenfunction expansion for open systems described by the wave equation ii: linear space structure. *J. Phys. A: Math. Gen.*, 30:2153–2162, 1997.
- [55] P. T. Leung, W. M. Suen, C. P. Sun, and K. Young. Waves in open systems via a biorthogonal basis. *Phys. Rev. E*, 57(5):6101–6104, 1998.
- [56] K. C. Ho, P. T. Leung, A. M. van den Brink, and K. Young. Second quantization of open systems using quasinormal modes. *Phys. Rev. E*, 58(3):2965–2978, 1998.
- [57] K. M. Lee, P. T. Leung, and K. M. Pang. Dyadic formulation of morphology-dependent resonances. i. completeness relation. *J. Opt. Soc. Am. B*, 16(9):1409–1417, 1999.
- [58] K. M. Lee, P. T. Leung, and K. M. Pang. Dyadic formulation of morphology-dependent resonances. ii. perturbation theory. *J. Opt. Soc. Am. B*, 16(9):1418–1430, 1999.
- [59] S.W. Ng, P. T. Leung, and K. M. Lee. Dyadic formulation of morphology-dependent resonances. iii. degenerate perturbation theory. *J. Opt. Soc. Am. B*, 19(1):154–164, 2002.

- [60] T. A. Birks, J. C. Knight, and St. J. Russel. Endlessly single-mode photonic crystal fiber. *Optics Letters*, 22(13):961–963, 1997.
- [61] M. Midrio, M.P. Singh, and C.G. Someda. The space filling mode of holey fibres: an analytic vectorial solution. *J. Lightwave Technol.*, 18:1031–1048, 2000.
- [62] F. Brechet, J. Marcou, D. Pagnoux, and P. Roy. Complete analysis of the characteristics of propagation into photonic crystal fibers, by the finite element method. *Opt. Fibre. Technol.*, 6:181–191, 2000.
- [63] A. Ferrando, E. Silvestre, J. J. Miret, and P. Andrés. Vector description of higher-order modes in photonic crystal fibers. *J. Opt. Soc. Am. A*, 17:1333–1340, 2000.
- [64] A.A. Maradudin and A.R. McGurn. Out-of-plane propagation of electromagnetic-waves in a 2-dimensional periodic dielectric medium. *J. Mod. Optic*, 41:275–284, 1994.
- [65] J. Broeng, T. Sondergaard, S. E. Barkou, P. M. Barbeito, and A. Bjarklev. Waveguide guidance by the photonic bandgap effect in optical fibre. *J. Opt. A- Pure Appl. Opt.*, 1:477–482, 1999.
- [66] T. M. Monro, D.J. Richardson, N.G.R. Broderick, and P.J. Bennett. Holey optical fibers: an efficient modal model. *J. Lightwave Technol.*, 17:1093–1102, 2000.
- [67] D. Mogilevtsev, T.A. Birks, and P. St. J. Russell. Localized function method for modeling defect modes in 2-d photonic crystals. *J. Lightwave Technol.*, 17:2078–2081, 2000.
- [68] B.J. Eggleton, P.S. Westbrook, C.A. White, C. Kerbage, R.S. Windeler, and G.L. Burdge. Cladding-mode-resonances in air-silica microstructure optical fibers. *J. Lightwave Technol.*, 18:1084–1100, 2000.
- [69] J. K. Ranka, R. S. Windeler, and A. J. Stentz. Optical properties of high-delta air-silica microstructure optical fibres. *Opt. Lett.*, 25:796–797, 2000.
- [70] K. Saitoh, M. Koshiba, T. Hasegawa, and E. Sasaoka. Chromatic dispersion control in photonic crystal fibers: application to ultra-flattened dispersion. *Opt. Express*, 11(8):843–852, 2003. <http://www.opticsexpress.org/abstract.cfm?URI=OPEX-11-8-843>.
- [71] A. Nicolet, S. Guenneau, F. Zolla, C. Geuzaine, B. Kuhlmei, and G. Renversez. Numerical investigation of photonic crystal fibres by means of finite element and multipole methods. In *Proceedings of IUTAM 2002, Asymptotics, singularities and homogenization in problems of mechanics*, Liverpool, to be published, 2003. IUTAM, Kluwer Academic Press.
- [72] L. Poladian, N. I. Issa, and T. M. Monro. Fourier decomposition algorithm for leaky modes of fibres with arbitrary geometry. *Opt. Express*, 10(10):449–454, 2002.
- [73] N. A. Issa and L. Poladian. Vector wave expansion method for leaky modes of microstructured optical fibres. *J. Lightwave Technol.*, 20, April 2003.
- [74] N. A. Issa. Private communication, May 2003.

- [75] K.M. Lo, R.C. McPhedran, I.M. Bassett, and G. W. Milton. An electromagnetic theory of dielectric waveguides with multiple embedded cylinders. *J. Lightwave Technol.*, 12:396–410, 1994.
- [76] P. R. McIsaac. Symmetry-induced modal characteristics of uniform waveguides-I: Summary of results. *IEEE Trans. Microwave Theory Tech.*, MTT-23:421–429, 1975.
- [77] D. Felbacq, G. Tayeb, and D. Maystre. Scattering by a random set of parallel cylinders. *Journal of The Optical Society of America A*, 9:2526–2538, 1994.
- [78] E. Yamashita, S. Ozeki, and K. Atsuki. Modal analysis method for optical fibers with symmetrically distributed multiple cores. *J. Lightwave Technol.*, 3:341–346, 1985.
- [79] R. F. Cregan, J. C. Knight, P. St. J. Russell, and P. J. Roberts. Distribution of spontaneous emission from an  $\text{Er}^{3+}$ -doped photonic crystal fiber. *J. Lightwave Technol.*, 17(11):2138–2141, 1999.
- [80] W. Wijngaard. Guided normal modes of two parallel circular dielectric rods. *J. Opt. Soc. Am.*, 63:944–949, 1973.
- [81] C.S. Chang and H.C. Chang. Theory of the circular harmonics expansion method for multiple-optical-fiber system. *J. Lightwave Technol.*, 12(3):415–417, 1994.
- [82] M. Abramowitz and I. A. Stegun. *Handbook of mathematical functions*. Dover Publications, Inc., New York, 9 edition, 1965.
- [83] D. Maystre and P. Vincent. Diffraction d’une onde électromagnétique plane par un objet cylindrique non-infiniment conducteur de section arbitraire. *Optics Communications*, 5(5):327–330, August 1972.
- [84] B.T. Kuhlmeier, T.P. White, G. Renversez, D. Maystre, L. C. Botten, C.M. de Sterke, and R.C. McPhedran. Multipole method for microstructured optical fibers. II. Implementation and results. *J. Opt. Soc. Am. B*, 19(10):2331–2340, 2002.
- [85] T. White. Microstructured optical fibres - a multipole formulation. Honours degree thesis, School of Physics, University of Sydney, October 2000.
- [86] W. H. Press, B. P. Flannery, S. A. Teukolsky, and W. T. Vetterling. *Numerical recipes*. Cambridge University Press, Cambridge, 1986.
- [87] P. Kravanja and M. Van Barel. *Computing the zeros of analytic functions*. Springer, Berlin, 2000.
- [88] L. C. Botten, M. S. Craig, and R. C. McPhedran. Complex zeros of analytic functions. *Comp. Phys. Comm.*, 29:245–259, 1983.
- [89] C. G. Broyden. A class of methods for solving nonlinear simultaneous equations. *Mathematics of Computation*, 19:577–593, 1965.
- [90] F. Zolla and R. Petit. Method of fictitious sources as applied to the electromagnetic diffraction of a plane wave by a grating in conical mounts. *J. Opt. Soc. Am. A*, 13(4):1087–1096, April 1996.

- [91] E. Centeno and D. Felbacq. Rigorous vector diffraction of electromagnetic waves by bidimensional photonic crystals. *J. Opt. Soc. Am. A*, 17(2):320–327, February 2000.
- [92] H. Kubota, K. Suzuki, S. Kawanishi, M. Nakazawa, M. Tanaka, and M. Fujita. Low-loss, 2 km-long photonic crystal fiber with zero gvd in the near ir suitable for picosecond pulse propagation at the 800 nm band. In *OSA Trends in Optics and Photonics, Conf. Lasers and Electro-Optics (CLEO 2001), Technical Digest*, volume 56, page CPD3. Optical Society of America, Washington DC, 2001, 2001.
- [93] G. Allaire, C. Conca, and M. Vanninathan. The Bloch transform and applications. In ESAIM Proceedings, editor, *Actes du 29<sup>ème</sup> Congrès d’analyse numérique: CANUM’97*, volume 3, pages 65–84, 1998. URL <http://www.emath.fr/proc/vol.3/>.
- [94] B. T. Kuhlmeiy, R.C. McPhedran, and C.M. de Sterke. Modal cutoff in microstructured optical fibers. *Opt. Lett.*, 27(19):1684–1686, 2002.
- [95] B.T. Kuhlmeiy, R.C. McPhedran, C.M. de Sterke, P.A. Robinson, G. Renversez, and D. Maystre. Microstructured optical fibers : Where’s the edge ? *Opt. Express*, 10:1285–1290, 2002. <http://www.opticsexpress.org/abstract.cfm?URI=OPEX-10-22-1285>.
- [96] J. D. Joannopoulos, R. D. Meade, and J. N. Winn. *Photonic crystals – molding the flow of light*. Princeton University Press, 1995.
- [97] J. C. Knight, T. A. Birks, and St. J. Russell. Properties of photonic crystal fiber and the effective index model. *Journal of The Optical Society of America A*, 15(4):746–750, 1998.
- [98] N. A. Mortensen. Effective area of photonic crystal fibers. *Opt. Express*, 10:341–348, 2002. <http://www.opticsexpress.org/abstract.cfm?URI=OPEX-10-7-341>.
- [99] J. Broeng, D. Mogilevstev, S. E. Barkou, and A. Bjarklev. Photonic crystal fibers: A new class of optical waveguides. *Opt. Fiber Technol.*, 5:305–330, 1999.
- [100] J. R. Folkenberg, N. A. Mortensen, K. P. Hansen, T. P. Hansen, H. R. Simonsen, and C. Jacobsen. Experimental investigation of cut-off phenomena in non-linear photonic crystal fibers. *Submitted to Opt. Lett.*, 2002.
- [101] N. A. Mortensen, J. R. Folkenberg, M. D. Nielsen, and K. P. Hansen. Modal cut-off and the  $v$ -parameter in photonic crystal fibers. *Sumbitted to Opt. Lett.*, 2003.
- [102] G. W. Milton. *The Theory of Composites*. Cambridge University Press, 2002.
- [103] B. K. P. Scaife. *Principles of Dielectrics*. Clarendon Press, Oxford, 1998.
- [104] C. G. Poulton. *Asymptotics and wave propagation in cylindrical geometries*. PhD thesis, University of Sydney, 1999.
- [105] R. C. McPhedran, C. G. Poulton, N. A. Nicorovici, and A. B. Movchan. Low frequency corrections to the static effective dielectric constant of a two-dimensional composite material. *P. Roy. Soc. Lond. A. Mat.*, 452:2231–2245, 1996.
- [106] N. S. Kapany and J. J. Burke. *Optical Waveguides*. Academic Press, New York and London, 1972.

- [107] G. H. Smith, L. C. Botten, R. C. McPhedran, and N. A. Nicorovici. Cylinder gratings in conical incidence with applications to modes of air-cored photonic crystal fibers. *Phys. Rev. E*, 66:art. no. 056604, 2002.
- [108] L. C. Botten, N. A. Nicorovici, R. C. McPhedran, C.M. de Sterke, and A. A. Asatryan. Photonic band structure calculations using scattering matrices. *Phys. Rev. E*, 64:art. no. 056604, 2001.
- [109] J. Broeng T. Sorensen, A. Bjarklev, E. Knudsen, and S. E. B. Libori. Macro-bending loss properties of photonic crystal fibre. *Electron. Lett.*, 37:287–289, 2001.
- [110] T. Sørensen, J. Broeng, A. Bjarklev, T.P. Hansen, E. Knudsen, S. E. B. Libori, H. R. Simonsen, and J. R. Jensen. Spectral macro-bending loss considerations for photonic crystal fibres. *IEE P.-Optoelectron.*, 149:206–210, 2002.
- [111] T. Monro, P. J. Bennett, N. G. Broderick, and D. J. Richardson. Holey fibers with random cladding distributions. *Opt. Lett.*, 25:206–208, 2000.
- [112] E. Snitzer, H. Po, F. Hakimi, R. Tumminelli, , and B. C. McCollum. Double-clad, offset core nd fiber laser. In *Optical Fiber Sensors*, OSA Technical Digest Series, page paper PD5. Optical Society of America, Washington, D.C., 1988.
- [113] K. Furusawa, A. Malinowski, J. H. V. Price, T. M. Monro, J. K. Sahu, J. Nilsson, and D. J. Richardson. Cladding pumped ytterbium-doped fiber laser with holey inner and outer cladding. *Opt. Express*, 9:714–720, 2000. <http://www.opticsexpress.org/abstract.cfm?URI=OPEX-9-13-714>.
- [114] J. Limpert, T. Schreiber, S. Nolte, H. Zellmer, A. Tünnermann, R. Iliew, F. Lederer, J. Broeng, G. Vienne, A. Petersson, and C. Jakobsen. High-power air-clad large-mode-area photonic crystal fiber laser. *Opt. Express*, 2003.
- [115] M. D. Nielsen, G. Vienne, J. R. Folkenberg, and A. Bjarklev. Investigation of microdeformation-induced attenuation spectra in a photonic crystal fiber. *Opt. Lett.*, 28:236–238, 2003.
- [116] A. Ferrando, E. Silvestre, P. Andrés, J. Miret, and M. Andrés. Designing the properties of dispersion-flattened photonic crystal fibers. *Opt. Express*, 9(13):687–697, 2001. <http://www.opticsexpress.org/abstract.cfm?URI=OPEX-9-13-687>.
- [117] G. Renversez, B. Kuhlmeier, and R. McPhedran. Dispersion management with microstructured optical fibers: Ultra-flattened chromatic dispersion with low losses. *Opt. Lett.*, 28(12), June 2003.
- [118] J. W. Fleming. Material dispersion in lightguide glasses. *Electron. Lett.*, 14(11):326–328, 1978.
- [119] T.P. White, R.C. McPhedran, C.M. de Sterke, and M.J. Steel. Confinement losses in microstructured optical fibres. *Opt. Lett.*, 26(21):1660–1662, 2001.
- [120] M. J. Gander, R. McBride, J. C. D. Jones, D. Mogilevtsev, T. A. Birks, J. C. Knight, and P. St. J. Russell. Experimental measurement of group velocity dispersion in photonic crystal fibre. *Electron. Lett.*, 35(1):63–64, 1999.

- [121] N. A. Mortensen, M. D. Nielsen, J. R. Folkenberg, A. Petersson, and H. R. Simonsen. Improved large-mode-area endlessly single-mode photonic crystal fibers. *Opt. Lett.*, 28(6):393–395, 2003.
- [122] N. A. Mortensen. Private communication, April 2003.
- [123] R. Petit, editor. *Electromagnetic theory of gratings*, chapter 5. The homogeneous Problem by M. Nevière, pages 127–129. Topics in Current Physics. Springer-Verlag, Berlin, Heidelberg, New-York, 1980.
- [124] L. Schwartz. *Mathematics for the physical sciences*. Addison-Wesley, Reading MA, 1966.